ÉCOLE DE TECHNOLOGIE SUPÉRIEURE
UNIVERSITÉ DU QUÉBEC

THESIS PRESENTED TO
ÉCOLE DE TECHNOLOGIE SUPÉRIEURE

IN PARTIAL FULFILLEMENT OF THE REQUIREMENTS FOR
THE DEGREE OF DOCTOR OF PHILOSOPHY
Ph.D.

BY
Mukhtiar SINGH

ADAPTIVE NETWORK-BASED FUZZY INFERENCE SYSTEMS FOR SENSORLESS CONTROL OF PMSG BASED WIND TURBINE WITH POWER QUALITY IMPROVEMENT FEATURES

MONTREAL, 16 JULY 2010

THIS THESIS HAS BEEN EVALUATED

BY THE FOLLOWING BOARD OF EXAMINERS

M. Ambrish Chandra, Thesis Supervisor
Département de génie électrique à l'École de technologie supérieure

M. Alain Abran, President of the Board of Examiner
Département de génie logiciel et des TI à l'École de technologie supérieure

M. Kamal Al-Haddad, Examiner
Département de génie électrique à l'École de technologie supérieure

M. Philippe Lautier, External Examiner
Vice-President, Vestas, Denmark

M. Sheldon Williamson, External Examiner
Department of Electrical and Computer Engineering, Concordia University.

THIS THESIS WAS PRESENTED AND DEFENDED

BEFORE A BOARD OF EXAMINERS AND PUBLIC

JUNE 22, 2010

AT ÉCOLE DE TECHNOLOGIE SUPÉRIEURE

ACKNOWLEDGMENT

I am deeply indebted to my research director Prof. Ambrish Chandra for his guidance, support, and continuous encouragement. I have been immensely benefitted from his technical expertise and experience in developing my research skills. I am also highly obliged for his unlimited support on my personal front without which it would not have been possible for me to finish my work.

I would also like to express my sincere gratitude to my graduate jury members Prof. Alain Abran, Prof. Kamal Al-Haddad, Dr. Philippe Lautier, and Prof. Sheldon Williamson for their valuable and constructive comments. Special thanks to Dr. Philippe Lautier and Prof. Kamal Al-Haddad for sponsoring the various hardware components required in the development of test-bench.

I was fortunate enough to work with many exceptional fellow colleagues in my research group. Among them, I especially thank Dr. Vinod Khadkikar for his wonderful company and help in developing the hardware prototype. I would like to show my gratitude to Mr. Yves Robitaille and Mr. George, the technical support staff at the electrical engineering department at ÉTS for their help in assembling the PMSG test bench. I would also like to thank my colleagues, Mr. Aslain Ovono Zué, Mr. Etienne Tremblay, Mr. Wilson Santana, Mr. Sergio Atayde, Mr. Ali Chikh and Mr. Abdelhamid Hamadi for their wonderful company and support. There are other numerous names of friends that should be mentioned here, especially Dr. Sheldon Williamson, Mr. Manu Jain, and Mr. Sanad Lageli, who have made my stay at Montreal quite memorable.

I would like to acknowledge the Ministry of social justice & empowerment, Govt. of India for the scholarship and High Commission of India, Ottawa for the timely payment of dues towards my studies. I am also thankful to my employer C. R. State College of Engineering, Murthal, Sonepat (D. C. R. University of Science & Technology, Murthal),

the provincial Govt. of Haryana for granting me study leave. I would also like to thank the École de technologie supérieure for providing me the opportunity to pursue Ph.D. studies and also for the three consecutive annual graduate merit awards from the university (bourse aux mérites – 2008, 2009, and 2010). I also offer sincere thanks to IEEE, Industrial electronics society for awarding me the student scholarship at IECON'08-Orlando, Florida, USA.

I would also like to express my special gratitude to Dr. D. K. Jain, and Ms. Gitanjali Pandove for helping me out in the fulfillment of all legal formalities with the Govt. of Haryana and Govt. of India respectively.

Last but not least, I am always indebted to my parents Smt. & Late Sh. Attar Singh, my uncle Sh. Suresh Chand, my brothers Mr. A. P. Singh, Mr. S. P. Singh, Mr. S. V. Singh and all other family members, who have been always there for my support just like a wall during all the ups and downs throughout my life. Special thanks to our loving sons Zullu and Jucy for the charm and happiness they have brought to our family.

Dedicated to my beloved father Late Sh. Attar Singh

ADAPTIVE NETWORK-BASED FUZZY INFERENCE SYSTEMS FOR SENSORLESS CONTROL OF PMSG BASED WIND TURBINE WITH POWER QUALITY IMPROVEMENT FEATURES

Mukhtiar SINGH

RÉSUMÉ

Le coût de la generation d'énergie éolienne devient concurrentiel à celui de la génération d'énergie électrique des sources d'énergies fossiles dites conventionnelles. Il est d'ailleurs à parité avec le coût de génération des centrales au charbon et au gaz. Les générateurs éoliens sont de tailles plus imposantes et leur conception a évolué d'un contrôle vitesse avec entraînement à boîte de vitesse à un contrôle d'hélice de vitesse variable avec ou sans boîte de vitesse. Les progrès réalisés en électronique de puissance stimulent cette tendance vers les éoliennes à vitesse variable. Aujourd'hui, les turbines éoliennes sur le marché comportent de nombreux concepts innovateurs avec une techonologie de pointe autant en génération qu'en interface de puissance. Toutefois, la forte pénétration de larges centrales éoliennes dans les réseaux électriques actuels pose d'autres problèmes à cause de leur nature intermittente. Cela motive les concepteurs de systèmes éoliens à développer des contrôleurs sophistiqués de génératrices et des systèmes de puissance.

Récemment, les machines éoliennes à aimant permanent de vitesse variable deviennent plus attrayantes que les machines à vitesse fixe pour les systèmes de generation éolienne. Dans le cas des systèmes de génération à vitesse variable, les aéromoteurs peuvent opérer au point de puissance maximum sur une large gamme de vitesse en ajustant la vitesse de l'arbre de manière optimale. Plus encore, l'utilisation de machines à aimant permanent réduit la taille du système de génération éolien puisque ni les enroulements d'aimantation et leur système d'excitation ne sont requis. Cc type de configuration s'applique aussi de manière préférentielle en off-shore que la machine éolienne asynchrone à double alimentation qui requiert une maintenance régulière à cause de l'usure des broches et de la boîte de vitesse.

Pour réaliser la poursuite de puissance maximum à diverses vitesses de vent, il est nécessaire d'opérer la machine à aimant permanent à vitesse variable. Pour ce faire, la commande vectorielle est habituellement favorisée car elle permet le contrôle indépendant du couple et du champ comme dans le cas du contrôle des moteurs continus. La commande vectorielle de la machine à aimant permanent requiert essentiellement la position du rotor et la vitesse. A cet effet, un tachomètre et un capteur de position montés sur l'arbre de la machine sont utilisés. Ces capteurs augmentent le coût et la complexité du système. Afin d'éliminer les capteurs de position et de vitesse ainsi que les problèmes qui leur sont associés, une novelle architecture de système d'inférence flou avec réseaux de neurones (ANFIS) est proposé en vue d'estimer la

vitesse et la position du rotor sur une large gamme de vitesses d'opération. L'architecture ANFIS a comme avantage de modéliser un système hautement non linéaire puisqu'il combine les aptitudes de la logique floue par rapport à la prise en charge d'incertitudes paramétriques et les aptitudes d'apprentissage des réseaux de neurones. Alors l'ANFIS est utilisé pour développer un modèle adaptatif de la machine à aimant permanent à vitesse variable sous des conditions d'opération incertaines et compense aussi l'effet de la variation des paramètres tels que l'inductance er la résistance etc.

Dans ces travaux, un système de génération éolienne à aimant permanent est modélisé autant en application autonome qu'en interconnection au réseau. En mode autonome, un système hybride batterie et éolienne est présenté. Le système de stockage à batterie permet d'amortir les fluctuations de l'énergie éolienne et de la demande à la charge. Pour le système éolien connecté au réseau, la capacité d'élimination de défaut est démontrée sous des conditions de sauts et des creux de tension.

Un autre objectif du travail est de développer un contrôleur avancé de l'onduleur situé du côté réseau. Comme l'onduleur fonctionne dans des conditions d'opération variables, il n'est pas possible de fixer les gains des régulateurs PI de manière optimale sans entraver le fonctionnement de l'onduleur. Pour résoudre ce problème, un contrôleur neuronal flou adaptatif est développé. Ce contrôleur présente l'avantage de modéliser et de contrôler des systèmes hautement non linéaires. L'objectif principal de ce contrôleur est d'assurer une operation régulière de l'onduleur côté réseau lors des changements brusques de la dynamique du système contrairement aux PI conventionnels.

De plus, dans ces travaux, la puissance nominale de l'onduleur du côté réseau est optimisée de manière optimale. Normalement, la puissance de l'onduleur situé du côté réseau a un faible facteur d'utilisation de 20-30% avec un pic 60% de puissance nominale à cause de l'intermittence du vent. Par conséquent si le même onduleur est utilisé pour résoudre les problèmes de qualité de l'onde au point de raccordement commun en plus de ses fonctions normales, alors le coût additionnel d'achat d'équipements de puissance tels que le filtre actif, le STATCOM ou le compensateur de puissance réactive est épargné. Alors l'auteur propose une solution simple de coût competitive consistant à utiliser l'onduleur du côté réseau comme compensateur d'harmoniques de courant, de puissance réactive à la charge et de déséquilibre d'une charge triphasé à quatre fils non linéaire et déséquilibrée située au point de raccordement commun au réseau de distribution en plus d'injecter de la puissance active. Egalement, nous montrons que le convertisseur côté réseau peut servir à maintenir la tension constante malgré des sauts ou des creux de tension.

Mots clés: Energy éolienne, Génératrice synchrone à aimant permanent, Systèmes neuronaux flous et adaptatifs, Contôle sans capteur, Qualité de l'onde, Filtre actif.

ADAPTIVE NETWORK-BASED FUZZY INFERENCE SYSTEMS FOR SENSORLESS CONTROL OF PMSG BASED WIND TURBINE WITH POWER QUALITY IMPROVEMENT FEATURES

Mukhtiar SINGH

ABSTRACT

The wind power generation is rapidly becoming competitive with conventional fossil fuel sources and already today is at par with new coal or gas fired power stations. The wind turbine design objectives have changed over the past decade from being convention-driven to being optimized driven within the operating regime and market environment. The wind turbines are growing in size, designs are progressing from fixed-speed, stall-controlled having drive trains with gearboxes, to become pitch controlled, variable speed and with or without gearboxes. The advancement in power electronics devices further supports the trend toward variable speed turbines. Today, the wind turbines in the market have a variety of innovative concepts, with proven technology for both generators and power electronics interface. However, the increasing penetration of large wind farms into electrical power systems also poses different kind of challenges due to their intermittent nature. This inspires the designers to develop both custom generators and power electronics devices with sophisticated modern control system strategies.

Recently, variable-speed permanent magnet synchronous generator (PMSG) based wind energy conversion systems (WECS) are becoming more attractive in comparison to fixed-speed WECS. In the variable-speed generation system, the wind turbine can be operated at maximum power operating points over a wide speed range by adjusting the shaft speed optimally. Moreover, the use of Permanent Magnet reduces size, and weight of overall WECS, as there is no need of field winding and its excitation system. The absence of rotor winding also reduces heat dissipation in the rotor and hence improves the overall efficiency. This kind of configuration also find special favor for off-shore wind application, where the geared doubly fed induction generator requires regular maintenance due to tearing-wearing in brushes and gear box.

To perform maximum power point tracking at different wind speeds, the variable speed operation of PMSG is required. For the variable speed operation of PMSG, generally vector control is preferred as it allows the independent torque and field control just like a simple DC motor control. The vector control of PMSG essentially requires the rotor position and speed information. For this purpose, usually shaft mounted speed and position sensors are used, resulting into additional cost and complexity of the system. In order to eliminate the sensors and their associated problems, a novel adaptive network-based fuzzy-inference system (ANFIS) architecture is proposed for rotor position and

speed estimation over wide range of speed operation. The ANFIS architecture has well known advantages of modeling a highly non-linear system, as it combines the capability of fuzzy reasoning in handling the uncertainties and capability of artificial neural network (ANN) in learning from processes. Thus, the ANFIS is used to develop an adaptive model of variable speed PMSG under highly uncertain operating conditions, which also automatically compensates any variation in parameters such as inductance, resistance etc. An error gradient based dynamic back propagation method has been used for the on-line tuning of ANFIS architecture.

In the proposed work a PMSG based WECS is modeled for both isolated and grid connected system. In the isolated WECS operation, a wind-battery hybrid system is presented. The battery energy storage system (BESS) in the isolated system is used to absorb the wind power fluctuations and varying load demand. In grid connected system, the fault ride through capability of WECS is demonstrated under grid voltage sag/swell conditions.

Another objective is to develop an advance controller for grid side inverter. Since the inverter works under highly fluctuating operating conditions, it is not possible to set the optimal value of gains for the conventional proportional-integral (*PI*) regulator. This may lead to false operation of inverter. To alleviate this problem an adaptive neuro-fuzzy controller is developed, which has well known advantages in modeling and control of a highly non-linear system. The main objective is to achieve smooth operation of grid side inverter, where the conventional *PI* controller may fail due to the rapid change in the dynamics of the overall system. The combined capability of neuro-fuzzy controller in handling the uncertainties and learning from the processes is proved to be advantageous while controlling the inverter under fluctuating operating conditions.

Moreover, in the proposed work, the grid side inverter rating is also optimally utilized by incorporating the power quality improvement features. Normally, the grid interfacing inverter has very low utilization factor 20-30 % with a possible peak of 60% of rated output due to the intermittent nature of wind. Therefore, if the same inverter is utilized for solving power quality problem at point of common coupling (PCC) in addition to its normal task, then the additional hardware cost for custom power devices like APF, STATCOM or VAR compensator can be saved. Thus, the author have proposed a very simple and cost effective solution by using the grid side inverter as a load harmonics, load reactive power and load unbalance compensator of a 3P4W non-linear unbalanced load at PCC in a distribution network, in addition to its normal task of wind power injection in to the grid. Similarly, it has also been shown that the grid side inverter can also be used to maintain constant voltage at PCC for a dedicated load despite of voltage sag/swell and unbalance in grid side voltage.

Keywords: Wind Energy, Permanent Magnet Synchronous Generator, Adaptive Neuro-Fuzzy Systems, Sensorless control, Power Quality, Active Power Filter.

TABLE OF CONTENTS

Page

LIST OF TABLES

LIST OF FIGURES

LIST OF ABBREVIATIONS

3P3W	Three-phase three-wire
3P4W	Three-phase four-wire
AC	Alternating current
ANFIS	Adaptive network-based Fuzzy-inference system
ANN	Artifical neural network
APF	Active power filter
ASD	Adjustable speed drive
BBC	Back to back converter
DC	Direct current
DFIG	Doubly-fed induction generator
DVR	Dynamic voltage restorer
FACTS	Flexible AC transmission systems
FFT	Fast fourier transform
GRÉPCI	Grupe de recherche en électronique de puissance et commande industrielle
HP	Horse power
HPF	High pass filter
IGBT	Insulated gate bipolar transistor
LPF	Low pass filter
LVRT	Low voltage ride-through
NFC	Neuro-fuzzy controller

PCC	Point of common coupling
p. f.	Power factor
PFC	Power factor correction
PI	Proportional-Integral
PLL	Phase-locked loop
PMSG	Permanent magnet synchronous generator
PMSM	Permanent magnet synchronous motor
PWM	Pulse width modulation
rms	Root mean square
RPM	Revoluation per minute
SCIG	Squirel cage induction generator
SEIG	Self-excited induction generator
SSC	Static series compensator
STATCOM	Static var compensator
THD	Total harmonics distortion
UPF	Unity power factor
VSI	Voltage source inverter
w.r.t.	with respect to
WRIG	Wound rotor induction generator
WECS	Wind energy conversion system

INTRODUCTION

The global demand for electrical energy and fossil fuel is increasing at breathtaking pace worldwide. Whilst demand is increasing, the days of overcapacity in electricity production are coming to an end. Many older power plants will soon reach to the end of their working lives. About half of the estimated capacity will be required to replace the existing aging power plants. The world may have to face a severe energy crisis in future in the absence of suitable precautionary measures, especially when there is already shortage of the fossil fuels widely used for power generation. The fossil fuels provides about three quarters of the world's energy. The burning of fossil fuels produces lot of carbon dioxide, one of the main greenhouse gases, which is also considered as the main culprit for global warming and other environmental hazards like melting of the polar ice caps, flooding of low-lying land, storms, droughts and violent changes in weather patterns. Considering all these problems associated with fossil fuels, there is sudden need of the more efficient ways the world produces and consumes energy. Alongside the more efficient generation and use of energy, renewable sources of energy offer the great potential for deep cuts in carbon dioxide emissions. Despite the global abundance of renewable energy resources, renewable energy generation capacity represents merely 3% of the world's installed power capacity. Since the past decade, however, there has been a renewed interest in many countries on renewable energy for power generation. Governments have intervened to promote renewable energy investments. In several developed countries, renewable energy policy interventions were driven by policy objectives such as greenhouse gas emission mitigation, internalization of environmental externalities and energy security.

Among the renewable energy sources, wind energy is considered as the most efficient and economic mean of electricity generation, costing between 4-6 cents per kilowatt-hour, depending upon the size of a particular project. Moreover, wind is indigenous, clean, fuel free and enough wind blows across the globe to cope with the ever increasing

electricity demand. This is enough to demonstrate that wind technology is not a dream for the future – it is real, it is mature and it can be deployed on a large scale. Some of the facts associated with wind energy are being discussed as under.

Demand for a Reliable and Everlasting Energy Source

The worldwide demand for energy is increasing day by day. The International Energy Agency (IEA) predicts that by 2030, the world's energy needs will be almost 60% higher than now. Two-thirds of this increase will occur in China, India and other rapidly developing economies; these countries will account for almost half of global energy consumption by 2030. If this sharp increase in world energy demand actually takes place, it would require significant investment in new generating capacity and grid infrastructure, especially in the developing world. The IEA estimates that the global power sector will need to build some 4,800 GW of new capacity between now and 2030. This will require investment of approximately US$2 trillion (€1.7 trillion) in power generation and US$1.8 trillion in transmission and distribution networks. Industrialized countries face a different but parallel situation. The IEA predicts that by 2030, over 2,000 GW of power generation capacity will need to be built in the Organization for Economic Cooperation and Development (OECD) countries, including the replacement of retiring plants. Without energy efficiency measures, electricity demand in the European Union is expected to increase by 51% by the end of 2030, requiring investments in power generation of around €625 billion (US$ 760 billion). However, the potential effect of energy saving on global demand could be considerable. According to the study by Ecofys, electricity demand could increase by only 30% by 2030, if a wide range of technologies and initiatives were introduced. Although this 'High energy efficiency' scenario recognizes the limitations set by cost and other obstacles, global electricity demand would be 39% lower in 2030 than currently estimated by the IEA's Reference scenario.

Just as energy demand continues to increase, in the absence of such efficiency measures, supplies of the main fossil fuels used in power generation, especially gas, are dwindling. One result is that some of the major economies of the world have to rely increasingly on imported fuel, sometimes from regions of the world where conflict and political instability threaten the security of that supply. In Europe, sources of indigenous oil and gas, mainly from the North Sea, are in rapid decline. At present, 50% of Europe's energy supplies are imported. Within two decades this is expected to increase to 70%. Even uranium, which currently supplies the fuel for over 30% of European electricity, has a global lifetime estimated at no more than 40 years, whilst the EU countries contain less than 2% of the world's uranium reserves. Driven by these pressures, the last two years have seen unprecedented volatility in the prices of both oil and gas. Recently the highly volatile Oil market has witnessed the oil prices from US$40 to US$140 per barrel, with the expectation that the price will remain high for some years to come. Rising gas wholesale costs have seen domestic electricity increased prices across the world. Analysts point out that the cumulative increase in real crude oil prices since 2002 is close to that of the oil shocks of the 1970s, which produced two global recessions and an unprecedented surge in inflation. Increasingly, governments around the world are waking up to the threat that the current shaky supply situation is posing to their economic growth. By contrast to the uncertainties surrounding supplies of conventional fuels, and volatile prices, wind energy is a massive indigenous power source which is permanently available in virtually every country in the world. There are no fuel costs, no geo-political risk and no supply dependence on imported fuels from politically unstable regions.

Environmental Concerns

The impetus behind wind power expansion has come increasingly from the urgent need to combat global climate change. This is now accepted to be the greatest environmental threat, being faced by the world. The UN's Intergovernmental Panel on Climate Change

projects that average temperatures around the world will increase by up to 5.8°C over the coming century. This is predicted to result in a wide range of climate shifts, including melting of the polar ice caps, flooding of low-lying land, storms, droughts and violent changes in weather patterns. Responsibility for climate change lies with the excessive build-up of greenhouse gases in the atmosphere, a trend encouraged by the world's growing industrialization. Within energy use, the main culprit is fossil fuels, whose combustion produces carbon dioxide, one of the main greenhouse gases. A shift in the way the world produces and consumes energy is therefore essential. Alongside more efficient use of energy, renewable sources of energy offer the potential for deep cuts in carbon dioxide emissions. The main international driver for combating climate change has been the 1997 Kyoto Protocol. This set national targets for OECD member states to cut their CO_2 emissions by an average of 5.2% from their 1990 levels by 2012. Combating climate change is only a secondary driver for wind energy in the developing world, however. More immediate concern comes from the direct environmental effects of burning fossil fuels, particularly air pollution. This is a major issue in countries like India and China, which use large quantities of coal for power generation. Recently in Copenhagen accord, both India and China has voluntary agreed to cut their CO_2 emissions by 20% in between 2005 to 2020. Other environmental effects resulting from the range of fuels currently used to generate electricity include the landscape degradation and dangers of fossil fuel exploration & mining, the pollution caused by accidental oil spills and the health risks associated with radiation produced by the routine operation & waste management of the nuclear fuel cycle. Exploiting renewable sources of energy, including wind power, avoids these risks and hazards.

Economic Benefits

As the global market has grown, wind power has seen a dramatic fall in cost. A modern wind turbine annually produces 180 times more electricity and at less than 80% the cost per unit (kWh) than its equivalent twenty years ago. In the early 1980's, when the first

utility-scale wind turbines were installed, wind-generated electricity costs as much as 30 cents per kilowatt-hour. Now, the state-of-the-art wind power plants at excellent sites are generating electricity at less than 5 cents/kWh. Costs are continuing to decline as more and larger plants are built and advanced technology is introduced. At good locations wind can compete with the cost of both coal and gas-fired power. The cost of wind power generation falls as the average wind speed rises. Analysis by industry magazine Wind power Monthly (Jan 2006) shows that at a site with an average wind speed of more than 7 m/s, and a capital cost per installed kilowatt of approximately € 1,000 (US$1240), is already cheaper than gas, coal and nuclear. The competitiveness of wind power has been further enhanced by the recent rise in the price of fossil fuels, in particular the gas used to fuel power stations. In the United States, this has made wind generated electricity an increasingly attractive option for power utilities facing the rising fuel cost. Against the volatility of conventional electricity cost, wind offers an energy source which has no fuel element and is unaffected by world trade issues. Direct cost comparisons between wind power and other generation technologies are misleading, however, because they do not account for the "external costs" to society and the environment derived from burning of fossil fuels or from nuclear generation. These external costs, including the effects of air pollution and radiation emissions, are not included in electricity prices. The pan-European study, known as the "ExternE" project, conducted across all 15 original EU member states, has assessed these costs for a range of fuels. Its latest results, published in 2002, showed wind power as having the lowest range of these hidden costs - 0.15 to 0.25 € cents/kWh – compared to 2 to 15 € cents/kWh for coal. The study concluded that the cost of electricity from coal or oil would double, and that from gas increase by 30%, if their external cost associated with the environment and health was taken into account. The polluting effect of fossil fuels has now been reflected through carbon reduction measures to limit the amount of carbon dioxide which can be emitted by all major industrial enterprises.

Employment and Local Community Service

Wind energy also provides economic benefit through the employment which the industry generates. Manufacturing wind turbines and their components offers major job opportunities, often building on existing engineering skills and raw materials. In rural areas, wind energy can bring investment and jobs to isolated communities; hosting wind farms provides farmers with a steady income whilst they continue to graze or crop their land. Employment levels vary from country to country. The numbers of jobs created worldwide by the end of 2008 were 440,000. A recent study in the US by the government's National Renewable Energy Laboratory concluded that investment in wind power had a greater economic impact on the rural regions where it was developed - through new jobs, income and taxes - than a fossil fuel power station. In the developing world, wind power is attractive as a means of providing a cheap and flexible electricity supply to dispersed communities, often through off-grid stand-alone systems. Its effect on economic development can be dramatic. Supplying enough power for just basic lighting and a television or computer can make a substantial difference to domestic life, educational opportunities and the viability of small businesses.

The Summarization of Major Advantages of Wind Energy

- Low cost – can be competitive with nuclear, coal and gas on a level playing field.
- The fuel is free, abundant and inexhaustible.
- Clean energy - no resulting carbon dioxide emissions.
- Provides a hedge against fuel price volatility.
- Security of supply - avoids reliance on imported fuels.
- Modular and rapid to install.
- Provides bulk power equivalent to conventional sources.
- Land friendly - agricultural/industrial activity can continue around it.

The Global Wind Energy at a Glance

The global market for wind power has been expanding faster than any other source of renewable energy. From just 4,800 MW in 1995 the world total has multiplied more than thirty-fold to reach over 151,000 MW at the end of 2009. The total annual world wind market turnover reported by the end of 2008 was more than € 40 billion, with an estimated 440,000 people employed around the world. The success of the industry has attracted investors from the mainstream finance and traditional energy sectors. In a number of countries the proportion of electricity generated by wind power is now challenging conventional fuels. In Denmark, 20% of the country's electricity is currently supplied by the wind. In Spain, the contribution has reached 8%, and is set to rise to 15% by the end of the decade. These figures show that wind power is already able to provide a significant input of carbon-free electricity. In 2008, the global wind energy sector registered another record year, with a total of 27,261 MW of new capacity installed, which represent almost 30% annual growth rate. Wind power is now established as an energy source in over 50 countries around the world. Those with the highest totals in 2008 were USA (25,170 MW), Germany (23,903 MW), Spain (16,740 MW), China (12,210 MW), India (9,587 MW) and Italy (3,736 MW). A number of other countries, including France, Denmark, the UK, the Netherlands, Japan and Portugal, have also reached the 2,000 MW mark. Although the wind power industry has up to now been most dynamic in the countries of the European Union, this is changing. The United States and Canada are both experiencing a surge of activity, whilst new markets are opening up in Asia and South America. A new frontier for wind power development has also been established in the sea, with offshore wind parks beginning to make a contribution.

Modern wind turbines have lot of commercially available topologies based on induction generator (fixed speed) and doubly fed induction generator/synchronous generator/PMSG (Variable speed). The variable speed wind turbines are more attractive,

as they can extract maximum power at different wind velocities, and thus reduces the mechanical stress on WECS by absorbing the wind power fluctuations. Recently the Permanent Magnet Synchronous Generator (PMSG) has received worldwide attention for wind power generation, due to their small size, higher power density, high efficiency and higher torque to inertia ratio.

In variable speed wind energy conversion systems, the power electronics interface plays an important role. With the vector control, the PMSG can be rotated at variable speed according to varying wind, in order to extract maximum power at different wind velocities. The variable speed PMSG generates power at variable voltage both in frequency and amplitude. The power electronic interface is required to convert the variable voltage and frequency in to a constant grid voltage and frequency. Different kind of power converter configurations can be used for such type of variable speed PMSG based wind turbine applications. In this thesis, two back-to-back PWM-VSI based bi-directional power converter topology is used. To achieve full control of the grid current, the DC-link voltage must be boosted to a level higher than the amplitude of the grid line-line voltage. The power flow of the grid side converter is controlled in order to keep the DC-link voltage constant, while the control of the generator side is set to suit the magnetization demand and the reference speed command according to maximum power point tracking. As such kind of WECS employs the full rating power converters, the PMSG can be controlled over wide-speed range and the grid side inverter also have full control over its output active and reactive power. The only disadvantage of such kind of system is higher installation cost due to the involvement of full rating power electronics converters.

For the precise control of PMSG, the information about rotor speed and position is essentially required: either using sensors or estimator/observer. To avoid the additional sensor cost, complexity and the other associated problems, there has been significant interest in the sensor-less control of PMSG. Moreover, the elimination of these sensors

and their connecting leads increases the mechanical robustness and reliability of overall system. All these factors have made the sensorless control of PMSG more attractive. But the rotor speed and position typically requires the accurate knowledge of PMSG parameters, which may not be easily available or difficult to obtain, especially under varying weather and operating conditions. Several rotor speed and position estimation techniques have been reported in literature, especially the back-emf based rotor speed estimation is quite common. This method works satisfactorily at higher speeds. However, the speed estimation becomes very difficult at lower speeds, due to small and distorted emf signal. Some state observer methods based on Extended Kalman Filter (EKF), Extended Luenburger Observer (ELO), and Sliding Mode Observer etc. have also been reported. Most of them suffer due to complex computation, sensitivity to parameter variation and need of accurate initial conditions. However, the EKF has the advantage of estimating the parameters and speed simultaneously by considering them as state, but at the increased cost of computational burden. The sliding mode observer is simple and offers a limited robustness against the parameter variation. However, sliding mode being a discontinuous control with variable switching characteristics has chattering problems, which may affect the control accuracy. Recently, some more advanced adaptive estimation techniques based on Artificial Neural Network (ANN) and Fuzzy Logic Control (FLC) have also been reported. However, the estimation accuracy depends on number of neurons and fuzzy membership functions used for rule base.

Thus, the main objective of the thesis is to achieve speed and position sensorless control of PMSG and also to utilize the grid side inverter rating optimally by incorporating power quality improvement features to it. The detailed discussion about the problematics, objectives and methodology is provided in Chapter-1.

Thesis Outline

CHAPTER 1 presents a thorough literature review of the different kinds of wind energy conversion systems. On the basis of literature review, different kind of problems are identified and discussed in detailed. To solve the identified problems, the objectives are defined and discussed thoroughly. Finally, implementation methodology is discussed to achieve the desired objectives.

CHAPTER 2 is dedicated to system description and control. In this chapter the mathematical modeling of various components like, wind turbine, PMSG and power electronic converters is provided. Moreover, a brief introduction to controller design for power converter is also provided.

CHAPTER 3 is dedicated to two different kinds of configurations. In first case, PMSG based wind-battery hybrid system is simulated, where the main objective is to achieve the power balance under fluctuating wind and dynamic load conditions in an isolated system. In second configuration the grid connected WECS is simulated under voltage sag/swell conditions to demonstrate its fault ride-through capabilities. Moreover, simulation study is also carried out to maintain constant voltage at point of common coupling (PCC) with the help of grid side inverter, despite of having voltage unbalance and sag/swell on grid voltage.

CHAPTER 4 presents the variable speed operation of WECS with power quality improvement features incorporated to grid side inverter. In this section, it is demonstrated that the grid side inverter rating can be optimally utilised by using it as a multifunction device, where it is able to inject the generated power and also to compensate the non-linear load at PCC simultaneously. This enables the grid to always supply/absorb the fundamental active power, even in the presence of non-linear load at

PCC. The simulation and experimental study is carried out under 3-phase 3-wire (3P3W) and 3-phase 4-wire (3P4W) load conditions.

CHAPTER 5 is dedicated to adaptive network-based fuzzy inferences system (ANFIS), where a novel ANFIS based PMSG adaptive model is developed to estimate the rotor speed and position accurately under dynamic operating conditions. An ANFIS based control algorithm is also developed for grid interfacing inverter with non-linear load compensation capabilities. Besides this, a comparative study of ANFIS and sliding mode observers is also provided. All of the ANFIS based algorithms are successfully simulated and implemented in hardware laboratory to validate their control and estimation capabilities.

The major conclusions of thesis and future recommendation are also provided. In the end of thesis, the list of references and appendix regarding hardware implementation are provided.

CHAPTER 1

LITERATURE REVIEW

Thanks to twenty years of technological progress, wind turbines have come a long way and a wind farm today acts much more like a conventional power station. Moreover, wind power generation is rapidly becoming competitive with conventional fossil fuel sources and already today is at par with new coal or gas fired power stations. Wind turbine technology has matured during the last decade. Wind turbine design objectives have changed over these years from being convention-driven to being optimized driven within the operating regime and market environment. The wind turbine are growing in size, designs are progressing from fixed-speed, stall-controlled having drive trains with gearboxes, to become pitch controlled, variable speed and with or without gearboxes. The availability of low-cost power electronics devices further supports the trend toward variable speed turbines. Today, the wind turbines on the market have a variety of innovative concepts, with proven technology for both generators and power electronics interface. The increasing penetration of large wind farms into electrical power systems also poses different kind of challenges. This inspires the designers to develop both custom generators and power electronics devices with sophisticated modern control system strategies.

1.1 Wind Turbine Configuration

With the advancement in wind turbine technology, the size of wind energy conversion system is getting bigger and bigger with passage of time. These days, the WECS are available in different sizes, ranging from fractional kW to 5 MW. The development in power electronics has further revolutionized the mode of wind energy harvesting. The wind turbines are now transforming from constant speed to variable speed wind turbines, gear to gearless, onshore to offshore. In terms of type of generator, the WECS are

generally based on induction generator (IG) and synchronous generator (SG). The different types of WECS configurations are being discussed in the following section.

1.1.1 Induction Generator based WECS

The induction generator for wind power application is mainly based on squirrel cage induction generator (SCIG), wound rotor induction generator (WRIG)/doubly fed induction generator (DFIG). Due to the simple, robust, and brush maintenance free design of SCIG, it got lot of popularity in the early stage of wind turbine technology. The SCIG is mainly used in constant speed WECS, where it is connected to grid through soft starter. The soft starter functions during the startup operation and is usually by-passed under normal operation. The generator speed is decided by the grid frequency and can be varied in a very small range above synchronous speed. The main drawback of such a kind of system is that it draws high amount of reactive current from grid, and thus makes it necessary to have power correction unit (PFC) at the point of common coupling (PCC) (Elnashar *et al.*, 2008); (Ching-Yin *et al.*, 2009). Moreover, due to constant speed operation it cannot perform maximum power point tracking (MPPT). An improved version of SCIG is used by Suzlon and Siemens, where stator consists of multiple windings with different number of poles. Thus, the system can be operated at different speeds by changing the number of poles. A typical SCIG based Danish style constant speed WECS is shown in Fig. 1.1(a). The SCIG are also used for variable speed wind turbines through a full rating power electronics interface as shown in Fig. 1.1(b) (Agarwal *et al.*, 2010; Bayindir *et al.*, 2009).

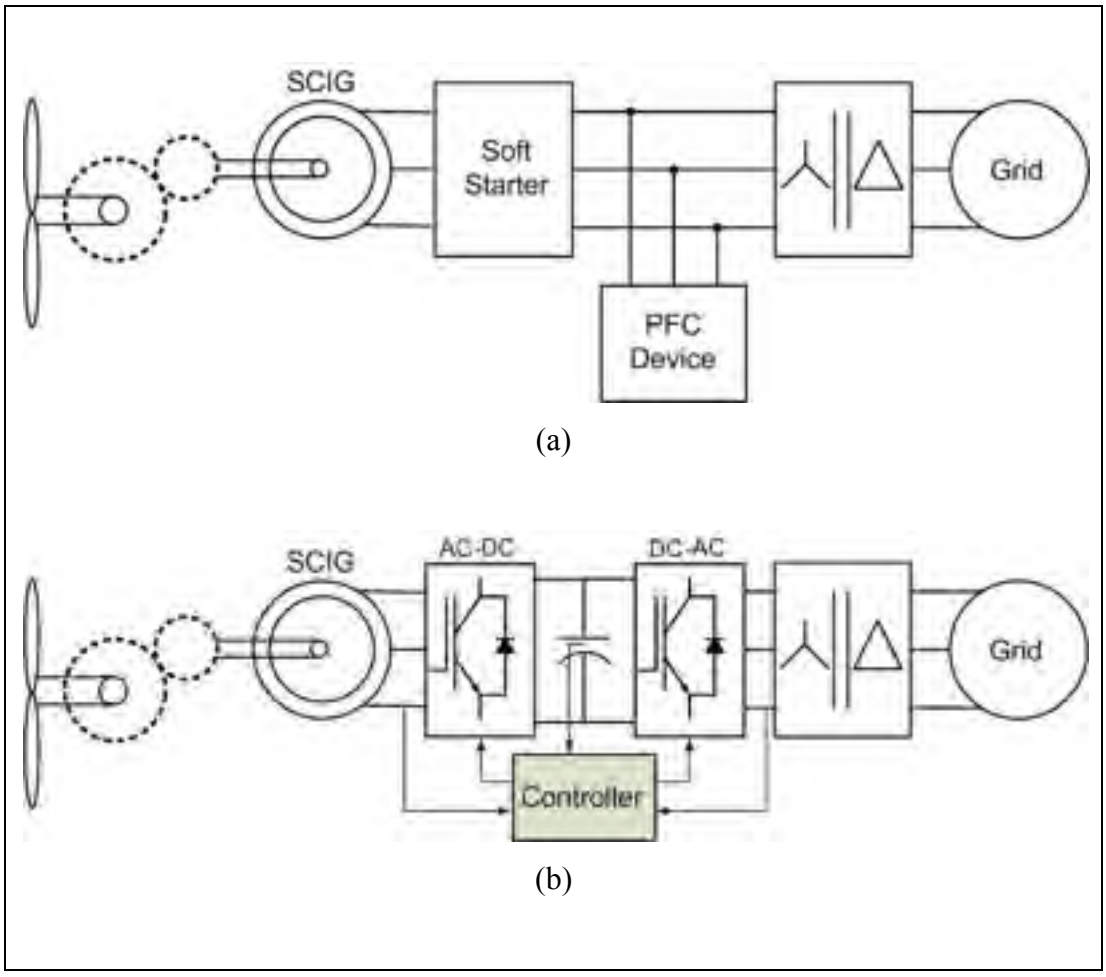

Figure 1.1 SCIG based WECS Configurations.

Some of the wind turbine manufacturers also use WRIG, where the generator is controlled by varying the external rotor resistance through power converter (Kinjo, Wallace et von Jouanne, 2004). With such kind of configuration, the generator speed can be varied up to $\pm$ 30% around the synchronous speed. However, some sort of power dissipation takes place across the external rotor resistance in the form of heat. The Vestas and Suzlon use similar kind of technology under their trade name *optispeed* and *macroslip* respectively. The block diagram of such kind of topology is shown in Fig. 1.2.

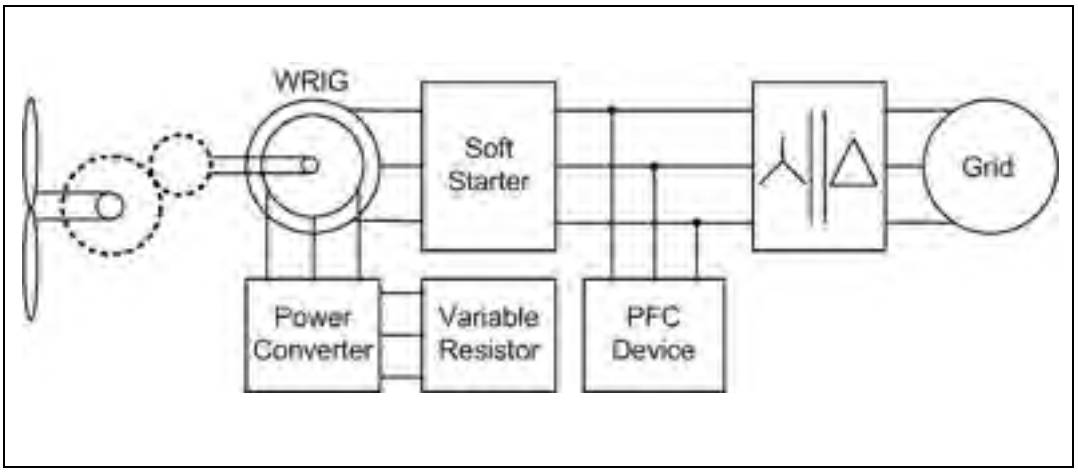

Figure 1.2 WRIG based WECS Configurations.

The other well known configuration, where the rotor of WRIG is connected to grid through *AC/DC/AC* conversion is known as DFIG. The DFIG topology has edge over variable resistance controlled WRIG in terms of improved controllability and increased efficiency. The converters are generally designed to handle the power up to 30% of nominal rating, and hence the speed can be varied in the $\pm$30% range of rated speed. Such kind of topology draws lot of favor in large size or MW range wind turbine (Muljadi *et al.*, 2007b), (Yazhou *et al.*, 2006). However, it requires regular maintenance of slip rings and carbon brushes. The inverter switching frequencies accumulate charge in the parasitic capacitances between stator and rotor, which further develop voltage across the bearings that eventually discharges and damages the bearings (Garcia, Holmes et Lipo, 2006). Moreover, any kind of grid voltage fluctuation may produce oscillations in stator output power and rotor torque pulsation (Lie et Yi, 2007); (Wei, Harley et Venayagamoorthy, 2009). These kinds of machines are being used by Hydro-Quebec and supplied by General Electric. The block diagram of DFIG based wind turbine is shown in Fig. 1.3.

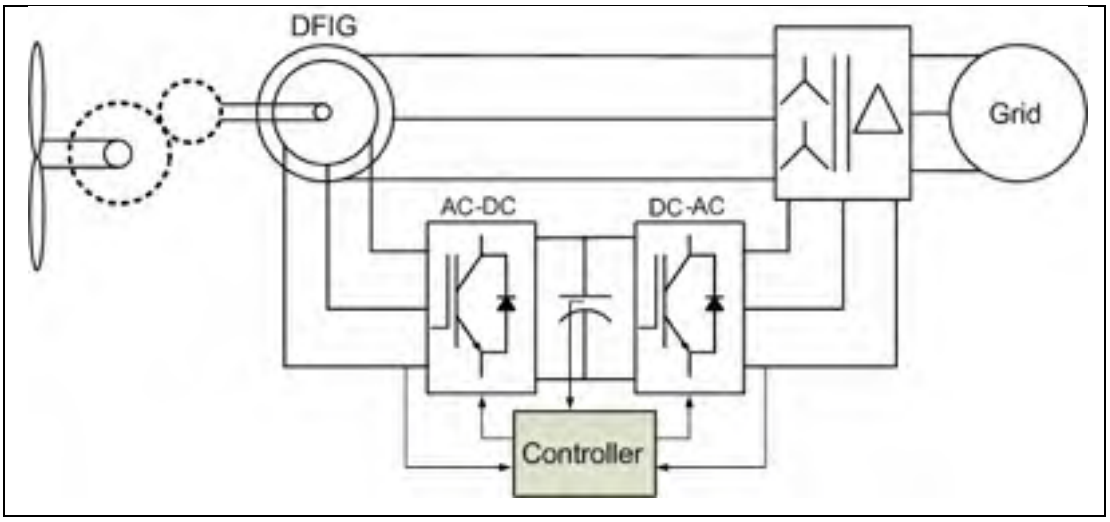

Figure 1.3 DFIG based WECS Configuration.

1.1.2 Synchronous Generator based WECS

The synchronous generators are widely used in different kinds of power plants for electromechanical power conversion. The synchronous generators have the capability of controlling their output terminal voltage and the reactive power easily with the proper control of their excitation winding. These kinds of generators are also preferred over induction machines due to their higher efficiency, especially at higher power rating (Baroudi, Dinavahi et Knight, 2007). The synchronous generators generally carry armature winding on stator and field winding on rotor. Depending on the type of field excitation, the synchronous generators are mainly divided into two categories: (a) Wound rotor synchronous generator (WRSG) and (b) Permanent magnet synchronous generator (PMSG).

In WRSG system, the main disadvantage is the need of external DC source or rotor mounted rectifier with the slip ring and carbon brushes for the field winding excitation (Zhe, Guerrero et Blaabjerg, 2009). The WRSG used for wind power application have various types of configuration. In Fig. 1.4 (a), a WRSG based constant speed WECS

with gear box is shown, where due to constant speed operation it has no MPPT option. Another configuration based on WRSG is variable speed wind turbine as shown in Fig. 1.4(b), where the stator winding is connected to grid through a full rating AC/DC/AC power conversion system (Sánchez *et al.*, 2008). This kind of configuration can be used either as a directly driven WECS or through a gear box. The directly driven WECS are more preferable, as the mechanical losses and maintenance problem associated with gear box can be eliminated. But, the low speed operation of WECS requires large size generator to accommodate higher no. of poles, which also increases the tower and foundation cost. To overcome the problems associated with large size WRSG and its excitation system, there is need of more efficient, reduced size and higher power density generators for directly driven WECS.

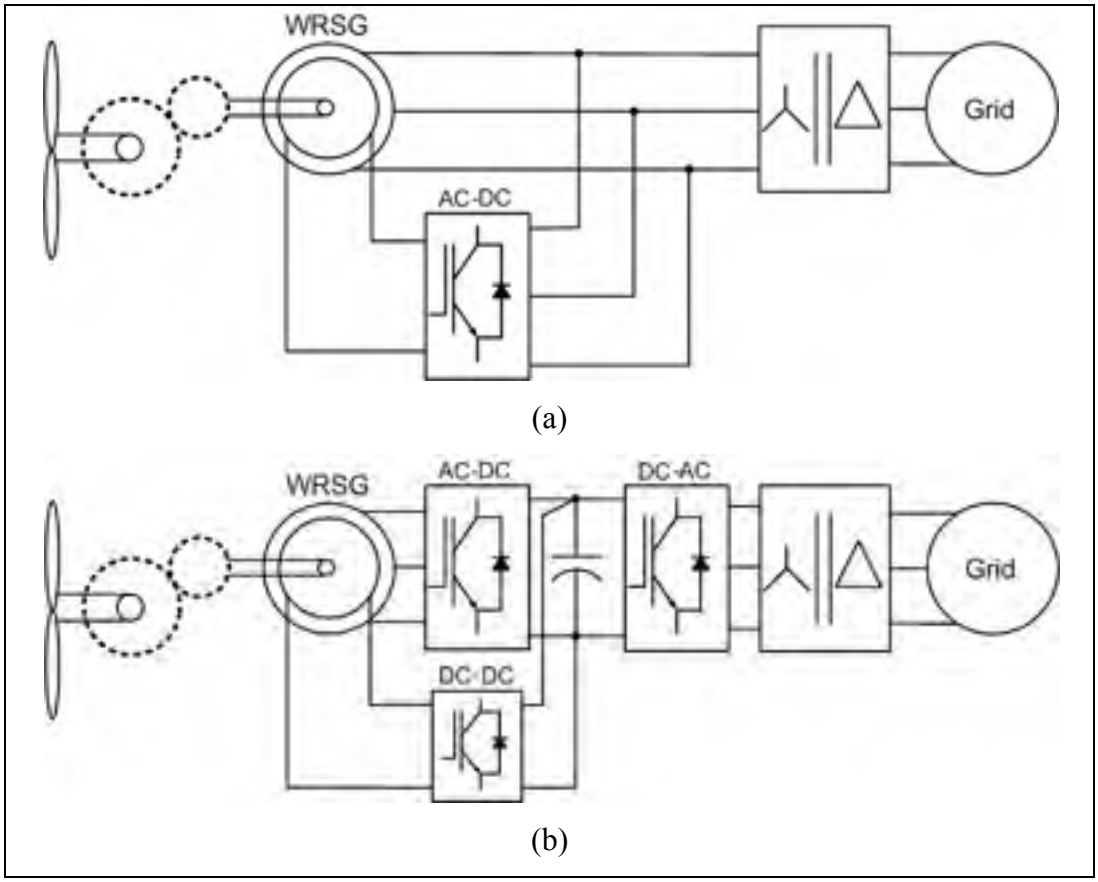

Figure 1.4 WRSG based WECS Configurations.

1.2 PMSG based WECS

The DC excitation of field winding in wound rotor synchronous generator can be provided by permanent magnet. The use of permanent magnet on rotor eliminates the rotor winding, its copper losses and its other related components. This makes the PMSG more efficient with reduced size and higher power density in comparison to the WRSG of same power rating (Bianchi et Lorenzoni, 1996). The main disadvantage of PMSG is higher cost of permanent magnet and variation in its magnetic characteristics with the passage of time. Moreover, due to the fixed magnetic excitation, the output voltage of PMSG varies with the variation in its speed. From practical consideration point of view, it is desirable that the voltage regulation of the generator should be minimized. This may be accomplished by capacitor compensation, or power electronic conversion. Tze-Fun has provided a detailed survey on different type of PMSG used in distribution generation (Tze-Fun et Lai, 2007). For windmill applications, generally switched load with a fixed capacitor in parallel is used for approximate load matching between the turbine and generator power characteristics.

However, the advancement in magnetic material science may reduce the cost of permanent magnet and improve its characteristics in the near future. Recently, the PMSG based WECS are changing their profile from prototype to main stream WECS, being installed on large scale. The main configurations of PMSG based directly driven WECS are shown in Fig. 1.5, where the full rating AC/DC/AC conversion system is used to convert variable frequency into a compatible grid frequency. In this dissertation PMSG based WECS is opted as a subject of research.

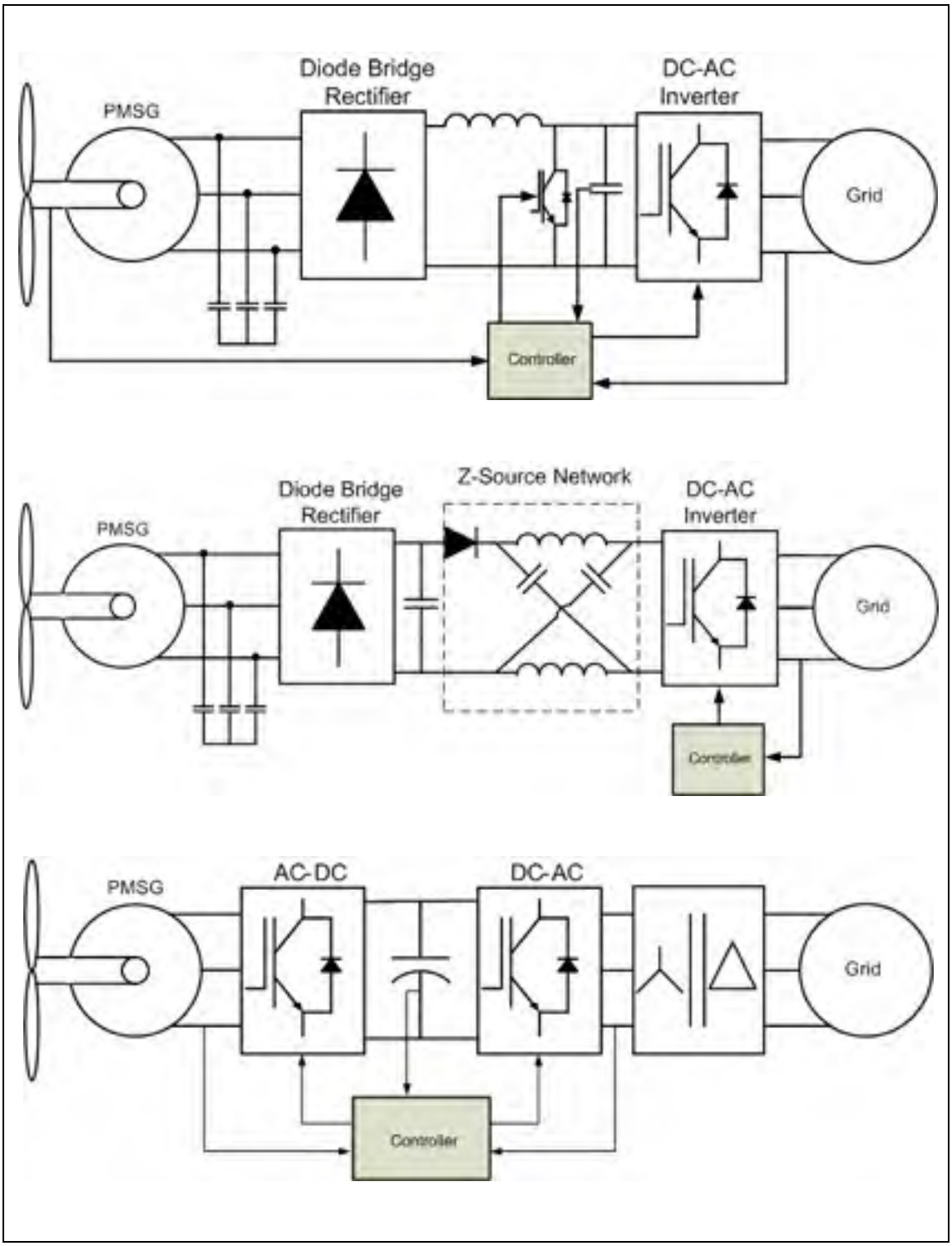

Figure 1.5 PMSG based WECS Configurations.

1.2.1 Control Description

The control of PMSG based WECS is mainly dependent on AC/DC and DC/AC power converters, generally termed as generator side converter and grid side inverter respectively. The presence of dc-link in between the PMSG and Grid decouples them from each other and hence allows their independent control. Several PMSG based wind turbine configurations are available in literature. Jingya and Bin have presented a current-source converter based configuration, where the proposed control scheme reduces the DC link current to a minimum value to reduce converter conduction loss (Jingya, Xu et Bin, 2009; Strachan et Jovcic, 2008). However, it is extremely difficult to design a controller due to the presence of dc-link choke and filtering capacitor. A pitch controlled directly driven wind turbine connected to grid via full converter system is presented in (Strachan et Jovcic, 2008), where an energy storage system is connected on dc-link to sustain grid disturbance during faulty conditions. A variable-speed WECS with a PMSG and *Z*-source inverter is proposed in (Dehghan, Mohamadian et Varjani, 2009; Xiaoyu *et al.*, 2009). The characteristics of *Z*-source inverter are used for maximum power point tracking control and delivering power to the grid, simultaneously. But in such kind of configuration, a well designed inductor is required to minimize the inductor current ripples under variable operating conditions, due to presence of simple diode bridge rectifier. A six-phase PMSG based WECS is presented in (Weihao *et al.*, 2009a), where four 3-phase converters are required in addition to two active switches at dc-link. A similar topology is also presented in (Li *et al.*, 2008). The main idea is to reduce the current rating of power devices, however at the increased cost and complexity. In some papers (Abbes, Belhadj et Ben Abdelghani Bennani, 2010; Behera, Wenzhong et Ojo, 2009; Rossi *et al.*, 2009; Vilathgamuwa, Jayasinghe et Madawala, 2009) the multilevel inverter based WECS also presented, but again the increased number of devices increase the cost and complexity of system. Two back to back converter based configuration is presented in (Chinchilla, Arnaltes et Burgos, 2006; Fu *et al.*, 2009; Keyuan *et al.*, 2008), where the grid side inverter is used for dc-link

regulation and generator side converter for speed control of PMSG. In this thesis also back to back converter configuration is used for the proposed research on PMSG based WECS.

a) Generator Side Control : The main purpose of generator side converter is to perform MPPT according to variable wind speeds. This enables in achieving maximum aerodynamic efficiency and minimizes the stresses of wind power fluctuations. The PMSG is controlled according to the reference speed obtained from power speed characteristic of wind turbine. A lot of control strategies are available in the literature for PMSG control, mainly based on field oriented vector control (Nayar *et al.*, 2007). The vector control of PMSG allows the independent control of flux and torque just like a simple dc machine control, where field and armature can be controlled independently (Zhang *et al.*, 2010). The quadrature axis current is used to control the speed, while direct axis current for field control. In (Wei, Liyan et Harley, 2009) a control strategy for interior PMSG is presented to compute the q-axis and d-axis current component while considering the effects of non-linearity caused by magnetic saturation. The rotor position and speed are essentially required for vector control of PMSG. Generally shaft mounted position and speed sensors/encoders are used for this purpose (Gonzalez *et al.*, 2009). However, some researchers have also suggested sensorless control of PMSG, which have been discussed in the chapter-5 of thesis. The block diagram of vector controlled PMSG is shown in Fig. 1.6.

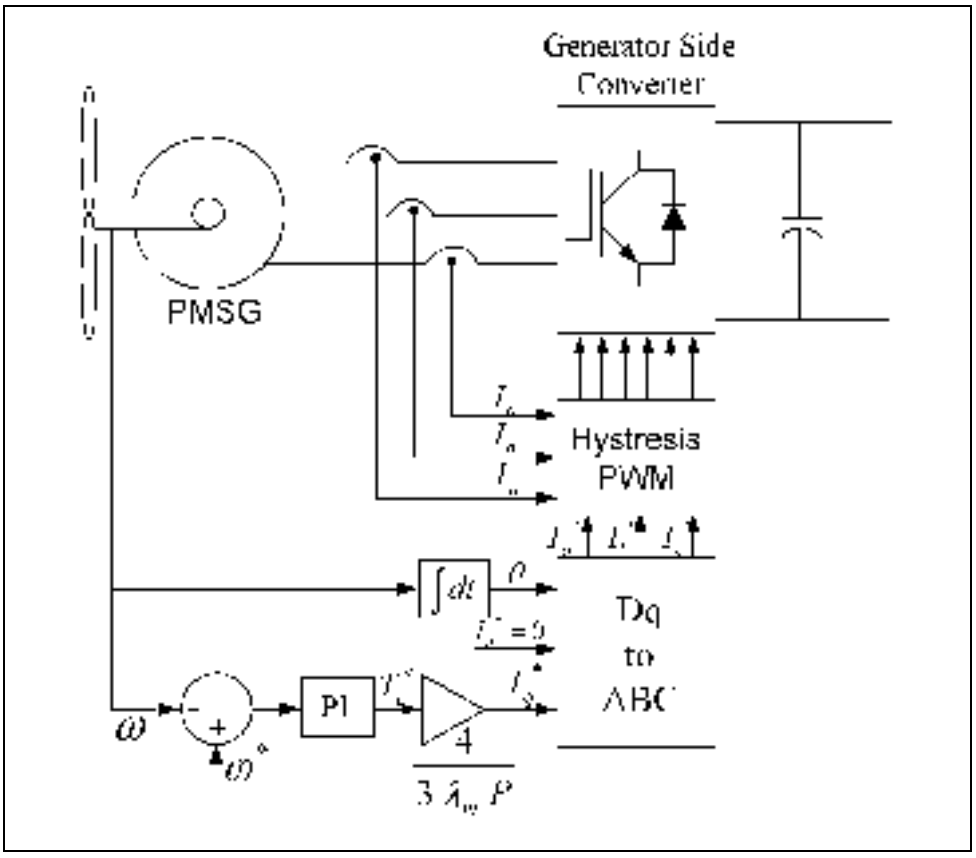

Figure 1.6 Converter based PMSG Control.

Another low cost PMSG control strategy is based on the combination of 3-phase diode bridge rectifier and dc-dc boost converter as shown in Fig. 1.7 (Haque, Negnevitsky et Muttaqi, 2010; Valenciaga et Puleston, 2008). The reference speed obtained from MPPT algorithm is compared with the actual PMSG speed and then the error is applied to speed controller. The output of outer speed control loops sets the reference current value for the inner current control loop. The main disadvantage of chopper based control is that it produces harmonics in PMSG due to the presence of 3-phase diode bridge rectifier. The harmonics in stator winding of PMSG results in to the additional losses, which further results in overheating of PMSG. A single-switch three-phase boost rectifier for PMSG control is provided in (Tonkoski, Lopes et Dos Reis, 2009), where it provides means for regulating the shaft speed by duty cycle variation while reducing the generator losses

when compared to the standard diode and capacitive filter scheme. This kind of topology requires three active switches on dc-link without any significant improvement in generator current profile as evident from the results provided by the authors.

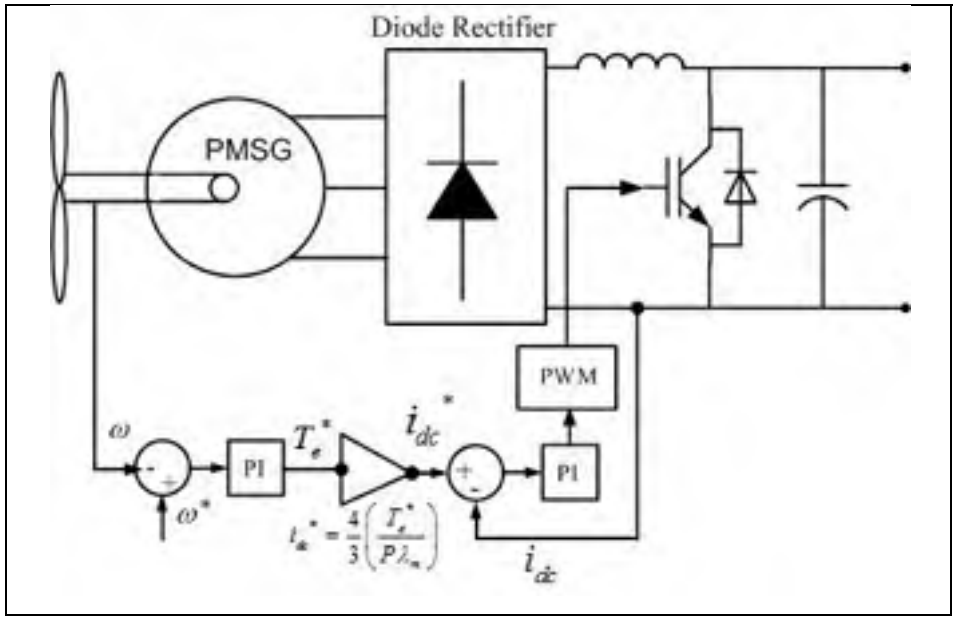

Figure 1.7 Chopper Based PMSG Control.

b) Grid Side Control: The power generated from WECS is injected in to grid through 3-phase inverter. The grid side inverter can be controlled for both active and reactive power flow. Generally, the inverter is controlled to maintain dc-link voltage constant, which automatically controls the flow of active power. The control strategies can be implemented in both stationary and synchronous reference frame (rotating reference frame) (Carrasco *et al.*, 2006; Haque, Negnevitsky et Muttaqi, 2010; Yang *et al.*, 2009). However, the synchronous reference frame is more suitable, as it converts the sinusoidal signals in to dc-signals, where dc-signals can be easily controlled by simple *PI* controllers. The synchronous reference frame transformation requires the grid synchronizing angle, which can be easily detected from grid voltage using phase lock loop (PLL) as shown in Fig. 1.9 (Fatu *et al.*, 2007; Shoudao *et al.*, 2009). One of the common control strategies for grid side inverter is shown in Fig. 1.8. In such kind of

control strategy, two cascaded loops are used. The inner control loops controls the active and reactive components of grid current, while the outer loops control the dc-link voltage and reactive power (Blaabjerg *et al.*, 2006).

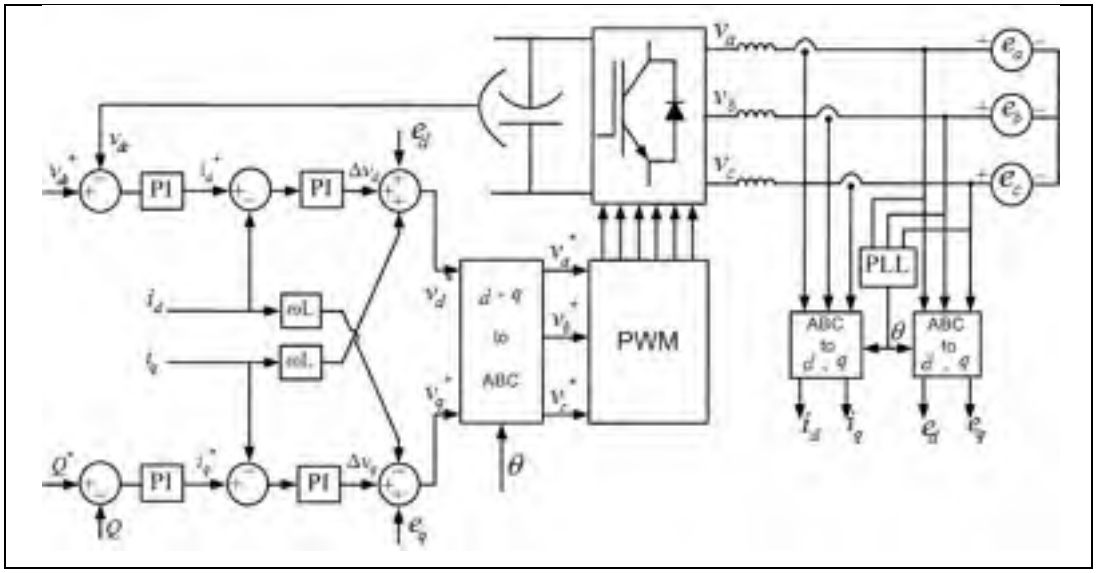

Figure 1.8 Grid Side Inverter Control.

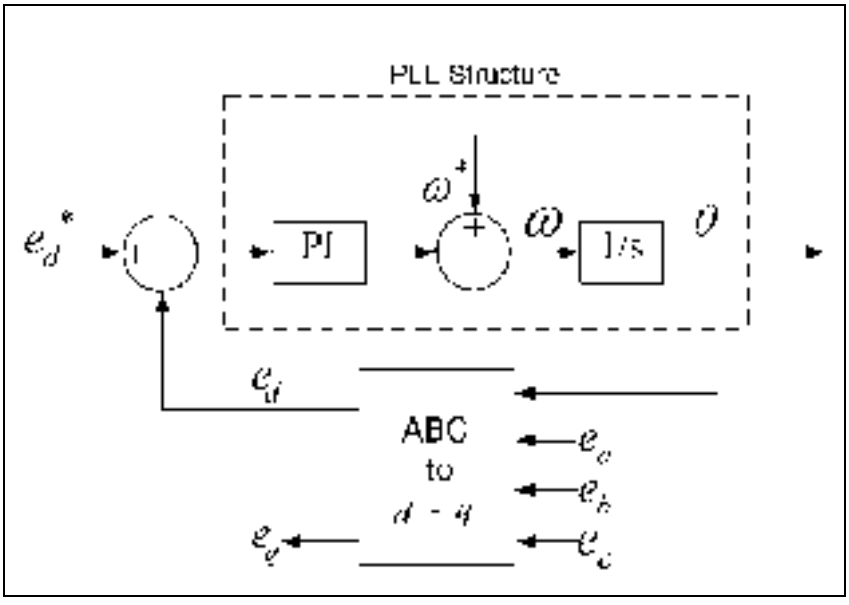

Figure 1.9 PLL Structure.

1.3 Problematic

Wind energy generation has experienced a annual growth rate of more than 30% in the last decade. Recently, variable-speed PMSG based WECS are becoming more attractive in comparison to fixed-speed WECS. In the variable-speed generation system, the wind turbine can be operated at maximum power operating points over a wide speed range by adjusting the shaft speed optimally. Moreover, the use of Permanent Magnet reduces size, and weight of overall WECS, as there is no need of field winding and its excitation system. The absence of rotor winding also reduces heat dissipation in the rotor and hence improves the overall efficiency. This kind of configuration also finds special favor for off-shore wind application, where the geared doubly fed induction generator requires regular maintenance due to tearing-wearing in brushes and gear box. However, the problems associated with their controllability, higher installation cost, and interconnection with grid are the major issues yet to be solved (Muyeen *et al.*, 2010), as this kind of WECS requires full rating AC/DC/AC conversion stages and control of various parameters like voltage, frequency, active/reactive power, harmonics etc. A brief introduction to some of the problematics associated with PMSG based WECS is provided in sections-1.3.1-1.3.3.

1.3.1 Need of Speed and Position Sensor

To perform maximum power point tracking at different wind speeds, the variable speed operation of PMSG is required. For the variable speed operation of PMSG, generally vector control is preferred as it allows the independent torque and field control just like a simple DC motor control. The vector control of PMSG essentially requires the rotor position and speed information. For this purpose, generally shaft mounted speed and position sensors are used. The use of these sensors may results in to following problems:

- Increased Cost & Complexity.

- Time Bound Maintenance requirement.
- Tearing & Wearing of Mechanical parts and Connecting leads.
- Added moment of inertia due to increased weight and size.
- Both ends of rotor shaft are occupied.
- False operation or Sudden breakdown of Sensors due to hostile weather & operating Conditions.

To alleviate the need of these sensors, several speed estimating algorithms based on Motional EMF, Flux-Linkage Variation and Kalman Filter have been introduced in the past, which are mainly dependent on mathematical model of PMSG (Acarnley et Watson, 2006; Brahmi, Krichen et Ouali, 2009; Tan et Islam, 2004). However, it is extremely difficult to develop an explicit mathematical model of PMSG due to non-ideal rotor flux distribution. Moreover, such kind of estimation algorithm also suffers because of simplified computations based on several assumptions, ignorance of parameter variations and inaccuracy involved with low voltage signal measurement at lower speed, especially in case of directly driven PMSG.

1.3.2 Underutilization of Inverter rating

The variable speed PMSG based WECS requires full rating power electronics installed capacity, which is rarely utilised up to its rated capacity through out the life span of WECS due to the intermittent nature of wind. According to the wind power generation pattern of Kansas wind farm during 2008, the total utilization factor varied in between 20%-30%, with a rare possible peak up to 60% of its rated installed capacity. Similarly, the capacity factor of Ontario wind farms at different locations is found to be in the range of 25%-35% during Jul.2009 - Dec.2009. This underutilization of inverter rating effectively increases the cost of wind power production. Moreover, the percentage of converter losses w.r.t. the amount of generated power also increases due to improper use of installed rating of power electronics devices.

1.3.3 Grid Interconnection Issues

Restructuring of the electric power industry and the elimination of the traditional vertically integrated utility is having significant impact on the wind power interconnection process. In the 1980's, wind project interconnection requirements were negotiated on a project-by project basis between the utility and the project developer. The low penetration levels represented by these early developments may have created local area transmission problems, but they had no impact on neighboring utilities or on regional reliability. In today's regulatory environment, bilateral agreements between utilities and developers have been replaced with standardized processes implemented under the jurisdiction of central electricity regulating agencies of various countries as per their own standards. This trend towards standardized interconnection processes has started not only in North America, but throughout much of the rest of the developed world. The evolution of national interconnection standards, also referred to as "Grid Codes", had its beginnings in Europe, stimulated by the electric power industry restructuring combined with strong incentives for renewable energy implemented in the late 1980's and early 1990's, a decade earlier than these trends emerged in North America. While work on these interconnection standards began in the late 1990's, it was not until 2003 that Germany's transmission system operators (TSOs) published their standard. This was quickly followed by Denmark in 2004 and Spain in early 2005. These were important developments in these three countries representing the first, fourth and second largest markets, respectively, for wind power in the world. North America, while slow to start relative to Europe, has been quick to catch up. Therefore, today's WECS are required to meet these stringent grid interconnection standards and transmission challenges. Most of these standards have some common issues which will be discussed in the following sections one by one.

a) Voltage Control: Most of the modern wind energy conversion systems have some capability to control voltage and power factor at the machine terminals. However, even

if the power factor and voltage at the individual WECS is kept constant as real power varies, the reactive power consumption of the wind farm as a whole will continue to vary as a result of reactive losses on the collection system. This full magnitude of the reactive losses cannot be easily compensated by the individual turbines. Thus, the wind farm's reactive power consumption generally increases with real power output unless ancillary reactive support equipment is installed (Varma, Auddy et Semsedini, 2008; Zobaa et Jovanovic, 2006). In the absence of proper VAR compensation, there can be significant voltage variation on the utility system, which can result in serious damage to expensive transmission grid equipments. This means that the wind farm has to maintain a reasonably constant transmission voltage, even for the megawatt output changes. Some of the international standards require the wind farm to supply power with a power factor that is variable between 0.95 lagging (inductive) and 0.95 leading (capacitive) at the high voltage side of the wind farm's main transformer (Muljadi *et al.*, 2007a). To protect against system stability degradation, utilities often require that the addition of the wind farm does not degrade system stability or result in violations of stability criteria. In these cases software simulations must be run to determine the wind farm's influence on the system (Ha et Saha, 2004). If it is determined that system stability has been unacceptably altered by the wind farm installation, it may be necessary to add auxiliary equipment to address the issue.

b) Control of Frequency: Stable operation of the interconnected power system is dependent on an instantaneous match between load and generation. System frequency is a primary indicator of this balance. When electric load on a synchronous generator exceeds mechanical input, the generator will begin to slow down as kinetic energy is extracted from the machine's rotational inertia and is converted to electric power. The decrease in shaft speed corresponds to a decrease in frequency in a synchronous generator. Conversely, when power supplied by a generator prime mover exceeds electric demand, the generator mechanical system will accelerate as the excess input is stored as rotational energy, with a corresponding frequency increase. This type of

continuous fluctuation in mechanical power input to wind energy conversion system is quite common as the mechanical power input to the wind turbine depends on the wind speed. So it is really a challenging task to maintain constant frequency under the varying wind conditions and especially in case of directly coupled variable speed generators (Yuan-zhang *et al.*, 2009). However, as long as wind power covers only a small percentage of the total load, the effect on frequency can in most cases be neglected. But the rate at which wind energy generation is growing worldwide, the penetration level of wind energy cannot be neglected. The integration of wind power in small isolated systems may certainly have an impact on the grid frequency, and thus it is a matter of great concern for grid interconnection of wind energy conversion system (Muyeen *et al.*, 2010).

c) Control of Active and Reactive Power: Often, the wind farm is required to use its reactive range to regulate its voltage to a specified level while incorporating complicated control characteristics. The requirement of this level of reactive power control is to ensure that the wind farm will be able to minimize system voltage variations and thus enabling to reduce any negative impact of the wind farm on the transmission grid's voltage performance. Such specific voltage control requirements necessitate special reactive support equipment with voltage measurement capabilities and closed loop control. This degree of control is often beyond what can be provided by the individual wind turbines. The ability of a wind turbine to survive a transient voltage dip without tripping is often referred to as the low voltage ride through (LVRT) capability of the turbine. LVRT capability is an important part of wind farm grid interconnection because if the wind farm were to trip off when the voltage dips due to a fault on a nearby power line, that single fault could result in the loss of two major system components, i.e., the line and the wind farm. This would violate the important grid code requirements of Hydro-Quebec (Bernard, Beaulieu et Trudel, 2005) and NERC standard (Reliability Standard TPL-002-0). LVRT is the other primary topic of FERC Order 661-A. FERC Order 661-A essentially requires that the wind farm remain in service during any three-

phase fault (when all three phases of a power circuit come in contact with the ground or each other) that is normally cleared as long as the clearing of that fault does not electrically separate the wind farm from the transmission system and the fault does not depress the voltage at the Point of Common Coupling (PCC) below 0.15 p.u. (15% of normal) voltage (T. Ackermann, 2005; IEEE15471, 2005). The addition of a large wind farm on a power system can alter the flow of power on the system. In some instances, the wind farm's effect on system flows can make certain fault and outage events on the transmission system more severe than they would have been prior to the wind installation and in some cases result in a violation of system stability requirements.

d) Stringent Power Quality Requirement: One of the major issues discussed in all international standards with regard to grid-tied systems is the quality of the distributed power (Enslin et Heskes, 2004). According to the standards in this field (Eltra et. Elkraft, 2004) the injected current in the grid should not have a total harmonic distortion larger than 5%. Moreover the most of standards are pressing very hard that the renewables must stay connected to grid during some fault or unbalance in the supply voltages. Some of the faults have the tendency to create voltage unbalance in the grid. While continuously varying load can also create voltage sag and swell problem. Besides the voltage unbalance, the harmonics and voltage flickers present in the supply system are also major power quality issues.

Harmonics: Voltage harmonics are periodic distortions of the supply voltage which can cause overheating of equipment such as transformers and motors, as well as disturb the operation of sensitive electronics that have been designed to operate from a sinusoidal source. Voltage harmonics result from the flow of harmonic currents generated by nonlinear loads or generators through the source impedance at the location of the nonlinear device. Power electronic devices (rectifiers, inverters, converters) are commonly associated with current distortion, but ubiquitous power system equipment such as transformers and rotating machines (motors and generators) are also sources of

harmonic currents, particularly when they are designed and operated near magnetic saturation.

Voltage Flicker: Voltage flicker is a momentary sag or swell in line voltage, either periodic or a non-periodic, that results in perceptible (often annoying) fluctuations in the intensity of light from lamps supplied by a time-varying voltage source. There are three potential sources of flicker associated with wind turbines as shown in Fig. 1.10. The first is due to voltage fluctuations that may occur as a direct result of power fluctuations from the wind turbine under normal operation in turbulent winds. A second source of flicker is voltage drop resulting from the magnetizing inrush current that occurs when the generator is first electrically connected to grid. When this connection is made at full voltage through a contactor or circuit breaker, the inrush is often several times the full load current of the generator, and can last for several line cycles, enough to be perceptible to the human eye. This effect is magnified when wind plant control systems allow many machines to be brought on line simultaneously.

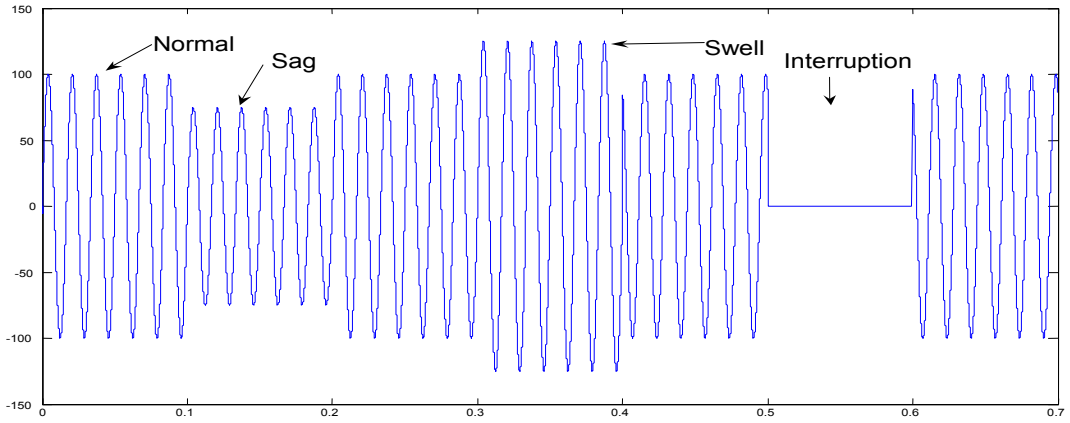

(a) Voltage Sag/Swell/Intreruption

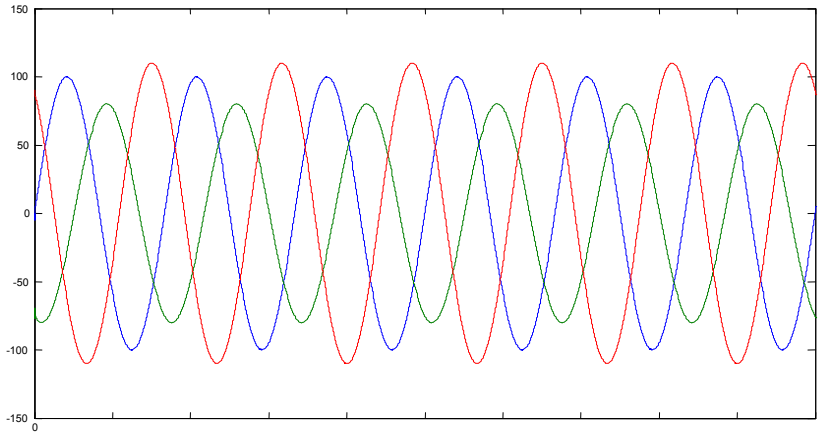

(b) Voltage Unbalance

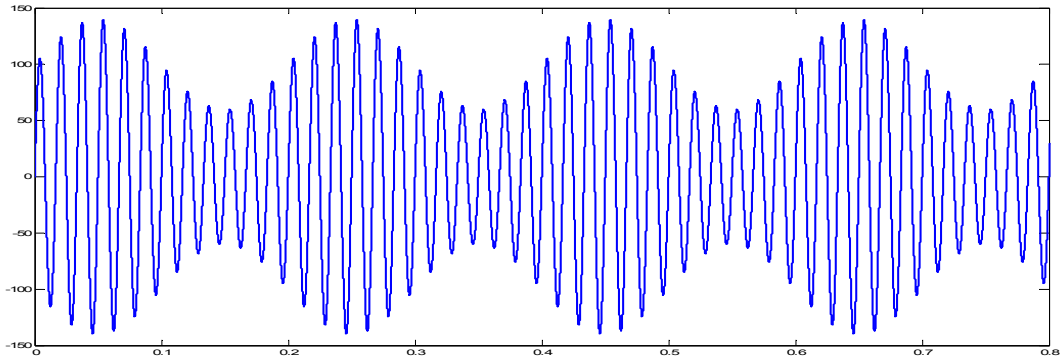

(c) Voltage Oscillations

Figure 1.10 Different Kinds of Voltage Events.

1.4 Objectives

Based on the problematics as discussed in section 1.3, the major objectives of thesis are as mentioned below:

- The rotor speed and position estimation for the sensorless control of PMSG to extract maximum power under fluctuating wind conditions.

- The optimal utilization of grid side inverter rating by using it as a multifunctional device by incorporating the power quality improvement features for the non-linear unbalance load compensation at the point of common coupling (PCC).

- Development of adaptive neuro-fuzzy controller for inverter under dynamic operating conditions.

- Modeling and simulation of an off-grid wind-battery hybrid system for isolated network.

1.5 Methodology

To achieve the objectives mentioned in previous section, a mathematical formulation of PMSG based WECS is carried out. Generally an explicit mathematical model of PMSG is required to estimate the rotor position and speed accurately, which may not be easily available due to variation in PMSG parameters. To replace an explicit model of PMSG an ANFIS based adaptive model of PMSG is developed. The ANFIS architecture has well known advantages of modeling a highly non-linear system, as it combines the capability of fuzzy reasoning in handling the uncertainties and capability of ANN in learning from the processes. An ANFIS based model reference adaptive system (MRAS) is continuously tuned with actual PMSG to neutralize the effect of parameter variations

such as stator resistance, inductance and torque constant. This ANFIS tuned estimator is able to estimate the rotor position and speed accurately over a wide speed range. An error gradient based dynamic back propagation method has been used for the on-line tuning of ANFIS architecture. This estimated rotor speed is further utilized to find out the maximum possible power using power-speed characteristic of PMSG.

Similarly, the control algorithms for both generator and grid side inverters are developed in synchronous reference frame. The generator side converter is used to perform MPPT, while the grid side inverter is used as multi-purpose device. The multifunctional use of grid side inverter justifies the cost of full rating inverter, as the additional hardware cost for custom power devices like APF, STATCOM or VAR compensator can be saved. The grid side inverter is actively controlled to inject the generated wind power and to compensate the harmonics, unbalance and reactive component of unbalance non-linear load at PCC, simultaneously. The duty ratio of inverter switches are varied in a power cycle such that the combination of non-linear unbalance loads and inverter injected power appears as balanced resistive load to the grid. This enables the grid to always supply/absorb only the fundamental active power, which automatically enhances the quality of power and network stability.

The proportional integral (*PI*) controllers are generally used to control the grid side inverter due to their simplicity, where they give satisfactory performance under steady state conditions. However, their performance deteriorates under dynamic operating conditions, as it is very difficult to set the optimal gains of *PI* for rapidly changing operating conditions. To overcome this drawback of *PI* controller, an adaptive neuro-fuzzy controller is developed, where the fuzzy membership functions are continuously tuned using neural network methods. The combined capability of neuro-fuzzy controller is well known, as it reduces the number of fuzzy rule bases and the number of neurons for the fast convergence of control, without compromising the controller performance.

The PMSG based WECS is modeled and simulated in MATLAB/Simulink environment by using the different toolboxes. The different block sets of SIMPOWERSYSTEM toolbox are specially used to design the electrical model of the proposed system, while the discrete components from various toolboxes are used to implement the control algorithms. The simulation results are provided to validate the control approach.

To validate the simulation studies, an experimental scaled prototype is developed in laboratory. An induction motor controlled with ABB ACS800 industrial drive is used to emulate the wind turbine, which in turn rotates the PMSG. The PMSG is connected to the grid through two back to back connected inverters with a common DC-link in between. The control algorithms developed in MATLAB/Simulink environment are successfully implemented in real time using *dSPACE.* The measured signals are sent to *dSPACE* through A/D converters and the control signals from *dSPACE* are applied to real hardware through D/A converters. Finally, the simulation results supported by experimental results are provided to validate the control strategies.

CHAPTER 2

SYSTEM MODELING AND CONTROL

In this chapter the main components of PMSG based WECS are discussed one by one. The system description gives a brief idea about the working and operational behavior of each component. Besides this the mathematical formulation of each component is carried out which further helps in developing the control strategies for the whole system.

2.1 Modeling of Wind Turbine

A wind turbine basically consists of rotor blades and generator. The rotor blades transform the linear kinetic wind energy into rotational kinetic energy in a first step and finally the rotational kinetic energy is converted into electrical energy with the help of generator. To determine the effectiveness of this energy conversion, the amount of energy present in wind needs to be determined first. Actually, the small air particles having mass *m* and moving with velocity *V,* are the energy carrier in wind. With the assumption that all particles at different locations in space have the same motional speed before hitting the rotor, the kinetic energy carried by the wind particles can be represented by the following equation:

$$E_{kin} = \frac{1}{2} \cdot m \cdot V^2 \tag{2.1}$$

On substituting the particle mass with air density (ρ), wind speed (V), time (t) and applying a circular swept area (Λ) with radius r, we have

$$m = \rho \cdot \Lambda \cdot V \cdot t = \rho \cdot \pi \cdot r^2 \cdot V \cdot t \tag{2.2}$$

And the expression of the wind energy facing a virtual rotor disc, can be expressed as

$$E_{kin} = \frac{1}{2} \cdot \rho \cdot \pi \cdot r^2 \cdot V^3 \cdot t \tag{2.3}$$

From the equation (2.3), we can easily find the actual wind power at any time instance as:

$$P_{wind} = \frac{1}{2} \cdot \rho \cdot \pi \cdot r^2 \cdot V^3 \tag{2.4}$$

On analyzing the equation (2.4), it is quite evident that the most dominating parameter for wind power is wind speed, as the wind power is almost cubic function of wind speed. This means that there is much more energy in high-speed wind than in slow wind. Also, since the power is proportional to the rotor swept area, and thus to the square of the diameter, doubling the rotor diameter will quadruple the available power. Air density also plays a role in the amount of available mechanical power of the turbine; lower air densities (e.g. warm air) results in less available power in wind. A schematic of wind turbine showing its various components is given in Fig. 2.1.

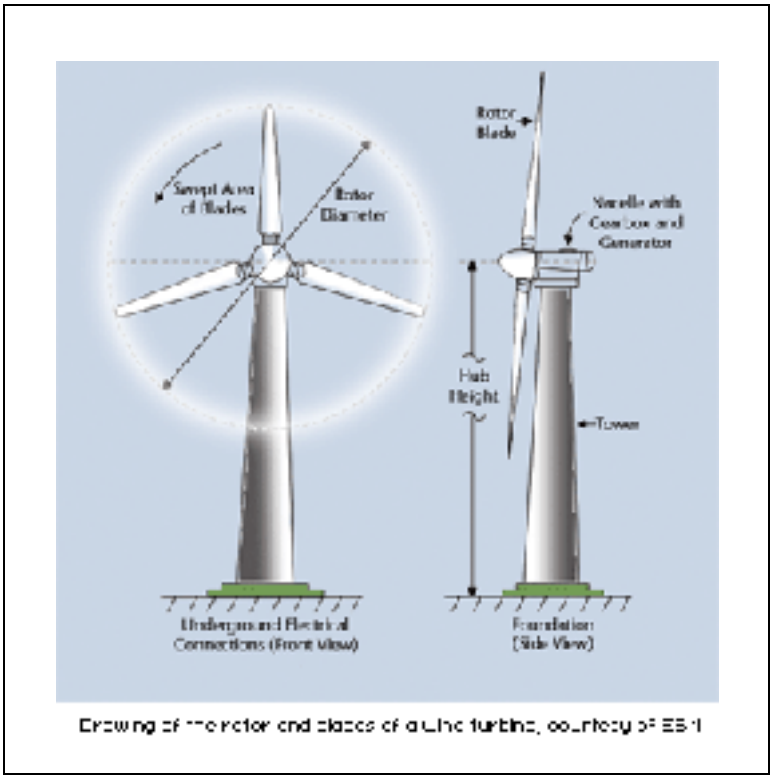

Figure 2.1 Wind Turbine Design.

Now the main question arises is that how effectively the power available in wind can be converted into useful electrical energy. It depends on the aerodynamic design of the rotor blades and their capability of capturing energy from the striking wind.

2.1.1 Wind Power Co-efficient

The rotor blades play an important role in extracting power from flowing wind. The speed of rotor slows down after extracting power, but it is not desirable to let the rotor come to standstill position, which means zero power has been extracted out of wind. In 1919, a German scientist Albert Betz had tried to express the action of wind braking on a disc like rotor. According to Betz's Law, the speed of wind decreases after striking the rotor blades, where the power captured by rotor blades depend on the difference of wind speed just before and after striking the rotor blades and can be expressed as :

$$P_{Turb} = \frac{1}{2} k_m \left(V_1 - V_2\right)^2 \tag{2.5}$$

here V_1 is the wind speed before striking the blade and V_2 is the wind speed after striking the blades. Here k_m is the mass flow rate and can be expressed as:

$$k_m = \rho \cdot \pi \cdot r^2 \cdot \frac{V_1 + V_2}{2} \tag{2.6}$$

On putting the wind speed far in front of the turbine into the right relation to the wind speed behind the turbine, Betz derived the equation for the so called *power coefficient* (*Cp*), which can be expressed as:

$$\frac{P_{Turb}}{P_{wind}} = C_p \tag{2.7}$$

On putting the value of P_{wind} in the above equation, we have :

$$P_{Turb} = P_{wind} \cdot C_p = \frac{1}{2} \cdot \rho \cdot \pi \cdot r^2 \cdot V^3 \cdot C_p \tag{2.8}$$

The power coefficient, according to Betz' Law can be defined as:

$$C_p = \frac{1}{2}\left(1 + \frac{V_2}{V_1}\right) \cdot \left(1 - \left(\frac{V_2}{V_1}\right)^2\right) \tag{2.9}$$

Actually, *Cp* indicates how much power we can take out of the wind by giving an equivalent braking. *Cp* does not show how this breaking is achieved. But, the formula

for *Cp* can show at least the theoretical maximum. This maximum is located between two scenarios. If we would take out all kinetic energy by our wind turbine the particle flow would almost come to standstill, air would accumulate in front and further particles would avoid and pass by the turbine. No braking of the particle flow means we will not take out any energy and the power would be zero.

For solving the equation (2.9) we introduce a braking action without units:

$$x = \frac{V_2}{V_1} \tag{2.10}$$

On putting the value of x in the equation (2.9) for power co-efficient, we have:

$$C_p = \frac{1}{2}.(1+x).(1-x^2) \tag{2.11}$$

Solving the equation (2.11) for the maximum, with $x = \frac{1}{3}$, we have:

$$C_{p\_\max} = \frac{16}{27} \approx 0.593 \tag{2.12}$$

This means, the highest possible power we can theoretically get out of the wind power is 59.3%. Therefore the wind will be broken down to 1/3 of its original speed. In practical blade design consideration, the maximum value of power co-efficient can be achieved anything between 0.4 to 0.54

2.1.2 Tip Speed Ratio

Unfortunately, for wind turbines *Cp* is not constant. The most common parameters, on which *Cp* depends, are the tip speed ratio λ and the pitch angle β.

$$\lambda = \frac{TipSpeed}{WindSpeed} = \frac{\omega_r r}{V} \tag{2.13}$$

The power coefficient $C_p = (\lambda, \beta)$ is a function of both parameters. Consequently different wind speeds will require the optimal values of tip speed and pitch angle to achieve a high *Cp* and therefore giving the highest power output at all available wind speeds. The mentioned aspects make it very clear - to get maximum power out of the wind we need to have a wind turbine that allows the change in rotor speed to reach optimal aerodynamic conditions. As every optimal $C_{p,optimal}$ has one optimal value of tip speed ratio $\lambda_{optimal}$, therefore we have to control our tip-speed according to the wind-speed. This task is well known as Maximum Power Point Tracking (MPPT).

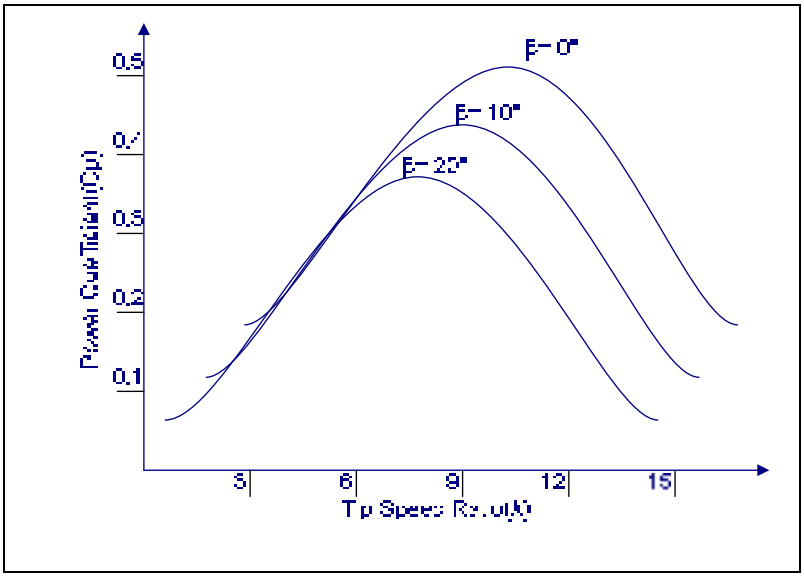

Figure 2.2 *C_P-TSR* Characteristic.

In Fig. 2.2, the change of the C_P-*TSR* curve as the pitch angle is adjusted is also shown. In low to medium wind speeds, the pitch angle is controlled to allow the wind turbine to operate at its optimum condition. In the high wind speed region, the pitch angle is increased to shed some of the aerodynamic power.

2.1.3 Turbine Operating Region

The wind turbine operational states can be divided in to three states as shown in Fig. 2.3.

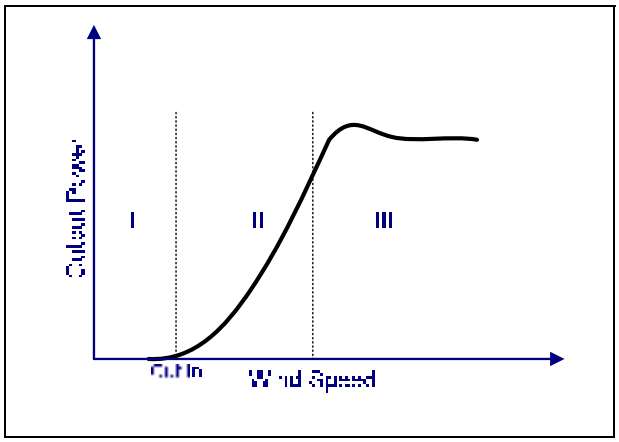

Figure 2.3 Turbine Operating Region.

1. **Standstill:** the wind power must be sufficient enough to overcome the friction and inertia of the wind turbine. This gives us an idea about Cut-in speed. The operational region I is related to Cut-in speed where the turbine will start spinning and moves in II region.

2. **Normal Operation (Lower to Medium wind speed) :** starting at cut-in wind speed the turbine follows the power curve if the regulation works properly. Ideally, the wind turbine should be operated at maximum C_P most of the time. In the lower wind speed, when the aerodynamic power produced by the wind turbine is below the maximum power rating of the power converter, the wind turbine is operated in the

C_{Pmax}. The pitch angle of the wind turbine is controlled to have the maximum possible value of C_{Pmax}. As the rpm changes, the pitch angle is kept at its optimum pitch angle.

3. **Pitched Operation (Higher wind speed region) :** the power captured by blades is kept within limit with the help of pitch control mechanism. Actually, the beginning cannot be defined at one specific wind speed as even short wind gusts can activate the pitching mechanism. As the wind speed increases, the power generated by the wind turbine also increases. Once the maximum rating of the power converter is reached, then the pitch angle must be increased to shed the aerodynamic power. As the pitch angle is increased, the wind turbine operates at lower efficiency. Figure (12) shows that the whole C_P -*TSR* curve is shifted downward when the pitch angle is increased. With this capability, the input mechanical power driving the generator can be easily controlled. Assuming the pitch control can be done instantaneously, the acceleration and deceleration can be made zero and the speed can be kept constant by controlling the P_{mech} to be exactly equal to P_{elect}. A higher pitch rate capability of a wind turbine can lessen the requirement for the generator and power converter rating. But the pitch rate capability is usually limited due to the presence of inertia of the system as evident from following relation

$$\frac{d\omega}{dt} = \frac{1}{J}\int (T_{mech.} - T_{elect.}).dt \tag{2.13}$$

Where the rate of rotor speed is proportional to the inverse of the inertia and difference between aerodynamic torque captured ($T_{mech.}$) from the wind and the electric torque load ($T_{elect.}$).

2.2 Generator Type Selection Criteria

When it comes to design a variable speed wind turbine, the important task is the selection of a suitable generator. The turbine generator set has to perform two major tasks. First, it is supposed to generate electrical energy – second, by adjusting the electrical load the generators braking torque will control the speed of the turbine to achieve the optimal tip speed ratio λ for a high *Cp* at present wind speed. The proposed system is supposed to be directly connected variable speed wind turbine. Therefore, a generator for low speeds (20-75 rpm) and with very high torques has to be used. To have an idea of desired load torque, a quick calculation can be done by using following relation

$$T = \frac{P}{\omega} \tag{2.17}$$

Suppose there is a 100 Kw generator with a rated speed of 75 rpm:

$$T = \frac{100kW}{2 \cdot \pi \cdot 75/60} \approx 12730Nm \tag{2.18}$$

Thus in comparison to a machine of same capacity at higher speed, the calculated torque is very high for low speed operation. To obtain such a high value of the torque we have to identify the parameters responsible for torque production with the help of following equation.

$$P = T \cdot \omega = \frac{\pi}{2} \cdot (\vec{B} \cdot \vec{A}) \cdot d^2 \cdot l \cdot \omega \tag{2.19}$$

From the above relation, it is evident that the torque is mainly determined by the magnetic flux density *B*, the electric loading *A*, the machine diameter *d* and the active

length *l*. In conclusion a low speed generator with high specific torque requires high magnetic flux density, high currents and rather big dimensions.

Another requirement of variable speed wind turbine generators is high efficiency across a wide speed range. As variable speed turbines is supposed to operate in different speed regions, therefore it is very important to assure good efficiencies under all operational states.

Last but not least, to reduce tower stress, production cost and shipping cost, the generator must have a good torque to weight ratio.

After considering all these requirements we can come to a conclusion that an ideal generator for such a system must have following qualities (Polinder *et al.*, 2006):

- High torque density
- Low cogging torque
- High torque/weight ratio
- High Robustness
- High efficiency over wide speed and load range

One topology that can meet all these requirements might be the permanent magnet synchronous machine (PMSM) in combination with a suitable control strategy.

2.2.1 Permanent Magnet Synchronous Machines

The PMSMs are synchronous ac machines. The PMSM consist of 3-phase stator winding similar to SCIG, while the rotor winding is replaced by the permanent magnets. The advantage of eliminating the rotor field winding are reduced copper losses, higher power density, lower rotor inertia and more robust construction of the rotor (Polinder *et*

al., 2007). The demerits are the loss of flexibility in field flux control, possible demagnetization/saturation of magnetic material and parameter variation with passage of time. On the basis of rotor design, the PMSM can be divided in to two parts. Depending on the magnet placement on the rotor they are called either surface permanent magnet machines (SPM) or interior permanent magnet machines (IPM) as shown in Fig. 2.4.

In SPM machines, the permanent magnets are glued on the rotor surface using epoxy adhesive. The rotor has an iron core which may be solid or made of punched laminations with skewed poles to minimize the cogging torque. The simple rotor design makes it easy to build. This kind of configuration is used for low speed operation, as there are chances that the magnet may fly during high speed operation. The permeability of magnetic material is almost close to air, which results in to an effective large air gap. Moreover, due to the smooth rotor surface design the saliency in rotor is supposed to be minimum. This contributes to low armature reaction effect due to low magnetization inductance.

In interior permanent magnet machines, the magnets are installed inside the rotor. Although a number of configurations are possible, a typical IPM is shown in Fig. (14). The rotor of IPM is little bit difficult to fabricate. But the robust design of IPM makes it more suitable for high speed applications. The unequal effective air gap distribution makes it as a salient pole machine, where the direct axis inductance is less than quadrature axis inductance ($L_d < L_q$).

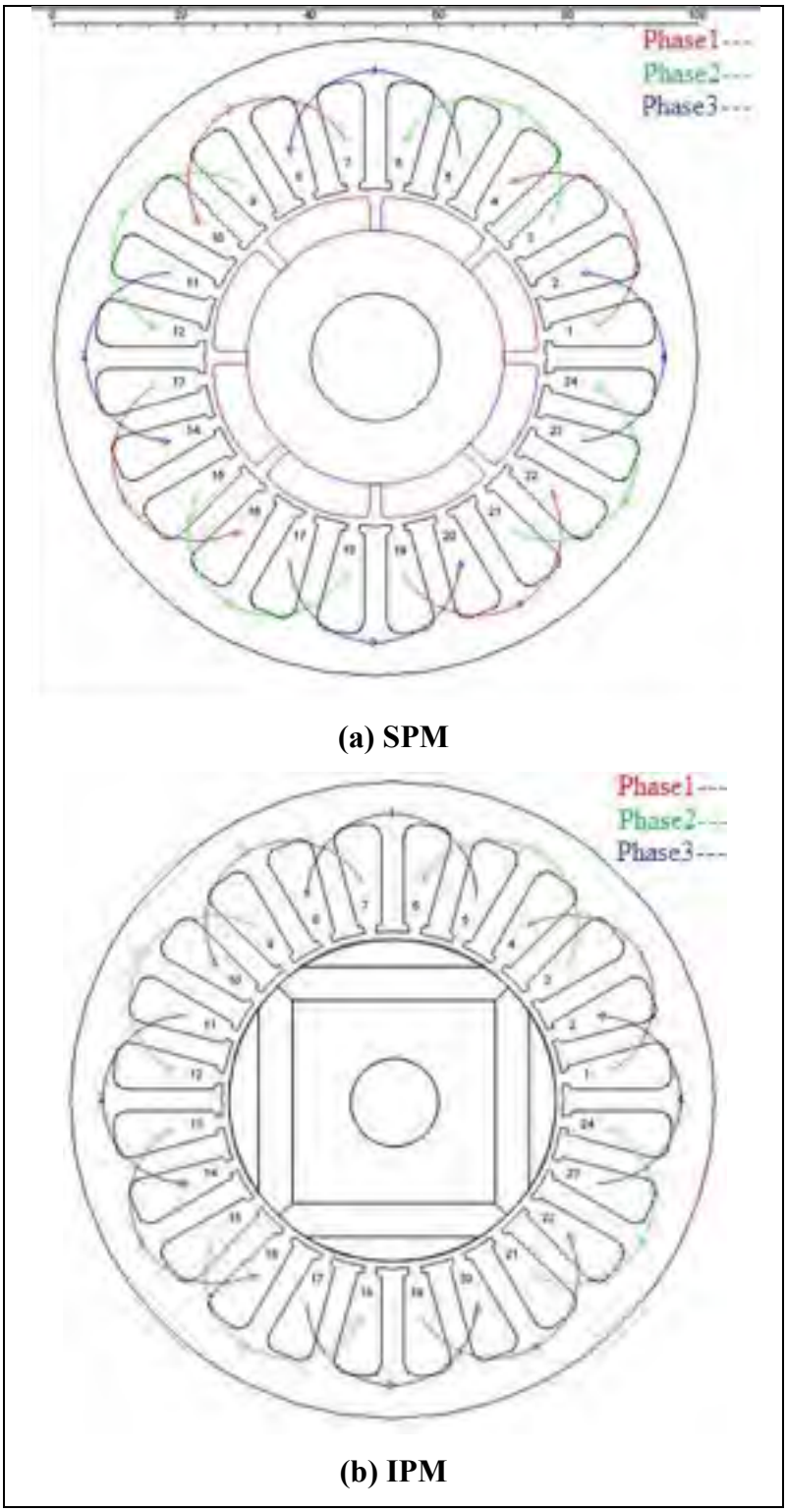

(a) SPM

(b) IPM

Figure 2.4 Design of PMSM.

a) Operating Principle of PMSM: In permanent magnet synchronous machines, the magnets are placed on rotor surface as alternate *N* and *S* poles. These surface mounted magnets cause development of magnetic flux in air gap. When the stator windings are excited, they develop their own magnetic flux. The close interaction between rotor and stator magnetic fields produces electromagnetic torque in the rotor.

Fig. 2.5 shows the simplified cross-section view of 3-phase, 2-pole PMSM with symmetrical stator windings, displaced by 120^{o} electrical angle from each other. The relative motion in between rotor and stator induces sinusoidal MMF waves centered on the magnetic axes of the respective phases. The phase difference between rotor magnetic flux (d-axis) and the magnetic axis of stator phase-a winding is known as rotor position angle (θ_r). The rate of change of rotor position angle further calculates the angular rotor speed (ω_r).

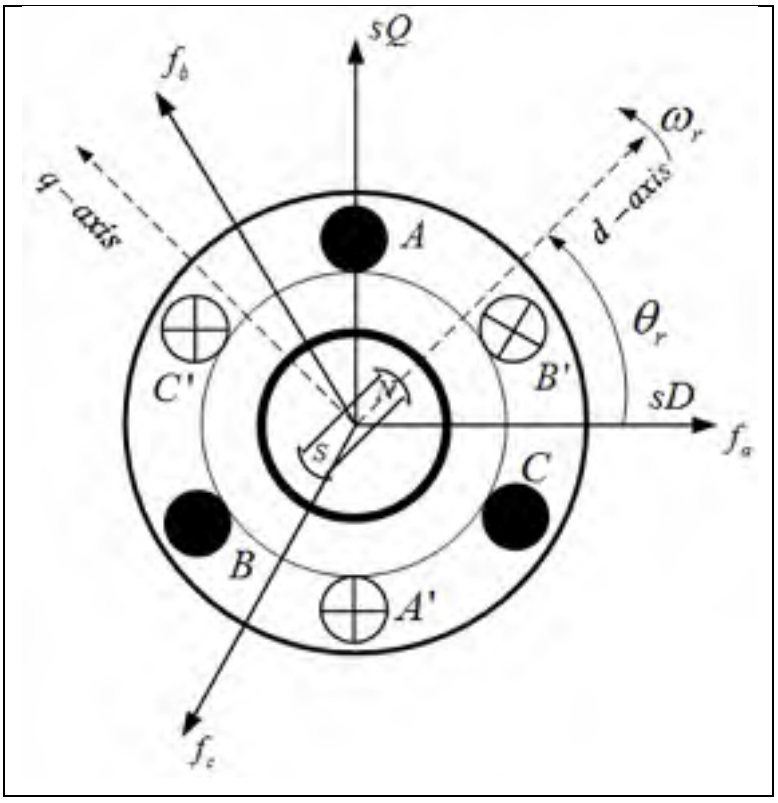

Figure 2.5 Cross-Section View of PMSM.

b) Generalized Model of PMSM: For a PMSM with sinusoidal flux distribution, there is no difference between the back e.m.f. induced by permanent magnet rotor or wound rotor. Hence, the mathematical model of PMSM is similar to that of wound rotor synchronous machine.

The PMSM stator voltage equations in *abc* ref. frame can be expressed in terms of instantaneous currents and stator flux linkages as (Peter.Vaas, 1998; Paul C. Krause, Wasynczuk et Sudhoff, 1986):

$$\vec{V}_{abc} = R_{sabc} \cdot \vec{i}_{abc} + p \cdot \vec{\lambda}_{abc} \tag{2.20}$$

Where

$$\begin{aligned} \vec{V}_{abc} &= \begin{bmatrix} V_a & V_b & V_c \end{bmatrix}^T \\ \vec{i}_{abc} &= \begin{bmatrix} i_a & i_b & i_c \end{bmatrix}^T \\ \vec{\lambda}_{abc} &= \begin{bmatrix} \lambda_a & \lambda_b & \lambda_c \end{bmatrix}^T \\ R_{sabc} &= diag\begin{bmatrix} R_s & R_s & R_s \end{bmatrix} \end{aligned} \tag{2.21}$$

Where R_s is the stator resistance and p is the differentiating operator d/dt. For a linear magnetic system, the stator flux linkage can be calculated as follows:

$$\vec{\lambda}_{abc} = L_{abc} \cdot \vec{i}_{abc} + \vec{\lambda}_{mabc} \tag{2.22}$$

Where

$$L_{abc} = \begin{bmatrix} L_{aa} & L_{ab} & L_{ac} \\ L_{ba} & L_{bb} & L_{bc} \\ L_{ca} & L_{cb} & L_{cc} \end{bmatrix} \tag{2.23}$$

$$\vec{\lambda}_{mabc} = \lambda_m \begin{bmatrix} \cos\theta_r \\ \cos(\theta_r - 2\pi/3) \\ \cos(\theta_r + 2\pi/3) \end{bmatrix} \tag{2.24}$$

The stator winding inductances in equation (2.23) can be expressed as:

$$L_{aa} = L_{ls} + L_{0s} + L_{2s}\cos 2\theta_r \tag{2.25}$$

$$L_{bb} = L_{ls} + L_{0s} + L_{2s}\cos 2\left(\theta_r - \frac{2\pi}{3}\right) \tag{2.26}$$

$$L_{cc} = L_{ls} + L_{0s} + L_{2s}\cos 2\left(\theta_r + \frac{2\pi}{3}\right) \tag{2.27}$$

$$L_{ab} = L_{ba} = -\frac{1}{2}L_{0s} + L_{2s}\cos 2\left(\theta_r - \frac{\pi}{3}\right) \tag{2.28}$$

$$L_{ac} = L_{ca} = -\frac{1}{2}L_{0s} + L_{2s}\cos 2\left(\theta_r + \frac{\pi}{3}\right) \tag{2.29}$$

$$L_{bc} = L_{cb} = -\frac{1}{2}L_{0s} + L_{2s}\cos 2\left(\theta_r + \pi\right) \tag{2.30}$$

In the above given equations, L_{aa}, L_{bb}, and L_{cc}, are the self inductances of each phase, L_{ab}, L_{bc}, and L_{ca} are the mutual inductances, and λ_m is the flux linkage established by the rotor magnets. The *leakage* inductance L_{ls} consists of magnetizing inductance components L_{0s} and L_{2s}, which are further dependent on rotor position. Here, generally L_{2s} is negative and L_{0s} is positive in case of interior permanent magnet motors (IPM) due to their unique rotor design. Therefore, the quadrature-axis magnetizing inductance L_{mq}

is larger than the direct-axis magnetizing inductance L_{md} of interior PM motor, which is opposite to general salient-pole synchronous machines.

The stator flux linkage in equation (2.22) can be written in extended form as:

$$\begin{bmatrix} \lambda_a \\ \lambda_b \\ \lambda_c \end{bmatrix} = \begin{bmatrix} L_{aa} & L_{ab} & L_{ac} \\ L_{ba} & L_{bb} & L_{bc} \\ L_{ca} & L_{cb} & L_{cc} \end{bmatrix} \begin{bmatrix} i_a \\ i_b \\ i_c \end{bmatrix} + \lambda_m \begin{bmatrix} \cos\theta_r \\ \cos(\theta_r - 2\pi/3) \\ \cos(\theta_r + 2\pi/3) \end{bmatrix} \tag{2.31}$$

c) Modeling of PMSM in *d-q* reference frame: The electromagnetic analysis of a PMSM is conveniently carried out in a *d-q* rotating reference frame, introduced by R. H. Park in the late 1920s. According to Park's transformation, the 3-phase machine is analysed on the basis of two –axis theory, where the fictitious direct- and quadrature-axis currents (i_d, i_q) flows through the virtual stator windings. Park's transformation eliminates all time-varying inductances from the voltage equations of the synchronous machine which occur due to electric circuits both in relative motion and with varying magnetic reluctance. Park Transformation and its inversion can be mathematically expressed in the following:

$$\begin{bmatrix} f_d \\ f_q \\ f_0 \end{bmatrix} = (T_{abc\to dq0}) \begin{bmatrix} f_a \\ f_b \\ f_c \end{bmatrix} = \frac{2}{3} \begin{bmatrix} \cos\theta_r & \cos(\theta_r - \frac{2\pi}{3}) & \cos(\theta_r + \frac{2\pi}{3}) \\ -\sin\theta_r & -\sin(\theta_r - \frac{2\pi}{3}) & -\sin(\theta_r + \frac{2\pi}{3}) \\ \frac{1}{2} & \frac{1}{2} & \frac{1}{2} \end{bmatrix} \begin{bmatrix} f_a \\ f_b \\ f_c \end{bmatrix} \tag{2.32}$$

$$\begin{bmatrix} f_a \\ f_b \\ f_c \end{bmatrix} = (T_{abc\to dq0})^{-1} \begin{bmatrix} f_d \\ f_q \\ f_o \end{bmatrix} = \begin{bmatrix} \cos\theta_r & -\sin\theta_r & 1 \\ \cos(\theta_r - \frac{2\pi}{3}) & -\sin(\theta_r - \frac{2\pi}{3}) & 1 \\ \cos(\theta_r + \frac{2\pi}{3}) & -\sin(\theta_r + \frac{2\pi}{3}) & 1 \end{bmatrix} \begin{bmatrix} f_d \\ f_q \\ f_o \end{bmatrix} \tag{2.33}$$

In the equations (2.32) and (2.33), *f* can represent either voltage, current or flux linkage vector variables. The frame of reference may rotate at any constant or varying angular velocity or it may remain stationary as in the Clark Transformation. For a three-phase balanced system, the transformation matrix in (2.32) can be reduced to

$$\begin{bmatrix} f_d \\ f_q \end{bmatrix} = (T_{abc\to dq}) \begin{bmatrix} f_a \\ f_b \\ f_c \end{bmatrix} = \frac{2}{3} \begin{bmatrix} \cos\theta_r & \cos(\theta_r - \frac{2\pi}{3}) & \cos(\theta_r + \frac{2\pi}{3}) \\ -\sin\theta_r & -\sin(\theta_r - \frac{2\pi}{3}) & -\sin(\theta_r + \frac{2\pi}{3}) \end{bmatrix} \begin{bmatrix} f_a \\ f_b \\ f_c \end{bmatrix} \tag{2.34}$$

Now the equation (2.20) can be re-written in rotating reference frame as given below:

$$\vec{V}_{dq0} = R_s \cdot \vec{i}_{dq0} + T_{abc\to dq0} \cdot p \cdot \left[(T_{abc\to dq0})^{-1} \right] \vec{\lambda}_{dq0} + p \cdot \vec{\lambda}_{dq0} \tag{2.35}$$

Where

$$\begin{aligned} \vec{V}_{dq0} &= \begin{bmatrix} V_d & V_q & V_0 \end{bmatrix}^T \\ \vec{i}_{dq0} &= \begin{bmatrix} i_d & i_q & i_0 \end{bmatrix}^T \\ \vec{\lambda}_{dq0} &= \begin{bmatrix} \lambda_d & \lambda_q & \lambda_0 \end{bmatrix}^T \end{aligned} \tag{2.36}$$

Similarly, the stator flux linkage as calculated in equation (2.22) can be written in rotating reference frame as:

$$\vec{\lambda}_{dq0} = L_{dq0} \cdot i_{dq0} + \vec{\lambda}_{dq0m} \tag{2.37}$$

Where, the magnetizing flux linkage lies in the direction of d-axis, and hence can be written in matrix form as given below :

$$\vec{\lambda}_{dq0m} = \begin{bmatrix} \lambda_m & 0 & 0 \end{bmatrix}^T \tag{2.38}$$

$$L_{dq0} = \begin{bmatrix} L_d & 0 & 0 \\ 0 & L_q & 0 \\ 0 & 0 & L_0 \end{bmatrix} \tag{2.39}$$

$$L_d = L_{ls} + L_{md} = L_{ls} + \frac{3}{2}\left(L_{0s} + L_{2s}\right) \tag{2.40}$$

$$L_q = L_{ls} + L_{mq} = L_{ls} + \frac{3}{2}\left(L_{0s} - L_{2s}\right) \tag{2.41}$$

$$L_0 = L_{ls} \tag{2.42}$$

Further the interrelationship between L_d, L_q and L_{0s}, L_{2s} can be given as:

$$L_{md} = \frac{3}{2}\left(L_{0s} + L_{2s}\right) \tag{2.43}$$

$$L_{mq} = \frac{3}{2}\left(L_{0s} - L_{2s}\right) \tag{2.44}$$

$$L_{0s} = \frac{2}{3}\left(\frac{L_{md} + L_{mq}}{2}\right) = \frac{1}{3}\left(L_{md} + L_{mq}\right) \tag{2.45}$$

$$L_{2s} = \frac{2}{3}\left(\frac{L_{md} - L_{mq}}{2}\right) = \frac{1}{3}\left(L_{md} - L_{mq}\right) \tag{2.46}$$

Here, L_d is termed as direct-axis stator inductance and L_q as the quadrature axis stator inductance.

Similarly we can have

$$p \cdot \left[(T_{abc\to dq0})^{-1}\right] = \omega_r \cdot \begin{bmatrix} -\sin\theta_r & -\cos\theta_r & 0 \\ -\sin(\theta_r - \frac{2\pi}{3}) & -\cos(\theta_r - \frac{2\pi}{3}) & 0 \\ -\sin(\theta_r + \frac{2\pi}{3}) & -\cos(\theta_r + \frac{2\pi}{3}) & 0 \end{bmatrix} \tag{2.47}$$

Thus, we can have

$$T_{abc\to dq0} \cdot p \cdot \left[(T_{abc\to dq0})^{-1}\right] = \omega_r \cdot \begin{bmatrix} 0 & -1 & 0 \\ 1 & 0 & 0 \\ 0 & 0 & 0 \end{bmatrix} \tag{2.48}$$

On putting all these terms from equations (2.36) to (2.48) in equation (2.35)

$$\begin{bmatrix} V_d \\ V_q \\ V_0 \end{bmatrix} = \begin{bmatrix} R_s & 0 & 0 \\ 0 & R_s & 0 \\ 0 & 0 & R_s \end{bmatrix} \begin{bmatrix} i_d \\ i_q \\ i_0 \end{bmatrix} + \omega_r \cdot \begin{bmatrix} 0 & -1 & 0 \\ 1 & 0 & 0 \\ 0 & 0 & 0 \end{bmatrix} \left[\begin{bmatrix} L_d & 0 & 0 \\ 0 & L_q & 0 \\ 0 & 0 & L_0 \end{bmatrix} \begin{bmatrix} i_d \\ i_q \\ i_0 \end{bmatrix} + \begin{bmatrix} \lambda_m \\ 0 \\ 0 \end{bmatrix} \right] + p \cdot \left[\begin{bmatrix} L_d & 0 & 0 \\ 0 & L_q & 0 \\ 0 & 0 & L_0 \end{bmatrix} \begin{bmatrix} i_d \\ i_q \\ i_0 \end{bmatrix} + \begin{bmatrix} \lambda_m \\ 0 \\ 0 \end{bmatrix} \right] \tag{2.49}$$

On simplifying the equation (2.49) and writing in extended form as:

$$V_d = R_s \cdot i_d + L_d \cdot \frac{di_d}{dt} - \omega_r \cdot L_q \cdot i_q \tag{2.50}$$

$$V_q = R_s \cdot i_q + L_q \cdot \frac{di_q}{dt} + \omega_r \cdot L_d \cdot i_d + \omega_r \cdot \lambda_m \tag{2.51}$$

$$V_0 = R_s \cdot i_0 + L_0 \cdot \frac{di_0}{dt} \tag{2.52}$$

For balanced operation of PMSM, the zero sequence equation can be neglected. The d-axis and q-axis equivalent diagram of PMSM are shown in Fig. 2.6.

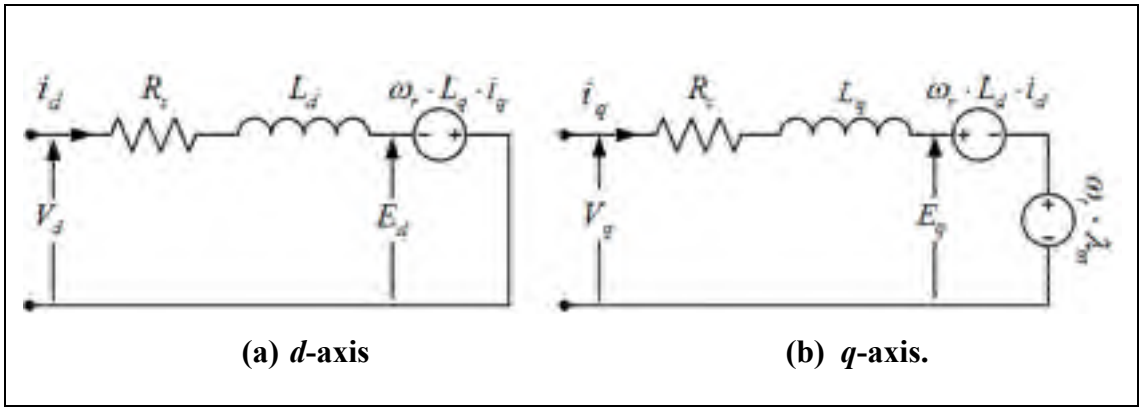

(a) *d*-axis **(b) *q*-axis.**

Figure 2.6 Equivalent Model of PMSM.

In the Fig 2.6, E_d, and E_q are the back e.m.f. of direct and quadrature axis respectively, which can be expressed as:

$$E_d = -\omega_r \lambda_q = -\omega_r L_q i_q \tag{2.53}$$

$$E_q = \omega_r \lambda_d = \omega_r L_d i_d + \omega_r \lambda_m \tag{2.54}$$

The mechanical power developed inside PMSM can be expressed as:

$$P_m = \frac{3}{2}\left(E_d i_d + E_q i_q\right) = \frac{3}{2}\left(\omega_r \lambda_d i_q - \omega_r \lambda_q i_d\right) \tag{2.55}$$

Similarly, from the above derived equations, the expression for electromagnetic torque in rotating reference frame can be written as:

$$T_e = \frac{P_m}{\omega_m} = \frac{P_m}{\omega_r}\left(\frac{P}{2}\right) \tag{2.56}$$

Where ω_m is the mechanical speed and P is the number of poles.

On substituting the equation (2.55) in equation (2.56), the expression for electromagnetic torque can be re-written as :

$$T_e = \left(\frac{3}{2}\right)\left(\frac{P}{2}\right)\left(\lambda_d \cdot i_q - \lambda_q \cdot i_d\right) \tag{2.57}$$

On substituting the appropriate values for stator flux linkage from equation (2.37) in equation (2.57), the equation for electromagnetic torque can be re-written as:

$$T_e = \left(\frac{3}{2}\right)\left(\frac{P}{2}\right)\left[\lambda_m \cdot i_q - \left(L_q - L_d\right) i_q \cdot i_d\right] \tag{2.58}$$

As the permanent magnet synchronous machine is to be operated in generating mode, so the flow of current in stator windings will be in opposite direction. On incorporating the opposite current flow sign convention, the voltage equations in generating mode can be written as:

$$V_d = -R_s \cdot i_d - L_d \cdot \frac{di_d}{dt} + \omega_r \cdot L_q \cdot i_q \tag{2.59}$$

$$V_q = -R_s \cdot i_q - L_q \cdot \frac{di_q}{dt} - \omega_r \cdot L_d \cdot i_d + \omega_r \cdot \lambda_m \tag{2.60}$$

The *d*-axis and *q*-axis equivalent diagrams of PMSM in generating mode are shown in Fig. 2.7.

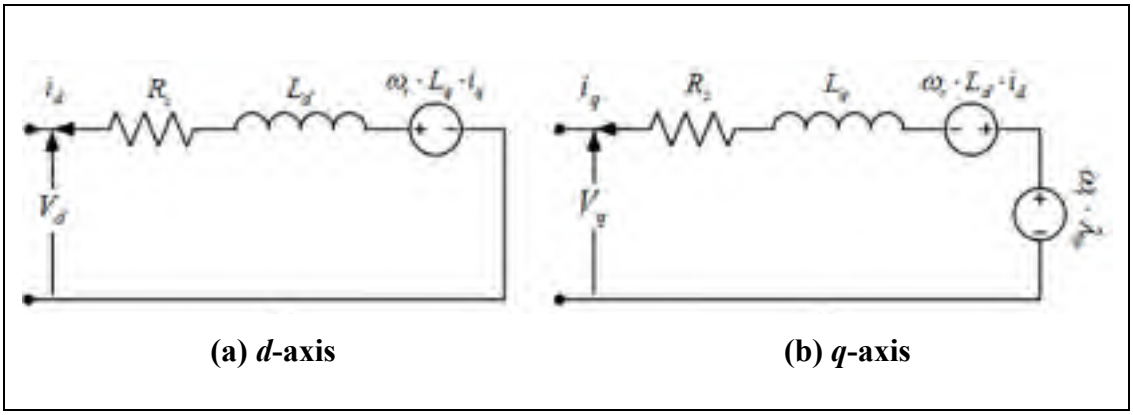

Figure 2.7 Equivalent Model of PMSG.

Since, the directly driven variable speed WECS is supposed to be operating at low speed, the surface mounted permanent magnet machine (SPM) is considered in this study. In SPMs the rotor design is almost smooth and thus offers equal reluctance in both *d*-axis and *q*-axis, which results in to equal *d*- and *q*-axis inductances (L_d=L_q).

On substituting the equal value of *d*- and *q*-axis inductances (L_d=L_q), the torque equation in (2.58) can be further modified as:

$$T_e = \left(\frac{3}{2}\right)\left(\frac{P}{2}\right)\lambda_m \cdot i_q \tag{2.61}$$

Being the rotor magnetic flux linkage constant in SPM, the electromagnetic torque is directly proportional to quadrature-axis stator current, as evident from equation (2.61). In other words, the electromagnetic torque in PMSG can be controlled by controlling its quadrature-axis current components.

2.3 Power Electronic Interface

Power electronics is a rapidly developing technology. The increasing component's current and voltage ratings with reduced power losses, the power electronic devices are gaining popularity for high performance applications. The devices are also very easy to control even at mega scale power amplification. Further, with the decreasing cost/kVA, the power electronics based converters are becoming attractive as a mean to improve the performance of variable speed wind turbines.

In the case of variable speed PMSG, the power is generated at variable voltage both in frequency and amplitude. The power electronic interface is required to convert the variable voltage and frequency in to a constant grid voltage and frequency. Different kind of power converter configurations can be used for such type of variable speed PMSG based wind turbine applications. In this thesis, two back-to-back (BBC) PWM-VSI based bi-directional power converter topology is used as shown in Fig. 2.8.

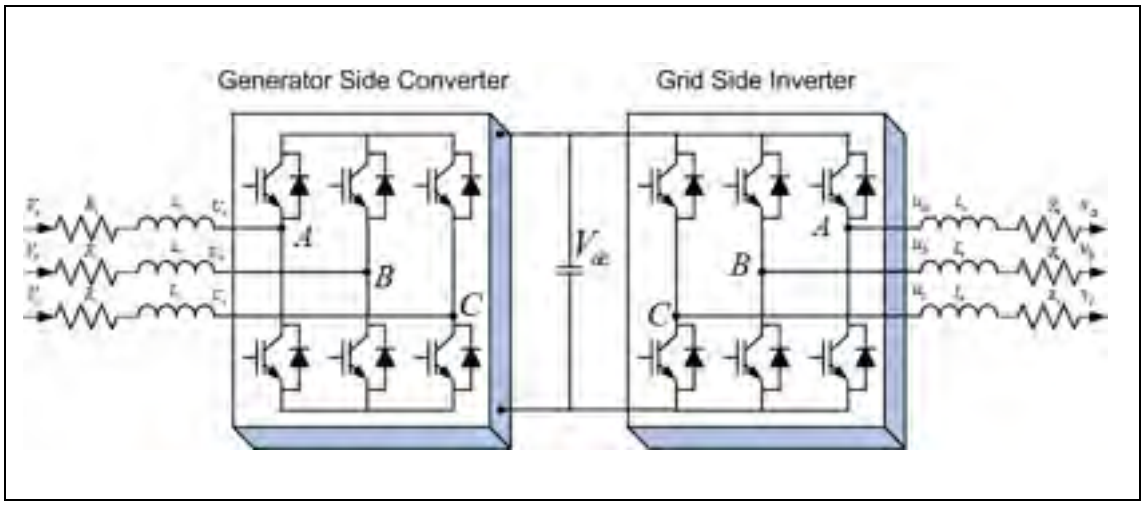

Figure 2.8 Schematic of Back-to-Back Converter.

For the proper operation of back-to-back converter, the DC-link voltage must be boosted to a level at least twice the peak value of grid voltage (Chaudhari et Suryawanshi, 2008).

$$V_{dc} = 2\sqrt{2}V_g \tag{2.62}$$

The power flow of the grid side converter is controlled in order to keep the DC-link voltage constant, while the control of the generator side is set to suit the magnetization demand and the reference speed. The control of the back-to-back PWM-VSI in the wind turbine application is described in several papers (Bueno *et al.*, 2008; Keyuan *et al.*, 2008; Portillo *et al.*, 2006; Shuhui et Haskew, 2007; Weihao *et al.*, 2009b).

2.3.1 Modeling of BBC in Stationary Frame

The BBC consists of two IGBT based 3-phase bridge voltage-source converters (Generator side rectifier and Grid side inverter). The only difference between rectifier and inverter is the definition of power sign. For the analysis of BBC circuit in real time, an average switch model is used. The average model makes it possible to analyse the circuit in continuous time, by replacing all instantaneous values with their averaged counterparts. The switching frequency of the converter is assumed to be sufficiently high to make an average analysis valid, which means that the switching ripple should be negligible compared to the averaged values (Alepuz *et al.*, 2006). The average model and equivalent model of back-to-back converter are shown in Fig. 2.9 and Fig. 2.10, respectively.

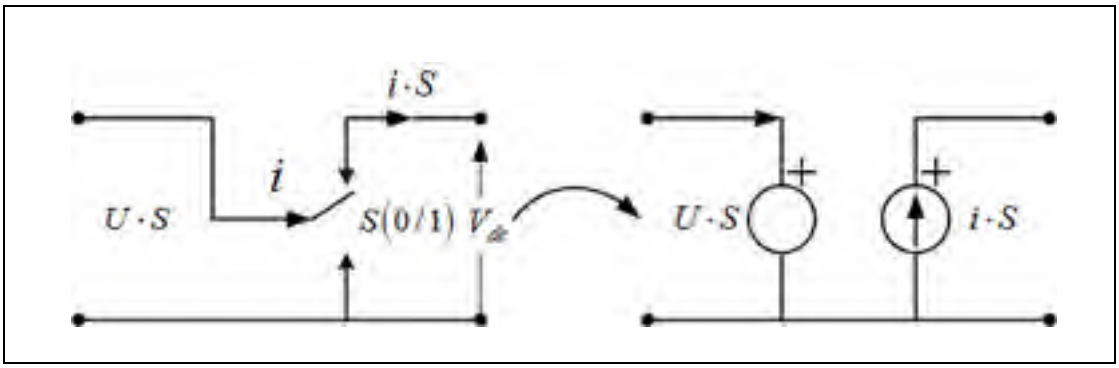

Figure 2.9 Average Model of Back-to-Back Converter.

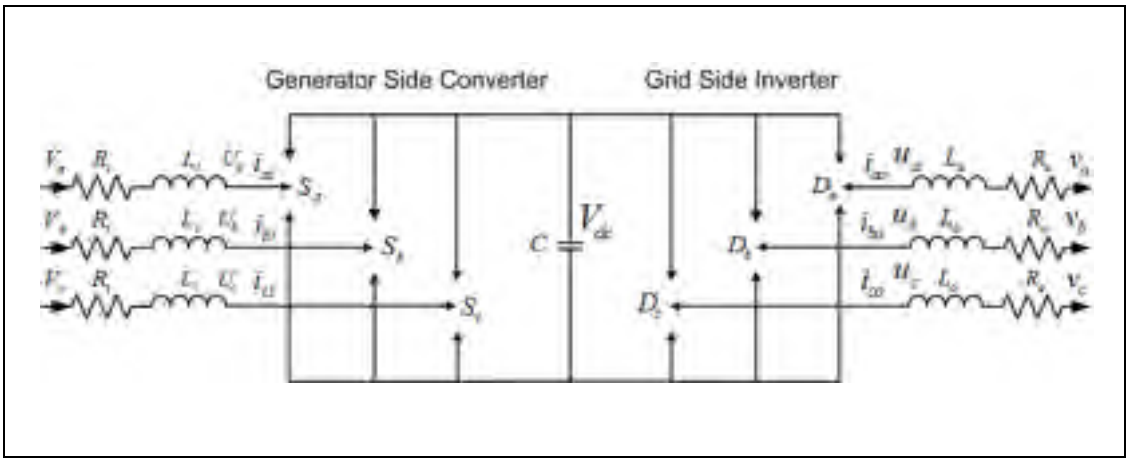

Figure 2.10 Eqivalent Model of Back-to-Back Converter.

The system equation for generator side converter can be written as:

$$\begin{cases} V_a = R_i \cdot i_{ai} + L_i \cdot \dfrac{di_{ai}}{dt} + U_a = R_i \cdot i_{ai} + L_i \cdot \dfrac{di_{ai}}{dt} + V_{dc} \cdot \dfrac{2S_a - S_b - S_c}{3} \\ V_b = R_i \cdot i_{bi} + L_i \cdot \dfrac{di_{bi}}{dt} + U_b = R_i \cdot i_{bi} + L_i \cdot \dfrac{di_{bi}}{dt} + V_{dc} \cdot \dfrac{-S_a + 2S_b - S_c}{3} \\ V_c = R_i \cdot i_{ci} + L_i \cdot \dfrac{di_{ci}}{dt} + U_c = R_i \cdot i_{ci} + L_i \cdot \dfrac{di_{ci}}{dt} + V_{dc} \cdot \dfrac{-S_a - S_b + 2S_c}{3} \end{cases} \tag{2.63}$$

Similarly the voltage equation for grid side inverter can be written as:

$$\begin{cases} v_a = -R_o \cdot i_{ao} - L_o \cdot \dfrac{di_{ao}}{dt} + u_a = -R_o \cdot i_{ao} - L_o \cdot \dfrac{di_{ao}}{dt} + V_{dc} \cdot \dfrac{2D_a - D_b - D_c}{3} \\ v_b = -R_o \cdot i_{bo} - L_o \cdot \dfrac{di_{bo}}{dt} + u_b = -R_o \cdot i_{bo} - L_o \cdot \dfrac{di_{bo}}{dt} + V_{dc} \cdot \dfrac{-D_a + 2D_b - D_c}{3} \\ v_c = -R_o \cdot i_{co} - L_o \cdot \dfrac{di_{co}}{dt} + u_c = -R_o \cdot i_{co} - L_o \cdot \dfrac{di_{co}}{dt} + V_{dc} \cdot \dfrac{-D_a - D_b + 2D_c}{3} \end{cases} \tag{2.64}$$

In the same manner, the system equation for dc-link capacitor can be written as:

$$C \cdot \frac{dV_{dc}}{dt} = S_a \cdot i_{ai} + S_b \cdot i_{bi} + S_c \cdot i_{ci} - (D_a \cdot i_{ao} + D_b \cdot i_{bo} + D_c \cdot i_{co}) \tag{2.65}$$

Where (S_a, S_b, S_c and D_a, D_b, D_c) indicate the switching positions of each phase for generator side converter and grid side inverter respectively; *S*, *D* can be either *0* or 1, with *S, D*=1 indicate that the output is connected to the positive terminal of the dc-link capacitor.

2.3.2 Modeling of BBC in Rotating Frame

The rotating reference frame (*d-q* ref. frame/Park's Transform) is used to model the system due to its well known advantages as mentioned below (Asiminoaei, Blaabjerg et Hansen, 2007):

- **Easy to develop control algorithm:** Since the Park's transformation converts the sinusoidal signals into equivalent dc signals, it becomes very easy to develop PI controllers for dc signals with enhanced steady-state performance.
- **Easy to filter out the noise in dc signals:** That's why the Park's transformation is widely used for active power filtering application.
- **Decouples the active and reactive power:** This is very helpful in controlling the active and reactive power independently.

The system equation (2.58) can be written in matrix form as given below:

$$\begin{bmatrix} V_a \\ V_b \\ V_c \end{bmatrix} = \begin{bmatrix} R_i & 0 & 0 \\ 0 & R_i & 0 \\ 0 & 0 & R_i \end{bmatrix} \begin{bmatrix} i_{ai} \\ i_{bi} \\ i_{ci} \end{bmatrix} + \begin{bmatrix} L_i & 0 & 0 \\ 0 & L_i & 0 \\ 0 & 0 & L_i \end{bmatrix} p \cdot \begin{bmatrix} i_{ai} \\ i_{bi} \\ i_{ci} \end{bmatrix} + \begin{bmatrix} U_a \\ U_b \\ U_c \end{bmatrix} \tag{2.66}$$

On applying Park's transformation in equation (2.66), we get

$$\left[T_{abc\to dq0}\right]^{-1}\begin{bmatrix}V_d\\V_q\\V_0\end{bmatrix}=\begin{bmatrix}R_i & 0 & 0\\0 & R_i & 0\\0 & 0 & R_i\end{bmatrix}\left[T_{abc\to dq0}\right]^{-1}\begin{bmatrix}i_{di}\\i_{qi}\\i_{0i}\end{bmatrix}+\begin{bmatrix}L_i & 0 & 0\\0 & L_i & 0\\0 & 0 & L_i\end{bmatrix}p\cdot\left\{\left[T_{abc\to dq0}\right]^{-1}\begin{bmatrix}i_{di}\\i_{qi}\\i_{0i}\end{bmatrix}\right\}+\left[T_{abc\to dq0}\right]^{-1}\begin{bmatrix}U_d\\U_q\\U_0\end{bmatrix} \tag{2.67}$$

$$\begin{bmatrix}V_d\\V_q\\V_0\end{bmatrix}=\begin{bmatrix}R_i & 0 & 0\\0 & R_i & 0\\0 & 0 & R_i\end{bmatrix}\begin{bmatrix}i_{di}\\i_{qi}\\i_{0i}\end{bmatrix}+\begin{bmatrix}L_i & 0 & 0\\0 & L_i & 0\\0 & 0 & L_i\end{bmatrix}\left\{\left[T_{abc\to dq0}\right]p.\left[T_{abc\to dq0}\right]^{-1}\begin{bmatrix}i_{di}\\i_{qi}\\i_{0i}\end{bmatrix}+\left[T_{abc\to dq0}\right]\left[T_{abc\to dq0}\right]^{-1}p\cdot\begin{bmatrix}i_{di}\\i_{qi}\\i_{0i}\end{bmatrix}\right\}+\begin{bmatrix}U_d\\U_q\\U_0\end{bmatrix} \tag{2.68}$$

On applying the terms $[T_{abc\to dq}]p.[\ T_{abc\to dq}]^{-1}$ from equation (2.48) in to equation (2.68), we have:

$$\begin{bmatrix}V_d\\V_q\\V_0\end{bmatrix}=\begin{bmatrix}R_i & 0 & 0\\0 & R_i & 0\\0 & 0 & R_i\end{bmatrix}\begin{bmatrix}i_{di}\\i_{qi}\\i_{0i}\end{bmatrix}+\begin{bmatrix}L_i & 0 & 0\\0 & L_i & 0\\0 & 0 & L_i\end{bmatrix}\cdot\left\{\begin{bmatrix}0 & -\omega_r & 0\\\omega_r & 0 & 0\\0 & 0 & 0\end{bmatrix}\cdot\begin{bmatrix}i_{di}\\i_{qi}\\i_{0i}\end{bmatrix}+p\cdot\begin{bmatrix}i_{di}\\i_{qi}\\i_{0i}\end{bmatrix}\right\}+\begin{bmatrix}U_d\\U_q\\U_0\end{bmatrix} \tag{2.69}$$

On simplifying the equation (2.69) and eliminating the zero sequence components for balanced 3-phase system, we have:

$$\begin{cases}V_d=R_i\cdot i_{di}+L_i\cdot\dfrac{di_{di}}{dt}-\omega_r\cdot L_i\cdot i_{qi}+U_d\\[2ex]V_q=R_i\cdot i_{qi}+L_i\cdot\dfrac{di_{qi}}{dt}+\omega_r\cdot L_i\cdot i_{di}+U_q\end{cases} \tag{2.70}$$

In the same manner the grid side inverter in *d-q* ref. frame can be written as:

$$\begin{cases}u_d=R_o\cdot i_{do}+L_o\cdot\dfrac{di_{do}}{dt}-\omega_o\cdot L_o\cdot i_{qo}+v_d\\[2ex]u_q=R_o\cdot i_{qo}+L_o\cdot\dfrac{di_{qo}}{dt}+\omega_o\cdot L_o\cdot i_{do}+v_q\end{cases} \tag{2.71}$$

On rearranging the equations (2.71), we can have:

$$\begin{cases} v_d = -R_o \cdot i_{do} - L_o \cdot \dfrac{di_{do}}{dt} + \omega_o \cdot L_o \cdot i_{qo} + u_d \\ v_q = -R_o \cdot i_{qo} - L_o \cdot \dfrac{di_{qo}}{dt} - \omega_o \cdot L_o \cdot i_{do} + u_q \end{cases} \tag{2.72}$$

Similarly, the equation for dc-link can be written in terms of *d-q* components as given below:

$$C \cdot \frac{dV_{dc}}{dt} = \frac{U_d}{V_{dc}} \cdot i_{di} + \frac{U_q}{V_{dc}} \cdot i_{qi} - \left(\frac{u_d}{V_{dc}} \cdot i_{do} + \frac{u_d}{V_{dc}} \cdot i_{qo} \right) \tag{2.73}$$

2.3.3 Controller Design in Rotating Frame

Since the proposed BBC configuration consists of current controlled voltage source converters, therefore in this section current controller design for grid side inverter is considered. The same kind of current controller can be easily used for generator side converter also. The equation (2.71) for grid side inverter can be represented as a coupled electrical system as shown in Fig. 2.11.

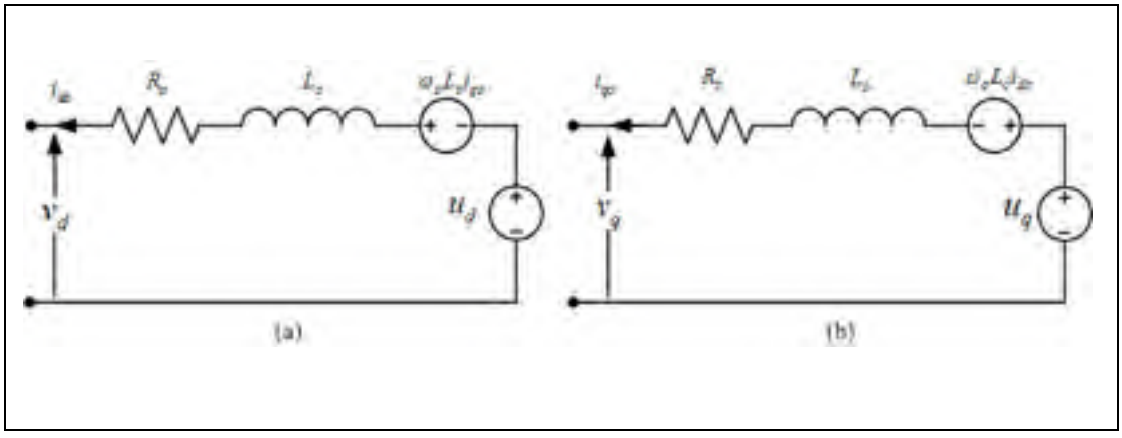

Figure 2.11 d-q Model of Grid side Inverter.

Using Laplace's transformation, we can re-write the equation (2.71) as:

$$\begin{cases} u_d(s) = (R_o + L_o s) \cdot i_{do}(s) - \omega_o \cdot L_o \cdot i_{qo}(s) + v_d(s) \\ u_q(s) = (R_o + L_o s) \cdot i_{qo}(s) + \omega_o \cdot L_o \cdot i_{do}(s) + v_q(s) \end{cases} \tag{2.74}$$

The block diagram of the equation (2.74) is shown in Fig. 2.12.

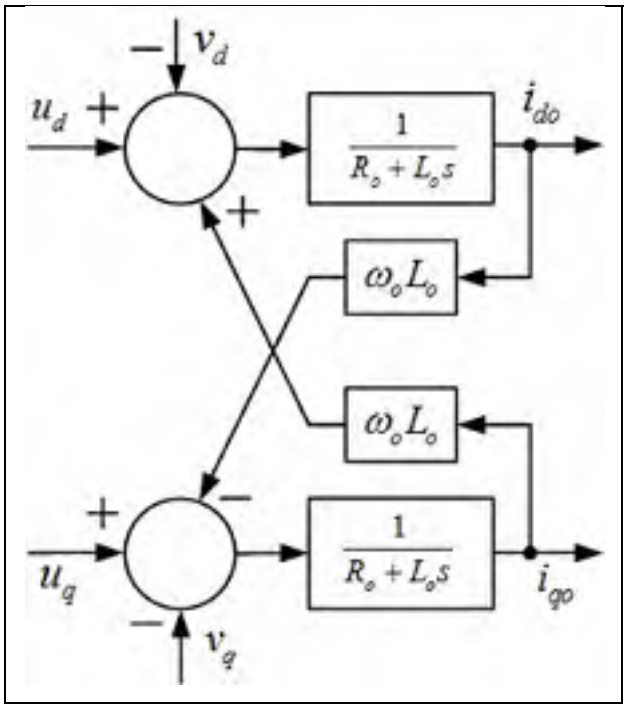

Figure 2.12 Block Diagram of d-q Model of Inverter.

Inverter current is the critical variable to be controlled for Current controlled voltage source inverter (CC-VSI). In actual practice, the outer voltage regulator, power regulator, speed regulator, dc-link voltage regulator, flux regulator etc. sets the reference current for the inner current regulators. That's why the current controllers are designed to meet the basic requirements of higher accuracy and bandwidth.

The inverter's terminal voltage required to generate the desired inverter current can be determined as given below:

$$\begin{cases} u_d = R_o \cdot i_{do} + L_o \cdot \dfrac{di_{do}}{dt} - \omega_o \cdot L_o \cdot i_{qo} + v_d = \Delta v_d + v_d - \omega_o \cdot L_o \cdot i_{qo} \\ u_q = R_o \cdot i_{qo} + L_o \cdot \dfrac{di_{qo}}{dt} + \omega_o \cdot L_o \cdot i_{do} + v_q = \Delta v_q + v_q + \omega_o \cdot L_o \cdot i_{do} \end{cases} \tag{2.75}$$

The voltage drop Δv is due to the presence of filter inductance and resistance, which can be compensated by the optimal design of *PI* controller. Fig. 2.13 shows the inverter's current controller implementation for the inverter given in equation (2.74). Here the character ^ over a constant or variable indicates the estimated or measured quantity, which may have some measurement or estimated error.

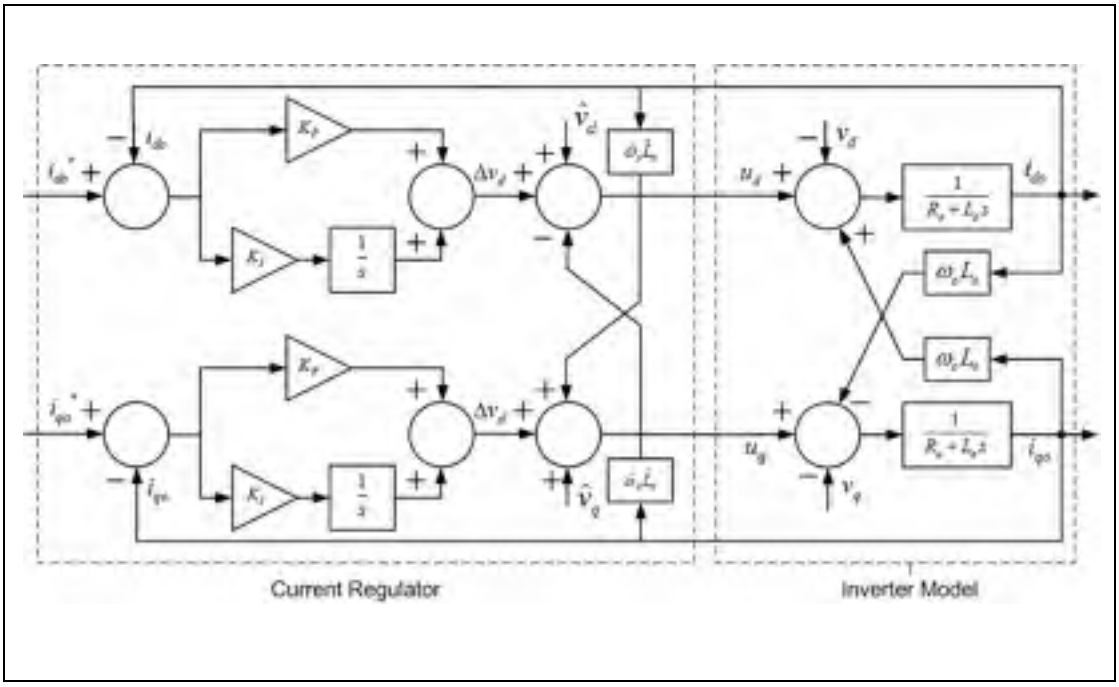

Figure 2.13 Design of Current Regulator in *d-q* Frame.

In order to set the optimal gains for current regulator, the cross-coupling factors may be assumed to cancel out each others effect. This kind of assumptions led to a simple current regulator design as shown in Fig. 2.14.

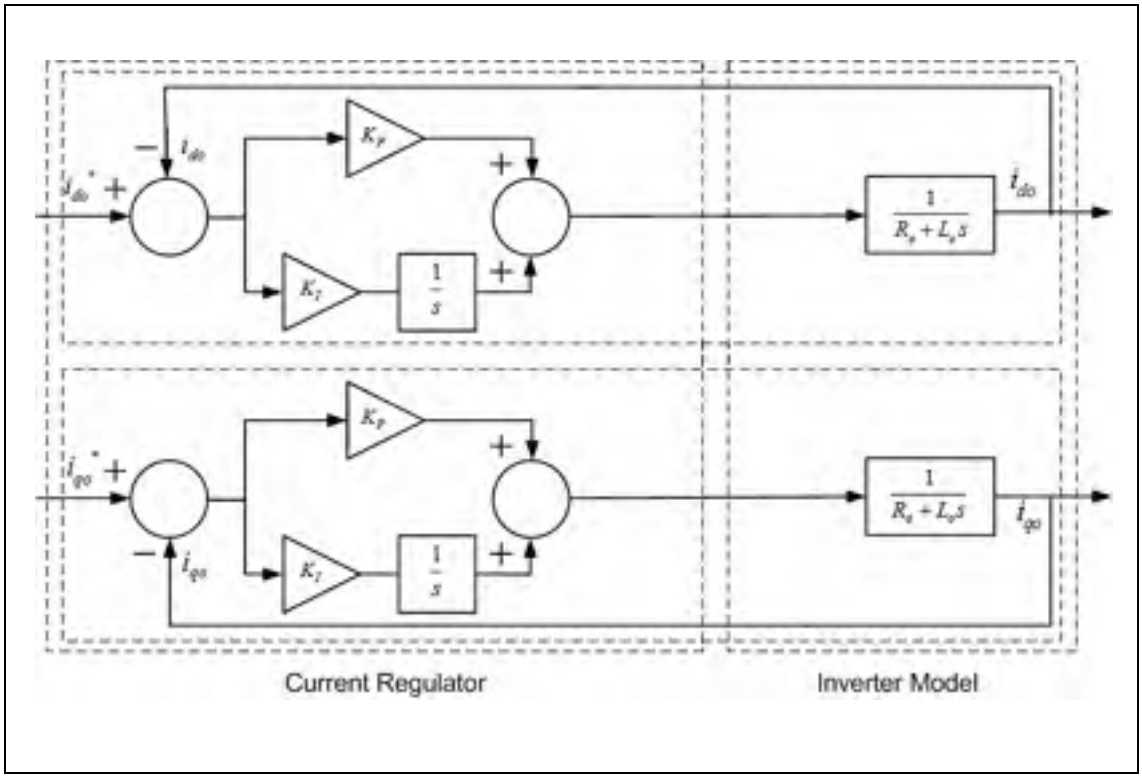

Figure 2.14 Simplified Design of Current Regulator in *d-q* Frame.

This kind of simplified system behaves linearly, and therefore linear control techniques can be used to determine the optimal gains of current controller. Moreover, only an estimation of filter resistance and inductance is required to design the current regulator. The closed loop transfer function of the system shown in Fig. 2.15 can be derived for the given filter parameters as given in equation (2.76).

$$H(s) = \frac{i}{i^*} = \frac{K_P \cdot s + K_I}{L_o \cdot s + (R_o + K_P)s + K_I} \tag{2.76}$$

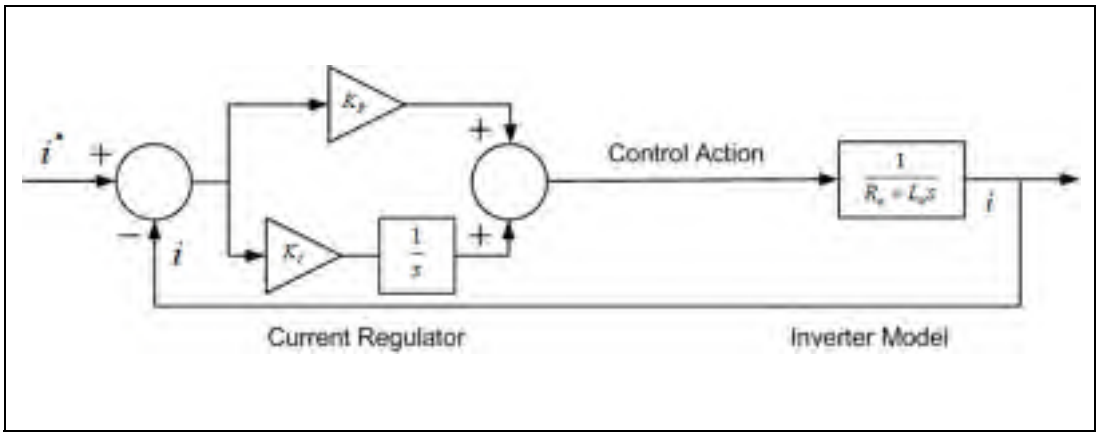

Figure 2.15 Equivalent of Current Regulator Transfer Function.

From the above given transfer function, the controller gains can be easily determined for the desired performance, subject to the condition of accurate information about system parameters.

CHAPTER 3

CONTROL OF PMSG BASED WECS

In this chapter the PMSG based WECS is simulated for both isolated and grid connected systems. In the isolated WECS operation, a wind-battery hybrid system is presented. The battery energy storage system (BESS) in the isolated system is used to absorb the wind power fluctuations and varying load demand. In grid connected system, the fault ride through capability of WECS is demonstrated under grid voltage sag/swell conditions.

3.1 Control of WECS in isolated System

The electricity is one of the main ingredients in the development of modern society and life without electricity is unimaginable in most of the industrialized countries. But many of us are not aware about the fact that more than two billion population all over world still live without electricity. Most of these people live in small pockets in the isolated regions. The integration of these isolated regions to electrical grid is not feasible, neither technically nor economically. The renewable energy sources are proving to be a good solution to all these kind of problems. Among the renewable energy sources, wind energy is one of the fastest growing, cost effective and environmental friendly mean of electricity generation. But the intermittent nature of wind produces lot of power fluctuations. To overcome the problem of power fluctuations, an alternate source of energy with a battery back-up is required and combination is termed as hybrid system. Diesel generator is generally used as alternate source in hybrid system (Cardenas *et al.*, 2004), but in the proposed study only wind-battery mode is considered.

A lot of control strategies for wind-diesel hybrid system based on fixed and variable speed generator had been proposed in(Cardenas *et al.*, 2006; Goel *et al.*, 2009; Iglesias *et al.*, 2000). Most of these WECS are based on doubly-fed induction generator (DFIG),

self-excited induction generator (SEIG) and synchronous generator. In (Hurtado *et al.*, 2002; Sanchez *et al.*, 2003), simulation results of a wind–diesel system based on a variable-speed wind turbine are presented in which continuous operation of the diesel engine regulates the voltage and frequency at the grid, and power balancing is achieved by regulating the energy captured by the WECS using pitch control. However, continuous operation of the diesel is not desirable because of the high fuel consumption, high fuel cost, increased environment pollution and maintenance cost, while power balancing using active pitch control mechanism has relatively slow dynamics. In (Chen et Hu, 2003)a simulation study investigates a wind turbine and the diesel engine, both operating at variable speed for maximum power point tracking (MPPT) and optimal diesel fuel consumption; however, the paper does not consider the control for power balancing, grid voltage, and frequency regulation. Another simulation study (Cardenas *et al.*, 2003) investigates a variable-speed wind turbine connected to an isolated ac grid incorporating power balance between generation and load demand. Scalar control is used in the WECS front-end converter. Similarly in (Cardenas *et al.*, 2006) the vector control based interface of power converters is discussed; the control uses the WECS converter to regulate the ac load voltage and the ESS converter to regulate the power flow to achieve a power balance. In (Tafticht, Agbossou et Cheriti, 2006) a buck-boost converter design is presented to interface battery at dc-link. PMSG based isolated WECS is also presented in (Haque, Muttaqi et Negnevitsky, 2008), where dump load is used to regulate the dc-link voltage. However, use of dump load reduces the system efficiency considerably.

3.1.1 System Description and Control

In the proposed work, a PMSG based variable speed wind energy conversion system (WECS) is used to generate electrical energy (Singh et Chandra, 2009). A diode-bridge rectifier is used as an AC-DC converter and then chopper based generator speed control is implemented in order to achieve maximum power at all available wind speeds. A

battery energy storage system is interfaced on the DC-link with the help of a battery charger. The main purpose of BESS is to absorb wind power fluctuations under varying wind conditions. The BESS stores energy during peak power generation and release the same during least generation in order to maintain power balance between supply and load demand. There can be instances when the dc-link voltage becomes more than its maximum nominal voltage, under these conditions the extra generated power is supplied to dump load in order to keep dc-link voltage constant. Similarly, at some instances the dc-link voltage may fall below minimum nominal voltage due to low power generation, under these conditions the auxiliary energy source, such as diesel generator can be synchronized with the system to meet extra load demand and to charge the battery up to its nominal voltage. In this article only wind-battery hybrid system is considered. However, diesel generator can be connected in the system when the battery state of charge (SOC) level reaches a critical value. The complete block diagram of a typical wind-battery hybrid system is shown in Fig. 3.1.

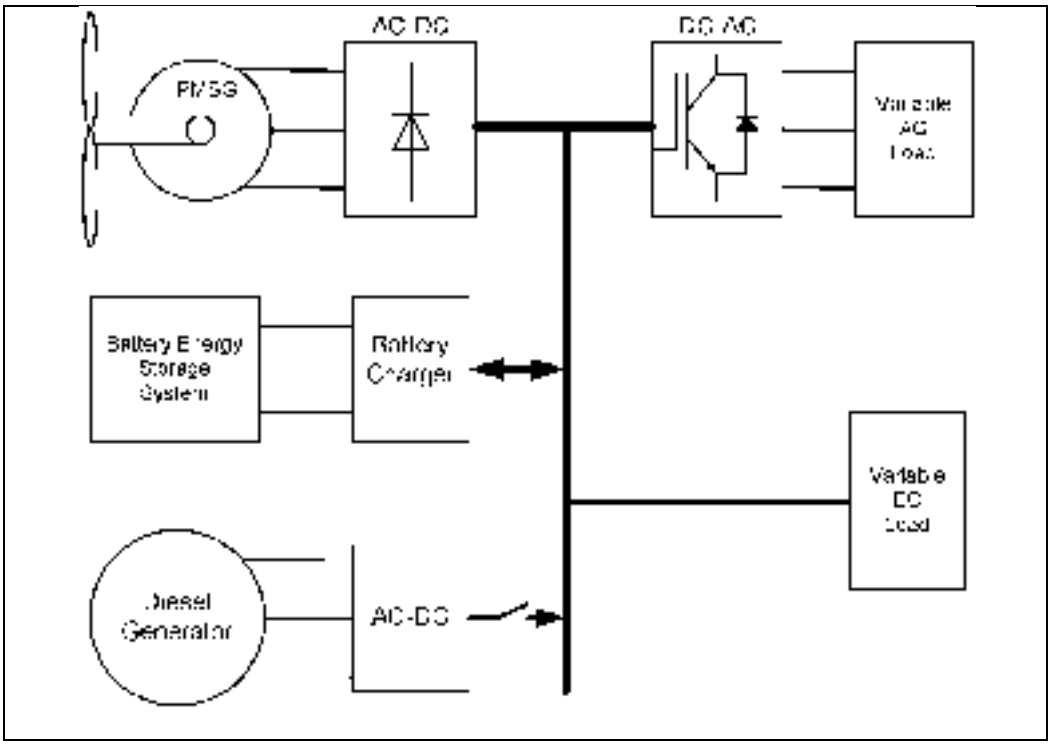

Figure 3.1 Block Diagram of a Typical Hybrid System.

a) Control of PMSG: The main aim of variable speed wind energy conversion system is to extract maximum power at all available wind velocities. In a variable speed WECS; the maximum power at different wind velocities is almost a cubic function of generator speed as shown in Fig. 3.2. Therefore the generator speed is controlled in order to follow the Power-speed characteristic. For this purpose, the power at dc-link is used to obtain reference speed by using power-speed curve of generator. Then the error of this reference speed and actual speed is given to *PI* regulator to obtain reference torque of the generator expressed as:

$$T_e^* = \left(K_{P\omega} + \frac{K_{I\omega}}{S} \right) \left(\omega_r^* - \omega_r \right) \tag{3.1}$$

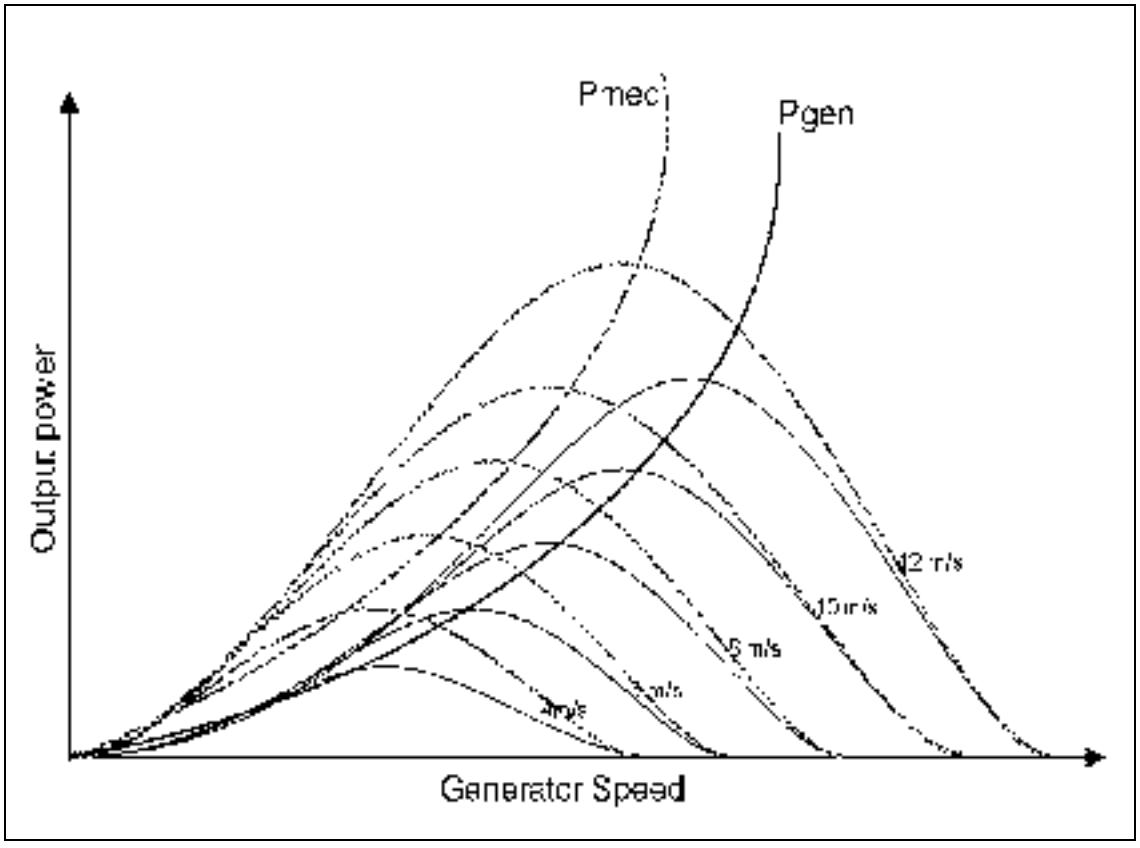

Figure 3.2 PMSG Power-Speed Characteristics at various Wind Velocities.

Where, $K_{P\omega}$ and $K_{I\omega}$ are proportional and integral gains for generator speed control. The q-axis reference current component (torque controlling current component) can be found using (2.57).

$$i_q^* = \frac{4}{3}\left(\frac{T_e^*}{P\lambda_m}\right) \tag{3.2}$$

An inner current loop is used to provide more robustness to control law against any kind of disturbance due to its fast response in comparision to outer loop (Singh et Chandra, 2009). The output of inner controller is applied to PWM comparator, which in turn generates the switching sinal for the IGBT. The proposed control diagram is shown in Fig. 3.3.

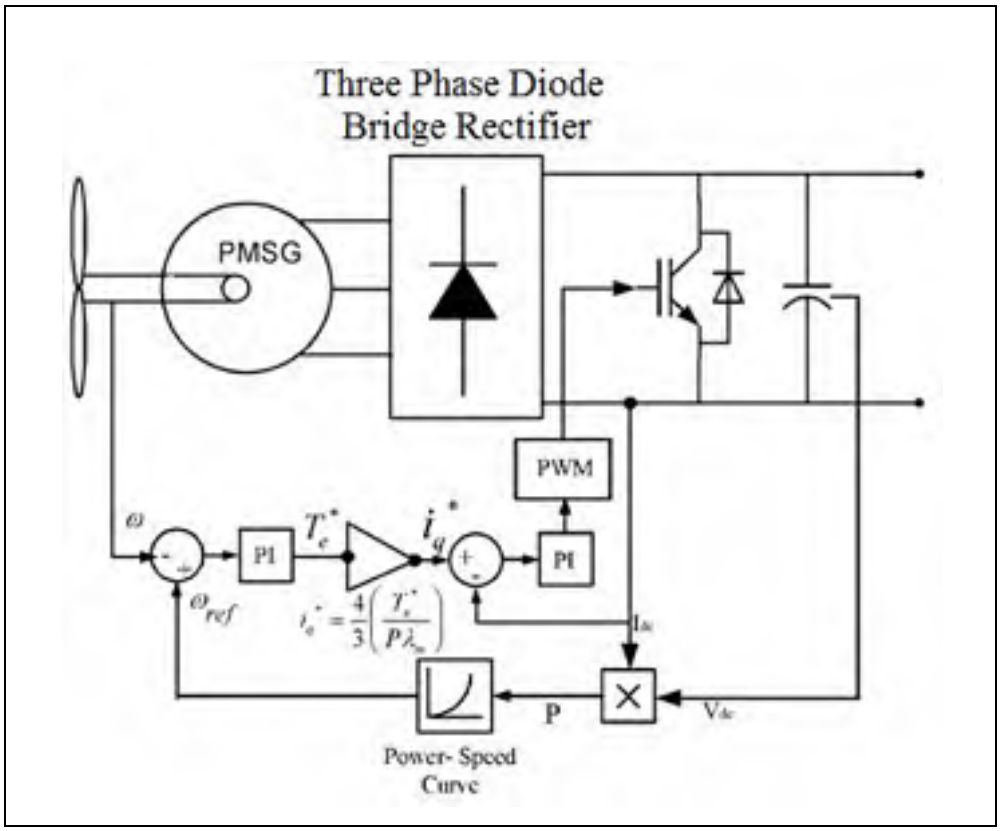

Figure 3.3 PMSG Control for Maximum Power Point Tracking (MPPT).

b) Control of Battery Energy Storage System (BESS): The modeling of battery is a complex task as its parameters varies with the mode of operation (charging and discharging mode). A Thevenin's equivalent model of battery is connected on dc-link as shown in Fig. 3.4., where R_S is the equivalent series/parallel resistance of battery which is usually very small. The parallel circuit of R_b and C_b is used to describe the stored energy and voltage during charging or discharging. R_b in parallel with C_b represents self-discharging of the battery (Singh et Kasal, 2008). Since the self-discharging current of a battery is small, the resistance R_b is large. The energy storing capacity of battery is given in terms of Kilowatthours (kWh) and its capacitance can be determined as:

$$C_b = \frac{kWh \times 3600 \times 10^3}{0.5(V^2_{dcO\max} - V^2_{dcO\min})} \tag{3.3}$$

The interfacing of battery on dc-link is achieved with the help of buck-boost DC/DC converter. The dc-link voltage is regulated by two PI loops. The measured dc-link voltage V_{dcO} is compared with reference dc-link voltage $V_{dcOref.}$ and the difference is applied to the controller. The output of voltage control loop sets the reference battery charging/discharging current i_c, which is further compared with actual battery current i_B. The difference of actual and reference battery currents is applied to inner current control loop and the output control signal is compared with PWM wave, which in turn generates the switching pulses for battery charger. Thus the outer voltage loop regulates the voltage while the inner current loop is used to provide more robustness to control law against any kind of disturbance due to its fast response in comparision to outer voltage loop. When the generated power is more than the load demand, the switch S_6 is turned on and the charging of battery takes place. Similarly, when the generated power is less than the load demand, the power flows back to dc-link and the switch S_5 is switched on to maintain dc-link voltage constant. Thus the charging/discharging of battery maintains the power balance between fluctuating wind power and time varying load. The complete control diagram of buck-boost converter with battery is shown in Fig. 3.4.

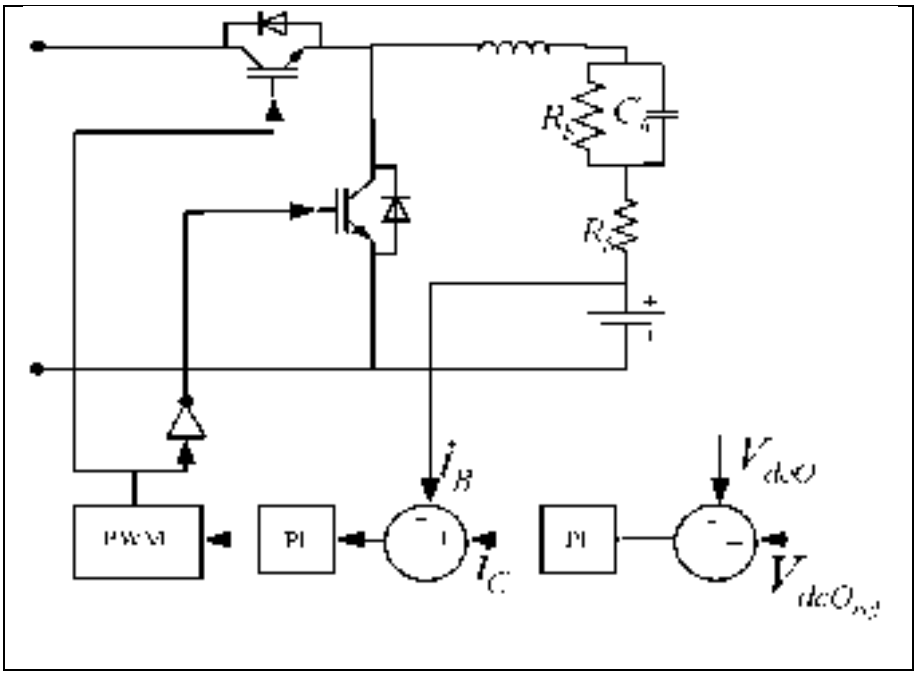

Figure 3.4 Control of Buck-Boost DC/DC Converter.

c) Inverter Control : A single-phase IGBT based full bridge inverter is used to convert 200 V dc in to 110 V ac supply. The nominal ac voltage is maintained under varying load conditions with the help of two control loops. The measured output load voltage V_{ac} is compared with reference load voltage $V_{acref.}$ and the difference is applied to the controller. The output of outer voltage control loop sets the reference current $I_{ref.}$ for inner current loop .

$$I_{ref.} = \left(K_P + \frac{K_I}{S} \right) \left(V_{acref} - V_{ac} \right) \tag{3.4}$$

The I_{ref} obtained from Eq. (3.4) is compared with the actual load current and the error is given to PWM controller to generate control pulses for the IGBT based inverter. The inverter control diagram is shown in Fig. 3.5. A passive LC filter is also used to remove the higher switching frequencies from the output AC-Voltage. The complete off-grid hybrid system is shown in Fig. 3.6.

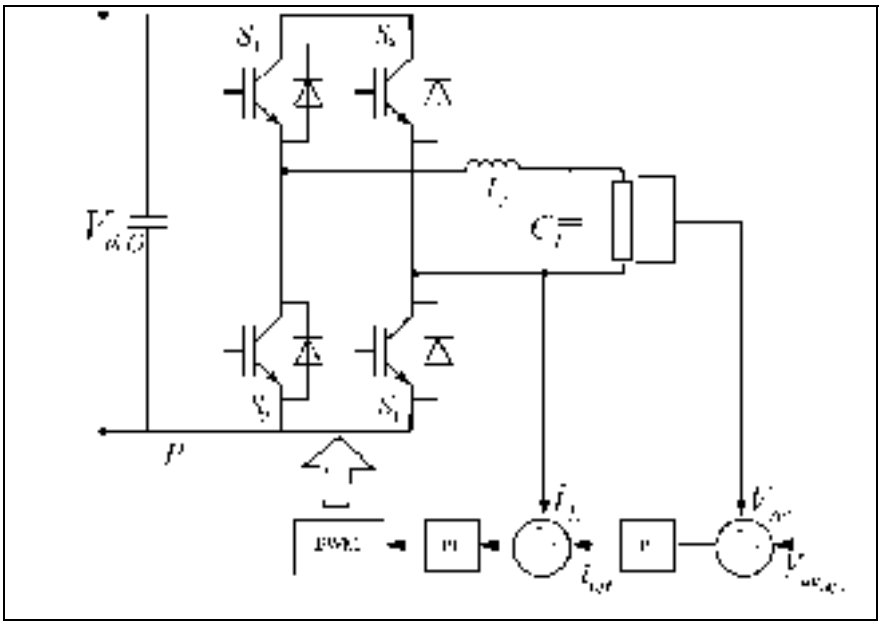

Figure 3.5 Inverter Control Diagram.

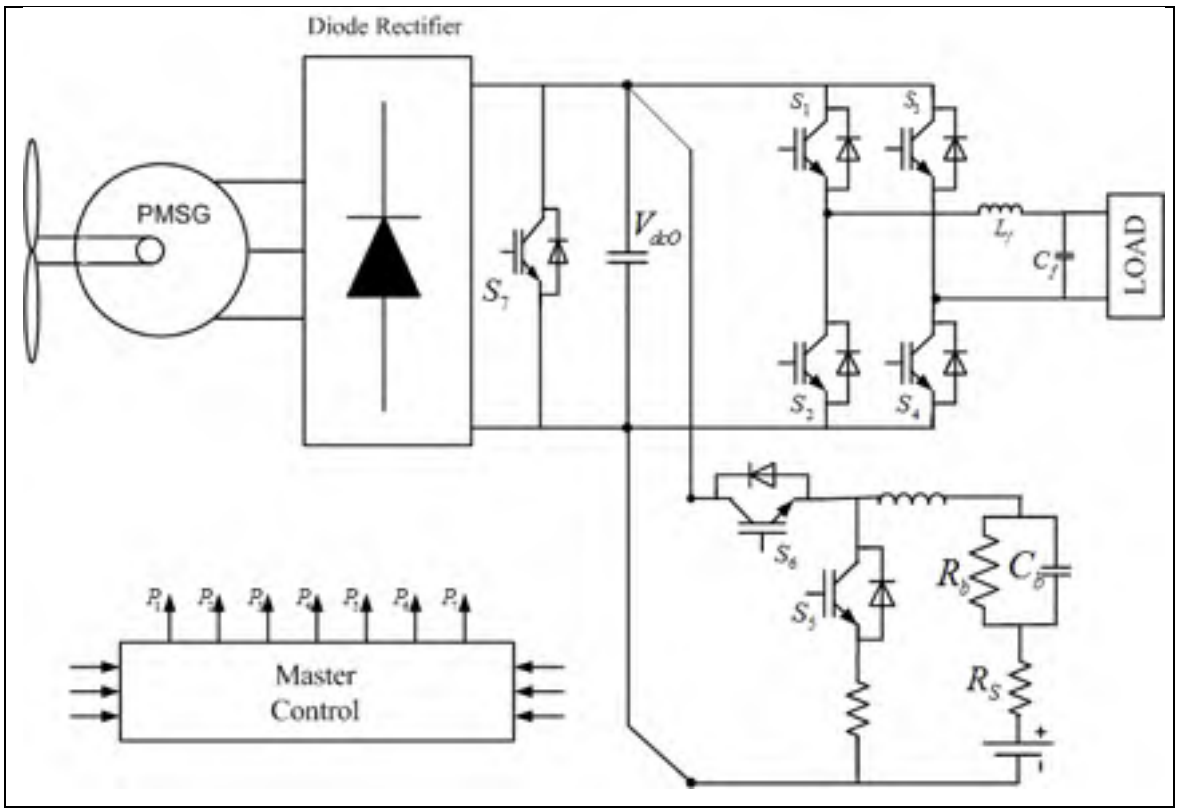

Figure 3.6 Complete Off-Grid Hybrid System.

3.1.2 Simulation Results and Discussion

The proposed control strategy for PMSG based variable speed hybrid wind-battery energy conversion system for off-grid application is simulated in MATLAB/Sim Power System environment under different operating conditions. The simulation results in Fig. 3.7 demonstrate the effectiveness of MPPT control strategy, while in Fig. 3.8 the results under dynamic load conditions are shown. The performance of the controller can be easily evaluated by analyzing the simulation results for both maximum power point tracking and to meet the variable load demand.

a) Performance under Varying Wind Conditions: The main purpose of variable speed wind energy conversion system is to extract maximum power at various wind velocities. In the proposed control strategy the speed of PMSG is actively controlled with the help of a chopper as shown in Fig.3.3. Initially the generator is rotating at a speed of 300 rpm according to the input torque produced by the available wind velocity. At this stage the power produced by the generator is 3500 Watt. But after 1 sec. duration, the generator speed is increased to 400 rpm due to increase in wind velocity. Now the power generated is increased to 10500 Watts. After 1.5 sec. duration, the turbine speed is again decreased to 300 rpm in response to decrease in wind velocity and the system behaves as in the beginning. The simulation results also shows the torque controlling reference current as well as both the actual and the reference speeds just to demonstrate the capability of control strategy, how closely the actual speed follows the reference speed according to torque command.

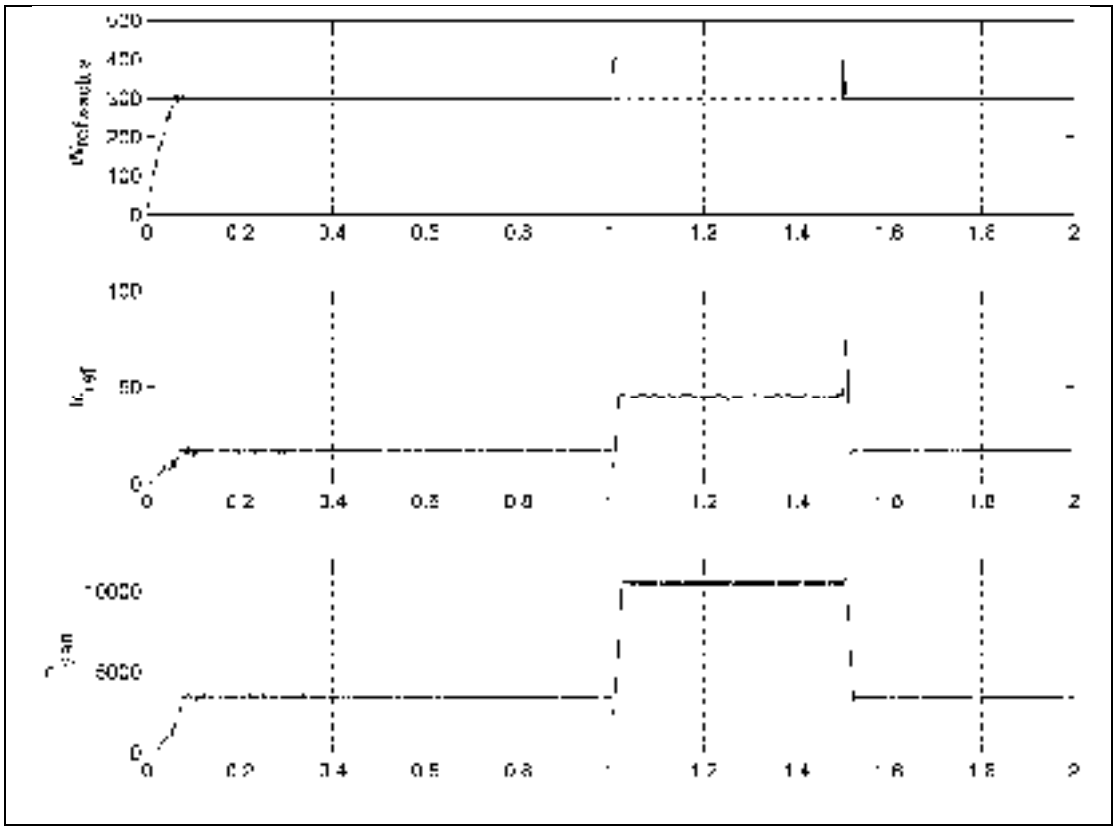

Figure 3.7 Simulation Results for Off-Grid PMSG Under Varying Wind Condition.

b) Performance Under Dynamic Load Conditions: The simulation results for varying load conditions are shown in Fig. 3.8. Initially, the power generated and load power demand are 3500 and 2500 Watts respectively. In order to maintain the power balance, the extra generated power (1000 Watt) is utilized to charge the battery, which is clearly indicated by the negative sign of battery power. At t=1, the generated power is 10500 Watts, but the load demand is still 2500 Watts only and again the excessive power is utilized for charging the battery. At t=1.25, the load demand is increased upto 4800 Watts and generator is still generating 10500 Watts. Now the extra available power to charge the battery is 5700 Watts only. At t=1.5, the generated power is decreased to 3500 Watt, but the load demand is still 4800 Watt. So now the excessive load demand of 1300 Watt is supplied by the battery, that's why now the battery power is of positive sign. At t=1.75, the load demand is decreased to 2500 Watts and now the system

behaves as in the beginning. During all kind of wind and load fluctuations, the dc-link voltage is well maintained nearly to 200 V.

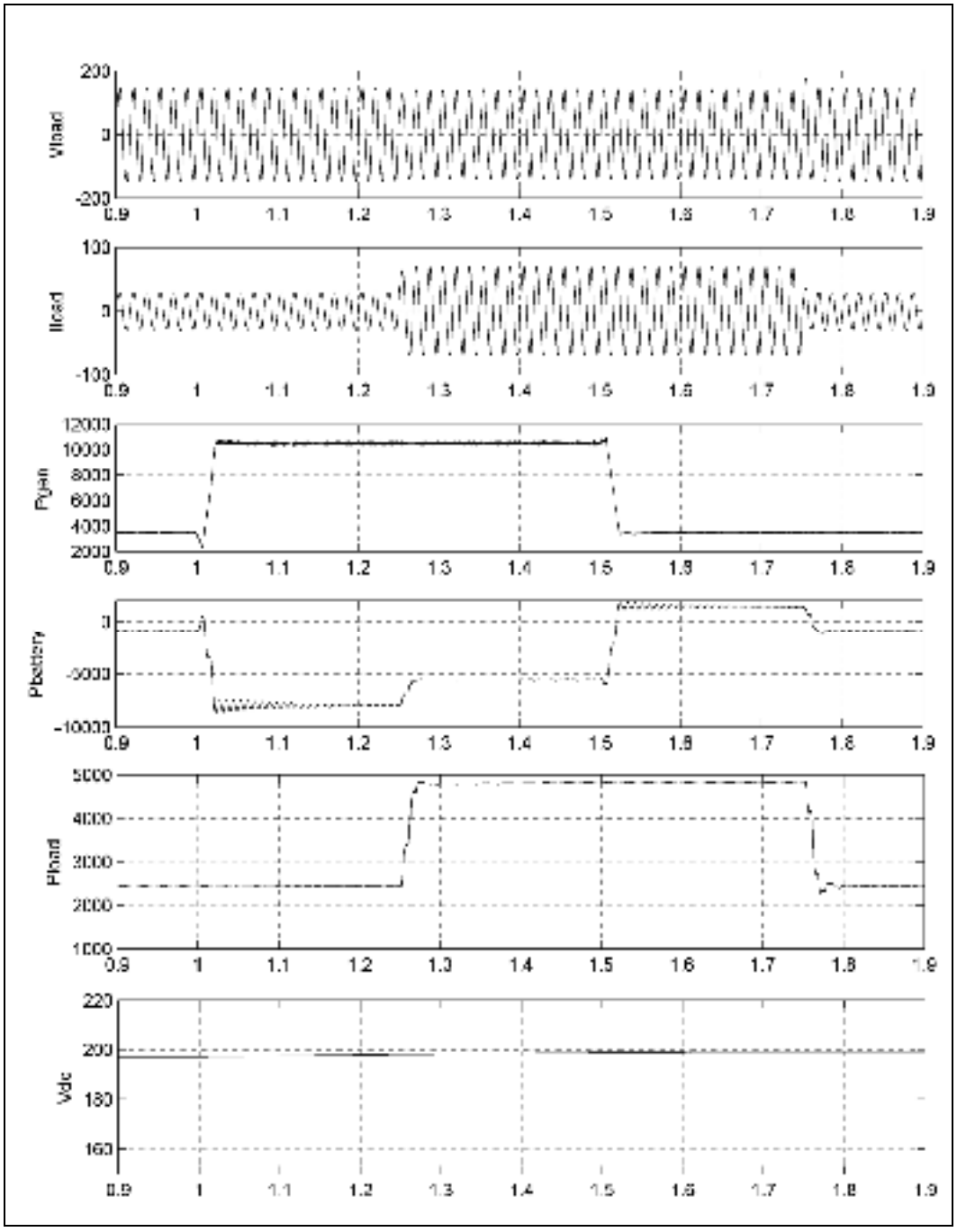

Figure 3.8 Simulation Results for Off-Grid Hybrid System Under Dynamic load Conditions.

3.2 Grid Connected System

The increasing penetration level of wind energy can have a significant impact on grid stability, especially under abnormal conditions. As a result the interconnection of large-scale wind farms to power grids and their relevant influences on the host grids need to be carefully investigated. Wind farms are now required to comply with stringent connection requirements including reactive power support, transient recovery, system stability and voltage/frequency regulation. Further to increase the maximum power extraction the variable speed generators are being employed. These variable speed generators necessitate a AC-DC-AC conversion systems. In this case, the converter handles the total generator power to the grid and therefore no size economies are possible. The latest grid codes require that wind farms must remain in operation during severe grid disturbances, ensure fast restoration of active power to the prefault levels, as soon as the fault is cleared, and in certain cases produce reactive current in order to support grid voltage during disturbances. Depending on their type and control technology, wind turbines can fulfill these requirements to different degrees, as explained in the following sections.

3.2.1 Fault Ride through Capability of PMSG based WECS

While work on the grid interconnection standards began in the late 1990's, it was not until 2003 that Germany's transmission system operators (TSOs) published their standard. This was quickly followed by Denmark in 2004, Spain in early 2005 (Hansen et Michalke, 2009; IEEE Application Guide for IEEE Std 1547, IEEE Standard for Interconnecting Distributed Resources with Electric Power Systems, 2009). According to these standards, now the wind turbines are required to survive during any kind of fault in grid. The ability of a wind turbine to survive of a short duration voltage dip without tripping is often referred to as the low voltage ride through (LVRT) capability of the turbine. LVRT capability is an important part of wind farm grid interconnection because

if the wind farm were to trip off when the voltage dips due to a fault on a nearby power line, the whole system may collapse (Muyeen *et al.*, 2010). The ride-through capability is now a major issue on which most of the researchers and manufacturers are working. Modern wind turbines have lot of commercially available topologies mainly based on induction generator, doubly-fed induction generator (DFIG) and synchronous generator with innovative power electronics interface. The conventional wind turbine usually consists of static VAR compensators (SVCs), static-compensators (STATCOM) or synchronous compensators for voltage stability at the point of common coupling (PCC) (Senjyu *et al.*, 2004a; Sun, Chen et Blaabjerg, 2004). In (Morren et de Haan, 2005), ride-through capability for DFIG has been discussed to limit the rotor current during grid fault. In (Saccomando, Svensson et Sannino, 2002b), dc-link regulator using current feed forward has been discussed by considering different voltage sag conditions. In (Fatu *et al.*, 2007), ride through capability for symmetrical and asymmetrical faults has been demonstrated. Similarly in (Fujin et Zhe, 2009), the fault ride-through capabilities of variable speed PMSG based wind turbine has been discussed. The most of researchers have emphasised on voltage sags and little bit attention has been paid to voltage swell and current harmonics injected in the network.

The proposed work demonstrates the ride through capability for both under Voltage sags and swells (Singh et Chandra, 2008). Besides this, the current harmonics injected in grid has been reduced substantially. The system under consideration employs PMSG based variable speed wind energy conversion system consisting two back to back converters. The generators side converter controls generator speed in order to achieve maximum power point tracking, while grid side inverter regulates dc-link voltage under fluctuating wind and grid disturbances apart from injecting generated power in the grid. The block diagram of proposed system is shown in Fig. 3.9.

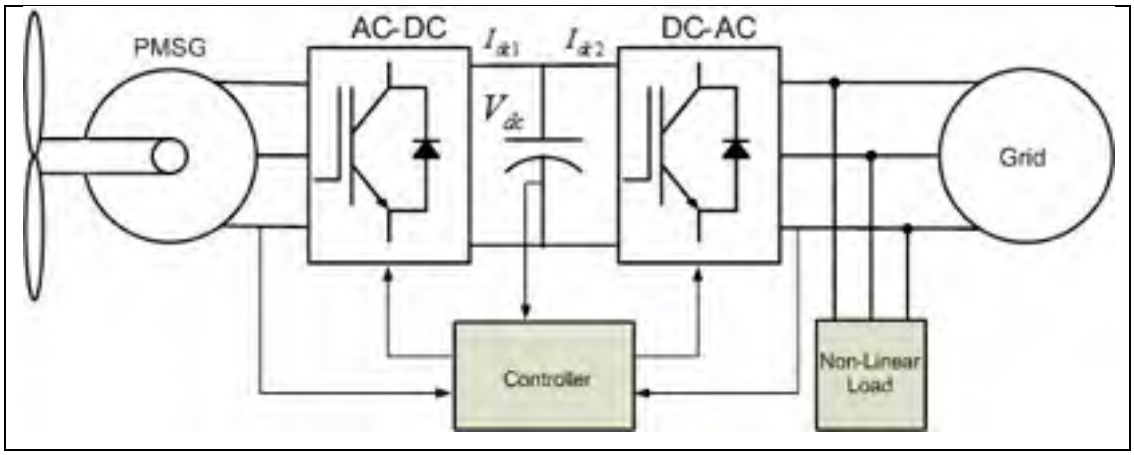

Figure 3.9 Block Diagram of Proposed System.

a) System Description: The power electronic interface plays an important role in the wind energy conversion systems. As the wind turbine operates at variable speed according to available wind velocity, the voltage generated is of variable magnitude and frequency. Therefore the power generated is needed to be processed before feeding it to grid or isolated network. Several types of power electronic interfaces have been investigated for variable speed wind turbines (Senjyu *et al.*, 2004a; Sun, Chen et Blaabjerg, 2004). The proposed system consists of two back to back fully controlled converters decoupled by a dc-link. The converters have been realized by using six IGBT switches for each converter. Since PMSG is connected to grid through AC/DC/AC system, only active power of PMSG can be transferred to grid and exchange of reactive power can not take place due to presence of dc-link. The generator side converter injects current I_{dc1} into dc-link at voltage level V_{dc} and can be expressed as:

$$I_{dc1} = \frac{P_G}{V_{dc}} \tag{3.5}$$

While the current received on the other side of dc-link is:

$$I_{dc2} = \frac{P_{GC}}{V_{dc}} = \frac{P_S + P_L}{V_{dc}} \tag{3.6}$$

Where P_S is active power supplied to load and P_L is converter losses. If converter losses are negligible then P_G=$P_{GC.}$ The dc-link equivalent system is shown in Fig. 3.10.

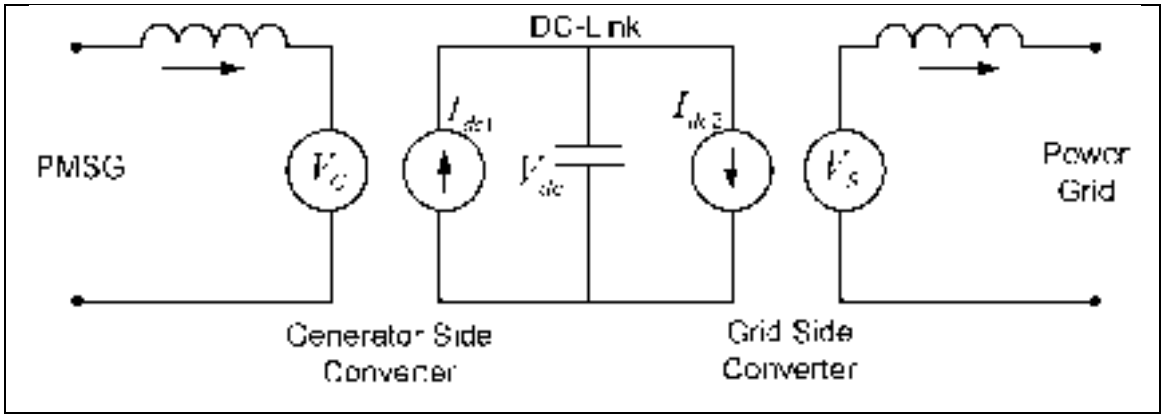

Figure 3.10 Simplified Representation of AC/DC/AC Conversion System.

b) Back –to-Back Converter Control: The main function of generator side converter is to extract maximum power at all available wind velocities. In a variable speed wind energy conversion system, the maximum power at different wind velocity depends on its power co-efficient *Cp*. Unfortunately, for wind turbines *Cp* is not constant. The most common parameters for *Cp* are the tip speed ratio λ and the pitch angle β. Where

$$\lambda = \frac{TipSpeed}{WindSpeed} = \frac{\omega_r r}{V} \tag{3.7}$$

Here the power coefficient C_p=$f(\lambda, \beta)$ is a function of both parameters. Consequently different wind speeds will require the optimal values of tip speed and pitch angle to achieve a high *Cp* and therefore giving the highest power output at all available wind speeds. The mentioned aspects make it very clear - to get maximum power out of the wind we need to have a wind turbine that allows the change in rotor speed to reach optimal aerodynamic conditions. As every optimal $C_{p,optimal}$ has one optimal value of tip speed ratio $\lambda_{optimal}$, therefore it is required to control the tip-speed ratio according to the

wind-speed. This task is well known as Maximum Power Point Tracking (MPPT) and can be achieved by using power co-efficient versus tip-speed ratio for different pitch angles of the turbine as shown in Fig. 3.11. The active pitch control is used during high wind velocity to shed off the aerodynamic power. In active pitch control, the rotor blades are turned away by some angle from the direction of striking wind and this angle is known as pitch angle. The aerodynamic power captured by wind turbine is the cosine function of pitch angle. In the proposed system, the pitch angle is kept zero, which is a valid assumption for lower to medium wind velocities.

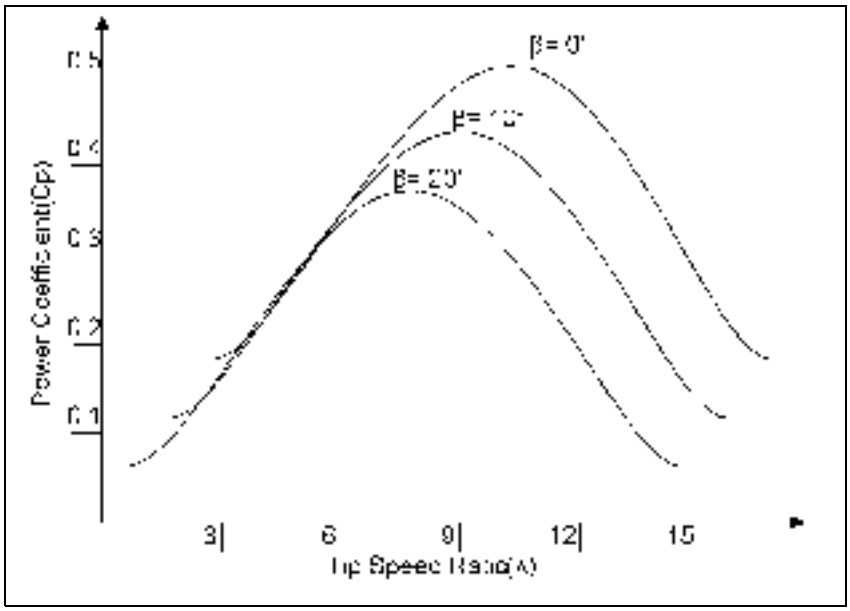

Figure 3.11 C_P-TSR Curve with Active Pitch Angle.

Now the main task is to match the electric loading of the generator according to the maximum power captured by the wind turbine. For this purpose the power-speed characacteristic as shown in Fig. 3.2. is used, where the torque controlling q-axis current is derived from the outer speed control loop, in the same way as discussed in previous section. The d-axis reference current component can be set to zero in order to obtain maximum torque at minimum current and therefore to minimize the resistive losses in

generator (Singh et Chandra, 2008). The proposed controller is realized using hysteresis current controller as shown in Fig.3.12.

The grid side inverter is used to regulate dc-link voltage under both fluctuating wind and grid disturbances. The control of this grid-side inverter comprises of two loops as shown in Fig.3.12. The outer dc voltage control loop is used to set the current reference for active power control. The output of *PI* controller in dc control loop is multiplied to in-phase unity vector templates of grid voltages to obtain the three phase reference currents for inner loop and to achieve unity power factor operation. The difference of three phase reference currents and actual currents is applied to hysteresis current controller to obtain control signals.

The in-phase unit vector templates U_a, U_b and U_c from three phase sinusoidal voltages V_a, V_b and V_c are computed as follows:

$$V_t = \sqrt{\frac{2}{3}\left(V_a^{\,2} + V_b^{\,2} + V_c^{\,2}\right)} \tag{3.8}$$

Then $U_a = \frac{V_a}{V_t}$; $U_b = \frac{V_b}{V_t}$; and $U_c = \frac{V_c}{V_t}$.

The output of *PI* controller for maintaining dc-link voltage constant under fluctuating conditions is expressed as:

$$I_{md}^{\,*} = \left(K_{PV_{dc}} + \frac{K_{IV_{dc}}}{S}\right)\left(V_{dc}^{\,*} - V_{dc}\right) \tag{3.9}$$

Where, K_{PVdc} and K_{IVdc} are proportional and integral gains of dc-voltage regulator. The reference three phase currents are computed as:

$$I_a^{\,*} = I_{md}^{\,*}.U_a \tag{3.10}$$

$$I_b^* = I_{md}^* . U_b \tag{3.11}$$

$$I_c^* = I_{md}^* . U_c \tag{3.12}$$

The reference three phase currents (I_a^*, I_b^* and I_c^*) are compared with sensed three phase line currents (I_a, I_b and I_c) and error signals are applied to hysteresis current controller in order to generate switching pulses for IGBTs. The complete schematic diagram of proposed controller is shown in Fig. 3.12.

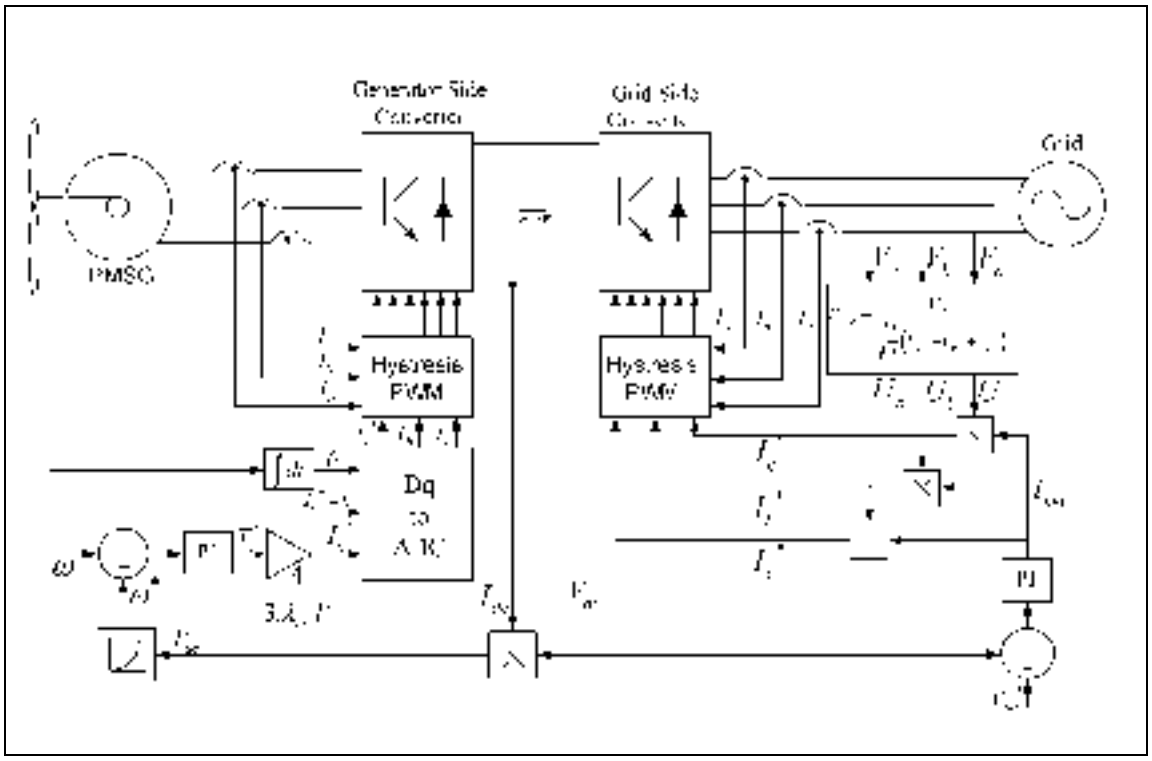

Figure 3.12 Complete Control Strategy for Variable Speed Wind Turbine.

3.2.2 Simulation Results and Discussion

The proposed control strategy for PMSG based variable speed wind energy conversion system is simulated using MATLAB/Sim Power System under different operating conditions. The simulation results in Fig. 3.13 demonstrate the effectiveness of MPPT

control strategy, while in Fig. 3.14 the results under voltage sags/swell conditions are shown. The performance of the controller is evaluated by analyzing the simulation results for various quantities. The quantities under consideration are generator terminal current (I_{gen}), generator speed, dc-link voltage (V_{dc}), inverter current (I_{inv}), grid current (I_{grid}), load current (I_{load}). Besides this, the power flow in between inverter, grid and load is also analyzed under fluctuating wind, voltage sag and voltage swell conditions.

a) Performance under variable wind Conditions: The main purpose of variable speed wind turbine is to extract maximum power at all available wind speeds and this technique is known as maximum power point tracking (MPPT). The simulation results for variable speed operation of wind turbine are shown in Fig. 3.13. In the proposed system, a 2Kw load is connected in between grid side converter and three phase AC source. Initially the generator is rotating at 120rpm and the generated power is 500W only. Therefore, to meet the required load demand the rest of power is supplied from source. At t=1s, the speed is increased to 170 rpm due to increased wind velocity. At this instant, the output power (Pinv) and injected current (Iinv) increase so that the power (Pgrid) and current (Igrid) supplied by the source is reduced in order to meet constant load demand (Pload) and load current (Iload). During t=1-1.25, the generated output power is 1350 W and the remaining 650 W is supplied by the source to meet 2Kw load demand. At t=1.25, again the generator speed is reduced to 120 rpm, so the generator output reduced to 500W and consequently the power supplied from source increases to 1500W in order to supply load demand. A well regulated dc-link voltage and smooth power flow is maintained under all these varying conditions. In the simulation results, actual and reference generator speeds are shown to validate the effectiveness of speed control strategy. The variable frequency of generator current under different speed region indicates the variable speed operation of wind turbine. On the other side, the current controlled voltage source inverter injects a harmonic free, pure sinusoidal current in grid.

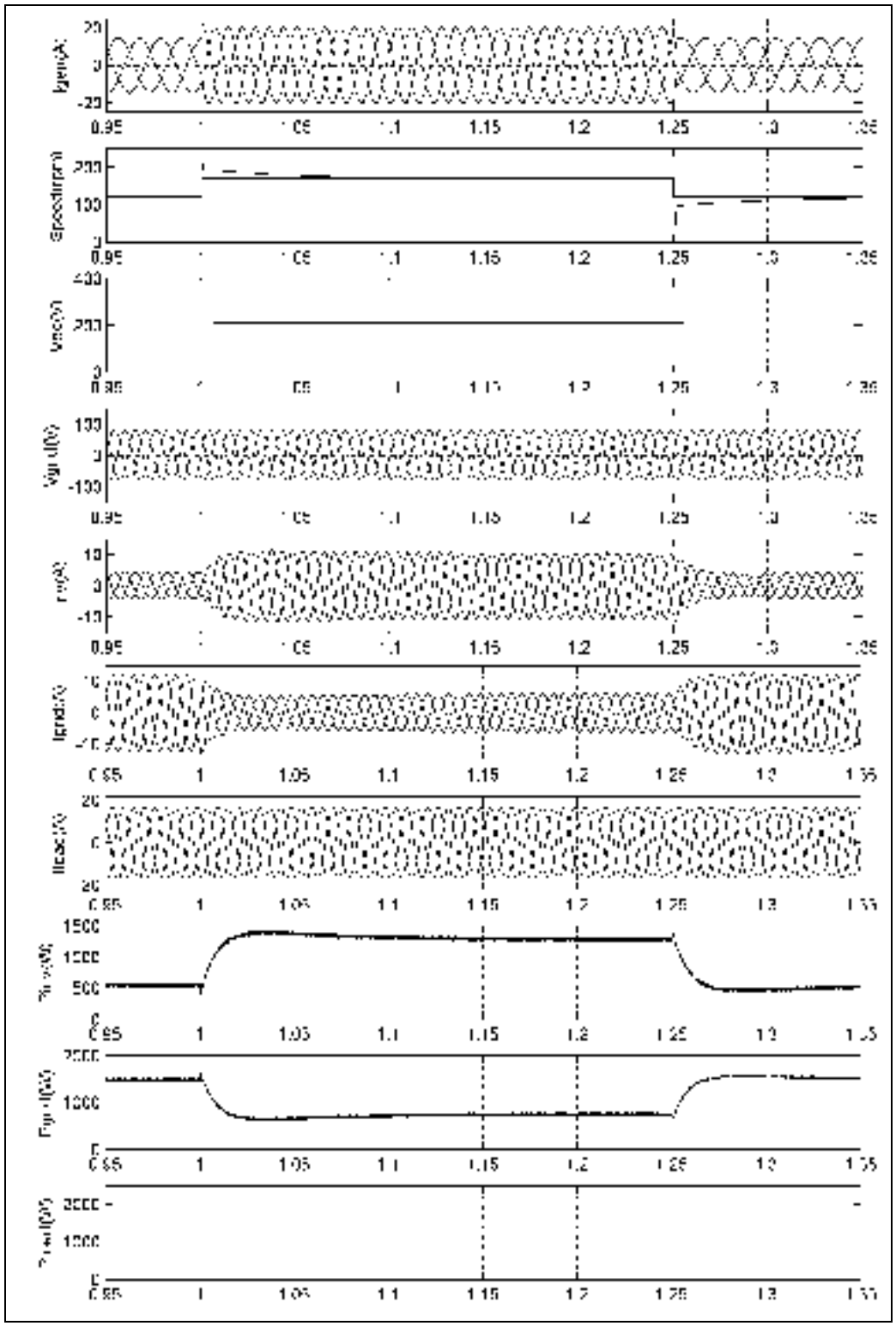

Figure 3.13 Performance under variable speed operation.

b) Performance under Voltage Sag and Swell Conditions: Fig. 3.14. Shows the simulation results under voltage sag and swell conditions. The generator speed is kept intentionally constant at 120 rpm just to see the impact of grid side disturbances on the performance of wind turbine. In the beginning, the grid side voltage is at nominal value, so both wind turbine and source are supplying 500 W and 1500 W respectively to meet 2Kw load demand. At 2s, voltage sag of 50% is introduced in the system and accordingly the load demand has decreased to 500W. The voltage sag lasts for 0.25s and during this period the load demand is totally met by wind turbine, as the power and current supplied from source side is almost zero. It is also seen that the current injected from inverter is increased in proportion to the voltage sag, just to pump the generated active power irrespective of any change in voltage. At 2.25s, the voltage sag is cleared and the system behaves as in the beginning. At 2.5s, a voltage swell of 50% of the nominal voltage is introduced in the system for duration of 0.25s. During this period the load demand is increased to 4500W. Again the power supplied from inverter is 500W only and rest of power is supplied from source. The current supplied from inverter is reduced in proportion to increase in voltage as it has to supply the generated power which is kept constant at 500W. The increase in system voltage results in to increase in supply current to meet the increased load demand. Here it should be noted that a load of constant resistance is used and that's why the power and current drawn by load changes in proportion to the any change in system voltage. At 2.75s, the voltage swell is cleared and the system behaves as in the beginning.

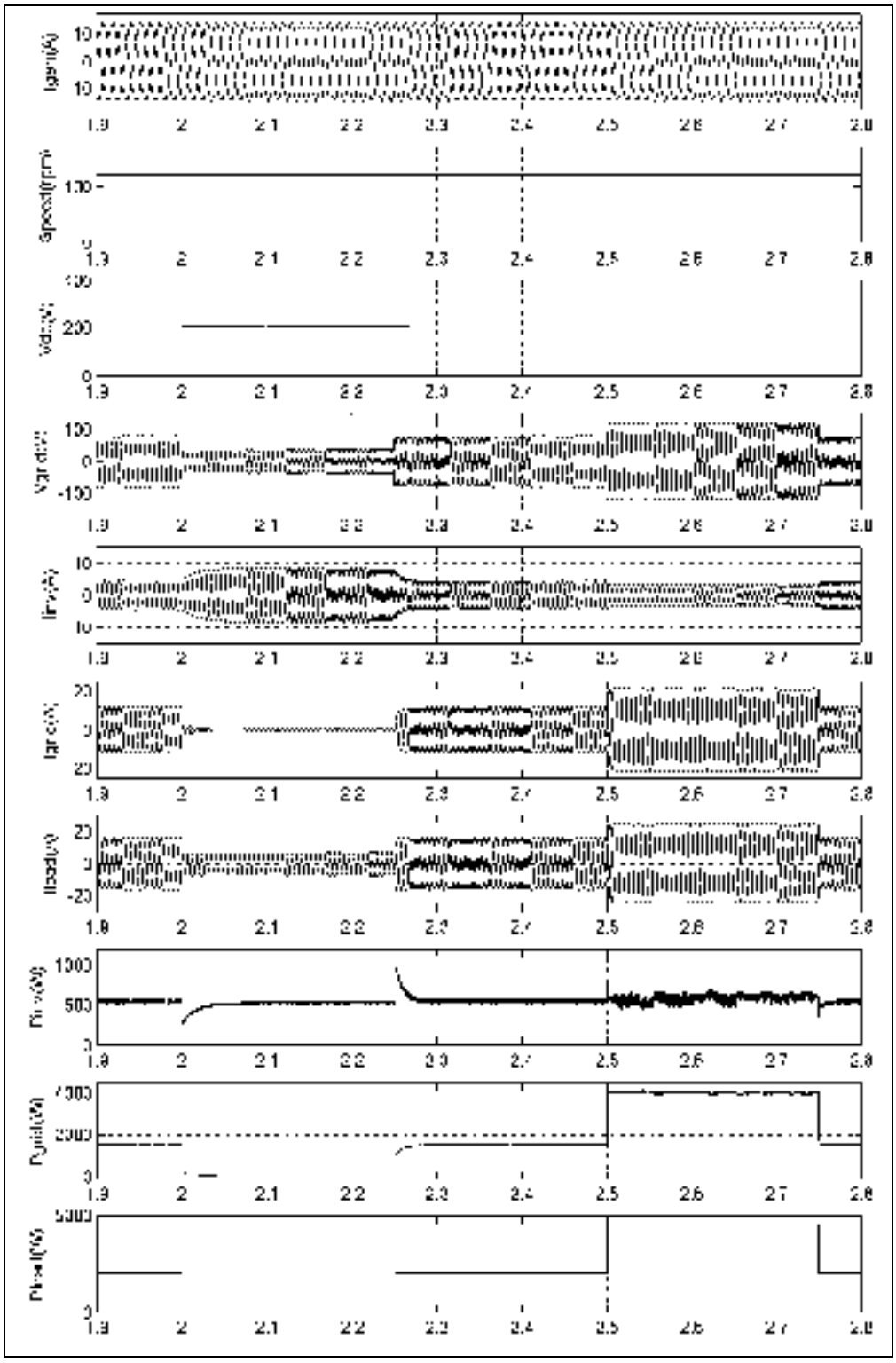

Figure 3.14 Performance under Voltage Sag and Swell conditions.

3.2.3 Voltage Sag/Swell and Unbalance Compensation at PCC

PMSG based Variable speed wind turbines with full power converters present the distinct advantage that the converter totally decouples the generator from the grid. Hence, the grid disturbances have no direct effect on the generator, whose current and torque variations during voltage dips are much lower compared to the DFIG and the respective transients fade out at much faster rate. Moreover, from the reactive output power point of view, the grid side converter can be controlled to produce reactive current during the voltage fluctuations, up to its rated current.

In the proposed work, a new grid side inverter control strategy is introduced, while the generator side control remains same as in the previous section. The main purpose of grid side inverter control is to inject the generated power and also to maintain constant voltage at PCC, despite of lot of fluctuation in grid voltage. The inverter reference current carries the reactive current component in proportion to the voltage fluctuation and active current component in proportion to the generated power. The PCC, at which the voltage is to be maintained, is isolated from grid by transformer or with suitable inductor.

a) Control Description of Grid side Inverter: The different kind of grid faults may results in to voltage sag/swell and unbalance in power distribution network. The voltage unbalance in 3-phase system can be completely described in the steady state operation through symmetrical components, named as positive sequence (v_1), negative sequence (v_2) and zero sequence components (v_0).

$$\begin{bmatrix} v_1 \\ v_2 \\ v_0 \end{bmatrix} = \frac{1}{3}\begin{bmatrix} 1 & a & a^2 \\ 1 & a^2 & a \\ 1 & 1 & 1 \end{bmatrix}\begin{bmatrix} v_a \\ v_b \\ v_c \end{bmatrix} \tag{3.13}$$

Where

$$a = \frac{1}{2} + j\frac{\sqrt{3}}{2} \tag{3.14}$$

To maintain constant balanced voltage at PCC or at the terminals of any dedicated load, it is necessary to control the positive sequence component according to the desired reference voltage. The three phase unbalance/distorted voltages are first decomposed in to their positive, negative and zero sequence components by using equation (3.13).Then, the positive sequence components are applied to *PLL* (Fig. 1.9.) in order to extract the grid synchronization angle (θ). The grid synchronization angle is utilized to generate the in-phase unity components (U_a, U_b and U_c) and quadrature unity components (W_a, W_b and W_c) as given below.

$$\left.\begin{aligned} U_a &= \sin(\omega t) \\ U_b &= \sin(\omega t - 120^o) \\ U_c &= \sin(\omega t + 120^o) \end{aligned}\right\} \tag{3.15}$$

$$\left.\begin{aligned} W_a &= \cos(\omega t) \\ W_b &= \cos(\omega t - 120^o) \\ W_c &= \cos(\omega t + 120^o) \end{aligned}\right\} \tag{3.16}$$

The multiplication of in-phase unity components with the output of outer dc-link voltage (i^*_{md}) results in to the active component of reference inverter current.

$$\left.\begin{aligned} i_{ad}^{\ *} &= i_{md}^{\ *}.U_a \\ i_{bd}^{\ *} &= i_{md}^{\ *}.U_b \\ i_{cd}^{\ *} &= i_{md}^{\ *}.U_c \end{aligned}\right\} \tag{3.17}$$

Similarly, the multiplication of quadrature unity components with the output of outer PCC voltage control loops (i^*_{maq}, i^*_{mbq}, and i^*_{mcq}) results in to the reactive component of reference inverter current.

$$\left.\begin{aligned} i_{aq}^{\ *} &= i_{maq}^{\ *}.W_a \\ i_{bq}^{\ *} &= i_{mbq}^{\ *}.W_b \\ i_{cq}^{\ *} &= i_{mcq}^{\ *}.W_c \end{aligned}\right\} \tag{3.18}$$

The algebraic sum of equation (3.17) and (3.18) gives the reference inverter current, which is further utilized to control inverter in *d-q* reference frame as shown in Fig. 3.15.

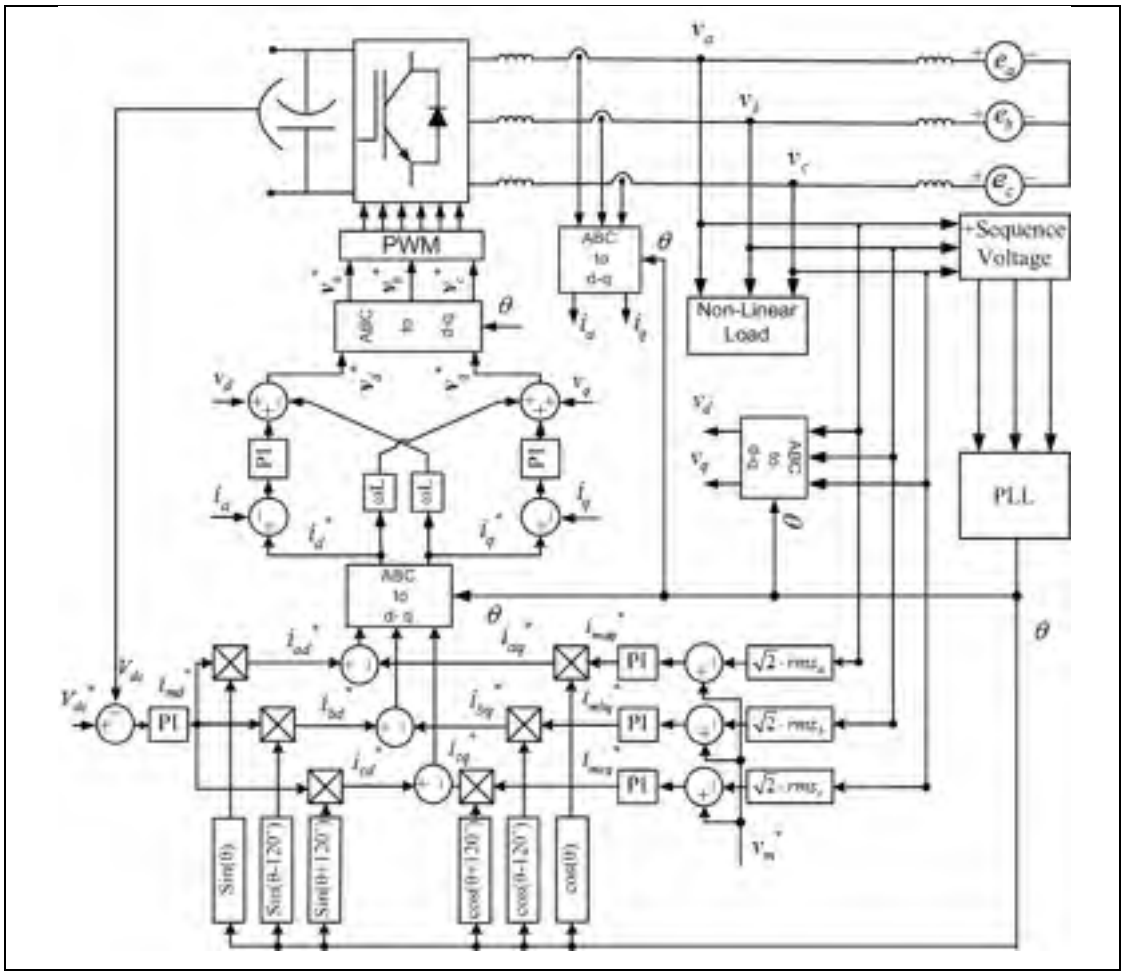

Figure 3.15 Grid side Inverter Control.

3.2.4 Simulation Results and Discussion

To verify the proposed approach under both variable speed and voltage fluctuation conditions, the simulation results are provided in two stages (*a*. 3-phase voltage sag/swell, and *b*. 1-phase voltage sag/swells). In Fig. 3.16., the traces of applied variable torque, generator speed, and generator terminal voltages are shown, where the torque is varied from *30N.m* to *35N.m* and back to *30N.m* at 0.3 *sec.* and *0.4 sec*. respectively. According to the variation in applied torque, the generator speed is varied from *120rad/s* to *140rad/s* and back to *120rad/s*, and the corresponding change in generator terminal voltage can visualized easily in Fig.3.16(a). The traces of grid voltage, voltage at PCC, grid current, load current, inverter current and dc-link voltages under voltage sag/swell and voltage unbalance are shown in Fig. 3.17 and Fig. 3.18 respectively. In Fig. 3.17, the 30% voltage swell of 0.1 *sec* is introduced at *0.5 sec.* and voltage sag of 30% of *0.1 sec.* is introduced at *0.7 sec.* In order to maintain constant voltage at PCC for a dedicated load, the inverter current injects generated active current and inductive reactive current from 0.5 sec.-0.6 sec., and similarly generated active current and capacitive reactive current from 0.7 sec.-0.8 sec.as evident from Fig.3.17(e). The corresponding change in grid current profile at the same instances can be noticed from Fig.3.17(c), where the change in grid current proile is reflected due to the algebraic sum of inverter and load current. In Fig.3.17 (f), the dc-link voltage is shown, which always remains constant despite of wind and grid side disturbances.

Similarly, In Fig. 3.18, the simulation results are provided under grid voltage unbalance conditions, where the 30% voltage swell of *0.1 sec* is introduced at *0.5 sec.* and a voltage sag of 30% of *0.1 sec.* is introduced at *0.7 sec* in the phase-a of grid voltage. In order to maintain constant voltage at PCC for a dedicated load, the inverter phase-a current carries the generated active current and inductive reactive current from 0.5 sec.-0.6 sec., and similarly generated active current and capacitive reactive current from 0.7 sec.-0.8 sec.as evident from Fig.3.18(e). The corresponding change in grid phase-a

current profile at the same instances can be noticed from Fig.3.18(c), where the change in grid phase-a current proile is reflected due to the algebraic sum of inverter and load current. In Fig.3.18(f), the dc-link voltage is shown, which always remains constant despite of wind and grid side disturbances.

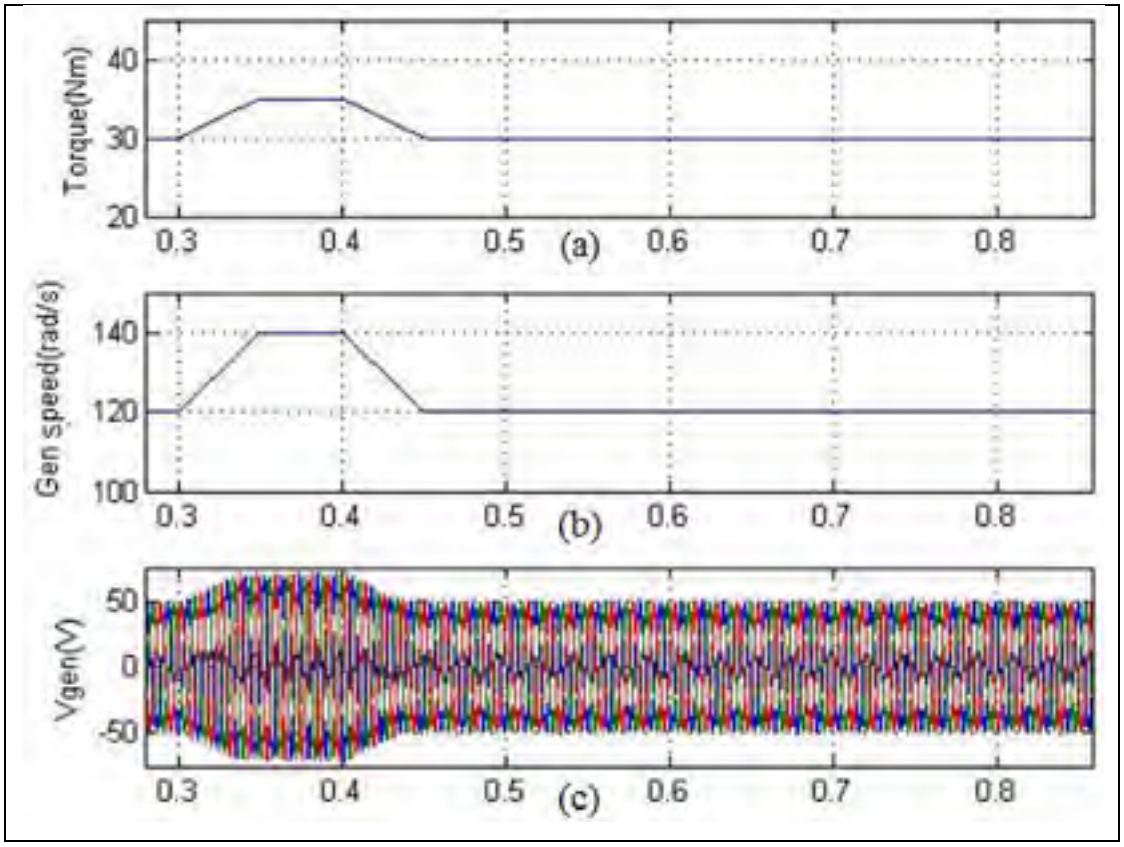

Figure 3.16 Generator Side Result under Varying Wind.

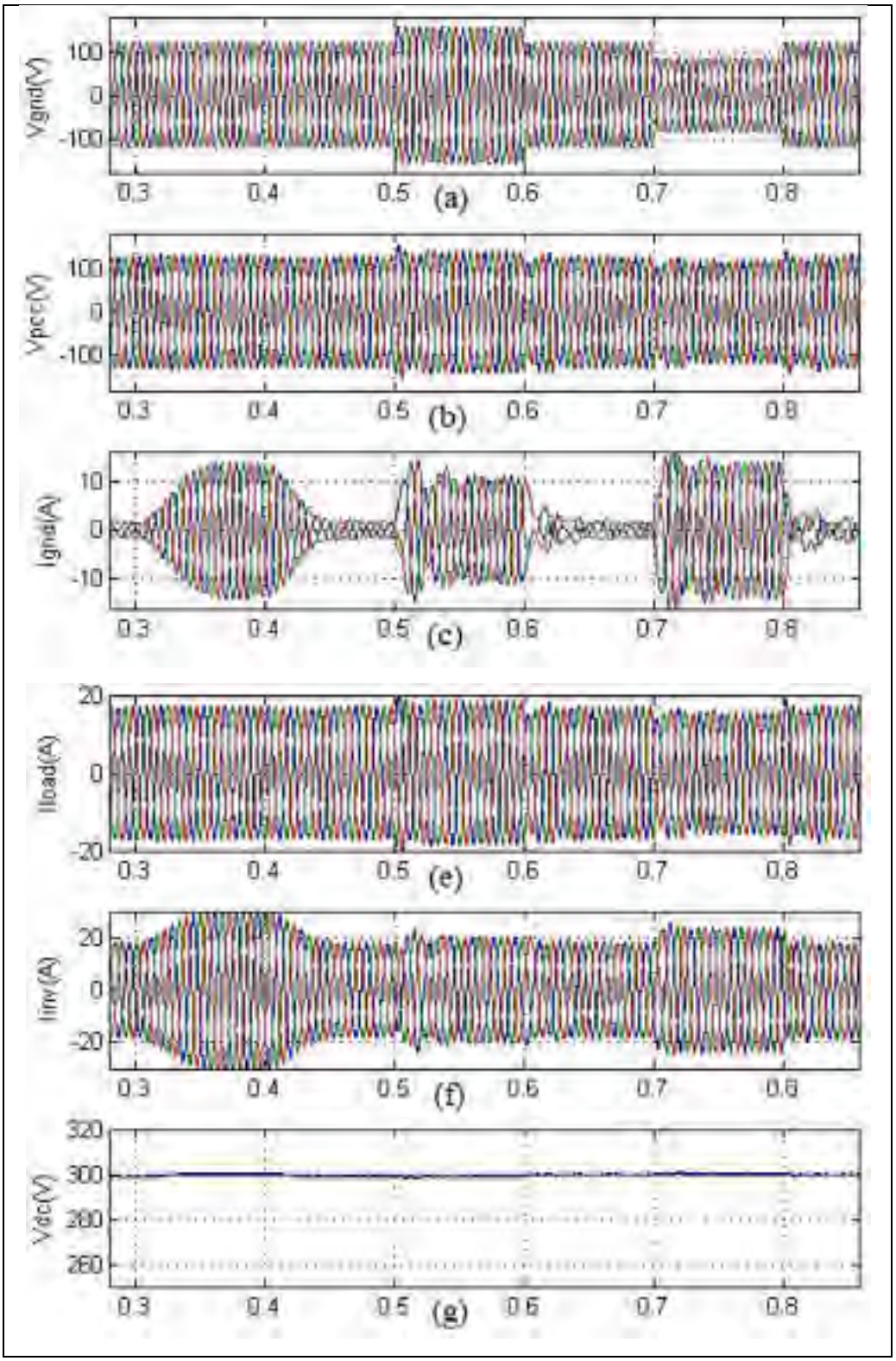

Figure 3.17 Grid Side Result with Voltage Sag/Swell Compensation.

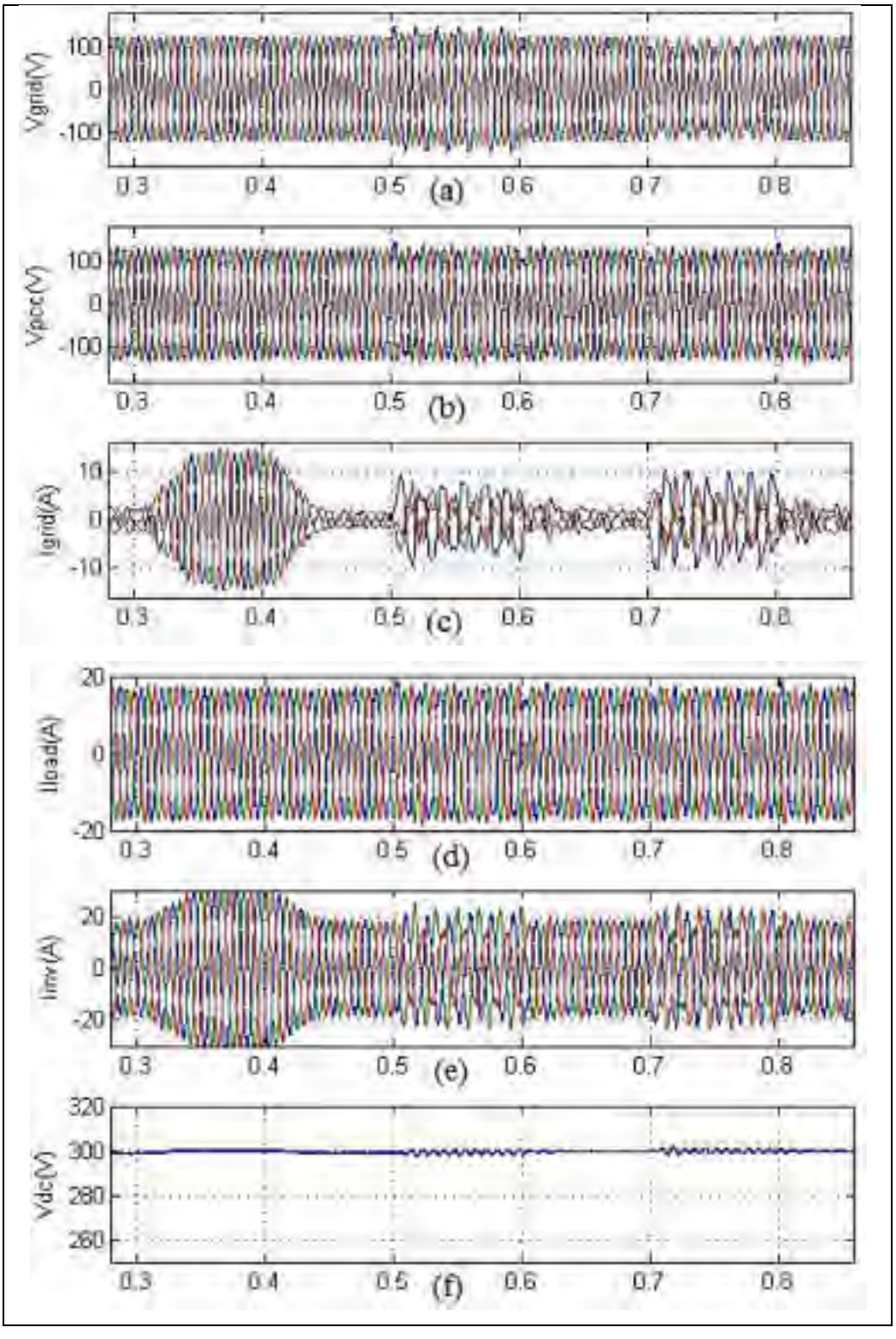

Figure 3.18 Grid Side Result with Voltage Unbalance Compensation.

CHAPTER 4

CONTROL OF WECS WITH POWER QUALITY IMPROVEMENT FEATURES

In this chapter the multifunctional capability of grid side inverter is demonstrated. The grid side inverter is actively controlled to inject the renewable power generation and non-linear load compensation at PCC simultaneously. The simulation and experimental studies are carried out for both 3-phase 3-wire (3P3W) and 3-pahse 4-wire (3P4W) load at PCC.

4.1 Control of WECS with 3P3W Non-linear Load Compensation

The power electronics plays an important role in the reliable operation of modern wind energy conversion system (WECS). Thanks to recent development in wind power technology, the modern wind turbines are now being deployed world-wide in large scale. The advancement in power electronics devices has further played an important role in the improvement of their reliability and controllability.

In the early 80's, the wind farms were installed with the help of financial support and incentives from government. The low penetration level of wind turbine during these early periods was having very little impact on the operational behavior, reliability and security of grid. But in the present scenario, the increasing penetration level of wind turbines has made it mandatory to take them in account while determining the stability of grid. The modern wind turbines are not only required to supply power but also to support the grid during any kind of fault and voltage unbalance. This kind of ability of wind turbine is known as ride through capability. The wind energy conversion system (WECS) should also be able to control its output reactive power automatically as a function of voltage at PCC. The conventional WECS usually consists of static VAR compensators (SVCs), static-compensators (STATCOM) or synchronous compensators

for voltage stability at the point of common coupling (PCC) (Senjyu *et al.*, 2004a). Modern wind turbines have several commercially available topologies mainly based on induction generator, doubly-fed induction generator (DFIG) and synchronous generator with innovative power electronics interface (Morren et de Haan, 2005; Saccomando, Svensson et Sannino, 2002a). Due to intensified grid codes, the wind turbines with full scale converters will be preferred in future, as the power converters fully decouples the wind turbine from grid disturbances and can be helpful in some sort of grid support. The major drawback of full converter rating is their higher installation cost. Moreover, due to intermittent nature of wind, the full converter rating is rarely utilized. Besides this, the increasing penetration level of WECS may lead to grid instability or even failure, if these systems are not controlled properly.

In this section, a novel control strategy for grid interconnection of WECS and to solve the power quality problems at PCC. The system under consideration employs PMSG based variable speed WECS consisting two back to back converters with a common dc-link. The generator side converter controls generator speed in order to achieve maximum power point tracking. The grid side inverter regulates dc-link voltage and injects the generated power into the grid. In addition to this, the grid side inverter is also utilized to compensate the reactive power and current harmonics generated by non-linear loads, if any, at PCC. This enables the grid to supply only sinusoidal current at unity power factor (UPF). The proposed control strategy utilises the grid side inverter rating optimally which is always underutilised due to lower wind capacity factor. According to Ref. (Boccard, 2009), the expected wind output during peak is nearly 60% of rated output, yet the annual capacity factor may be in the 20%-30% range. Thus, the proposed strategy helps to achieve IEEE standard requirements with improved power quality at PCC. The simulation and experimental results are provided to validate the active power injection as well as the harmonics and reactive power compensation capabilities simultaneously.

The system under consideration employs PMSG based variable speed WECS consisting two back to back converters with a common dc-link. Here the generator side control is the same, as discussed in section-3.2.1.2. The block diagram of variable speed WECS with power quality improvement features is shown in Fig. 4.1.

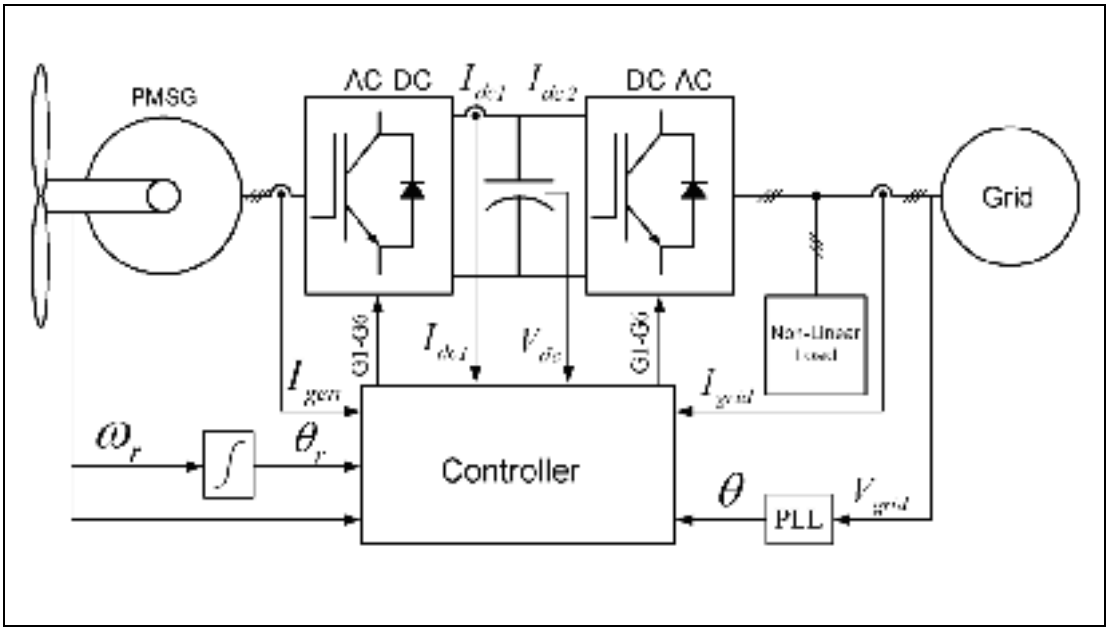

Figure 4.1 Block diagram of PMSG based variable speed WECS.

4.1.1 Grid Side Inverter Control

The grid side inverter is used to regulate dc-link voltage so that the power balance can be maintained under both fluctuating wind and grid disturbances. The control of this grid-side inverter comprises of two cascaded loops. The outer dc voltage control loop is used to set the current reference for active power control. The inner current loop is used to achieve harmonic and reactive power compensation, as per the demand of nonlinear load at PCC. The proposed control strategy is realized in synchronous rotating reference frame. By means of this reference frame, the control variables become dc quantities; thus filtering and controlling can be easily achieved. Moreover, the *PI* regulator gives

enhanced performance while regulating dc variables (Asiminoaei, Blaabjerg et Hansen, 2007). The basic principle of proposed control strategy is derived from three-phase shunt active power filter. In Fig.4.2, the inverter current consists of two components: full load harmonic compensation current i_h, and active current component in proportional to generated wind power i_w, where a part of active component of inverter goes to load ($\bar{i}_L$) and rest goes to grid (i_g), and full harmonic component of load current is locally provided by the inverter. Thus the inverter injected current supplied in the network can be given as:

$$i_{inv} = i_h + i_w = i_h + \bar{i}_L \pm i_g \tag{4.1}$$

Where i_g is the grid current and i_L is the non-linear load current to be compensated at the PCC. Here +VE sign of grid currents indicates that the power generated from wind is more than load demand, while the –VE sign indicates the power generated is less than the load demand. The non-linear load may consist of three components, the fundamental active component (in-phase component), the reactive component (quadrature component) and the harmonic currents (or harmonic reactive component). Therefore, if the grid side inverter supplies the active current proportional to generated wind power, the reactive and harmonic currents of non-linear load, then the grid needs only to supply remaining portion of active current to the load at PCC.

Let the three-phase grid side voltages are as follows:

$$\left.\begin{aligned} e_a &= E\cos(\omega t) \\ e_b &= E\cos(\omega t - \frac{2\pi}{3}) \\ e_c &= E\cos(\omega t + \frac{2\pi}{3}) \end{aligned}\right\} \tag{4.2}$$

Where E is the maximum phase voltage and ω is the angular frequency of the grid side supply. From (4.1), the load currents $i_{La,}$ i_{Lb} and i_{Lc} are the algebraic sum of injected inverter currents and the grid currents of each phase as follows:

$$\left.\begin{aligned} i_{La} &= i_{inva} \pm i_{ga} \\ i_{Lb} &= i_{invb} \pm i_{ga} \\ i_{Lc} &= i_{invc} \pm i_{ga} \end{aligned}\right\} \tag{4.3}$$

Where $i_{ga,}$ $i_{gb,}$ i_{gc} are grid currents and $i_{inva,}$ $i_{invb,}$ i_{invc} are inverter injected currents. If load current at PCC is negligible then $i_{inva}=i_{ga}=i_a$, and the voltage equations in *a-b-c* frame can be written as:

$$\left.\begin{aligned} e_a &= L\frac{di_a}{dt} + v_a \\ e_b &= L\frac{di_b}{dt} + v_b \\ e_c &= L\frac{di_c}{dt} + v_c \end{aligned}\right\} \tag{4.4}$$

Where $e_{a,}$ $e_{b,}$ e_c are grid side voltages, $v_{a,}$ $v_{b,}$ v_c are the inverter terminal voltages and L is the coupling inductance.

On converting the voltage equations (4.4) into synchronous *d-q* reference frame (as explained in section 2.3.2), we have:

$$\left.\begin{aligned} e_d &= L\frac{di_d}{dt} - \omega L i_q + v_d \\ e_q &= L\frac{di_q}{dt} + \omega L i_d + v_q \end{aligned}\right\} \tag{4.5}$$

Usually, the load current and either of the grid or inverter currents are required to control the inverter in order to compensate the load reactive power and harmonics. This makes it necessary to have at least six current sensors in addition to four voltage sensors. In the proposed strategy, only three current sensors and four voltage sensors are used to force the grid current to be purely sinusoidal without having any knowledge of inverter and load current profile. The main aim of the proposed controller is to generate the reference currents such that the grid always supplies only fundamental active power to the load at PCC. For UPF operation, the quadrature axis reference current $i_q^*=0$. The active power exchange between the WECS and the grid is directly proportional to the direct-axis current i_d and can be derived as follows:

$$P = \frac{3}{2}(e_d i_d + e_q i_q) = \frac{3}{2} e_d i_d \tag{4.6}$$

This direct-axis current i_d is also responsible for regulating the dc-link voltage. Therefore, the d-axis reference current i_d^* is generated from PI controller for dc-link voltage regulator expressed as:

$$i_d^* = \left(K_{PV_{dc}} + \frac{K_{IV_{dc}}}{S} \right) \left(V_{dc}^* - V_{dc} \right) \tag{4.7}$$

Where K_{PVdc} is proportional gain and K_{IVdc} is the integral gain of dc-voltage regulator.

Generally, the standard *PI* controllers perform satisfactorily in forcing the grid current to track the reference current exactly. However, the presence of coupling terms in equation (4.5) deteriorates the performance of *PI* regulator. To avoid this problem, the system can be decoupled in the form of first order linear dynamic system having better controllability, as follows:

$$\left.\begin{aligned} 0 &= L\frac{di_d}{dt} - \Delta v_d \\ 0 &= L\frac{di_q}{dt} - \Delta v_q \end{aligned}\right\} \tag{4.8}$$

Where, the output signals, Δv_d and Δv_q are derived from inner current controller loops as

$$\left.\begin{aligned} \Delta v_d &= K_p\left(i_d^{\,*} - i_d\right) + K_i\int\left(i_d^{\,*} - i_d\right).dt \\ \Delta v_q &= K_p\left(i_q^{\,*} - i_q\right) + K_i\int\left(i_q^{\,*} - i_q\right).dt \end{aligned}\right\} \tag{4.9}$$

Inclusion of these decoupled terms in equation (4.5), results in to the reference *d-q* voltages of inverter as follows:

$$\left.\begin{aligned} v_d^{\,*} &= e_d + \omega L.i_q - \Delta v_d \\ v_q^{\,*} &= e_q - \omega L.i_d - \Delta v_q \end{aligned}\right\} \tag{4.10}$$

The reference *d-q* voltages obtained from equation (4.10) are transformed into *a-b-c* reference voltages with the help of grid voltage phase angle θ. The grid synchronizing phase angle can be extracted using phase lock loop (*PLL*) technique. The reference voltages are then applied to PWM controller to generate control signals for grid side inverter. The complete control diagram of grid side inverter is shown in Fig. 4.2.

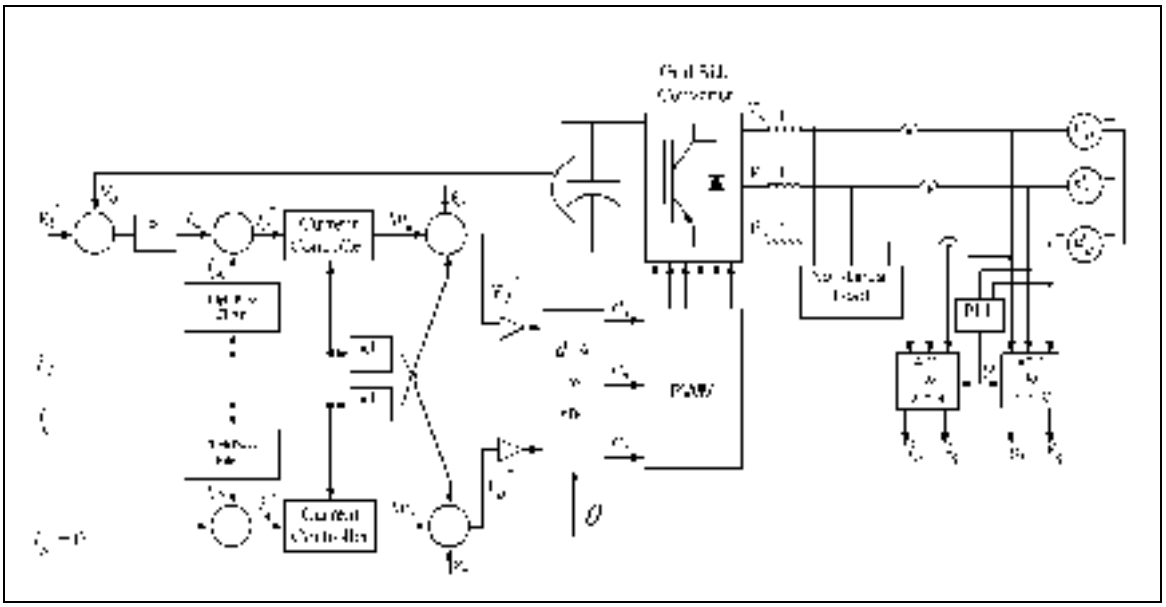

Figure 4.2 Grid side Inverter control.

4.1.2 Simulation Results and Discussion

The proposed control strategy for PMSG based variable speed WECS is simulated using MATLAB/SPS under different operating conditions. The simulation results in Fig. 4.3 show the traces of wind speed, the generator terminal voltage (v_{gen}), generator terminal current (i_{gen}), and the generator rotor speed (ω_r). In Fig. 4.4, the simulation results for grid voltage (v_{grid}), grid current (i_{grid}), load current (i_{load}) inverter current (i_{inv}), and dc-link voltage (v_{dc}), are shown. In Fig. 4.5, the power flow between inverter, grid and load is analyzed under fluctuating wind and non-linear load conditions. Furthermore, an efficiency curve (η) obtained using wind generator power and the actual inverter output power is also shown in Fig. 4.5.

a) Performance of Generator Side Controller : The simulation results for variable speed operation of wind turbine are shown in Fig. 4.3 A variable input torque in proportion to wind speed is applied to PMSG and accordingly reference speed is calculated using MPPT algorithm. Initially the applied wind speed is considered as 7.5

m/sec. This makes the generator to rotate at a speed of 85 *rad/sec*. The corresponding generator voltage and current are found as 50 V and 45 A, respectively. At t = 0.15 *sec*, the wind speed starts increasing and reaches to a new value of 11 *m/sec*. In response to this, the generator speed also starts increasing and get settled to a new value of 100 *rad/sec*. The corresponding increase in generator voltage and current can also be noticed from Fig. 4.3 At time t = 0.25 *sec*, the wind speed starts decreasing and reaches to the same value as in the beginning. The respective change in generator speed, voltage and current can also be easily noticed. From the simulation results, it is evident that the generator follows the reference speed very closely. The effect of change in wind speed can also be verified from the amount of current and active power injected into grid by the grid side inverter as shown in Fig. 4.4 and Fig.4.5, respectively.

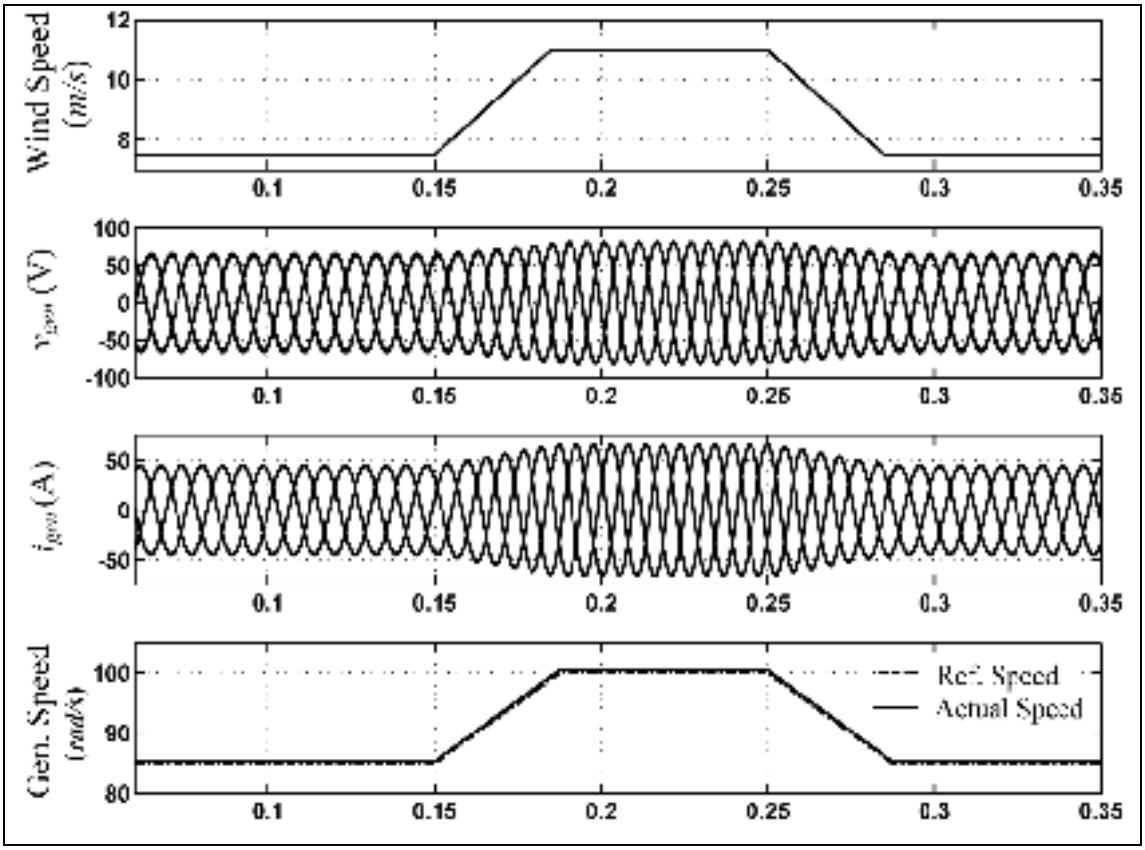

Figure 4.3 Simulation Results for Variable Speed PMSG Operation.

b) Performance of Grid Side Controller: The grid side inverter is actively controlled to inject the generated active power as well as to compensate the harmonic and reactive power demanded by the non-linear load at PCC, such that the current drawn from grid is purely sinusoidal at unity power factor. The simulation results in Fig. 4.4 show the grid voltage, grid current, load current, inverter current and dc- link voltage. The load current consists of active, reactive and harmonic components. Initially, the grid side inverter is intentionally switched off, just to demonstrate the capabilities of proposed controller. Thus the grid supplies the load current harmonics and reactive power demand. Therefore during this time period, the grid current profile is identical to load current profile. At time t = 0.09 *sec*, the grid side inverter is switched ON and the inverter starts injecting the current which is the sum of harmonic component, reactive component of non-linear load and active component in proportion to generated wind power. Due to this the grid supplies the sinusoidal current at unity power factor and at reduced magnitude depending on the amount of active power supplied by the inverter. At time t = 0.15 *sec*, the current injected from inverter increases due to increase in wind power, resulting in the proportional reduction in grid current. At t = 0.25 *sec*, the injected inverter current starts decreasing with decrease in wind velocity and in response to this, the grid current starts increasing to meet the load demand. The dc-link voltage is maintained at a constant level of 300 V irrespective of any change in grid operating conditions.

Fig. 4.5 shows the simulation results for power flow under different wind turbine speeds. Initially, the grid side inverter is not connected to grid, so the load active and reactive power demand of 9.6 kW and 4 kVAR is supplied by the grid. At time t = 0.09 *sec*, the inverter is connected with grid and it starts supplying the active as well as reactive power. Now the inverter feeds wind generated active power of 2.4 kW and grid supplies the remaining 7.2 kW to meet the load active power demand of 9.6 kW. Here it should be noticed that the reactive power demand of 4 kVAR is completely supplied from inverter in order to achieve UPF operation of grid. At time t = 0.15 *sec*, the injected active power of inverter starts increasing due to increase in wind speed and accordingly,

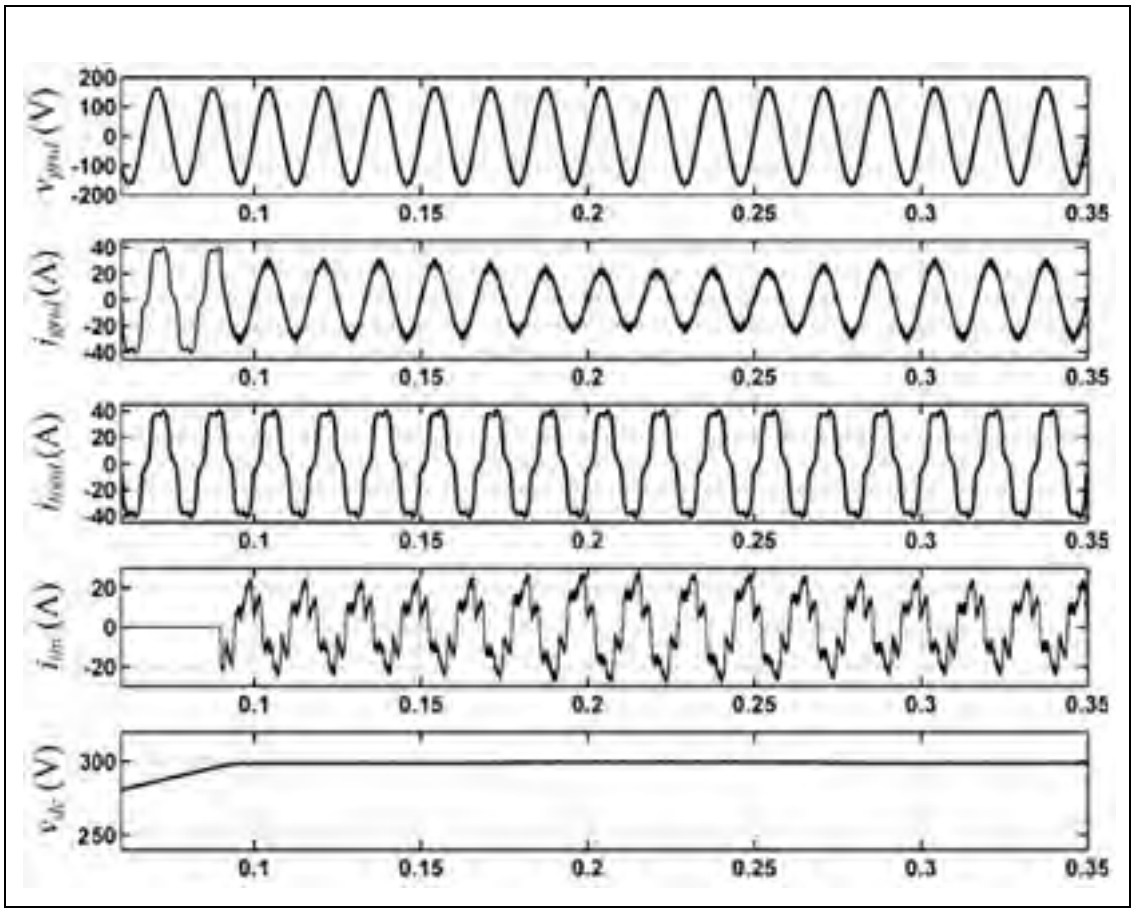

Figure 4.4 Grid Side Inverter Performance with Power Quality Improvement.

the grid active power decreases. At this condition, the active power supplied from inverter is 4.2 kW, therefore, 5.4 kW power is supplied from grid to meet 9.6 kW active load demand. Again at time t = 0.25 *sec*, the active power supplied from inverter starts decreasing with the decrease in wind velocity and corresponding change can be noticed in grid active power. In Fig. 4.5, the generator terminal power is also shown, which is slightly higher than the inverter injected active power due to the losses in two back to back converters. These losses are found as approximately 200 watts. The % efficiency (η) of proposed system varies from 92% to 97%.

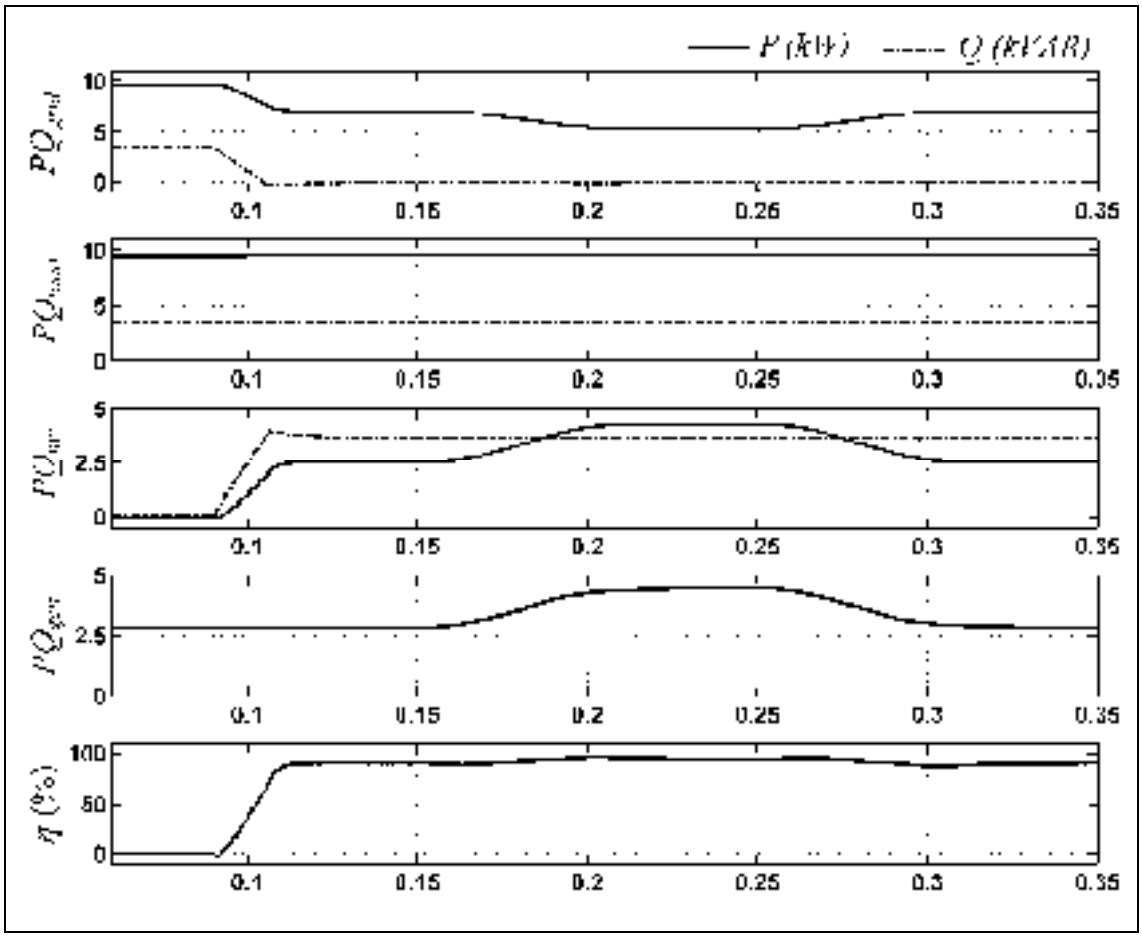

Figure 4.5 Simulation Results for Power Flow Analysis of WECS.

4.1.3 Experimental Results and Discussion

A scaled hardware prototype is developed to validate the proposed control strategy. Two back to back connected converters with a common dc-link are used to realize the wind energy conversion system. The one converter supplies the variable active power to the dc-link, while the other injects this active power as well as the reactive power and harmonics demanded by the loads at PCC. The control system is implemented using DS1104 DSP of dSPACE. The switching frequency of 5 kHz is used to control the IGBT based voltage source converter.

To highlight the capability of the proposed control approach, the grid side inverter operation is explained in four different modes of operations. The experimental results are given in Figs. (4.6- 4.10). All the voltage and current waveforms are captured utilizing an oscilloscope, whereas, the active and reactive powers are captured using *ControlDesk Developer* environment in real-time. The load connected to PCC is considered as a non-linear load which draws a distorted current [Fig. 4.6., trace-2] with total harmonics distortion (THD) of 28%.

a) Mode-I: Zero Active Power Support from WECS: The experimental results for mode-I are shown in Fig. 4.6. In this mode the WECS does not generate any active power and thus the grid supplies the power demanded by the load connected at PCC. Since the concept of the proposed study is to utilize the grid side converter optimally, it is controlled to compensate the current harmonics generated by non-linear load at PCC. This aspect of power quality enhancement can be viewed from the Fig. 4.6. Here the grid side converter injects the necessary current [Fig. 4.6(a), trace-4] such that the grid supplies only the fundamental sinusoidal current [Fig. 4.6(a), trace-3]. The unit power factor operation can be noticed from Fig. 4.6(a) by comparing trace-1 and trace-3. The gird side current THD is found as 3.6%. The active and reactive powers under this mode of operation are plotted in Fig. 4.6(b). Note that the grid supplies only fundamental active power to non-linear load (the reactive power supplied is almost zero), while the grid side converter supplies the reactive power locally. The gird side converter consumes small amount of active power to overcome the losses associated with switching devices and to maintain the dc-link voltage at constant level.

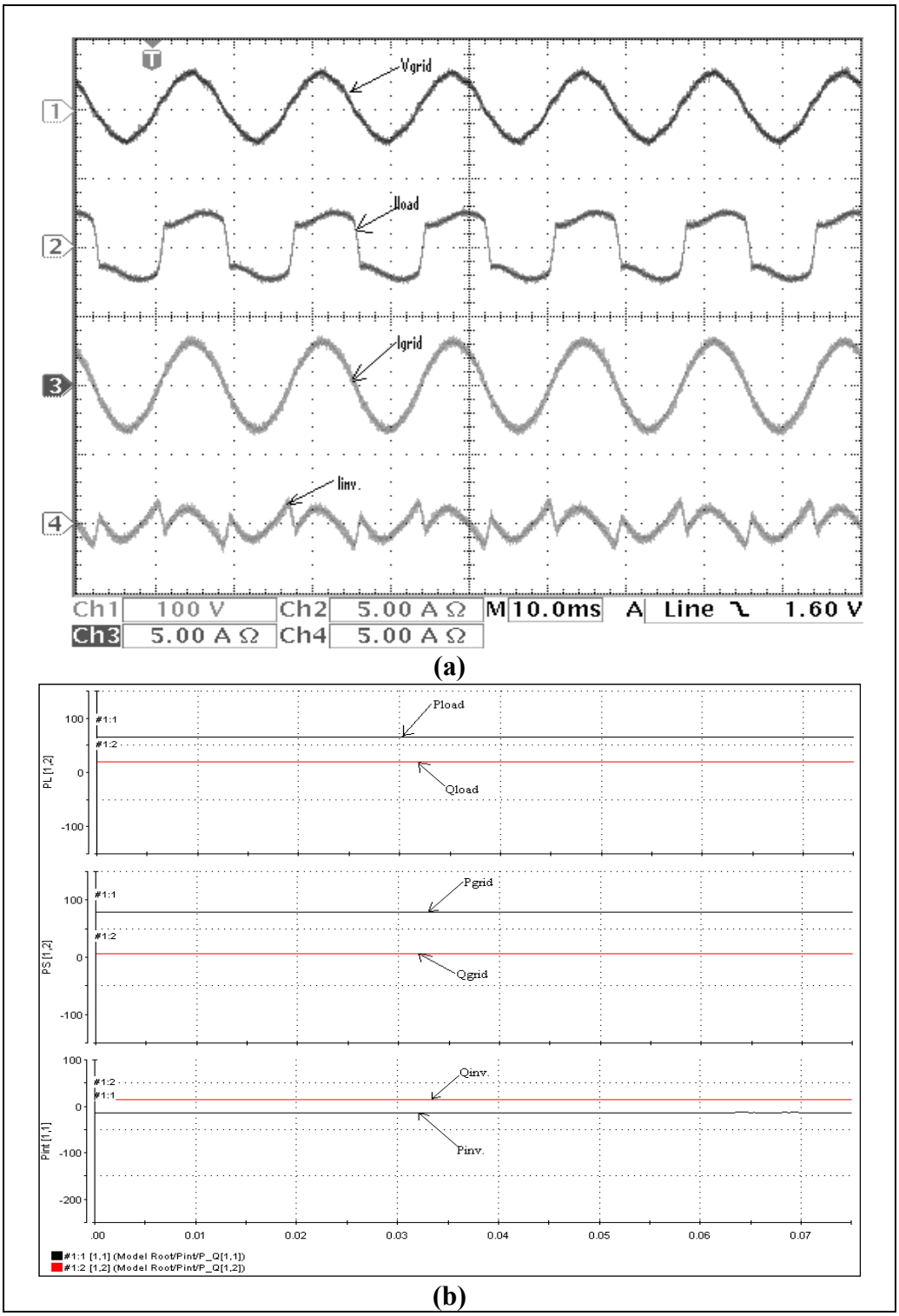

Figure 4.6 Experimental Results : zero- active power generation from WECS.

b) Mode-II: Partial Active Power Support: In second mode of operation it is considered that the WECS generates certain amount of power which is available at the dc-link. However this available power from WECS is not enough to support the full load. The experimental results during this operating condition are shown in Fig. 4.7. The gird side converter adequately manages this power and supports to the non-linear load in such a way that it maintains the sinusoidal gird current. The grid side converter injecting the current which is sum of harmonics component and generated active power component can be noticed from Fig. 4.7(a), trace-4. The reduction in grid current magnitude [Fig. 4.7(a), trace-3] also justifies the aforementioned operation. The active power supplied by grid side converter and the reduction in gird active power can be noticed from Fig. 4.7(b).

c) Mode-III: Full Load Support from WECS: In this section an interesting mode of operation is discussed It is considered that the power available from the WECS is exactly equal to the power demanded by the non-linear load at PCC. The experimental results during this full load support mode of operation are shown in Fig. 4.8. As noticed from Fig. 4.8(a), trace-4, the grid side converter supports the entire non-linear load and thus the grid supplies no current. The zero gird current can be noticed from the Fig. 4.8(a), trace-3. The powers supplied by grid side converter and the grid are plotted in Fig. 4.8(b). It is evident from the Fig. 4.8(b) that under full load support mode of operation the load power demand is entirely handled by the gird side converter. Note that the active as well as reactive powers drawn from the grid are almost zero.

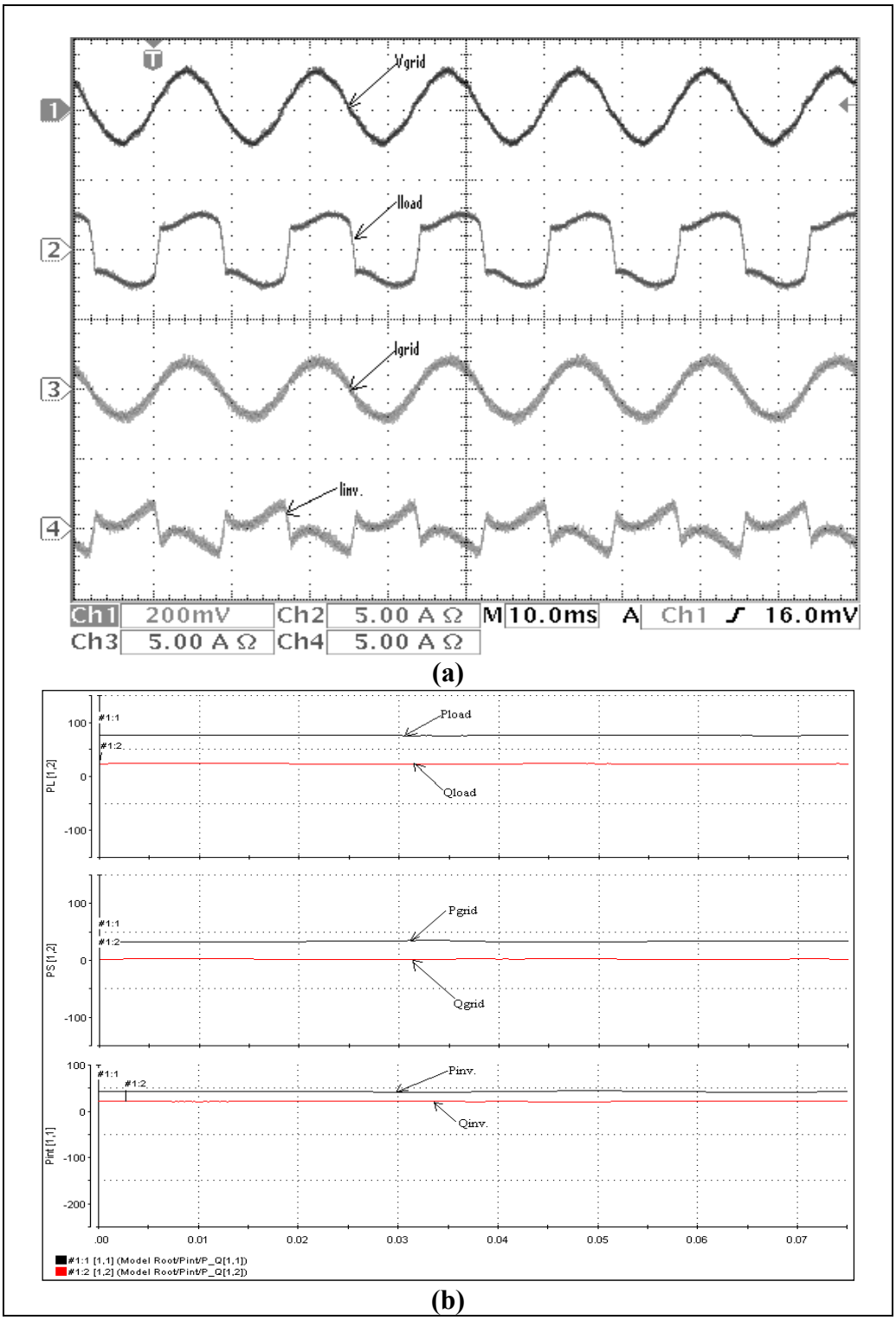

Figure 4.7 Results with Partial Active Power Support from WECS.

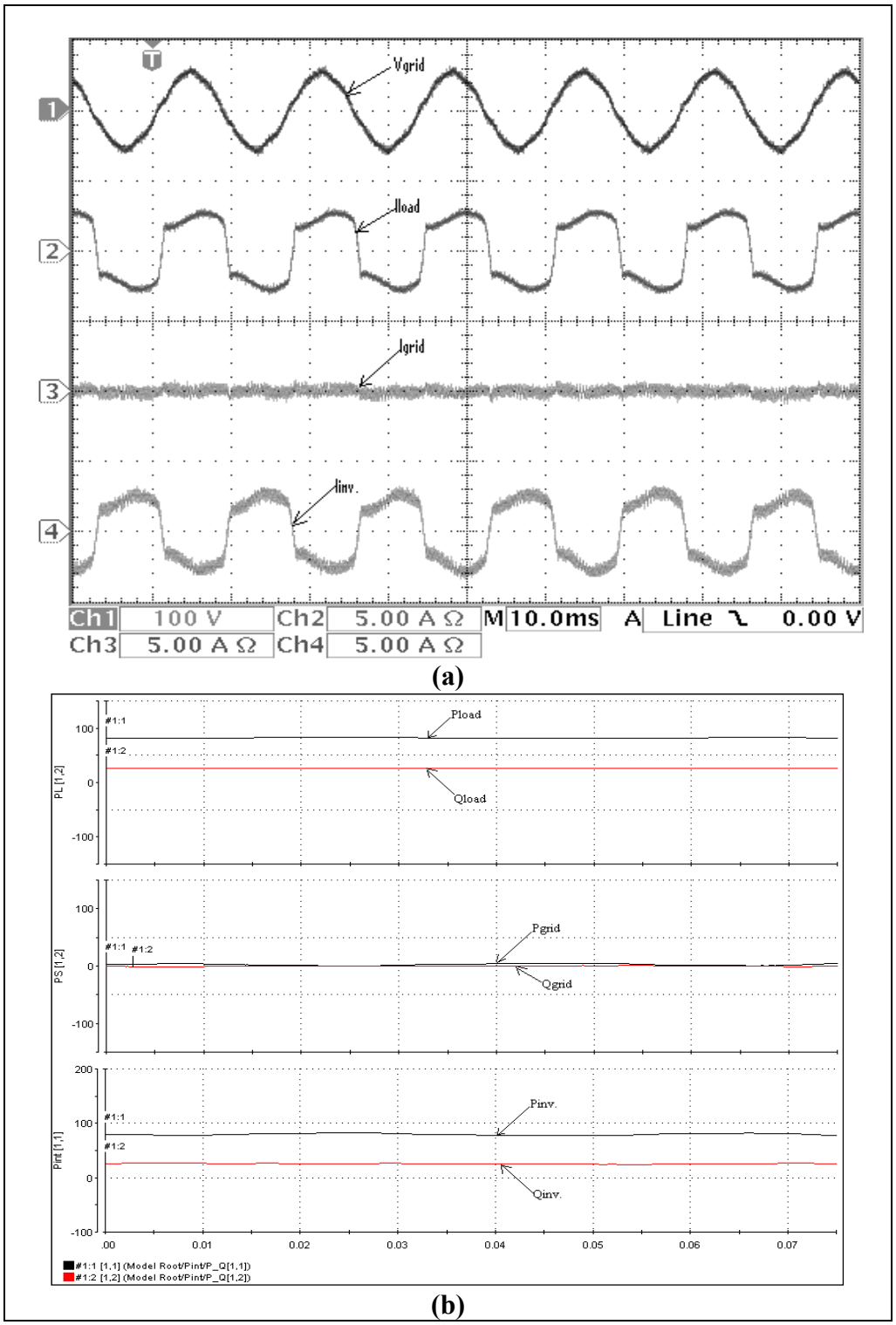

Figure 4.8 Experimental Results with Full Load Support from WECS.

d) Mode-IV: Active Power Support from WECS to Gird: Finally, it is considered that the WECS generates power in excess to load power demand at PCC. The experimental results under this mode of operation are shown in Fig. 4.9. Since the power available at gird side converter is more than the load power demand, the proposed controller manage this additional power effectively and feeds to the main grid. Under this condition the current injected by the grid side converter shown in Fig. 4.9(a) trace-4, is sum of the load current and current supplied to the grid. The grid current profile is shown in Fig. 4.9(a), trace-3. Note the out of phase relationship between the gird voltage and current justifies the fact that the additional generated power is injected into the main grid effectively. The active and reactive powers handled by the grid side converter are shown in Fig. 4.9(b).

e) Mode-V: Dynamic Performance of Proposed Control Approach: Fig. 4.10 shows the experimental results to validate the dynamic performance of proposed control approach under different modes of operation. Initially, it is considered that the system is working under mode-I operating condition (i.e. non-linear load current harmonics and reactive power compensation). The power at dc-link is suddenly increased which can be noticed from Fig. 4.10(b). The proposed controller mange this additional power precisely and feeds to the main grid. A smooth changeover from mode-I operating condition to the mode-IV can be noticed. The corresponding changes in active and reactive powers of voltage source inverter and the main grid can be viewed from the Fig. 4.10(b).

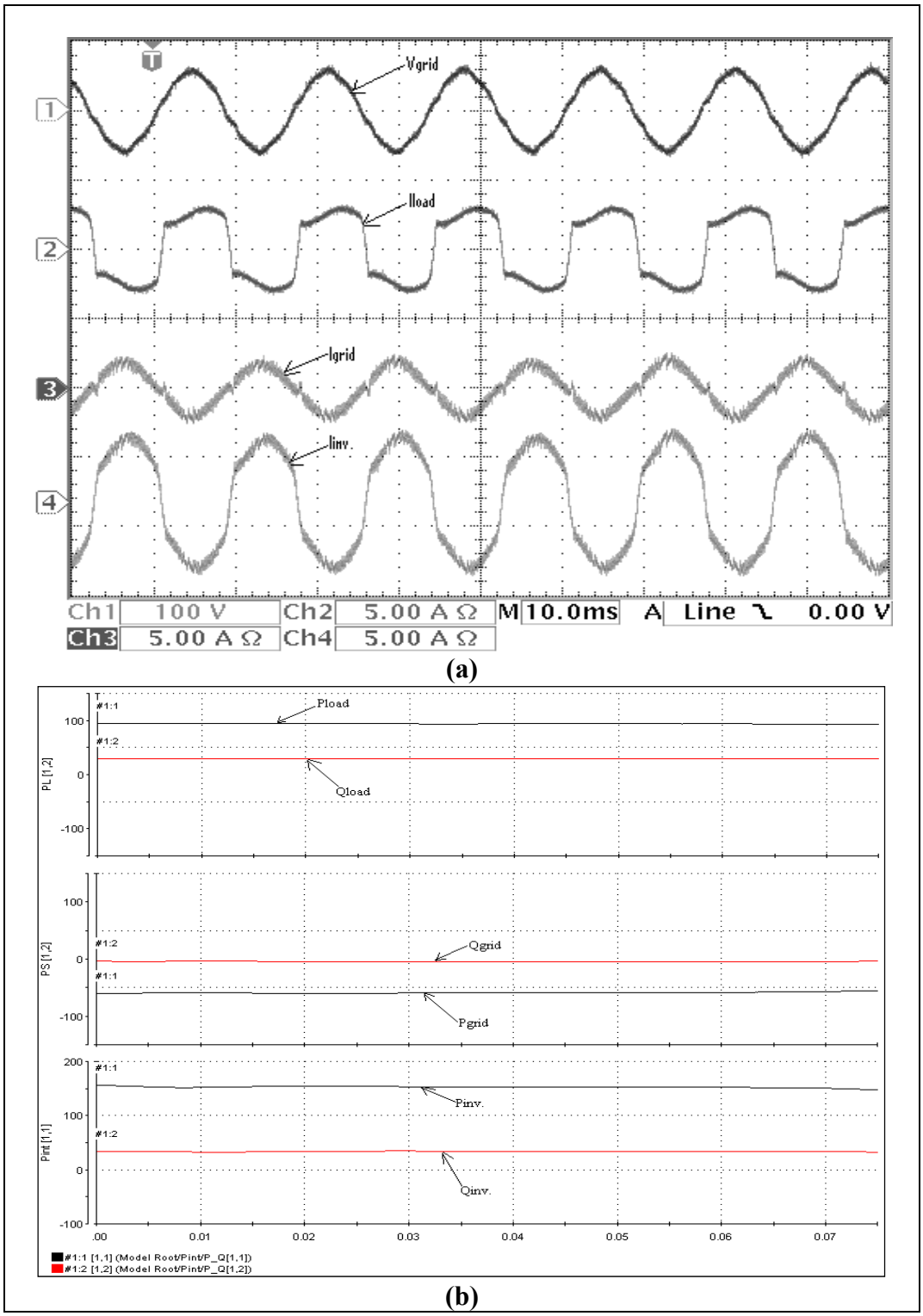

Figure 4.9 Experimental Results with Active Power Support from WECS to Grid.

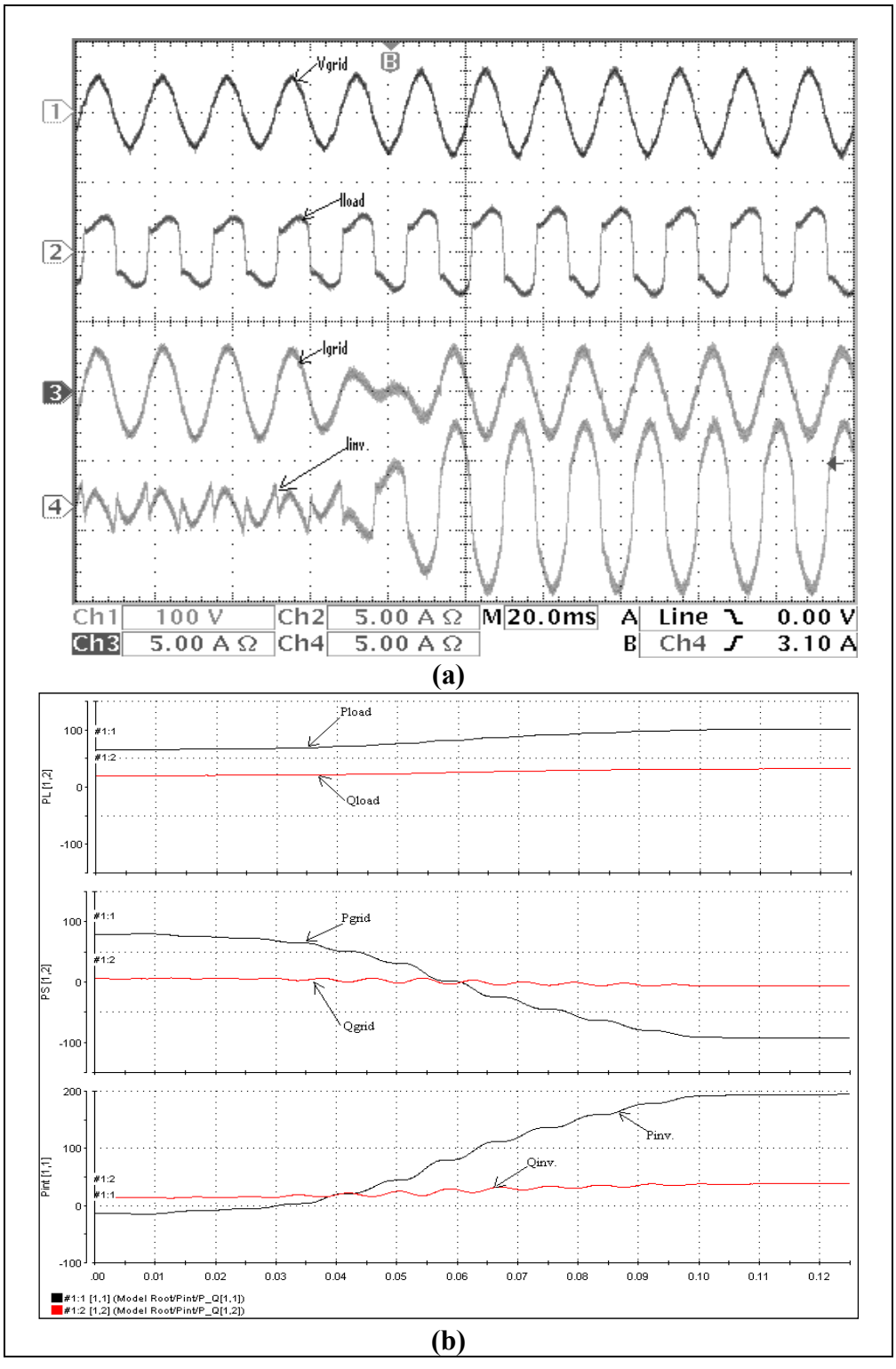

Figure 4.10 Dynamic Performance of Proposed Approach.

4.2 Grid Synchronization of RES with 3P4W Non-linear Load Compensation

Renewable energy source (RES) integrated at distribution level is termed as distributed generation (DG). The utility is concerned of the high penetration level of intermittent RES in distribution systems as it may pose a threat to network in terms of stability, voltage regulation and power quality issues. Therefore, the DG systems are required to comply with strict technical and regulatory frameworks to ensure safe, reliable and efficient operation of overall network. With the advancement in power electronics and digital control technology, the DG systems can now be actively controlled to enhance the system operation with improved power quality at PCC. However, the extensive use of power electronics based equipment and non-linear loads at PCC generate harmonic currents, which may deteriorate the quality of power (Enslin et Heskes, 2004; Guerrero *et al.*, 2004).

Generally, current controlled voltage source inverters are used to interface the intermittent RES in distributed system. Recently, a few control strategies for grid connected inverters incorporating power quality solution have been proposed. In (Borup, Blaabjerg et Enjeti, 2001) an inverter operates as active inductor at a certain frequency to absorb the harmonic current. But the exact calculation of network inductance in real-time is difficult and may deteriorate the control performance. A similar approach in which shunt active filter acts as active conductance to damp out the harmonics in distribution network is proposed in (Jintakosonwit *et al.*, 2002). In (Pregitzer *et al.*, 2007), a control strategy for renewable interfacing inverter based on *p-q* theory is proposed. In this strategy both load and inverter current sensing is required to compensate the load current harmonics.

The non-linear load current harmonics may result in voltage harmonics and can create a serious power quality problem in the power system network. Active power filters (APF) are extensively used to compensate the load current harmonics and load unbalance at

distribution level. This results in an additional hardware cost. It is proposed to incorporate the features of APF in the, conventional inverter interfacing renewable with the grid, without any additional hardware cost. Here, the main idea is the maximum utilization of inverter rating which is most of the time underutilized due to intermittent nature of RES. It is shown that the grid-interfacing inverter can effectively be utilized to perform following important functions: (i) transfer of active power harvested from the renewable resources (wind, solar, etc.), (*ii*) load reactive power demand support, (*iii*) current harmonics compensation at PCC and (*iv*) current unbalance and neutral current compensation in case of 3-phase 4-wire system. Moreover, with adequate control of grid-interfacing inverter, all the four objectives can be accomplished either individually or simultaneously. The power quality constraints at the PCC can therefore be strictly maintained within the utility standards without additional hardware cost.

4.2.1 System Description and Control

The proposed system consists of RES connected to the dc-link of a grid-interfacing inverter as shown in Fig. 4.11. The voltage source inverter is a key element of a DG system as it interfaces the renewable energy source to the grid and delivers the generated power. The RES may be a DC source or an AC source with rectifier coupled to dc-link. Usually, the fuel cell and photovoltaic energy sources generate power at variable low dc voltage, while the variable speed wind turbines generate power at variable ac voltage. Thus, the power generated from these renewable sources needs power conditioning (i.e. dc/dc or ac/dc) before connecting on dc-link (Blaabjerg *et al.*, 2006; Carrasco *et al.*, 2006; Renders *et al.*, 2008). The dc-capacitor decouples the RES from grid and also allows independent control of converters on either side of dc-link.

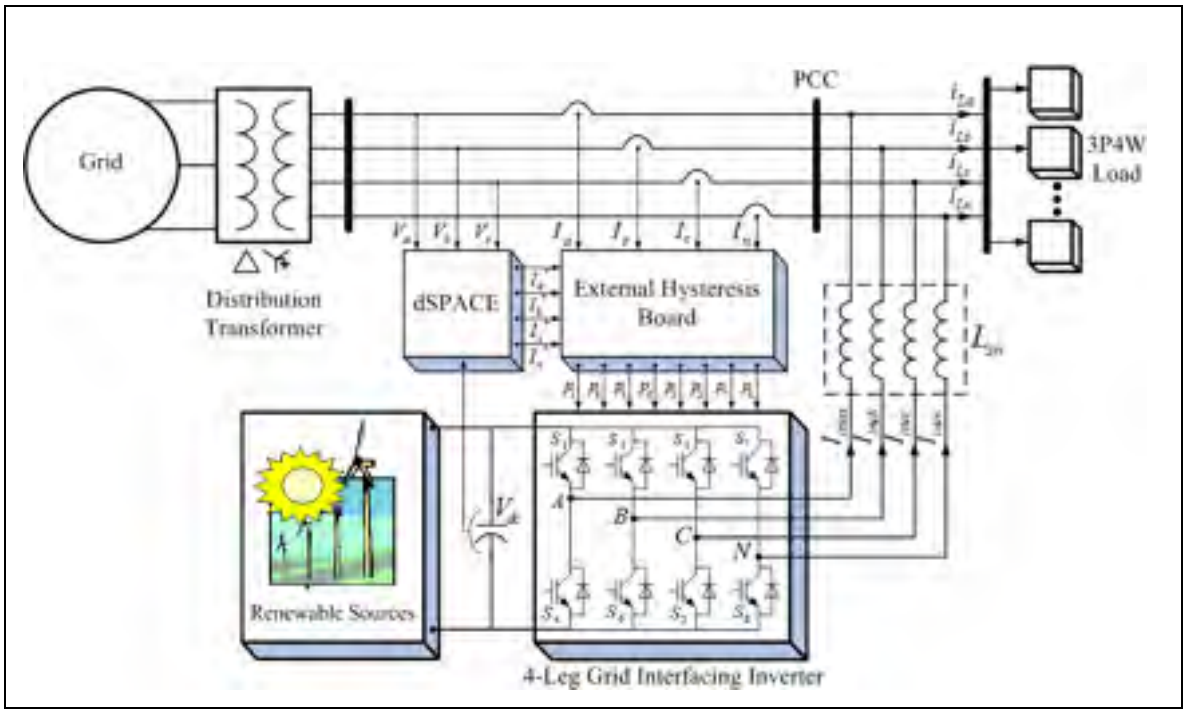

Figure 4.11 Schematic of Renewable Based Distributed Generation System.

a) DC-Link Voltage and Power Control Operation: Due to the intermittent nature of RES, the generated power is of variable nature. The dc-link plays an important role in transferring this variable power from renewable energy source to the grid. RES are represented as current sources connected to the dc-link of a grid-interfacing inverter. Fig. 4.12 shows the systematic representation of power transfer from the renewable energy resources to the grid via the dc-link. The current injected by renewable into dc-link at voltage level V_{dc} can be given as:

$$I_{dc1} = \frac{P_{RES}}{V_{dc}} \tag{4.11}$$

Where P_{RES} is the power generated from RES. The current flow on the other side of dc-link can be represented as:

$$I_{dc2} = \frac{P_{inv}}{V_{dc}} = \frac{P_G + P_{Loss}}{V_{dc}} \tag{4.12}$$

Where P_{inv}, P_G and P_{Loss} are total power available at grid-interfacing inverter side, active power supplied to the grid and inverter losses, respectively. If inverter losses are negligible then $P_{RES}=P_G$.

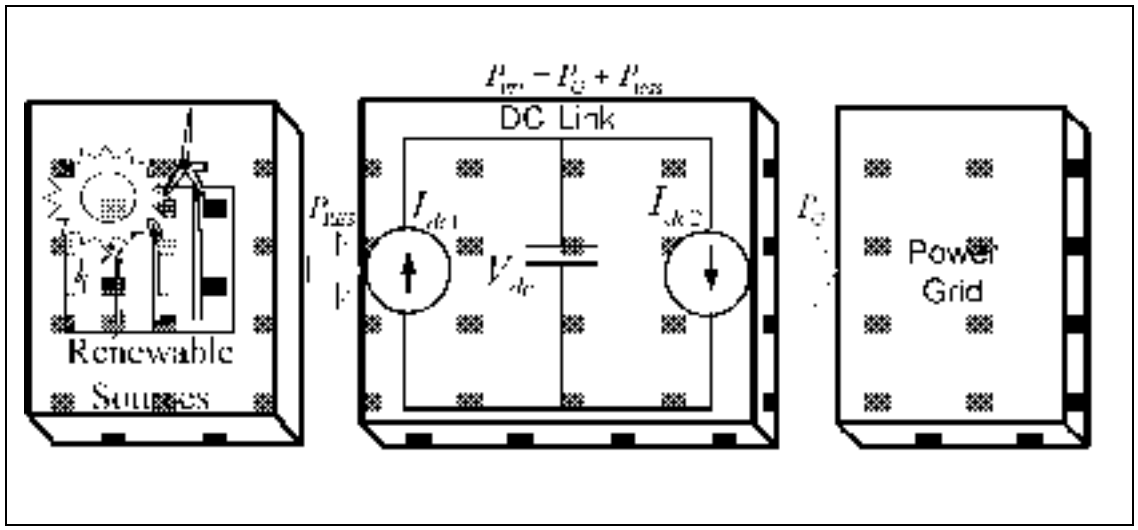

Figure 4.12 DC-Link Equivalent Diagram.

b) Control of Grid Interfacing Inverter: The control diagram of grid- interfacing inverter for a 3-phase 4-wire system is shown in Fig.4.13. The fourth leg of inverter is used to compensate the neutral current of load. The main aim of proposed approach is to regulate the power at PCC during – (*i*) $P_{RES} = 0$, (*ii*) P_{RES} < total load power (P_L), and (*iii*) $P_{RES} > P_L$. While performing the power management operation, the inverter is actively controlled in such a way that it always draws/ supplies fundamental active power from/ to the grid. If the load connected to the PCC is non-linear or unbalanced or the combination of both, the given control approach also compensates the harmonics, unbalance, and neutral current. The duty ratio of inverter switches are varied in a power cycle such that the combination of load and inverter injected power appears as balanced

resistive load to the grid. The regulation of dc-link voltage carries the information regarding the exchange of active power in between renewable source and grid. Thus the output of dc-link voltage regulator results in an active current or in-phase component of reference grid current (I_m). The multiplication of in-phase current component (I_m) with unity grid voltage vector templates (U_a, U_b, and U_c) generates the reference grid currents (I_a^*, I_b^*, and I_c^*). The reference grid neutral current (I_n^*) is set to zero, being the instantaneous sum of balanced grid currents. The grid synchronizing angle (θ) obtained from phase locked loop (PLL) is used to generate unity vector template as (Singh et Chandra, 2008):

$$U_a = Sin(\theta) \tag{4.13}$$

$$U_b = Sin(\theta - \frac{2\pi}{3}) \tag{4.14}$$

$$U_c = Sin(\theta + \frac{2\pi}{3}) \tag{4.15}$$

The actual dc-link voltage (V_{dc}) is sensed and passed through a first-order *low pass filter* (LPF) to eliminate the presence of switching ripples on the dc-link voltage and in the generated reference current signals. The difference of this filtered dc-link voltage and reference dc-link voltage (V_{dc}^*) is given to a discrete-*PI* regulator to maintain a constant dc-link voltage under varying generation and load conditions. The dc-link voltage error $V_{dcerr(n)}$ at n^{th} sampling instant is given as:

$$V_{dcerr(n)} = V_{dc(n)}^* - V_{dc(n)} \tag{4.16}$$

The output of discrete-*PI* regulator at n^{th} sampling instant is expressed as:

$$I_{m(n)} = I_{m(n-1)} + K_{PV_{dc}}\left(V_{dcerr(n)} - V_{dcerr(n-1)}\right) + K_{IV_{dc}}V_{dcerr(n)} \tag{4.17}$$

Where, K_{PVdc} and K_{IVdc} are proportional and integral gains of dc-voltage regulator. The instantaneous values of reference three phase grid currents are computed as:

$$I_a^* = I_m.U_a \tag{4.18}$$

$$I_b^* = I_m.U_b \tag{4.19}$$

$$I_c^* = I_m.U_c \tag{4.20}$$

The neutral current, present if any, due to the loads connected to the neutral conductor should be compensated by forth leg of grid-interfacing inverter and thus should not be drawn from the grid. In other words, the reference current for the grid neutral current is considered as zero and can be expressed as:

$$I_n^* = 0 \tag{4.21}$$

The reference grid currents (I_a^*, I_b^*, I_c^* and I_n^*) are compared with actual grid currents (I_a, I_b, I_c and I_n) to compute the current errors as:

$$I_{aerr} = I_a^* - I_a \tag{4.22}$$

$$I_{berr} = I_b^* - I_b \tag{4.23}$$

$$I_{cerr} = I_c^* - I_c \tag{4.24}$$

$$I_{nerr} = I_n^* - I_n \tag{4.25}$$

These current errors are given to hysteresis current controller. The hysteresis controller

then generates the switching pulses (P_1 *to* P_8) for the gate drives of grid-interfacing inverter.

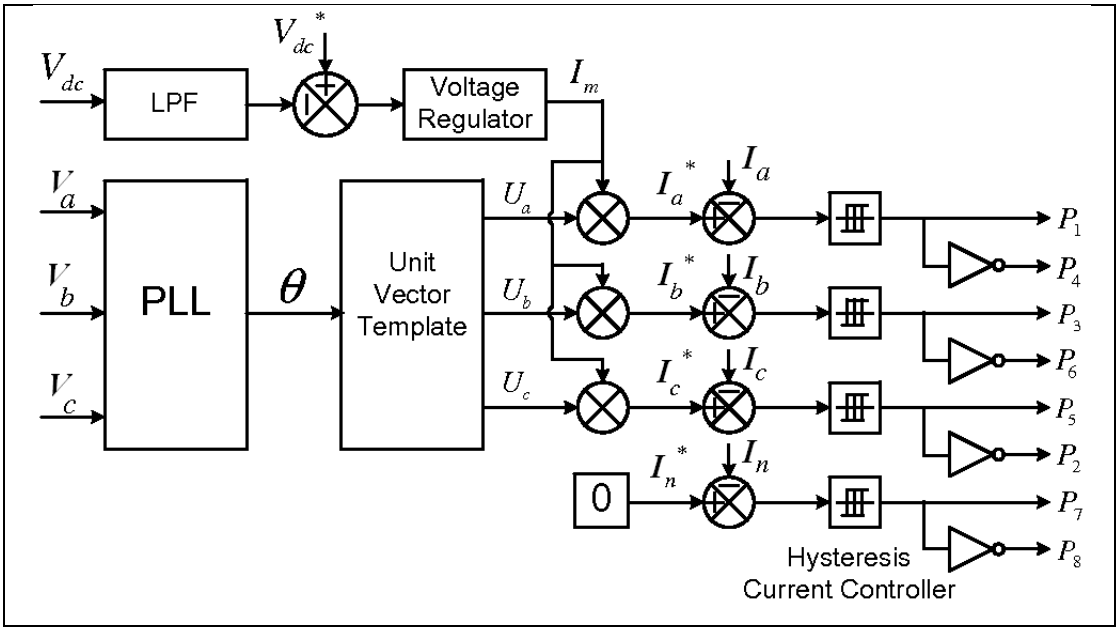

Figure 4.13 Control Diagram of RES Interfacing Inverter.

4.2.2 Simulation Results & Discussion

In order to verify the proposed control approach to achieve multi-objectives for grid interfaced DG systems connected to a 3-phase 4-wire network, an extensive simulation study is carried out using MATLAB/Simulink. A 4-leg current controlled voltage source inverter is actively controlled to achieve balanced sinusoidal grid currents at unity power factor (UPF) despite of highly unbalanced nonlinear load at PCC under varying renewable generating conditions. A RES with variable output power is connected on the dc-link of grid-interfacing inverter. An unbalanced 3-phase 4-wire nonlinear load, whose unbalance, harmonics, and reactive power need to be compensated, is connected on PCC. The waveforms of grid voltage (V_a, V_b, V_c), unbalanced load current (I_{la}, I_{lb} I_{lc}), traces of grid (I_a, I_b, I_c) and inverter currents (I_{inva}, I_{invb}, I_{invc}) are shown in Fig. 4.14. The

corresponding active-reactive powers of grid (P_{grid}, Q_{grid}), load (P_{load}, Q_{load}) and inverter (P_{inv}, Q_{inv}) are shown in Fig. 4.15. Positive values of grid active - reactive powers and inverter active - reactive powers imply that these powers flow from grid side towards PCC and from inverter towards PCC, respectively. The active and reactive powers absorbed by the load are denoted by positive signs. Initially, the grid-interfacing inverter is not connected to the network, i.e. the load power demand is totally supplied by the grid alone. Therefore, before time t=0.72 sec, the grid current profile in Fig. 4.14(c) is identical to the load current profile of Fig. 4.15(b). At t=0.72 sec, the grid-interfacing inverter is connected to the network. At this instant the inverter starts injecting the current in such a way that the profile of grid current starts changing from unbalanced non linear to balanced sinusoidal current as shown in Fig. 4.14(c). As the inverter also supplies the load neutral current demand, the grid neutral current (I_n) becomes zero after t=0.72 sec. At t=0.72 sec, the inverter starts injecting active power generated from RES ($P_{RES} \approx P_{inv}$). Since the generated power is more than the load power demand the additional power is fed back to the grid. The negative sign of P_{grid}, after time 0.72 sec suggests that the grid is now receiving power from RES. Moreover, the grid-interfacing inverter also supplies the load reactive power demand locally. Thus, once the inverter is in operation the grid only supplies/ receives fundamental active power. At t=0.82 sec, the active power from RES is increased to evaluate the performance of system under variable power generation from RES. This results in increased magnitude of inverter current. As the load power demand is considered as constant, this additional power generated from RES flows towards grid, which can be noticed from the increased magnitude of grid current as indicated by its profile. At t=0.92 sec, the power available from RES is reduced. The corresponding change in the inverter and grid currents can be seen from Fig. 4.14. The active and reactive power flows between the inverter, load and grid during increase and decrease of energy generation from RES can be noticed from Fig. 4.15. The dc-link voltage across the grid- interfacing inverter [Fig. 4.15(d)] during different operating condition is maintained at constant level in order to facilitate the active and reactive power flow. Thus from the simulation results, it is evident that the

grid-interfacing inverter can be effectively used to compensate the load reactive power, current unbalance and current harmonics in addition to active power injection from RES. This enables the grid to supply/ receive sinusoidal and balanced power at UPF.

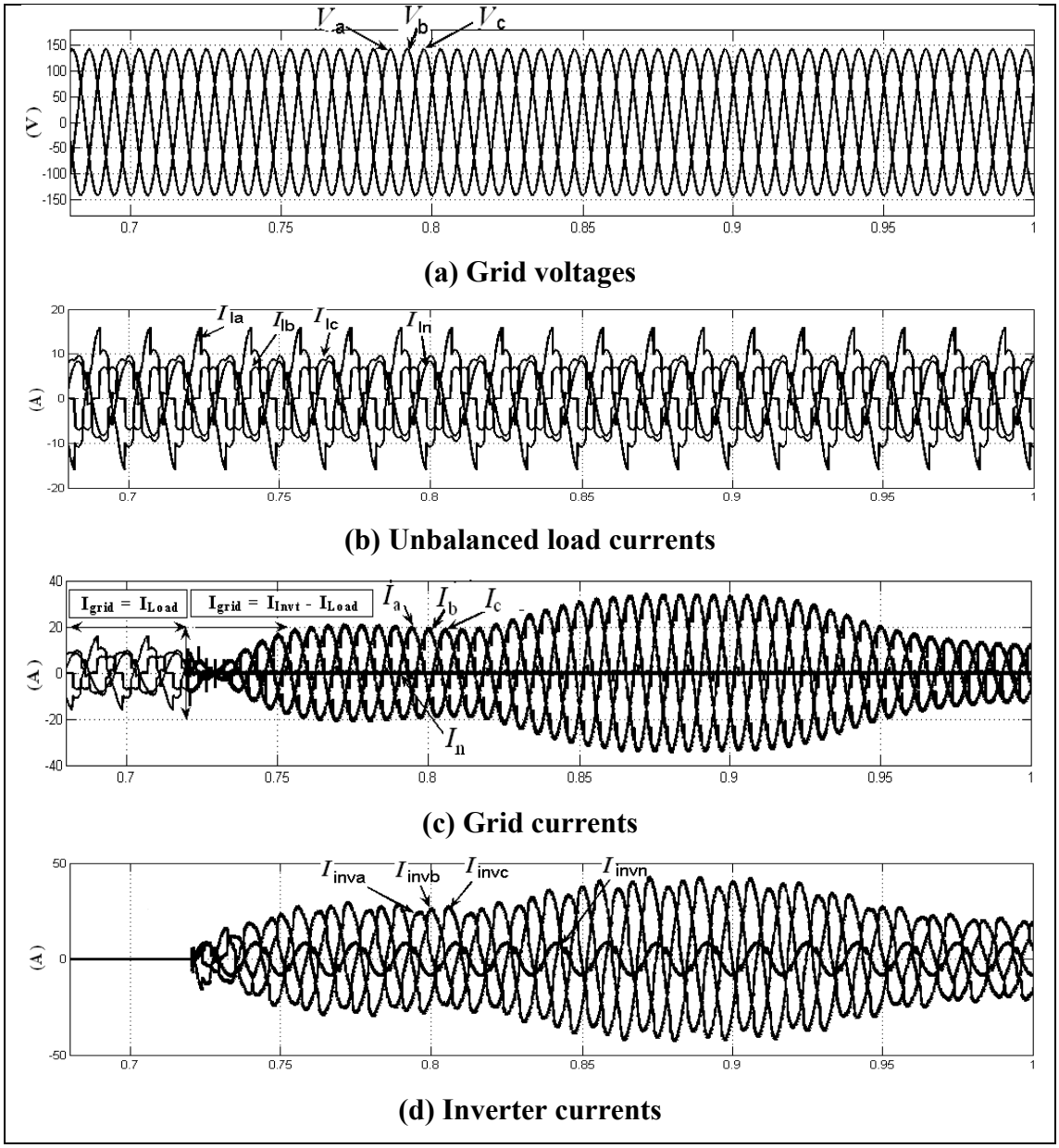

Figure 4.14 Simulation Results for RES Interfacing Inverter.

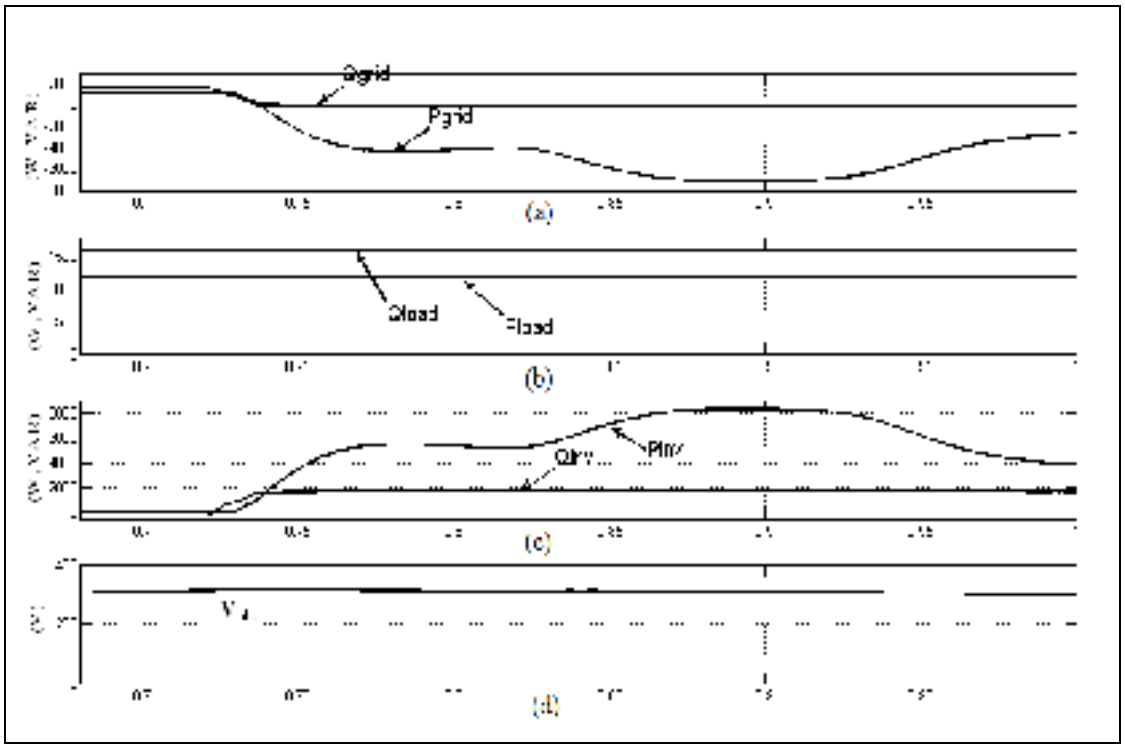

Figure 4.15 Power Flow Analysis for RES Interfacing Inverter.

4.2.3 Experimental Results & Discussion

The performance of proposed control approach is validated with the help of a scaled laboratory prototype. The RES is emulated using an auxiliary controlled converter, which injects varying active power at the dc-link of an insulated gate bipolar transistor (IGBT) based 4-leg voltage source inverter connected to grid. A 3-phase 4-wire nonlinear load, composed of 3-phase non-linear balanced load, 1-phase *R-L* load between phase *a* and neutral and 1-phase non-linear load between phase *c* and neutral, is connected to the grid as shown in Fig.4.16. The total harmonics distortions (THDs) of phase *a*, *b* and *c* load currents are noticed as 14.21%, 22.93%, and 16.21%, respectively. The *DS1104® DSP* board of *dSPACE* is utilized to generate the reference grid current signals in real-time. The difference of reference and actual grid current signals is applied

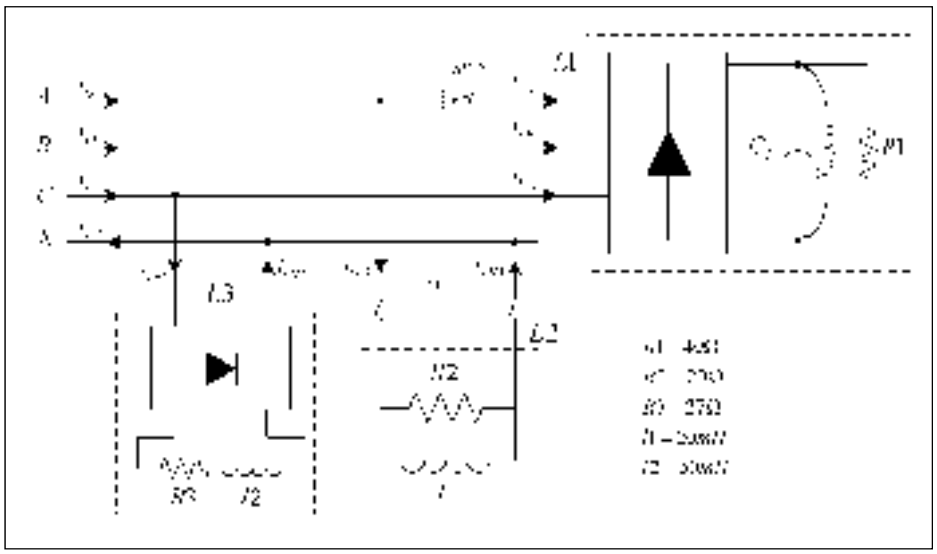

Figure 4.16 Schematic of 3P4W Non-linear Unbalanced Load.

to external hysteresis board to generate the gate pulses for IGBT's. The proposed control approach requires a sampling time of 75 μsec to execute the MATLAB/Simulink generated C-codes in real-time. The experimental results are divided into two different modes of operation in order to highlight the validity of proposed controller. First mode of operation considers a situation when there is no power generation from RES. Under such condition, the grid-interfacing inverter is utilized as shunt APF to enhance the quality of power at PCC. While in second mode of operation, the inverter injects RES active power into grid and also incorporates the active power filtering functionality. The experimental results are given in Fig. 4.17 – Fig. 4.20 All the voltage and current waveforms are captured utilizing an oscilloscope, whereas, the active and reactive powers are captured in real-time using *ControlDesk Developer* environment.

a) Mode -I - Power Quality Enhancement ($P_{RES}=0$): Fig. 4.17 shows the experimental results for active power filtering mode of operation when there is no power generation from RES. All the current waveforms are shown with respective to grid side phase *a* voltage (V_a). Fig. 4.17(a) shows the profile of the unbalance non-linear load currents. The grid current profile, when grid-interfacing inverter controlled as shunt APF, is

shown in Fig. 4.17(b). It can be noticed that the highly unbalanced load currents, after compensation, appear as pure sinusoidal balanced set of currents on grid side. The grid current THD's are reduced to 2.36%, 1.68%, 3.65% for *a*, *b* and *c* phases, respectively. In Fig. 4.17(c), the compensating inverter currents are shown for each phase along with dc-link voltage which is maintained at 100V. Fig. 4.17(d) shows the traces for neutral current of grid, load and inverter. The load neutral current due to single-phase loads is effectively compensated by the 4th leg of inverter such that the current in grid side neutral conductor is reduced to zero.

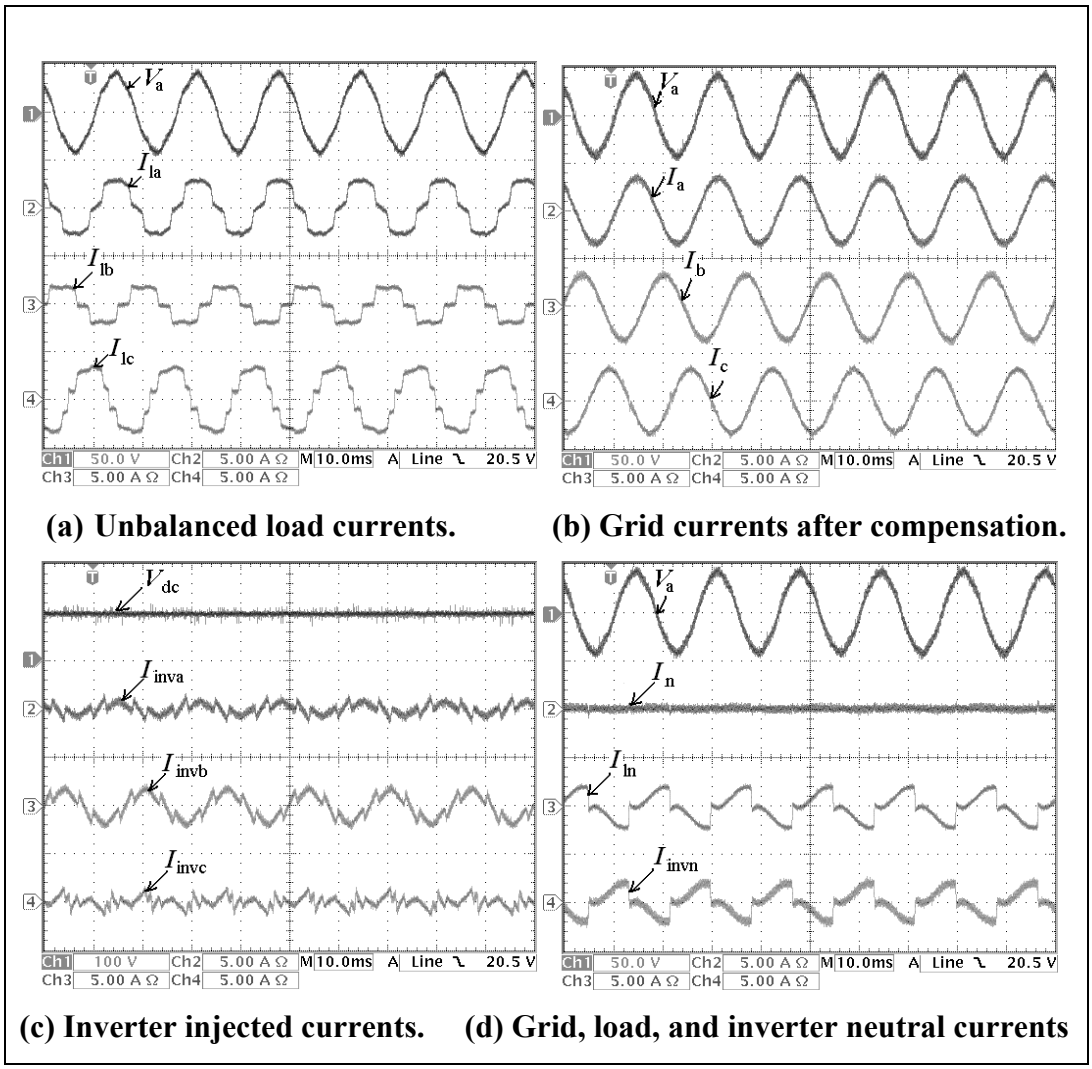

Figure 4.17 Experimental results for the active power filtering mode (P_{RES}=0).

Fig. 4.18 shows the total active and reactive powers of grid, load and inverter. In the APF mode of operation, the inverter consumes a small amount of active power to maintain the dc-link voltage and to overcome the losses associated with inverter, while most of the load reactive power need is supported by inverter effectively. Thus, this mode of operation validates the concept of utilization of grid-interfacing inverter as shunt APF when there is no power generation from the RES. The experimental results demonstrate the effective compensations of load current unbalance, harmonics and reactive power.

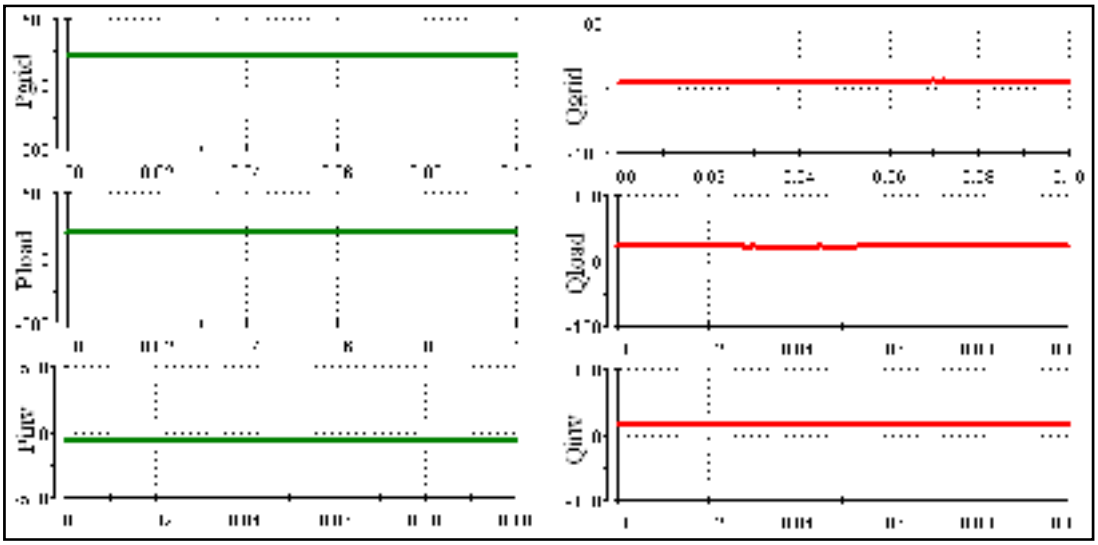

Figure 4.18 Real-time Power flow in active power filtering mode (P_{RES}=0).

b) Mode-II – Simultaneous Power Quality Enhancement and RES Power Injection (P_{RES}>P_L): The experimental results for simultaneous active power filtering and RES power injection mode are shown in Fig. 4.19. In this case study it is considered that the generated power at grid-interfacing inverter is more than the total load power demand. Therefore, after meeting the load power demand, the additional RES power flows towards grid. The profiles of grid, load and inverter currents for individual phases are shown in Fig. 4.19(a), (b) and (c) for phase *a*, *b* and *c*, respectively. As noticed from Fig. 4.19(a) to (c), the inverter currents consist of two components: (*i*) steady-state load

current component and (*ii*) grid active power injection component. Thus the grid-interfacing inverter now provides the entire load power demand (active, reactive and harmonics) locally and feeds the additional active power (sinusoidal and balanced) to the grid. The out-of phase relationship between phase –*a* grid voltage and phase –*a* grid current suggests that this additional power is fed to the grid at UPF. The three-phase grid currents [Fig. 4.19(d)] suggest that the injected active power from RES to the grid is supplied as balanced active power even the load on the system is unbalanced in nature. During both mode of operation, as the load on the system is considered constant, the load neutral current profile and its compensation is identical to the one already discussed in previous subsection and can also be noticed from Figs. 4.17(d) and 4.19(e).

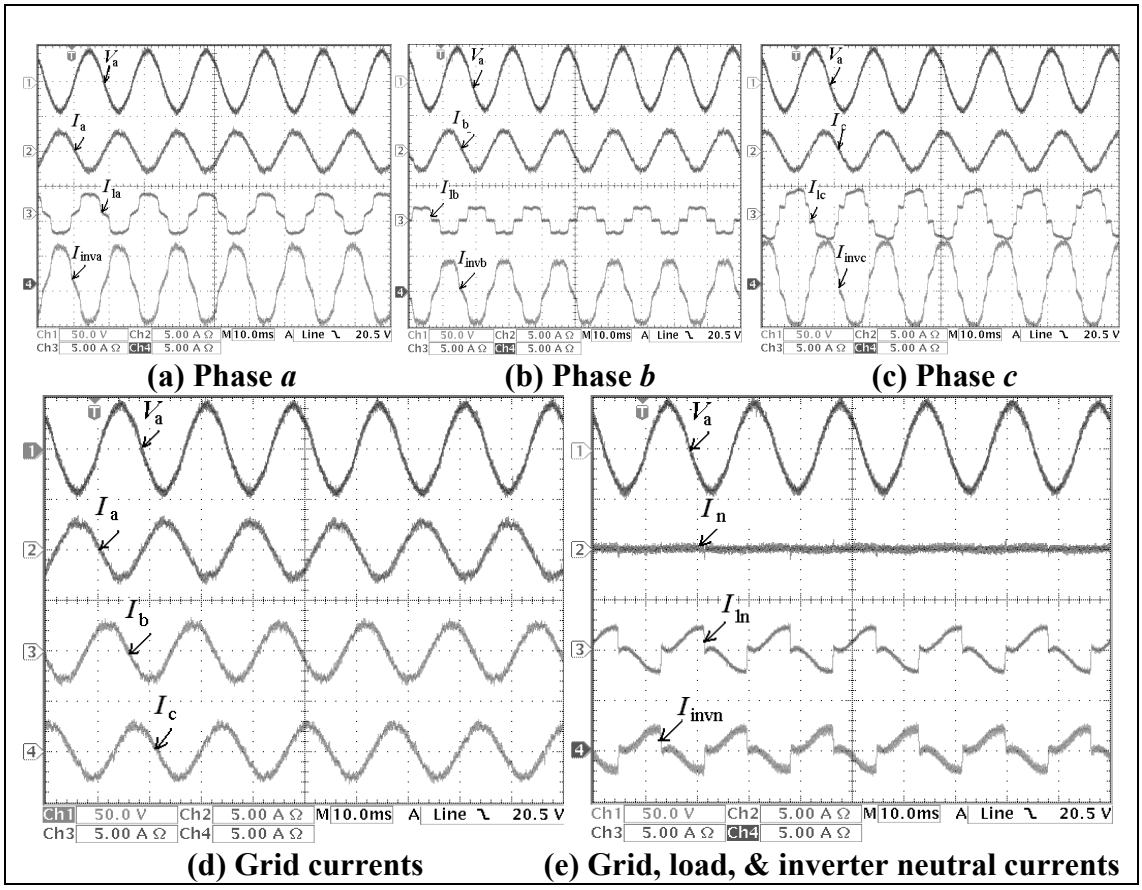

Figure 4.19 Experimental results for the active power filtering and renewable power injection mode (P_{RES}>P_L).

The exchange of total active and reactive powers between grid, load and inverter are shown in Fig. 4.20. The negative sign of total grid side active power suggests that the excess power generated by RES flows towards grid side. Thus, this case study demonstrates that the grid-interfacing inverter can simultaneously be utilized to inject power generated from RES to PCC and to improve the quality of power (current unbalance compensation, current harmonics compensation, load reactive power support, neutral current compensation) at PCC.

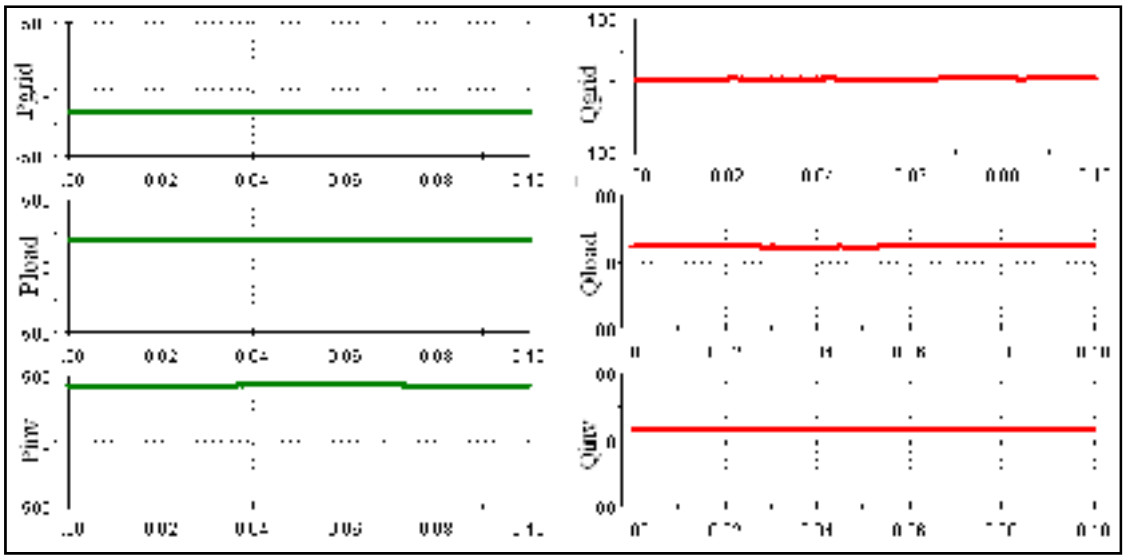

Figure 4.20 Real-time power flow in active power filtering and renewable power injection mode (P_{RES}>P_L).

CHAPTER 5

ANFIS BASED CONTROL ALGORITHMS FOR WECS

5.1 Introduction

The artificial intelligent control algorithms are well known for their ability in handling the non-linearities and uncertainities in a system. They need a simple and less intensive mathematical design for the effective control or modeling of a highly non-linear system with lot of uncertainities. Therefore, the artificial intelligent algorithms can be very advantageous in handling a system like variable speed PMSG based WECS, where the operating conditions change very rapidly due to the intermittent nature of wind. A simple Fuzzy logic controller (FLC) has a narrow operating range and needs much more manual adjustments by trial and error for higher performance. On the other hand, it is extremely difficult to create a series of training data for Artificial Neural Network (ANN) that can perform under different operating conditions. In the recent years, the researchers have tried to combine the advamatges of both FLC and ANN in a new form, known as Neuro-Fuzzy Controllers (NFC). The NFC utilises the linguistic representation of fuzzy sytstem with the learning capability of ANN. However, most of the NFC's use large numbers of membership functions and rule bases, which causes lot of computational burden and hence are not suitable for practical industrial application.

To overcome the limitations of NFC, an adaptive-network-based fuzzy inference system (ANFIS) is used for controlling and parameter estimation purpose. Some of the advantages of ANFIS are fast convergence due to hybrid learning and ability to adjust the shape of input membership functions. It has better tracking and adaptive capabilities than any other controller. The ANFIS generally utilises the Takagi-Sugeno-Kang (TSK) fuzzy rule-based systems, as they require less computations than Mamdani methods (Denai, Palis et Zeghbib, 2004; Jang, 1993).

5.2 ANFIS Architecture

In an ANFIS, as the name indicates, a fuzzy inference system is designed systematically using neural network design methods. This means that if the desired input/output data patterns are available for a fuzzy system, then the membership functions and if & but rule base table can be designed using the neural network training method (Rubaai *et al.*, 2005). Although, both zero-order and first-order Sugeno methods are widely available for ANFIS architecture, here only zero-order Sugeno system will be discussed to understand the principle of ANFIS architecture. Fig. 5.1. shows zero-order Sugeno system, where A_1, A_2, B_1, and B_2 are the triangular membership functions and f_1 and f_2 are the the singleton output membership functions.

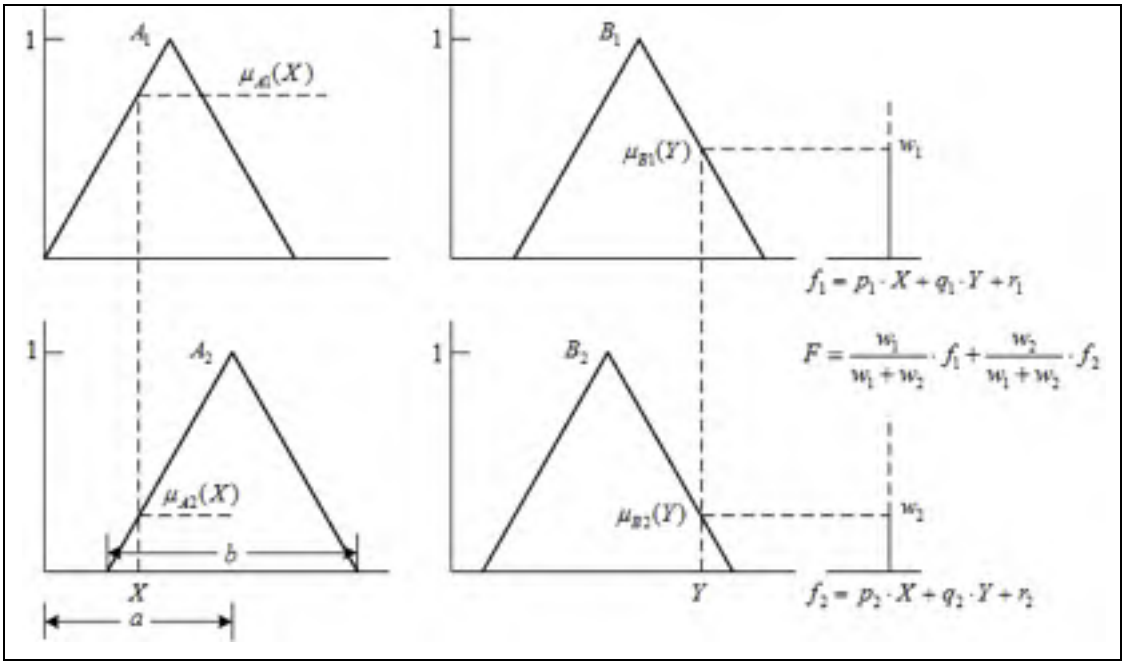

Figure 5.1 Sugeno Fuzzy-Inference System.

For simplicity, we assume that the ANFIS under consideration has two inputs X and Y and one output F. Let's suppose that the rule base contains two fuzzy *if-then* rules of TSK type as given below:

Rule 1: IF X is A_1 AND Y is B_1 THEN $f_1 = p_1 \cdot X + q_1 \cdot Y + r_1$

Rule 2: IF X is A_2 AND Y is B_2 THEN $f_2 = p_2 \cdot X + q_2 \cdot Y + r_2$

The output F can be constructed as:

$$F = \frac{w_1}{w_1 + w_2} \cdot f_1 + \frac{w_1}{w_1 + w_2} \cdot f_2 \tag{5.1}$$

where the parameters set (p_1, p_2, q_1, q_2, r_1, and r_2) are referred as *consequent parameters*, and w_1 and w_2 are the degrees of fulfillment (*DOF*) of *Rule 1* and *Rule 2*, respectively.

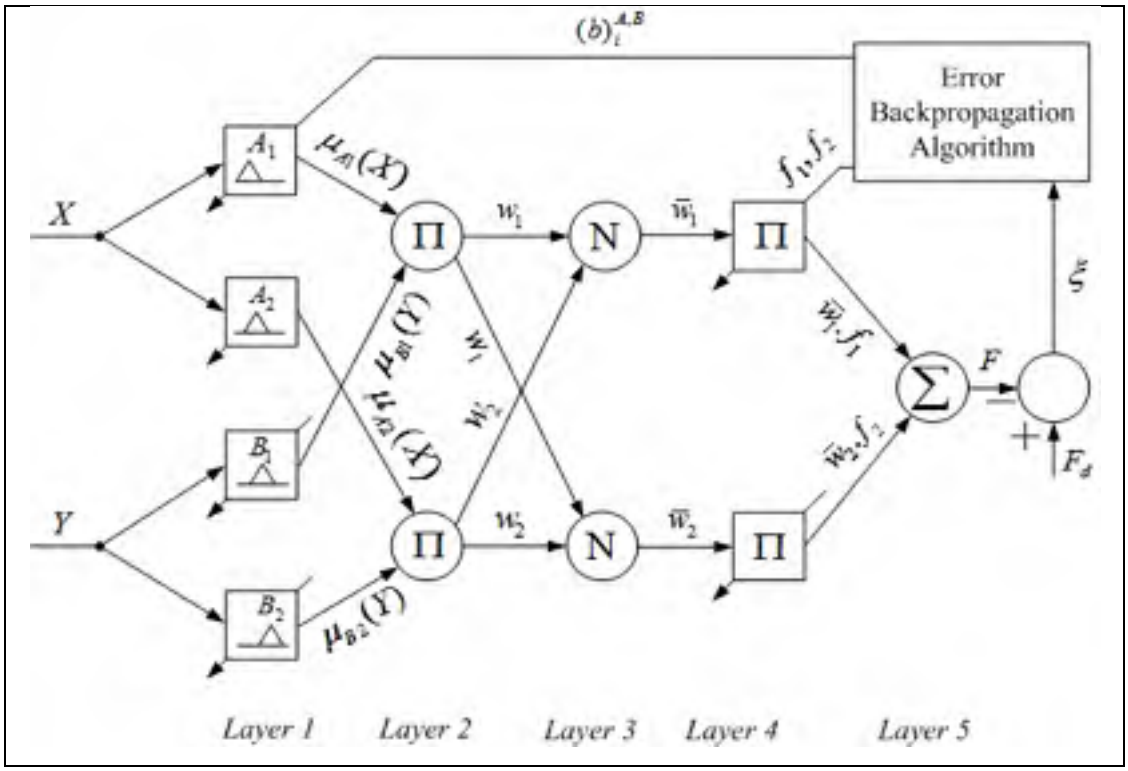

Figure 5.2 ANFIS Architecture.

The corresponding ANFIS architecture is shown in Fig. 5.2, where A_1, A_2, B_1, B_2, f_1 and f_2 are continuosly being tuned by backpropogation algorithm. The feedforward ANFIS architecture has five layers and the node function of each layer is summarised as below:

Layer 1: This layer is also known as fuzzification layer where each node is represented by square. Here, three membership functions are assigned to each input. The triangular membership functions are used to reduce the computation burden as given below:

$$\mu_A(X) = \mu_B(Y) = \begin{cases} 1 - \dfrac{X - a}{0.5b} & |X - a| \le 0.5b \\ 0 & |X - a| \ge 0.5b \end{cases} \tag{5.2}$$

where the value of parameters changes according to the error and accordingly generates the linguistic value of each membership function. Parameters in this layer are referred as *premise parameters* or *precondition parameters*.

Layer 2: Every node in this layer is a circle labeled as Π which multiplies the incoming signals and forwards it to next layer.

$$\begin{cases} w_1 = \mu_{A1}(X).\mu_{B1}(Y) \\ w_2 = \mu_{A2}(X).\mu_{B2}(Y) \end{cases} \tag{5.3}$$

Here, the output of each node represents the firing strength of a rule.

Layer 3: Every node in this layer is represented as circle. This layer calculates the normalized firing strength of each rule as given below:

$$\begin{cases} \overline{w}_1 = \dfrac{w_1}{w_1 + w_2} \\ \overline{w}_2 = \dfrac{w_2}{w_1 + w_2} \end{cases} \tag{5.4}$$

Layer 4: Every node in this layer is a square node with a node function

$$\begin{cases} O_1 = \overline{w}_1 . f_1 = \overline{w}_1 (p_1 \cdot X + q_1 \cdot Y + r_1) \\ O_2 = \overline{w}_2 . f_2 = \overline{w}_2 (p_2 \cdot X + q_2 \cdot Y + r_2) \end{cases} \tag{5.5}$$

where the parameters set (p_1, p_2, q_1, q_2, r_1, and r_2) are referred as *consequent parameters*.

Layer 5: This layer is also called output layer which computes the output as given below:

$$F = \overline{w}_1 . f_1 + \overline{w}_2 . f_2 \tag{5.6}$$

Thus from the proposed ANFIS architecture, it can be observed that for the given values of premise parameters, the overall output can be expressed as a linear combination of the consequent parameters, which can be updated with the help of suitable learning algorithm. For ANFIS architecture, hybrid learning algorithms are used, where the functional signals go forward till *layer 4* and the consequent parameters are updated using least square estimate. In the backward pass, the error rates are propogated backward and the premise parameters are updated by the gradient descent method. The complete leraning algorithm will be discussed in the following sections for different kind of applications.

5.3 ANFIS based Renewable Interfacing Inverter Control

The control of inverter plays an important role in grid interconnection of renewable sources. In the present scenario, the RES are supposed to supply only active power, which may results in to increased grid pollution due to the non-linear unbalance load at PCC as shown in Fig. 5.3. However, with the advancement in power electronics and digital control technology, the RES can now be actively controlled to enhance the system stability with improved power quality at the point of common coupling (PCC) as shown in Fig. 5.4.

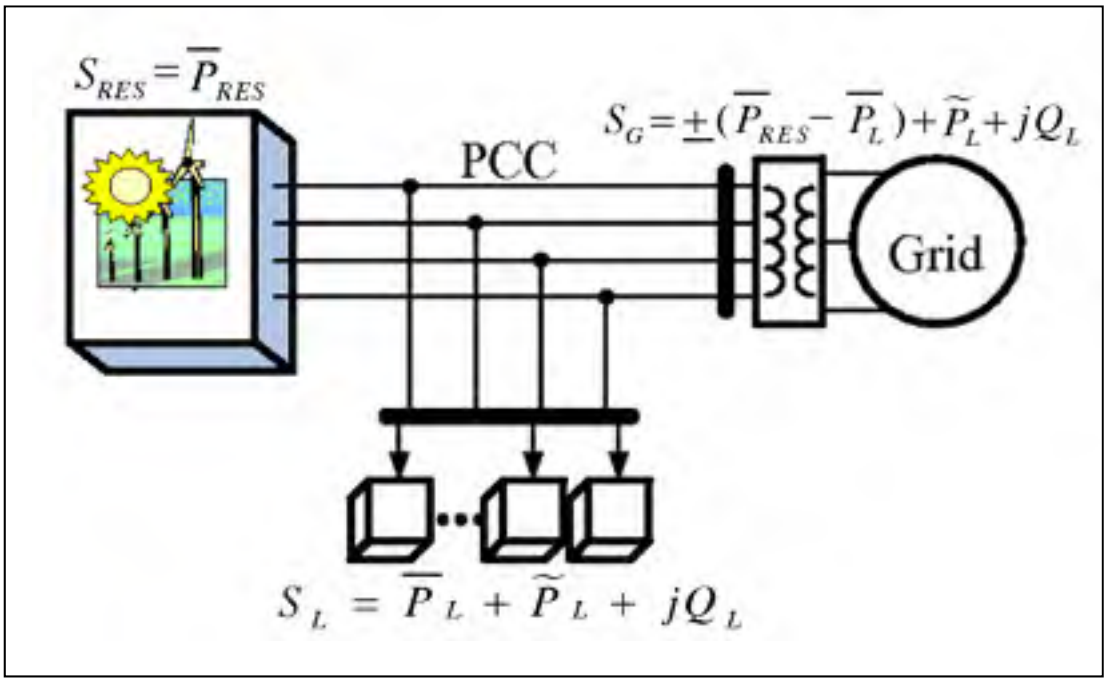

Figure 5.3 RES Supplying Active Power Only.

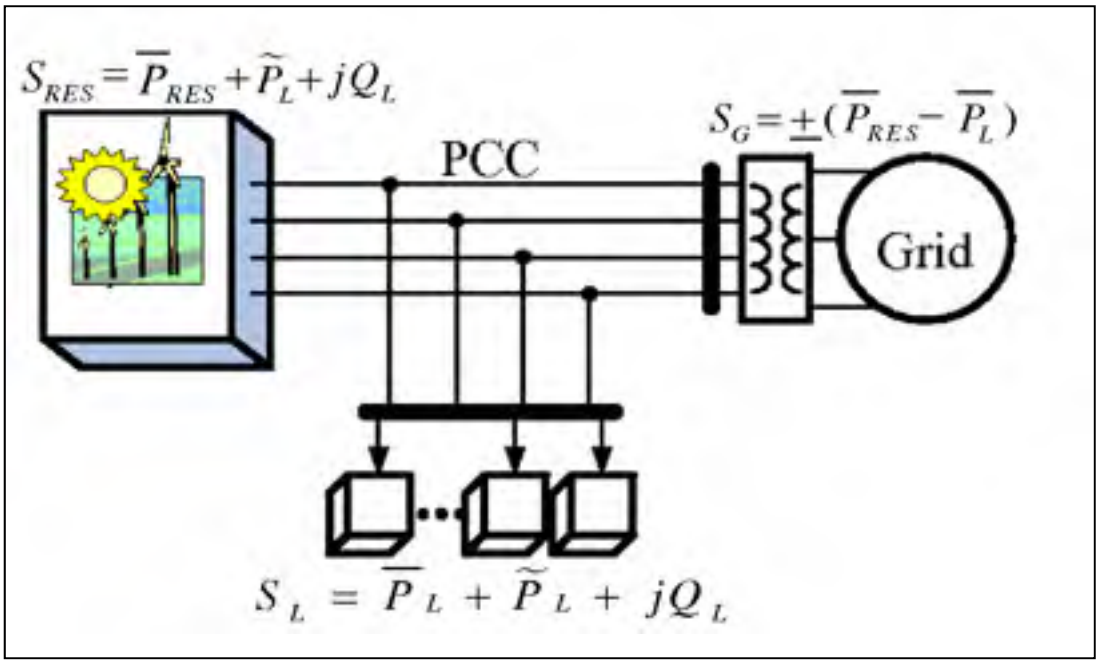

Figure 5.4 RES Supplying Active Power and Non-linear Unbalance Load Demand.

Recently a lot of control strategies for renewable interfacing inverter have been introduced (Blaabjerg *et al.*, 2006; Carrasco *et al.*, 2006; Enslin et Heskes, 2004; Jintakosonwit *et al.*, 2003). Some control strategies for grid connected inverters incorporating power quality solution have also been investigated by researchers. In (Borup, Blaabjerg et Enjeti, 2001) an inverter operates as an active inductor at a certain frequency to absorb the harmonic current. But the exact calculation of network inductance in real time is very difficult and may deteriorate the control performance. A similar approach in which shunt active filter acts as active conductance to damp out the harmonics in distribution network is proposed in (Jintakosonwit *et al.*, 2003). In (Aredes et Watanabe, 1995), a control strategy for renewable interfacing inverter based on *p-q* theory is proposed. A similar decoupled current control technique using PI regulator in d-q ref. frame is presented in (Rahmani *et al.*, 2009). In both of these strategies, the load and inverter current sensing is required to compensate the load current harmonics.

The current regulated voltage source inverters have very wide range of applications such as grid synchronization of RES, static reactive power compensation (STATCOM), UPS, active power filters (APF) and adjustable speed drives (ASD). But in case of very first application, the installed inverter rating have very low utilization factor due to intermittent nature of RES. According to Ref. (Boccard, 2009), the expected RES output during peak is nearly 60% of rated output, yet the annual capacity factor may be in the 20%-30% range. Therefore, the APF features have been incorporated in RES interfacing inverter to maximize its utilization without any additional hardware cost. Moreover, the proposed control strategy does not require the load current sensing. Therefore, only the grid current sensing is used for RES interfacing inverter. It further reduces the cost and complexity. The grid-interfacing inverter injects the generated active power from renewable as well as also compensates the load reactive power, current harmonics and load imbalance in a 3-phase 4-wire system. This enables the grid to always supply a balanced set of sinusoidal currents at unity power factor (UPF).

Since the inverter works under highly fluctuating operating conditions, it is not possible to set the optimal value of gains for the conventional *PI* regulator (Yacoubi *et al.*, 2006). This may lead to false operation of inverter. To alleviate this problem an adaptive neuro-fuzzy controller is developed, which has well known advantages in modeling and control of a highly non-linear system (Hui, Shi et McLaren, 2005; Jang, 1993). The main objective is to achieve smooth bidirectional power flow and non-linear unbalance load compensation simultaneously, where the conventional proportional-integral (*PI*) controller may fail due to the rapid change in the dynamics of the highly non-linear system. The combined capability of neuro-fuzzy controller in handling the uncertainties and learning from the processes is proved to be advantageous while controlling the inverter under fluctuating operating conditions.

5.3.1 System Configuration and Control of Grid Side Inverter

The system under consideration with control description is shown in Fig. 5.5., where a RES is connected on the dc-link of grid interfacing 4-leg inverter. The fourth leg of inverter is utilized to compensate the neutral current of 3-phase 4-wire network. Here the inverter is a key element, since it delivers the power from renewable to grid and also solves the power quality problem arising due to unbalance non-linear load at PCC. The duty ratio of inverter switches are varied in a power cycle such that the combination of load and inverter injected power appears as balanced resistive load to the grid, resulting into the UPF grid operation.

The renewable source may be a DC source or an AC source with rectifier coupled to dc-link. The regulation of dc-link voltage carries the information regarding the exchange of active power in between renewable source and grid. The error between reference dc-link voltage (V_{dc}^{*}) and actual dc-link voltage (V_{dc}) is given to the neuro-fuzzy controller and the same error is used to update the weights. The output of neuro-fuzzy controller is further modified by subtracting the renewable injected current (i_{Ren}). This results in to

the reference d-axis current (i_d^*), while the reference q-axis current (i_q^*) is set to zero for UPF grid operation. The grid synchronizing angle (θ) obtained from phase lock loop (PLL) is used to generate the reference grid currents (i_a^*, i_b^*, and i_c^*). The reference grid neutral current (i_n^*) is set to zero to achieve balanced grid current operation. The hysteresis current controller is utilized to force the actual grid currents to track the reference grid currents accurately. This enables the grid to supply/absorb only the fundamental active power, while the RES interfacing inverter fulfills the unbalance, reactive and non-linear current requirements of 3-phase 4-wire load at PCC.

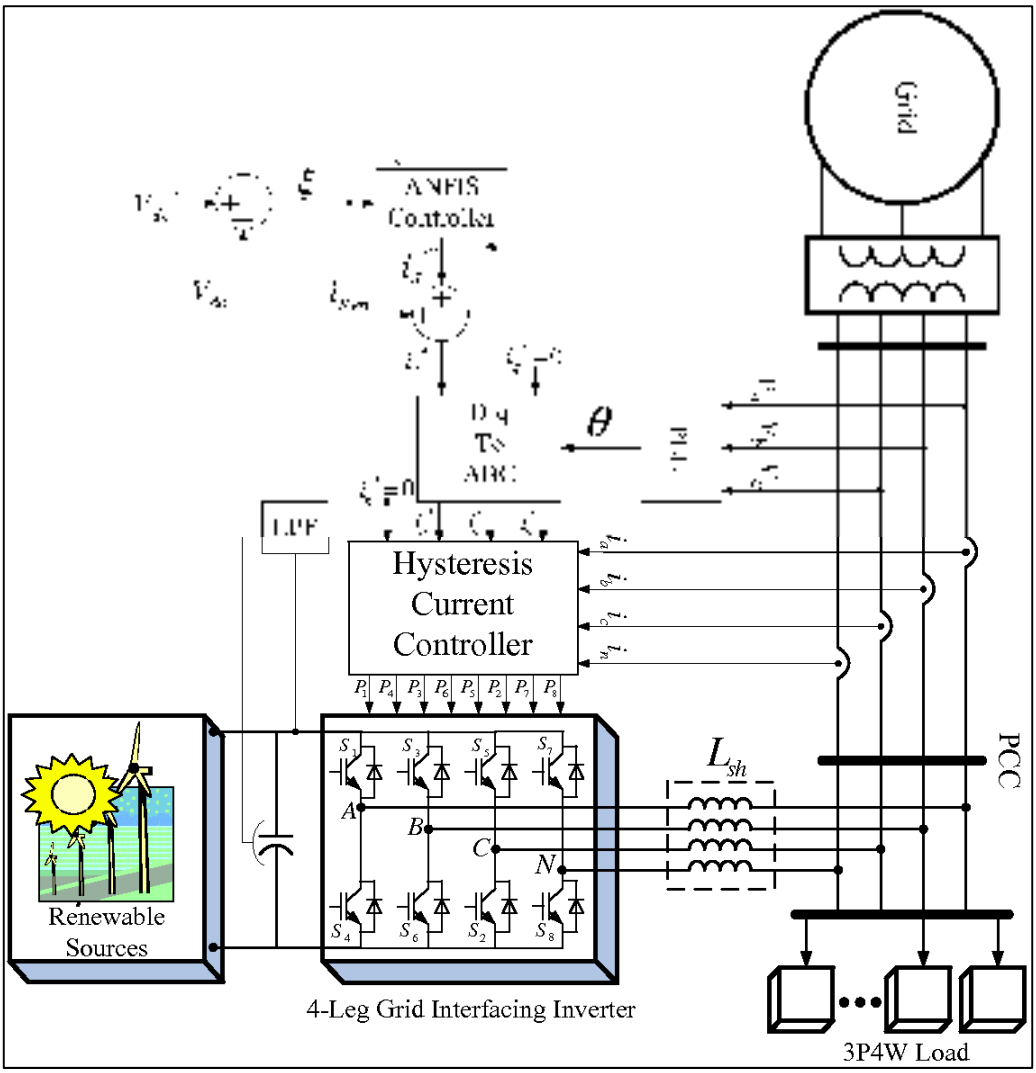

Figure 5.5 Proposed Control Description of RES Interfacing Inverter.

5.3.2 Design of Adaptive Neuro-Fuzzy Controller for Grid Side Inverter

In order to have an idea of optimized ANFIS architecture for proposed control, an initial data is generated from normal *PI* regulator and the data is saved in workspace of MATLAB . Then the ANFIS command window is opened by typing *anfiseditor* in the main MATLAB window. Then the data previously saved in workspace is loaded in the ANFIS command window to generate an optimized ANFIS architecture as shown in Fig. 5.6.

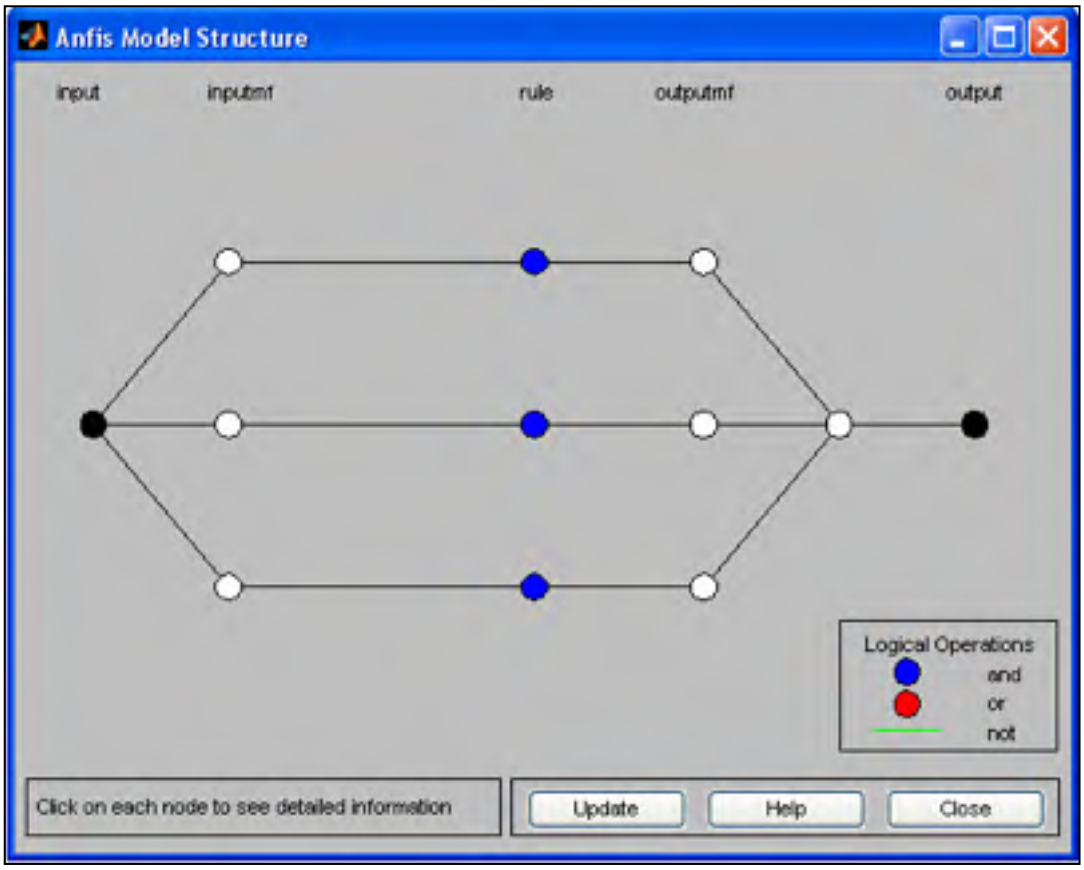

Figure 5.6 Optimized ANFIS architecture suggested by MATLAB/anfiseditor.

This Takagi-Sugeno-Kang (TSK) fuzzy model based ANFIS architecture has one input and one output, which is further tuned online using error backpropagation method as

shown in Fig.5.7. The error between reference dc-link voltage and actual dc-link voltage (ξ=V_{dc}^{*}-V_{dc}) is given to the neuro-fuzzy controller and the same error is used to tune the precondition and consequent parameters. The control of dc-link voltage gives the active power current component ($i_d^{*'}$), which is further modified to take in account of active current component injected from RES (i_{Ren}).The node functions of each layer in ANFIS architecture are as described below:

Layer 1: This layer is also known as fuzzification layer where each node is represented by square. Here, three membership functions are assigned to each input. The trapezoidal and triangular membership functions are used to reduce the computation burden as shown in Fig. 5.8. and their corresponding node equations are as given below:

$$\mu_{A_1}(\xi) = \begin{cases} 1 & \xi \le b_1 \\ \dfrac{\xi - a_1}{b_1 - a_1} & b_1 \langle \xi \langle\ a_1 \\ 0 & \xi \ge a_1 \end{cases} \tag{5.7}$$

$$\mu_{A_2}(\xi) = \begin{cases} 1 - \dfrac{\xi - a_2}{0.5 b_2} & \left|\xi - a_2\right| \le 0.5 b_2 \\ 0 & \left|\xi - a_2\right| \ge 0.5 b_2 \end{cases} \tag{5.8}$$

$$\mu_{A_3}(\xi) = \begin{cases} 0 & \xi \le a_3 \\ \dfrac{\xi - a_3}{b_3 - a_3} & a_3 \langle \xi \langle\ b_3 \\ 1 & \xi \ge b_3 \end{cases} \tag{5.9}$$

where the value of parameters (a_i, b_i) changes with the change in error and accordingly generates the linguistic value of each membership function. Parameters in this layer are referred as *premise parameters* or *precondition parameters*.

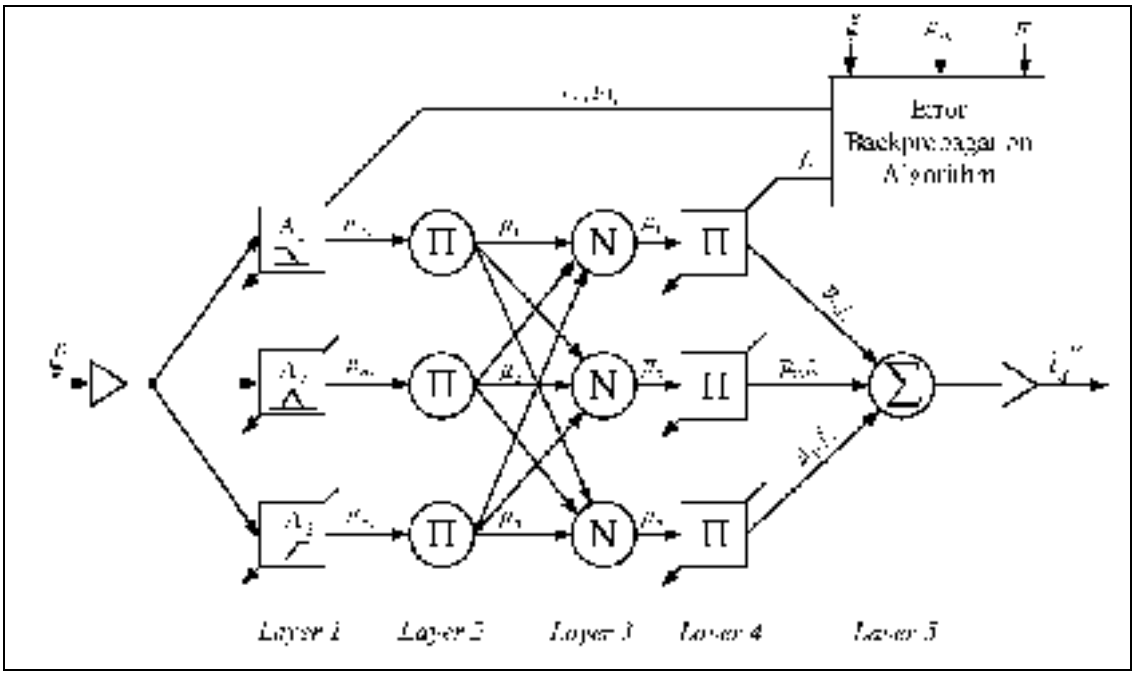

Figure 5.7 Schematic of Proposed ANFIS based control architecture.

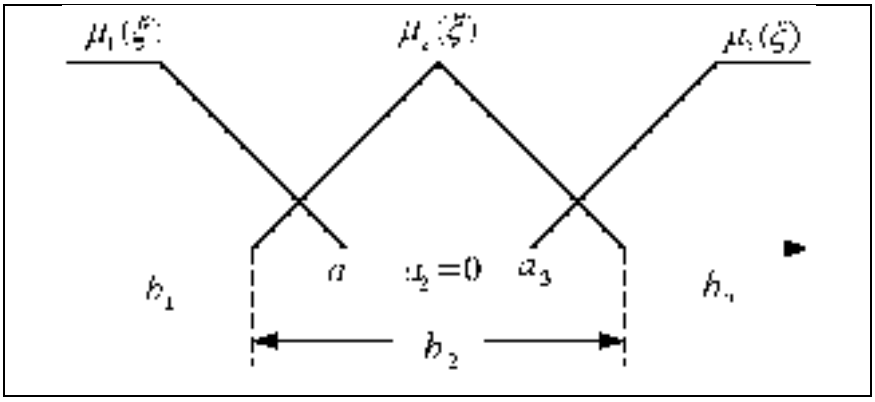

Figure 5.8 Fuzzy Membership Functions.

Layer 2: Every node in this layer is a circle labeled as Π which multiplies the incoming signals and forwards it to next layer.

$$\mu_i = \mu_{A_i}(\xi_1).\mu_{B_i}(\xi_2)...., \qquad i = 1, 2, 3. \tag{5.10}$$

But in our case there is only one input, so this layer can be ignored and the output of first layer will directly pass to the third layer. Here, the output of each node represents the firing strength of a rule.

Layer 3: Every node in this layer is represented as circle. This layer calculates the normalized firing strength of each rule as given below:

$$\overline{\mu}_i = \frac{\mu_i}{\mu_1 + \mu_2 + \mu_3} \qquad i = 1, 2, 3. \tag{5.11}$$

Layer 4: Every node in this layer is a square node with a node function

$$O_i = \overline{\mu}_i . f_i = \overline{\mu}_i (a_0^i + a_1^i . \xi), \qquad i = 1, 2, 3. \tag{5.12}$$

where the parameters (a_0^i, a_1^i) are tuned as the function of input (ξ). The parameters in this layer are also referred as *consequent parameters*.

Layer 5: This layer is also called output layer which computes the output as given below:

$$Y = \overline{\mu}_1 . f_1 + \overline{\mu}_2 . f_2 + \overline{\mu}_3 . f_3 \tag{5.13}$$

The output from this layer is multiplied with the normalizing factor to obtain the active power current component ($i_d^{*'}$).

5.3.3 On-line training of ANFIS Architecture

The ANFIS structure is tuned with gradient descent technique to reduce the error (usually a cost function given by the squared error), where the weights are iterated by propagating the error from output layer to input layer. This backward trip of such a

calculation is termed as “back propagation” (Jang, 1993). The training algorithm is completed in two stages, known as precondition parameter tuning and consequent parameter tuning, where the objective function to be minimized is defined as:

$$\xi^2 = (V_{dc}^{\ *} - V_{dc})^2 \tag{5.14}$$

a) *Precondition parameter tuning:* The Precondition parameters are required to update the fuzzy membership functions as discussed in previous section for *Layer1*. To minimize the error function ξ^2 by gradient descent method, the change in each precondition parameter must be proportional to the rate of change of the error function w.r.t. that particular precondition parameter, i.e.

$$\Delta a_{A_i} = -\eta \frac{\partial \xi^2}{\partial a_{A_i}} \qquad i = 1, 2, 3. \tag{5.15}$$

Where η is the constant of proportionality defined as the learning rate. Therefore, the new value of the consequent parameter is given as

$$a_{A_i}(n+1) = a_{A_i}(n) + \Delta a_{A_i} \qquad i = 1, 2, 3. \tag{5.16}$$

or

$$a_{A_i}(n+1) = a_{A_i}(n) - \eta \frac{\partial \xi^2}{\partial a_{A_i}} \qquad i = 1, 2, 3. \tag{5.17}$$

Now the partial derivative term in equation (5.17) can be found by the chain rule of differentiation as follows:

$$\frac{\partial \xi^2}{\partial a_{A_1}} = \frac{\partial \xi^2}{\partial V_{dc}} \cdot \frac{\partial V_{dc}}{\partial i_d^{\ *'}} \cdot \frac{\partial i_d^{\ *'}}{\partial \overline{\mu}_1} \cdot \frac{\partial \overline{\mu}_1}{\partial \mu_{A_1}} \cdot \frac{\partial \mu_{A_1}}{\partial a_{A_1}} \tag{5.18}$$

where

$$\frac{\partial \xi^2}{\partial V_{dc}} = -2(V_{dc}^{*} - V_{dc}) = -2\xi \quad ; \tag{5.18.a}$$

$$\frac{\partial V_{dc}}{\partial i_d^{*'}} = J \tag{5.18.b}$$

$$i_d^{*'} = \bar{\mu}_1 . f_1 + \bar{\mu}_2 . f_2 + \bar{\mu}_3 . f_3 \Rightarrow \frac{\partial i_d^{*'}}{\partial \bar{\mu}_1} = f_1 ; \tag{5.18.c}$$

$$\bar{\mu}_1 = \frac{\mu_{A_1}}{\mu_{A_1} + \mu_{A_2} + \mu_{A_3}} \Rightarrow \frac{\partial \bar{\mu}_1}{\partial \mu_{A_1}} = \frac{(\bar{\mu}_2 + \bar{\mu}_3)}{\mu_{A_1} + \mu_{A_2} + \mu_{A_3}} ; \tag{5.18.d}$$

$$\mu_{A_1} = \frac{\xi - a_{A_1}}{b_{A_1} - a_{A_1}} \Rightarrow \frac{\partial \mu_{A_1}}{\partial a_{A_1}} = \frac{\mu_{A_1} - 1}{b_{A_1} - a_{A_1}} ; \tag{5.18.e}$$

Where J is jacobian matrix, which can be taken as constant being single input single output ANFIS architecture and can be included in learning rate. On computing all the terms of equation (5.18) and putting in equation (5.17), we can find the updated value of parameter a_{A1} as follows:

$$a_{A_1}(n+1) = a_{A_1}(n) + 2 \cdot \eta \cdot \xi(n) \cdot f_1(n) \cdot \frac{\bar{\mu}_2(n) + \bar{\mu}_3(n)}{\mu_{A_1}(n) + \mu_{A_2}(n) + \mu_{A_3}(n)} \cdot \frac{\mu_{A_1}(n) - 1}{b_{A_1}(n) - a_{A_1}(n)} \tag{5.19}$$

Similarly

$$b_{A_1}(n+1) = b_{A_1}(n) - 2 \cdot \eta \cdot \xi(n) \cdot f_1(n) \cdot \frac{\bar{\mu}_2(n) + \bar{\mu}_3(n)}{\mu_{A_1}(n) + \mu_{A_2}(n) + \mu_{A_3}(n)} \cdot \frac{\mu_{A_1}(n)}{b_{A_1}(n) - a_{A_1}(n)} \tag{5.20}$$

In the same manner, the precondition parameters for the remaining fuzzy membership functions can be derived as follows:

$$b_{A_2}(n+1) = b_{A_2}(n) + 2\cdot\eta\cdot\xi(n)\cdot f_2(n)\cdot\frac{\overline{\mu}_1(n)+\overline{\mu}_3(n)}{\mu_{A_1}(n)+\mu_{A_2}(n)+\mu_{A_3}(n)}\cdot\frac{1-\mu_{A_2}(n)}{b_{A_2}(n)} \quad (5.21)$$

$$a_{A_3}(n+1) = a_{A_3}(n) + 2\cdot\eta\cdot\xi(n)\cdot f_3(n)\cdot\frac{\overline{\mu}_1(n)+\overline{\mu}_2(n)}{\mu_{A_1}(n)+\mu_{A_2}(n)+\mu_{A_3}(n)}\cdot\frac{\mu_{A_3}(n)-1}{b_{A_3}(n)-a_{A_3}(n)} \quad (5.22)$$

$$b_{A_3}(n+1) = b_{A_3}(n) - 2\cdot\eta\cdot\xi(n)\cdot f_3(n)\cdot\frac{\overline{\mu}_1(n)+\overline{\mu}_1(n)}{\mu_{A_1}(n)+\mu_{A_2}(n)+\mu_{A_3}(n)}\cdot\frac{\mu_{A_3}(n)}{b_{A_3}(n)-a_{A_3}(n)} \quad (5.23)$$

b) *Consequent Parameter Tuning:* To tune the consequent parameters as discussed in *Layer 4*, the following updated laws are developed:

$$a_{0_i}(n+1) = a_{0_i}(n) - \eta_c\cdot\frac{\partial\xi^2}{\partial a_{0_i}} \qquad i = 1,2,3. \quad (5.24)$$

$$a_{1_i}(n+1) = a_{1_i}(n) - \eta_c\cdot\frac{\partial\xi^2}{\partial a_{1_i}} \qquad i = 1,2,3. \quad (5.25)$$

where η_c is the learning rate for consequent parameters. The derivative terms in equations (5.24)-(5.25), can be found by the chain rule as already discussed in case of precondition parameters as follows:

$$\frac{\partial\xi^2}{\partial a_{0_i}} = \frac{\partial\xi^2}{\partial V_{dc}}\cdot\frac{\partial V_{dc}}{\partial i_d^{*'}}\cdot\frac{\partial i_d^{*'}}{\partial f_i}\cdot\frac{\partial f_i}{\partial a_{0_i}} \qquad i = 1,2,3. \quad (5.26)$$

$$\frac{\partial\xi^2}{\partial a_{1_i}} = \frac{\partial\xi^2}{\partial V_{dc}}\cdot\frac{\partial V_{dc}}{\partial i_d^{*'}}\cdot\frac{\partial i_d^{*'}}{\partial f_i}\cdot\frac{\partial f_i}{\partial a_{1_i}} \qquad i = 1,2,3. \quad (5.27)$$

In the above equations (5.26)-(5.27), the first two terms on R.H.S. are already known and the last two terms can be derived as:

$$\frac{\partial i_d^{*'}}{\partial f_i} = \frac{\mu_i}{\mu_{A_1} + \mu_{A_2} + \mu_{A_3}} \qquad i = 1, 2, 3. \tag{5.28}$$

$$\frac{\partial f_i}{\partial a_{0_i}} = 1 \qquad i = 1, 2, 3. \tag{5.29}$$

$$\frac{\partial f_i}{\partial a_{1_i}} = \xi \qquad i = 1, 2, 3. \tag{5.30}$$

On substituting the terms derived in equations (5.28)-(5.30) in to the equations (5.26)-(5.27), the updated value of consequent parameters can be derived as follows:

$$a_{0_i}(n+1) = a_{0_i}(n) + 2 \cdot \eta_c \cdot \xi \cdot \frac{\mu_i}{\mu_{A_1} + \mu_{A_2} + \mu_{A_3}} \qquad i = 1, 2, 3. \tag{5.31}$$

$$a_{1_i}(n+1) = a_{1_i}(n) + 2 \cdot \eta_c \cdot \xi \cdot \frac{\mu_i}{\mu_{A_1} + \mu_{A_2} + \mu_{A_3}} \cdot \xi \qquad i = 1, 2, 3. \tag{5.32}$$

5.3.4 Simulation Results and Discussion for Grid Side Inverter

An extensive simulation study has been carried out for renewable interfacing inverter in order to verify the proposed control strategy. The system under consideration is simulated using the *SimPowerSystem* tool box of MATLAB/Simulink. An IGBT based 4-leg current controlled voltage source inverter is actively controlled to achieve the balanced sinusoidal grid currents at unity power factor (UPF) despite of highly unbalanced nonlinear load at PCC under varying renewable generating conditions. A renewable energy source with variable output power is connected on the dc-link of grid-interfacing inverter. An unbalanced 3-phase 4-wire nonlinear variable load, whose harmonics, unbalance and reactive power are to be compensated, is connected on PCC. The waveforms of grid voltage (V), grid current (I), unbalanced load current (I_l) and

injected inverter currents (I_{inv}) are shown in Fig. 5.9. The traces of the corresponding active-reactive powers of grid (P_{grid}, Q_{grid}), load (P_{load}, Q_{load}) and inverter (P_{inv}, Q_{inv}) are shown in Fig. 5.10. Positive values of grid active - reactive powers imply that the grid is absorbing the power, while the positive sign of inverter active-reactive power indicates that it is injecting the power whereas the active and reactive powers absorbed by the load are denoted by positive signs. In Fig. 5.11, the traces of phase *a* grid current (I_a), phase *a* load current (I_{la}), and phase *a* inverter current (I_{inva}) are shown w.r.t. phase *a* grid voltage (V_a). Besides this, the waveforms of grid neutral current (I_n), load neutral current (I_{ln}) and inverter neutral current (I_{invn}) are also shown in the same diagram.

The main purpose of proposed control strategy is to inject the renewable active power, load harmonics and reactive power in such a way that only the injection/absorption of active power takes place with the grid. Initially, the power generated from renewable is more than the load active power demand, so the difference of these is being injected in to the grid. The inverter is also supplying the harmonics, neutral current and reactive power demand of the load simultaneously. This results in to the perfect balanced sinusoidal grid current even in the presence of 3-phase 4-wire unbalance non-linear load at PCC as shown in Fig. 5.9. The corresponding active-reactive power in Fig. 5.10 also shows that after meeting the load active power demand, the balanced active power is being injected to grid. Whereas the load unbalance and reactive power demand is fully supplied from the inverter, resulting in to the balanced grid operation with zero grid side reactive power. This fact can also be visualized from Fig. 5.11, where the phase *a* grid current (I_a) is purely sinusoidal and in phase opposition with the phase-*a* grid voltage (V_a). Here it can also be noticed that load neutral current (I_{ln}) is fully supplied by the inverter neutral current (I_{invn}). This results into the zero value of grid neutral current (I_n).

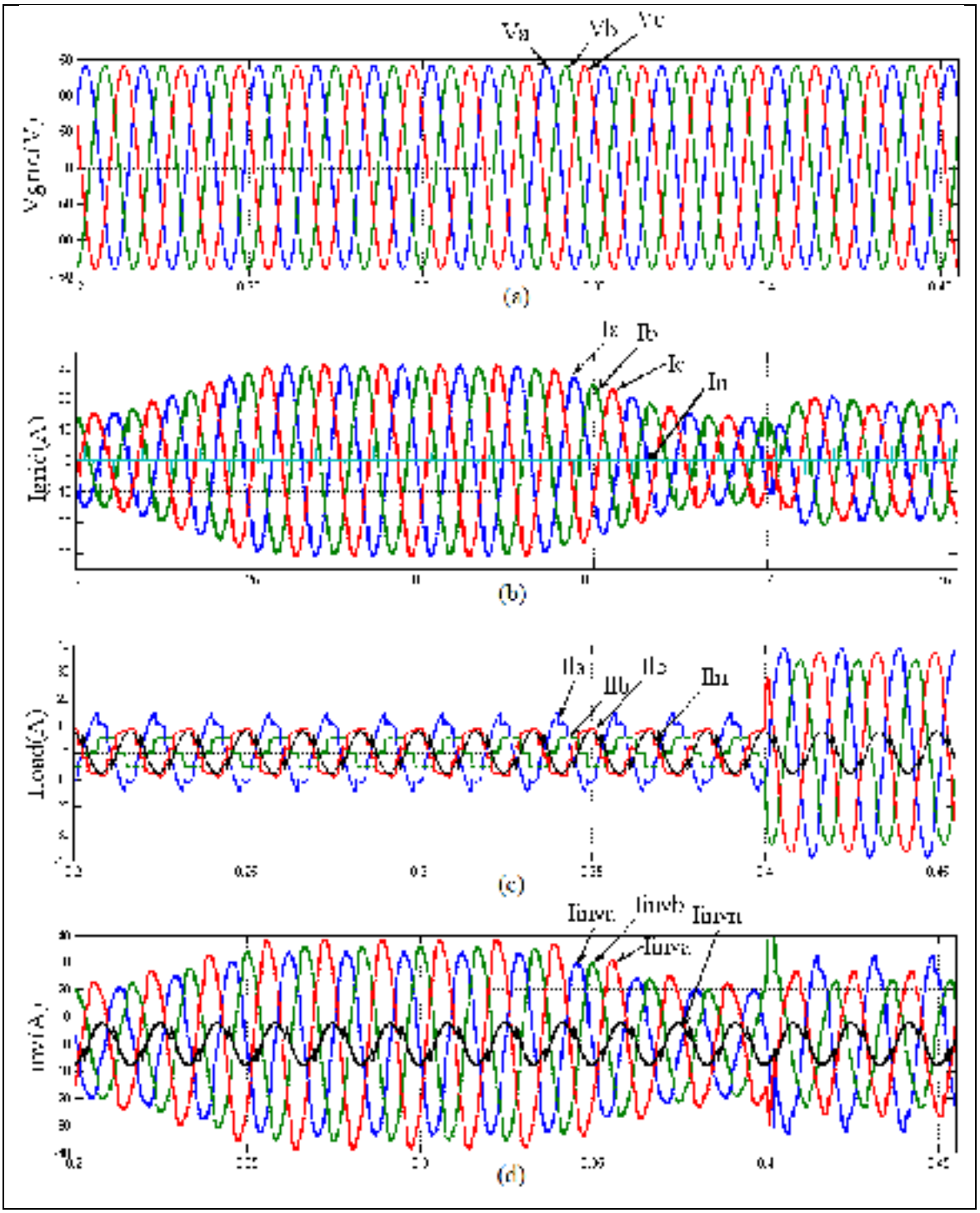

Figure 5.9 Simulation Results for ANFIS Control Based Grid Side Inverter.

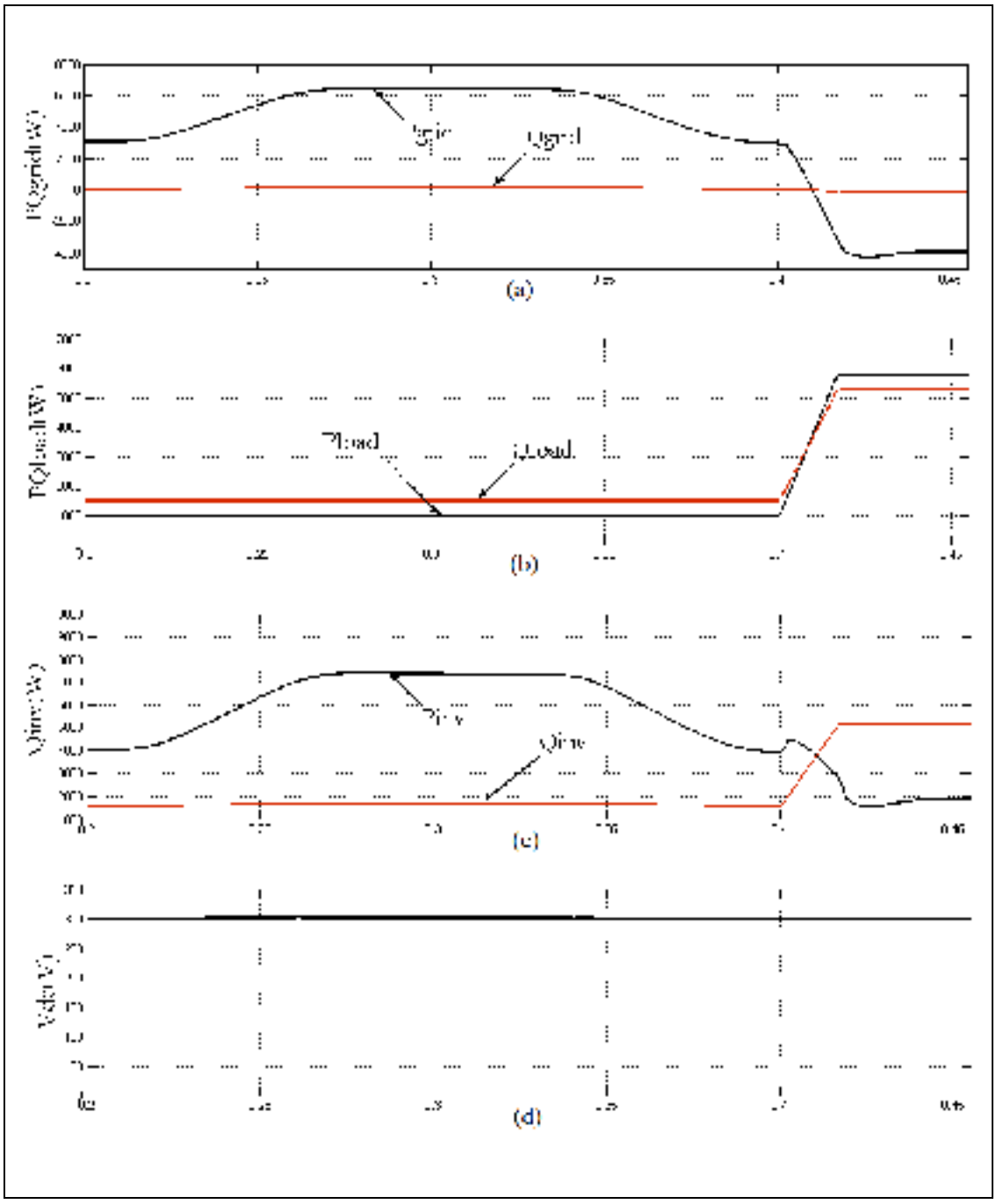

Figure 5.10 Simulation results for Power flow analysis.

At t=0.4 sec, there is sudden increase in the load power demand and the generated renewable active power is not sufficient enough to meet this enhanced demand. At this

instant, the renewable interfacing inverter supplies the generated active power and total load reactive power demand, while the grid supplies only the deficient amount of load active power. This fact can be verified from Fig. 5.11., where the phase *a* grid current was in opposite phase to grid voltage before t=0.4 sec., is now in phase with the grid voltage and the load neutral current is still being supplied from the inverter. Thus, from the simulation results it is clear that the grid always works at UPF under fluctuating renewable power generation and dynamic load conditions with an unbalanced non-linear load at PCC.

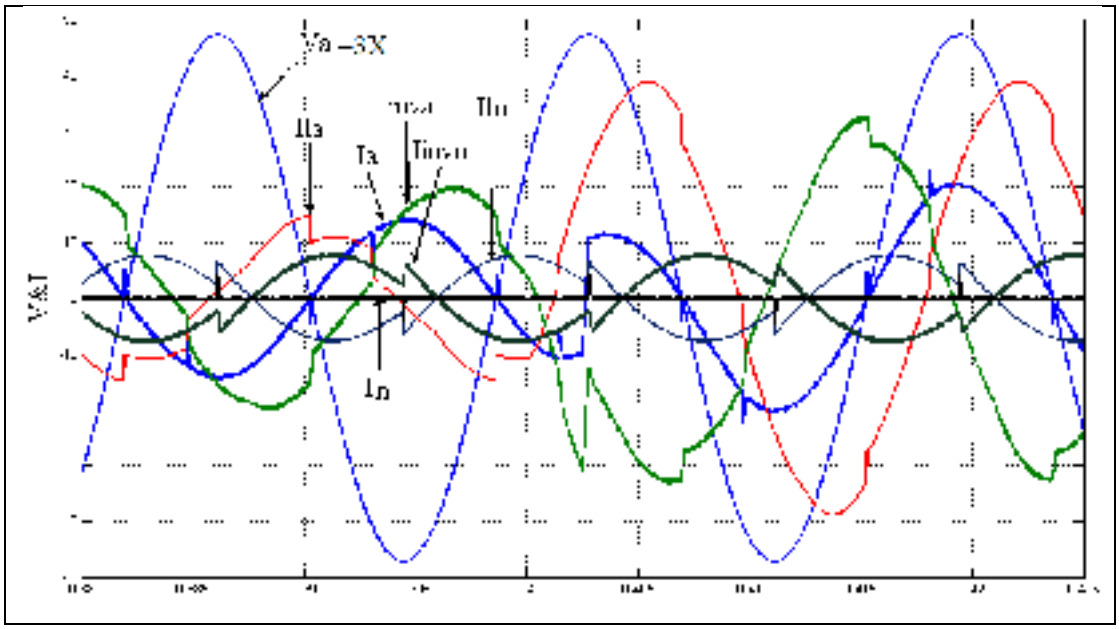

Figure 5.11 Simulation results: Grid, Load, Inverter currents of phase-a and neutral w.r.t. phase-a grid voltage.

5.3.5 Experimental Results and Discussion for ANFIS Based Control of Grid Side Inverter

The proposed Adaptive neuro-fuzzy controller is implemented in real time on 4-leg IGBT based inverter using *dSPACE DS1104*. Whereas the RES is emulated with an auxiliary converter connected on dc-link. It takes a sampling time of *75µsec* to realize

the proposed ANFIS controller in real time. The experimental study is carried out for both 3P3W and 3P4W non-linear load, where 3P3W non-linear load is composed of three phase diode-bridge rectifier with *RL* load, and 3P4W non-linear load composed of three phase diode-bridge rectifier with *RL* load, 1-phase diode-bridge rectifier with *RL* load connected in between phase-a and neutral, and a single phase *RL* load in between phase-b and neutral.

An extensive experimental study is carried out to highlight the performance of inverter as multi-objective device. The inverter operation is mainly divided into two parts: Renewable interfacing operation and active filter operation. All the experimental results are captured with an oscilloscope in real time.

a) Experimental Results for 3P3W Balanced Load:

Active Filtering Mode of Operation: In this mode of operation only active filtering capabilities of inverter are demonstrated. In Fig. 5.12.(a), the traces of 3P3W grid currents are shown before and after compensation w.r.t. phase-a grid voltage. Initially the inverter is not connected in the circuit and the grid has to supply the non-linear load current, which is highly undesirable. Once after the interconnection of inverter in the circuit, the grid supplies only the fundamental active component of load current, while the load current harmonics and reactive current is supplied from inverter side. These facts can be easily identified from Fig. 5.12., where grid current and inverter current profile are shown.

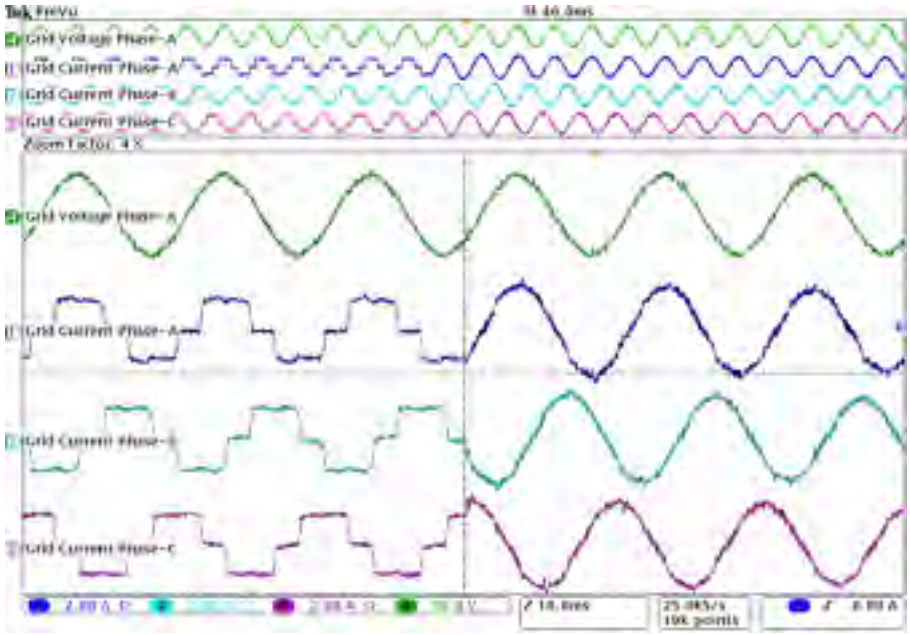

(a) Grid Currents Just Before and After Compensation.

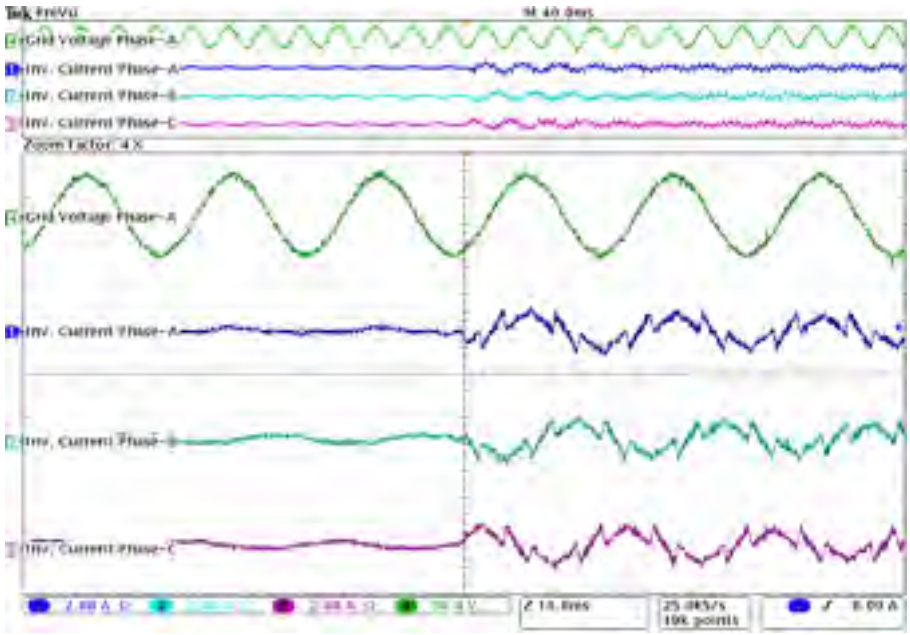

(b) Inverter Currents Just Before and After Compensation.

Figure 5.12 Experimental Results for ANFIS Based Control of Grid Side Inverter in Active Filtering Mode of Operation.

RES Interfacing and Power Filtering Mode of Operation: In this mode of operation, the bidirectional power flow capabilities of renewable interfacing inverter are discussed. Here, the main objective is not only the grid interfacing of renewable, but also to compensate the 3P3W non-linear load at PCC simultaneously. The inverter supplies the renewable injected current and non-linear component of load current. This enables the grid to always supply/absorb only the sinusoidal currents at unity power factor. In Fig. 5.13., the traces of phase-a grid voltage, phase-a grid current, phase-a load current and phase-a inverter current are shown under dynamic condition. When the inverter current supplies the load harmonics and generated active power simultaneously, the corresponding dip in grid current can be noticed, the load current being constant.

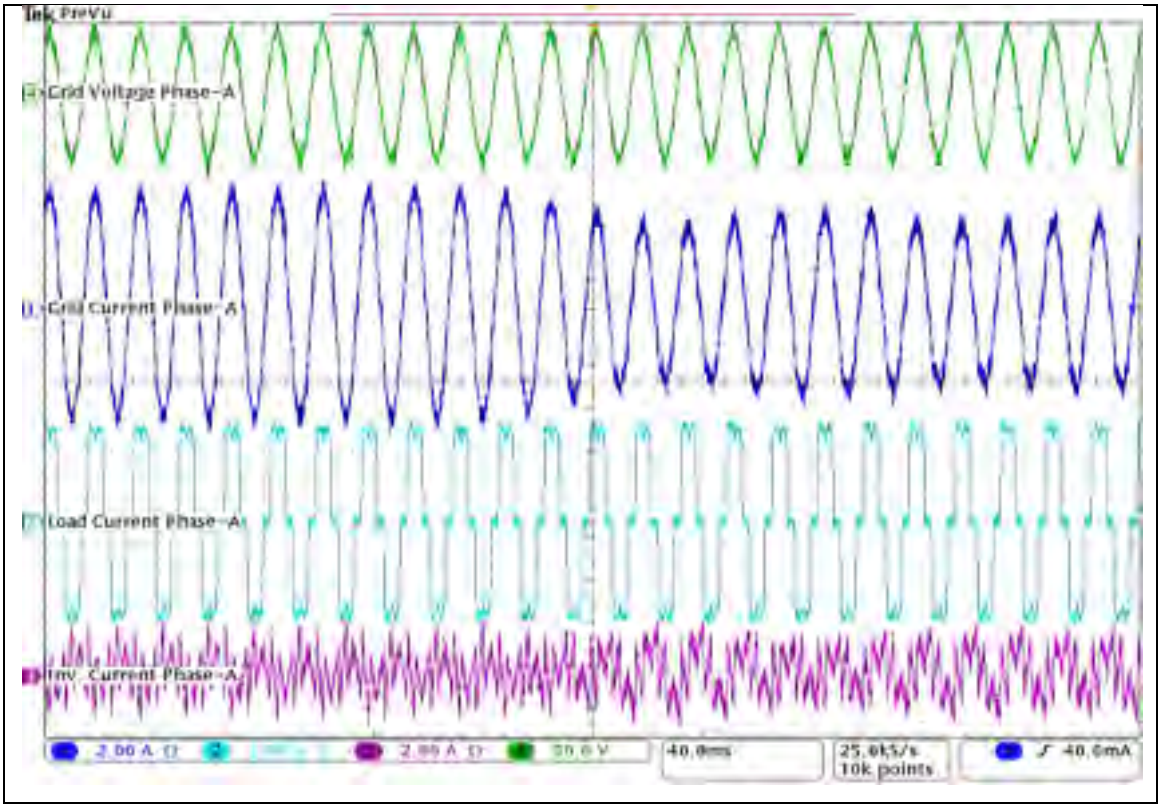

Figure 5.13 Experimental Results under RES Power Injection and Power Filtering Mode Simultaneously with ANFIS Control: Traces of Grid Voltage, Grid Current, Load Current, and Inverter Current in.

b) Experimental Results for 3P4W Unbalanced Non-Linear Load:

Active Filtering Mode of Operation: In this mode of operation only active filtering capabilities of inverter are demonstrated. In Fig. 5.14(a), the traces of 3P4W grid currents are shown before and after compensation. Initially, the grid supplies an unbalanced non-linear load current with a high neutral current, which is highly undesirable. In order to compensate this unbalance non-linear current, the inverter currents are injected in such a way that the combination of load and inverter current appears as a balanced set of fundamental currents. The traces of injected inverter currents are shown in Fig. 5.14(b), just before and after compensation. Here, it can be easily noticed that the grid currents are perfectly balanced with a sinusoidal profile. Moreover, the inverter is successfully able to supply the load neutral current demand locally, as evident from the zero value of grid neutral current (i_{gn}).

RES Interfacing and Power Filtering Mode of Operation: In this mode of operation, the bidirectional power flow capabilities of renewable interfacing inverter are discussed. Here, the main objective is not only the grid interfacing of renewable, but also to compensate the 3P4W non-linear unbalanced load at PCC simultaneously. The inverter supplies the renewable injected current and non-linear unbalance component of load current. This enables the grid to always supply/absorb only the balanced set of currents at unity power factor. In Fig. 5.15, the traces of grid voltage (V_g), grid current (i_g), load current (i_l) and inverter injected current (i_{inv}) are shown in different operating stages. Initially the inverter current is supporting the load current partially and it goes on increasing. At middle stage the inverter current is almost equal to load current and this forces the grid current to be almost zero. In the last stage, the inverter current is more than the load demand and at this stage the grid absorbs this excessive amount of current as evident by the out of phase relationship of grid voltage and current. Similarly, in the last stage, grid current is again shown from supplying to absorption mode and back to supplying mode with the corresponding change in the inverter current.

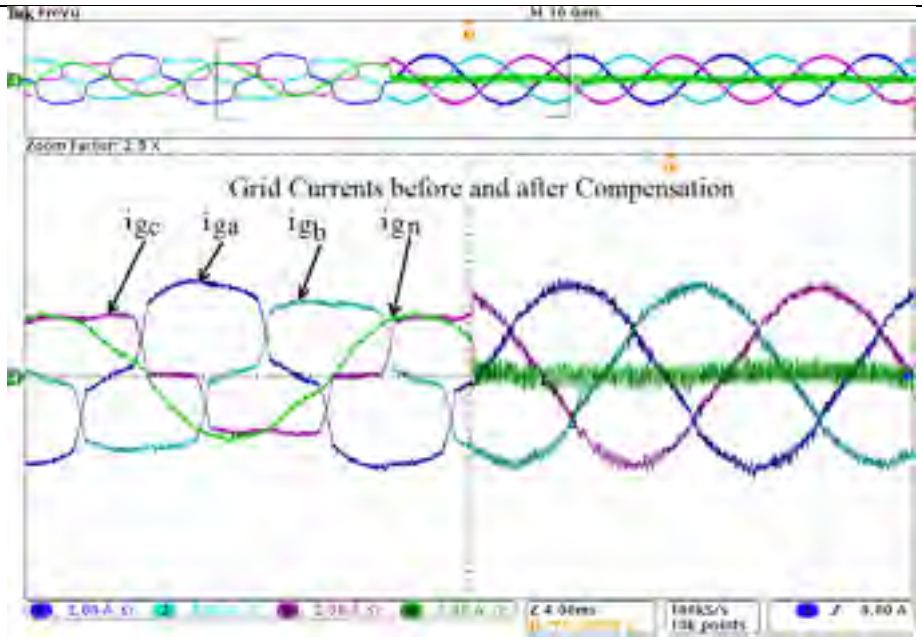

(a) Grid Currents Just Before and After Compensation

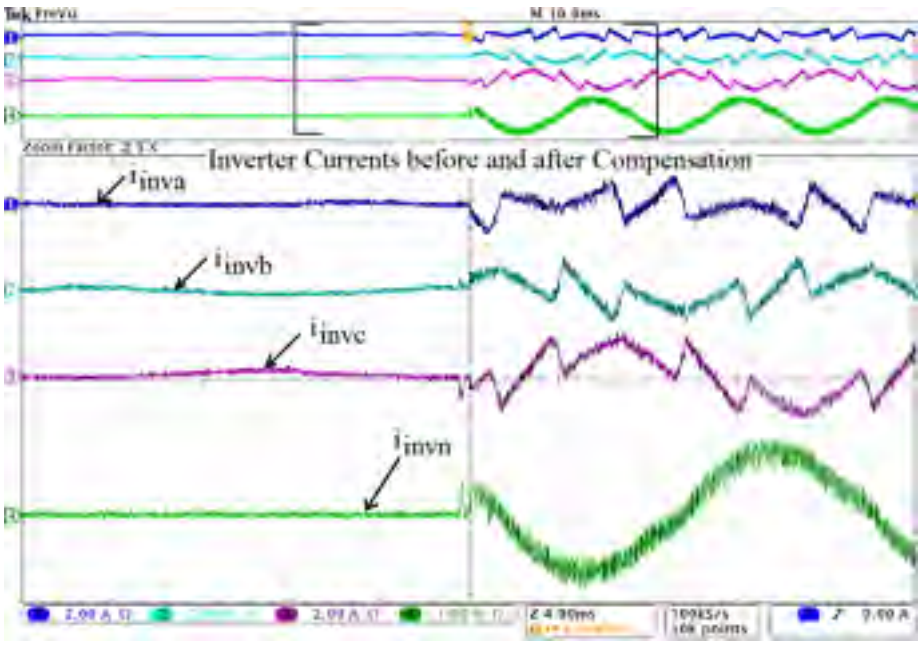

(b) Inverter Currents Just Before and After Compensation

Figure 5.14 Experimental Results for ANFIS Based Control of Grid Side Inverter in Active Filtering Mode of Operation for 3P4W Unbalance Load.

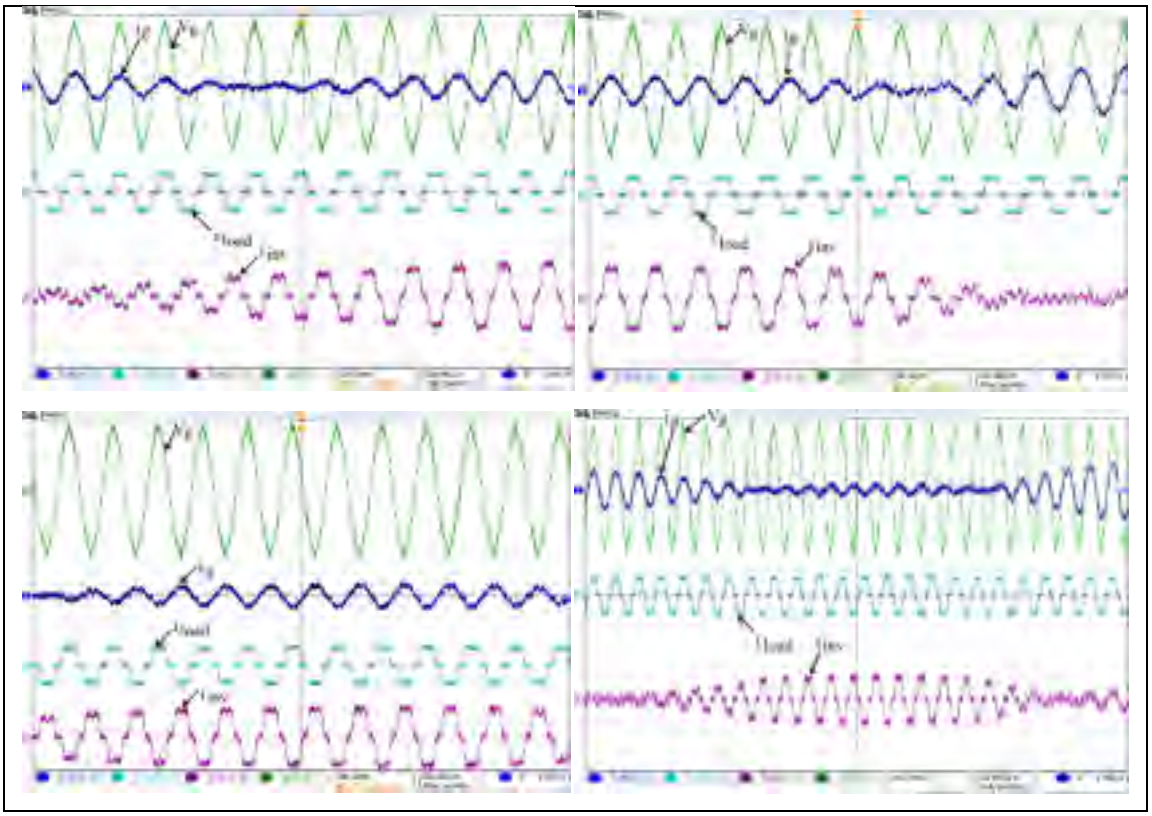

Figure 5.15 Traces of Grid Voltage, Grid Current, Load Current, and Inverter Current in RES Power Injection and Power Filtering Mode Simultaneously.

Table 5.1 Grid current details before and after compensation in APF Mode

Grid Currents	Before Compensation			After Compensation		
	Current (r.m.s.)	% THD	(%) Unbalance Factor	Current (r.m.s.)	% THD	(%) Unbalance Factor
Phase-A	2.96	14.7	20.48	2.74	2.9	0.7
Phase-B	2.47	18.2	0.41	2.72	2.7	0
Phase-C	1.94	23.2	21.07	2.7	2.7	0.7
Neutral	1.1			0		

5.4 Speed & Position Sensorless control of WECS with Power Quality Features.

Since, the maximum power in a wind turbine is almost cubic function of generator speed for a given tip speed ratio, the continuous information of generator position and speed is essentially required for vector control of PMSG to have optimal torque control. For this purpose, generally shaft mounted speed sensors are used, resulting into additional cost and complexity of the system. To avoid the additional sensor cost, complexity and the other associated problems, there has been significant interest in the sensor-less control of PMSG (Acarnley et Watson, 2006; Hui, Shi et McLaren, 2005; Senjyu *et al.*, 2004b; Tan et Islam, 2004). Moreover, the elimination of these sensors and their connecting leads increases the mechanical robustness and reliability of overall system. All these factors have made the sensorless control of PMSG more attractive. But the rotor speed and position estimation typically requires the accurate knowledge of PMSG parameters, which may not be easily available or difficult to obtain, especially under varying weather and operating conditions.

Several rotor speed and position estimation techniques have been reported in literature. In (Boldea, 2008; Taniguchi *et al.*, 2009; Zhiqian *et al.*, 2003), the back-emf based rotor speed estimation is reported. This method works satisfactorily at higher speeds. However, the speed estimation becomes very difficult at lower speeds, due to small and distorted emf signal. Some state observer methods based on Extended Kalman Filter (EKF), Extended Luenburger Observer (ELO), and Sliding Mode Observer etc. have also been reported (Bolognani, Tubiana et Zigliotto, 2003; Peixoto *et al.*, 1995). Most of them suffer due to complex computation, sensitivity to parameter variation and need of accurate initial conditions. However, the EKF has the advantage of estimating the parameters and speed simultaneously by considering them as state, but at the increased cost of computational burden (Maiti, Chakraborty et Sengupta, 2009). The sliding mode observer is simple and offers a limited robustness against the parameter variation. However, sliding mode, being a discontinuous control with variable switching

characteristics, has chattering problems, which may affect the control accuracy. Recently, some more advanced adaptive estimation techniques based on Artificial Neural Network (ANN) and Fuzzy Logic Control (FLC) have also been reported (Batzel et Lee, 2003; Elbuluk, Liu et Husain, 2002; Hamdi, Lachiver et Ghribi, 1995). However, the estimation accuracy depends on number of neurons and number of fuzzy membership functions used for rule base.

To overcome these problems, several indirect methods for maximum power extraction have also been introduced. Bhowmik (Bhowmik et Spee, 1998) has proposed power coefficient polynomial to estimate wind velocity. In this method, an iterative algorithm is employed to determine the roots of a polynomial. As the polynomial may be up to 7^{th} order, the exact calculation of the roots is very complex and time-consuming task. Tan (Tan et Islam, 2004) reported to apply a 2-D look-up table of power coefficient or power-mapping method to estimate the wind velocity. The mapping-power technique may occupy a lot of memory space. If saving the memory space by reducing the size of table, the control accuracy will be affected. Hui Li (Hui, Shi et McLaren, 2005) has also suggested a similar ANN based power co-efficient compensation method.

In the proposed work, a novel ANFIS based position and speed estimator of PMSG has been proposed for wide range of speed operation. The ANFIS architecture has well known advantages of modeling a highly non-linear system, as it combines the capability of fuzzy reasoning in handling uncertainties and capability of ANN in learning from processes (Jang, 1993). Thus, the ANFIS is used to develop an adaptive model of variable speed PMSG under highly uncertain operating conditions, which also automatically compensates any variation in parameters such as inductance, resistance etc. An error gradient based dynamic back propagation method has been used for the on-line tuning of ANFIS architecture. This estimated rotor speed is further utilized to find out the maximum possible power using power-speed characteristic of PMSG. An IGBT based rectifier is utilized to implement the proposed control strategy.

Moreover, in the proposed work, the power quality improvement features are also incorporated in the grid side inverter as discussed in section 5.3. Normally, the grid interfacing inverter has very low utilization factor 20-30 % with a possible peak of 60% of rated output due to the intermittent nature of wind (Boccard, 2009). Therefore, if the same inverter is utilized for solving power quality problem at PCC in addition to its normal task, then the additional hardware cost for custom power devices like APF, STATCOM or VAR compensator can be saved. Thus, a very simple and cost effective solution is proposed by using the grid side inverter as a load harmonics, load reactive power and load unbalance compensator of a 3P4W non-linear unbalanced load at PCC in a distribution network, in addition to its normal task of wind power injection in to the grid.

5.4.1 System Description and Control

The proposed system consists of a PMSG based variable speed WECS consisting two back to back inverters with a common dc-link. The generator side inverter controls its speed to extract maximum power at different speeds, while the grid side inverter delivers the renewable power to grid with 3P4W non-linear load compensation simultaneously. The block diagram of proposed variable speed WECS is shown in Fig.5.16.

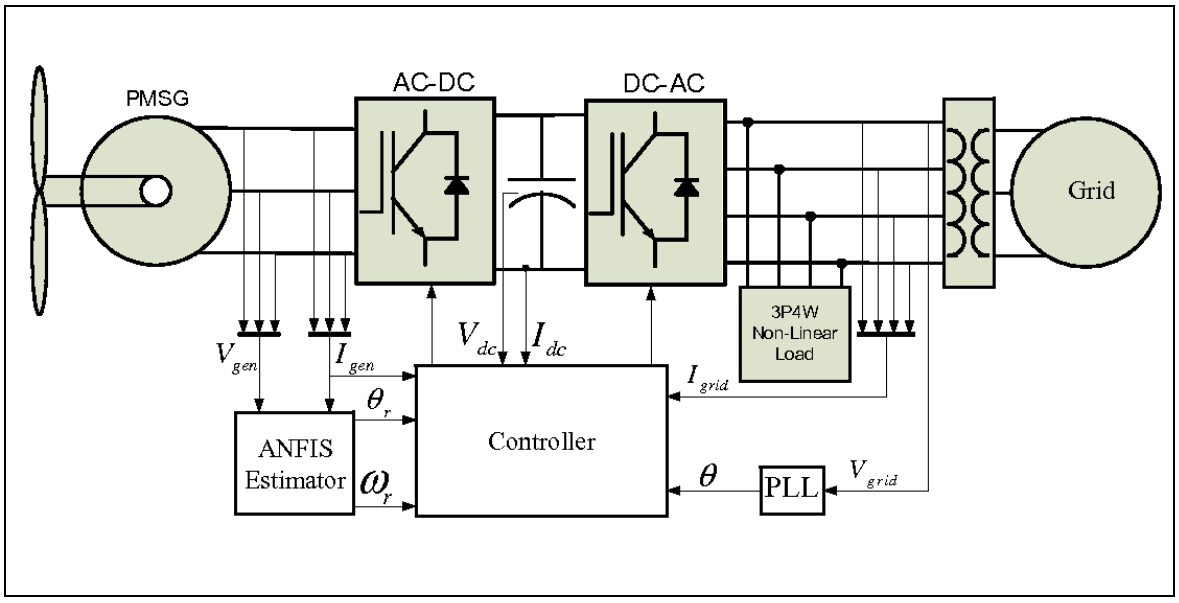

Figure 5.16 Block Diagram of Proposed System.

5.4.2 Speed & Position Estimation of PMSG and Control

The information about generator position and speed is very essential for optimal control of PMSG, in order to extract maximum power at different wind velocity. However, due to non-ideal rotor flux distribution, parameter variation and rapidly changing operating conditions, it is extremely difficult to reproduce the exact model of PMSG for control purpose. Therefore, in order to reject any such kind of external disturbances, an adaptive model is continuously tuned in parallel of PMSG with the help of ANFIS structure. The complete schematic diagram of proposed system is shown in Fig. 5.17.

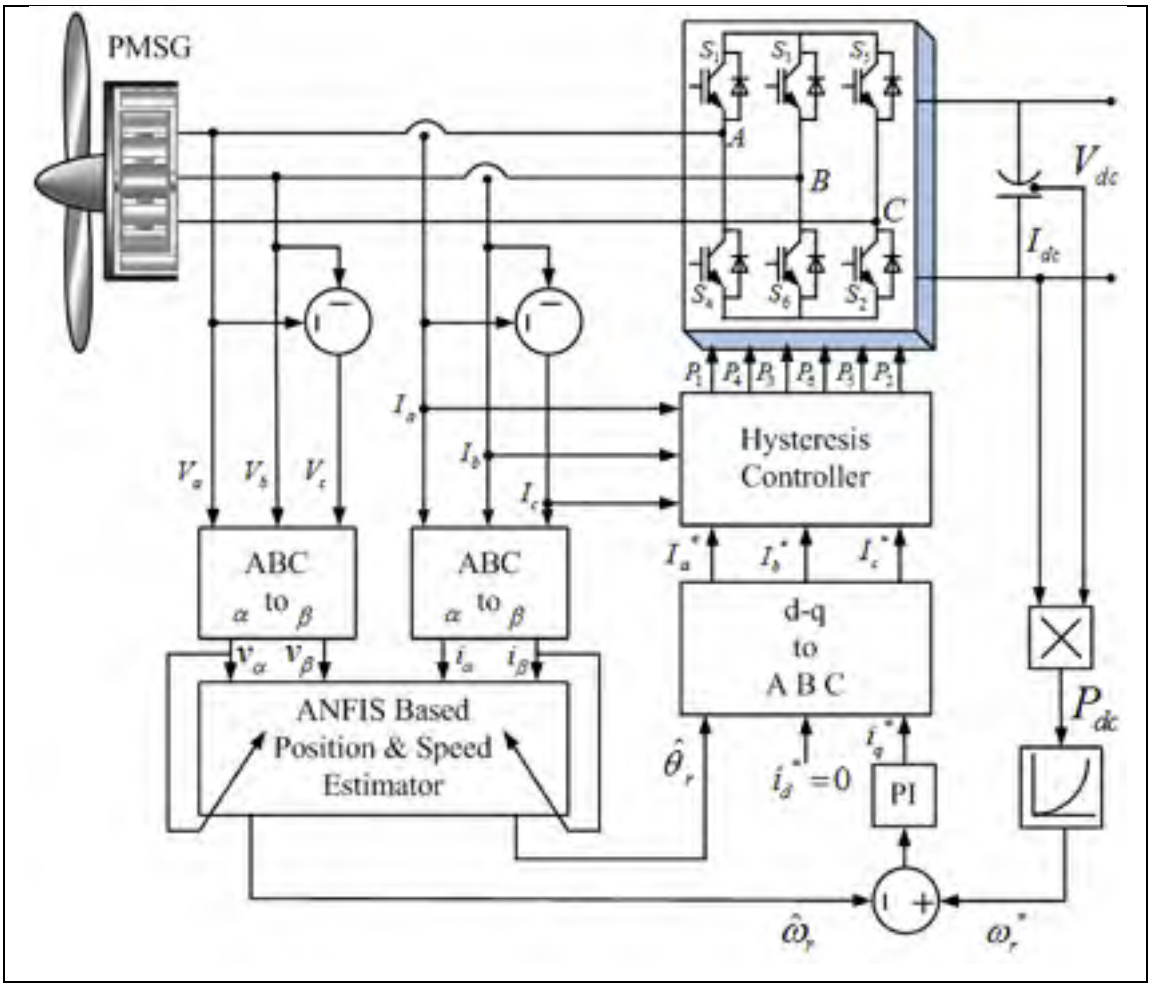

Figure 5.17 Generator Side Control Diagram.

a) Modeling of PMSG in Stationary Reference Frame: Since the back-emf is the function of rotor position in stationary reference frame, therefore, it is convenient to model PMSG in this frame. The voltage equations of PMSG are as given below:

$$V_\alpha = -R_s i_\alpha - L_s \frac{di_\alpha}{dt} + E_\alpha \tag{5.33}$$

$$V_\beta = -R_s i_\beta - L_s \frac{di_\beta}{dt} + E_\beta \tag{5.34}$$

Where $V_{\alpha\beta}$ are stator terminal voltages, R_s is stator resistance, L_s is stator inductance, $i_{\alpha\beta}$ are output currents and $E_{\alpha\beta}$ are back-emf.'s which can be given as:

$$E_{\alpha\beta} = \begin{bmatrix} E_\alpha \\ E_\beta \end{bmatrix} = \omega_r \lambda_m \begin{bmatrix} -\sin(\theta_r) \\ \cos(\theta_r) \end{bmatrix} \tag{5.35}$$

Here ω_r, θ_r and λ_m are rotor speed, rotor position and magnetic flux linkage respectively. On rearranging the equations (5.33) & (5.34) and re-writing them in matrix form, we have

$$\begin{bmatrix} \dot{i}_\alpha \\ \dot{i}_\beta \end{bmatrix} = \begin{bmatrix} -R_s/L_s & 0 \\ 0 & -R_s/L_s \end{bmatrix} \begin{bmatrix} i_\alpha \\ i_\beta \end{bmatrix} + \begin{bmatrix} -1/L_s & 0 \\ 0 & -1/L_s \end{bmatrix} \left(\begin{bmatrix} V_\alpha \\ V_\beta \end{bmatrix} - \begin{bmatrix} E_\alpha \\ E_\beta \end{bmatrix} \right) \tag{5.36}$$

Using the same structure for adaptive model, the current estimator can be designed as given below:

$$\dot{\hat{i}}_{\alpha\beta} = A.\hat{i}_{\alpha\beta} + B.(V_{\alpha\beta} - \hat{E}_{\alpha\beta}) \tag{5.37}$$

Where the cap '^' indicates the estimated variables and

$$A = \begin{bmatrix} -R_s/L_s & 0 \\ 0 & -R_s/L_s \end{bmatrix}; \qquad B = \begin{bmatrix} -1/L_s & 0 \\ 0 & -1/L_s \end{bmatrix}; \qquad \dot{\hat{i}}_{\alpha\beta} = \begin{bmatrix} \dot{\hat{i}}_\alpha \\ \dot{\hat{i}}_\beta \end{bmatrix};$$

$$\hat{i}_{\alpha\beta} = \begin{bmatrix} \hat{i}_\alpha \\ \hat{i}_\beta \end{bmatrix}; \qquad V_{\alpha\beta} = \begin{bmatrix} V_\alpha \\ V_\beta \end{bmatrix}; \qquad \text{and } \hat{E}_{\alpha\beta} = \begin{bmatrix} \hat{E}_\alpha \\ \hat{E}_\beta \end{bmatrix}$$

The state space equivalent diagram of equation (5.37) is shown in Fig. 5.18.

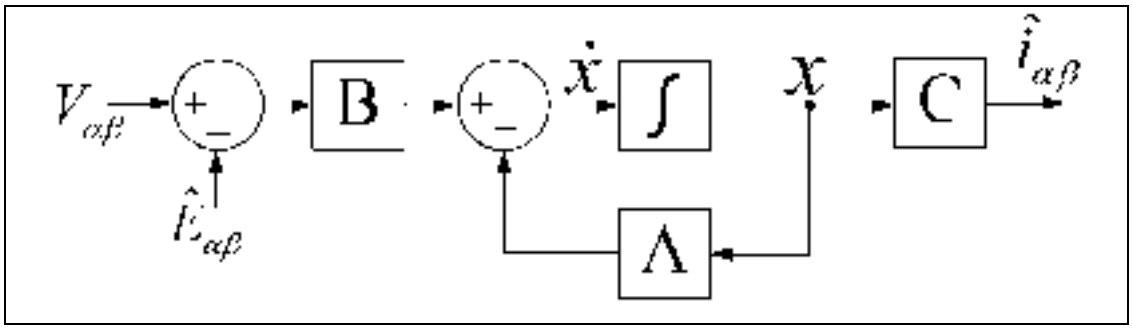

Figure 5.18 State Space Model of PMSG.

b) ANFIS Based Adaptive Model of PMSG: Since the system is highly non-linear and working under different operating conditions, it is extremely difficult to estimate the exact value of back e.m.f., which also carries the information about the rotor position and speed. To encounter this problem, an ANFIS based dynamic model of PMSG is developed. For ANFIS training, the explicit mathematical model of system is not required. Only the order of the system with adequate input/output data from actual system is needed to develop its adaptive model (Jang, 1993). The target output from the actual plant is compared with the output of ANFIS based dynamic model in parallel and error is used to update the weights. In the proposed work, the dynamic model is continuously tuned by forcing its estimated currents to track the actual currents of PMSG using ANFIS structure with dynamic back propagation method. Once the estimated currents are equal to actual currents, the adaptive model exactly represents the real model irrespective of any kind of parameter variations and external disturbances. This results in to the accurate estimation of back e.m.f's as given below:

$$\hat{E}_{\alpha\beta} = \begin{bmatrix} \hat{E}_{\alpha} \\ \hat{E}_{\beta} \end{bmatrix} = \hat{\omega}_r \lambda_m \begin{bmatrix} -\sin(\hat{\theta}_r) \\ \cos(\hat{\theta}_r) \end{bmatrix} \tag{5.38}$$

Now the position and speed can be easily estimated using the estimated value of back e.m.f.'s as

$\hat{\theta}_r = -\tan^{-1}\left(\frac{\hat{E}_\alpha}{\hat{E}_\beta}\right)$ and $\hat{\omega}_r = \frac{1}{p}\frac{d\hat{\theta}_r}{dt}$; Where p is the number of pole pairs. The estimated back e.m.f's are passed through low-pass filter to avoid the noise. The schematic diagram of rotor position and speed estimation is shown in Fig. 5.19.

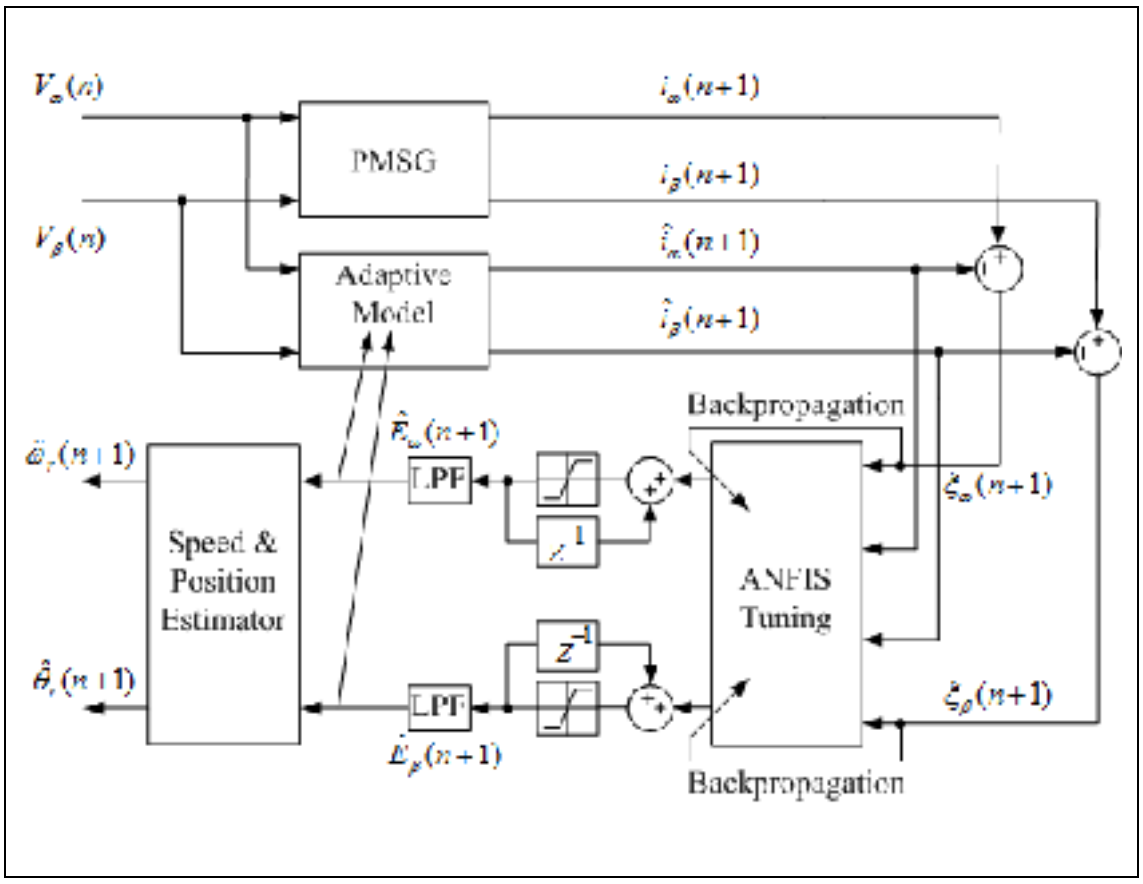

Figure 5.19 ANFIS Based Adaptive Model of PMSG.

c) ANFIS Architecture for Speed and Position Estimation: An ANFIS based on Takagi-Sugeno-Kang (TSK) method having 2 : 6 : 3 : 3 : 2 architecture with two inputs (estimated currents $\hat{i}_\alpha$ and $\hat{i}_\beta$) and two outputs (estimated back e.m.f.'s $\hat{E}_\alpha$ and $\hat{E}_\beta$) is used to develop the dynamic model of PMSG. The errors between the actual and estimated currents ($\xi_{\alpha\beta} = i_{\alpha\beta} - \hat{i}_{\alpha\beta}$) are used to tune the precondition and consequent

parameters. The diagram of ANFIS architecture is shown in Fig. 5.20 and the node functions of each layer are as described below:

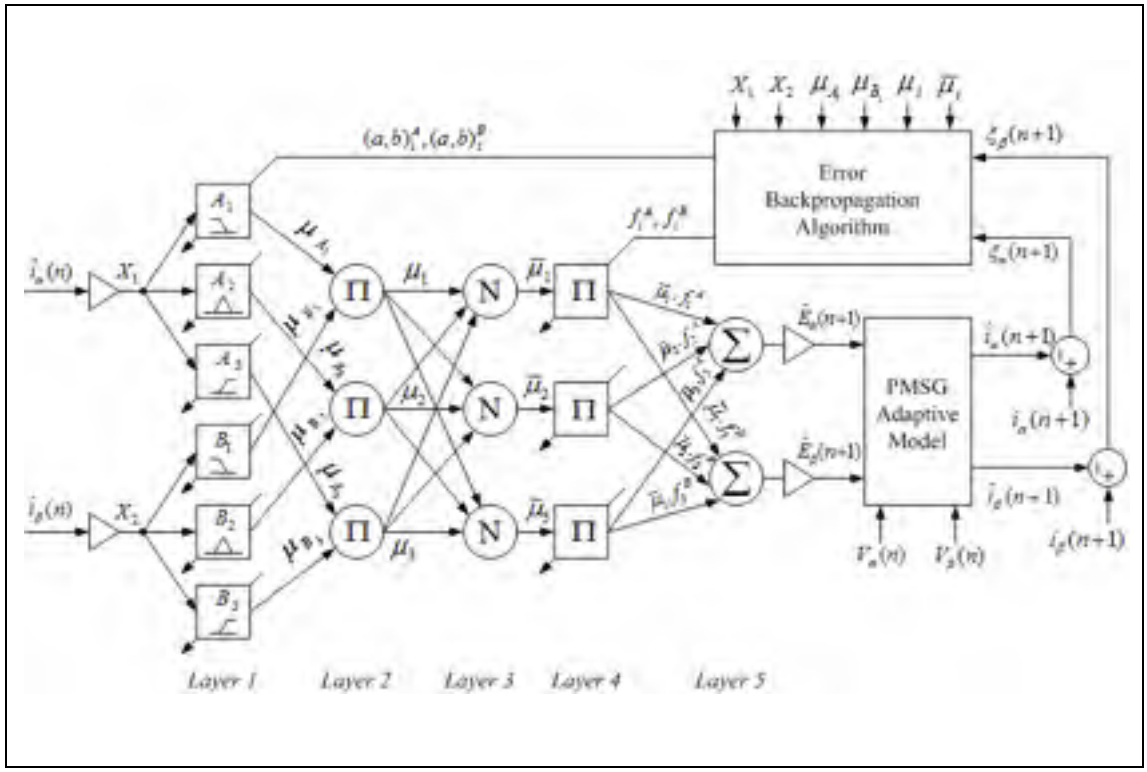

Figure 5.20 ANFIS Architecture for Speed and Position Estimation.

Layer 1: This layer is also known as fuzzification layer where each node is represented by square. Here, three membership functions are assigned to each input. The trapezoidal and triangular membership functions are used to reduce the computation burden as shown in Fig. 5.8 and their corresponding node equations are as given below:

$$\mu_{A_1}(X_\alpha) = \mu_{B_1}(X_\beta) = \begin{cases} 1 & X \le b_1 \\ \dfrac{X - a_1}{b_1 - a_1} & b_1 \langle X \langle\ a_1 \\ 0 & X \ge a_1 \end{cases} \tag{5.39}$$

$$\mu_{A_2}(X_\alpha) = \mu_{B_2}(X_\beta) = \begin{cases} 1 - \dfrac{X - a_2}{0.5b_2} & |X - a_2| \le 0.5b_2 \\ 0 & |X - a_2| \ge 0.5b_2 \end{cases} \tag{5.40}$$

$$\mu_{A_3}(X_\alpha) = \mu_{B_3}(X_\beta) = \begin{cases} 0 & X \le a_3 \\ \dfrac{X - a_3}{b_3 - a_3} & a_3 \langle X \langle\ b_3 \\ 1 & X \ge b_3 \end{cases} \tag{5.41}$$

where the value of parameters (a_i, b_i) changes according to the error and accordingly generates the linguistic value of each membership function. Parameters in this layer are referred as *premise parameters* or *precondition parameters*.

Layer 2: Every node in this layer is a circle labeled as Π which multiplies the incoming signals and forwards it to next layer.

$$\mu_i = \mu_{A_i}(X_\alpha).\mu_{B_i}(X_\beta), \qquad i = 1, 2, 3. \tag{5.42}$$

Here, the output of each node represents the firing strength of a rule.

Layer 3: Every node in this layer is represented as circle. This layer calculates the normalized firing strength of each rule as given below:

$$\overline{\mu}_i = \frac{\mu_i}{\mu_1 + \mu_2 + \mu_3} \qquad i = 1, 2, 3. \tag{5.43}$$

Layer 4: Every node in this layer is a square node with a node function

$$O_i = \overline{\mu}_i.f_i^j = \overline{\mu}_i(a_0^i + a_1^i.X_j), \qquad i = 1, 2, 3 \, and \quad j = \alpha, \beta. \tag{5.44}$$

where the parameters $\{a_0^i, a_1^i\}$ are tuned as the function of inputs $\{\hat{i}_\alpha, \hat{i}_\beta\}$. Parameters in this layer are also referred as *consequent parameters*.

Layer 5: This layer is also called output layer which computes the output as given below:

$$Y_1 = \overline{\mu}_1 . f_1^A + \overline{\mu}_2 . f_2^A + \overline{\mu}_3 . f_3^A \tag{5.45}$$

and

$$Y_2 = \overline{\mu}_1 . f_1^B + \overline{\mu}_2 . f_2^B + \overline{\mu}_3 . f_3^B \tag{5.46}$$

The outputs from this layer are now multiplied with the normalizing factor and passed through the low pass filter to find the estimated value of back e.m.f.'s $\hat{E}_\alpha$ and $\hat{E}_\beta$.

d) On-line training of ANFIS Architecture: For the proposed ANFIS architecture, a gradient descent technique is used to reduce the error (usually a cost function given by the squared error), where the weights are iterated by propagating the error from output layer to input layer. This backward trip of such a calculation is termed as "back propagation". The training algorithm is completed in two stages, known as precondition parameter tuning and consequent parameter tuning, where the objective function to be minimized is defined as:

$$\xi_{\alpha\beta}{}^2 = (i_{\alpha\beta} - \hat{i}_{\alpha\beta})^2 \tag{5.47}$$

Precondition parameter tuning: The Precondition parameters are required to update the fuzzy membership functions as discussed in previous section for *Layer1*. To minimize the error function $\xi_{\alpha\beta}{}^2$ by gradient descent method, the change in each precondition parameter must be proportional to the rate of change of the error function w.r.t. that particular precondition parameter, i.e.

$$\Delta a_{A_i} = -\eta \frac{\partial \xi_\alpha^{\,2}}{\partial a_{A_i}} \qquad i = 1, 2, 3. \tag{5.48}$$

Where η is the constant of proportionality defined as the learning rate. Therefore, the new value of the consequent parameter is given as:

$$a_{A_i}(n+1) = a_{A_i}(n) + \Delta a_{A_i} \qquad i = 1, 2, 3. \tag{5.49}$$

or

$$a_{A_i}(n+1) = a_{A_i}(n) - \eta \frac{\partial \xi_\alpha^{\,2}}{\partial a_{A_i}} \qquad i = 1, 2, 3. \tag{5.50}$$

Similarly

$$b_{A_i}(n+1) = b_{A_i}(n) - \eta \frac{\partial \xi_\alpha^{\,2}}{\partial b_{A_i}} \qquad i = 1, 2, 3. \tag{5.51}$$

Now the partial derivative in equation (5.50) can be found by the chain rule of differentiation as follows:

$$\frac{\partial \xi_\alpha^{\,2}}{\partial a_{A_1}} = \frac{\partial \xi_\alpha^{\,2}}{\partial \hat{i}_\alpha} \cdot \frac{\partial \hat{i}_\alpha}{\partial \hat{E}_\alpha} \cdot \frac{\partial \hat{E}_\alpha}{\partial \overline{\mu}_1} \cdot \frac{\partial \overline{\mu}_1}{\partial \mu_1} \cdot \frac{\partial \mu_1}{\partial \mu_{A_1}} \cdot \frac{\partial \mu_{A_1}}{\partial a_{A_1}} \tag{5.52}$$

where

$$\frac{\partial \xi_\alpha^{\,2}}{\partial \hat{i}_\alpha} = -2(i_\alpha - \hat{i}_\alpha) = -2\xi_\alpha \ ; \tag{5.52.a}$$

$$(i_\alpha - \hat{i}_\alpha) = k\hat{E}_\alpha \Rightarrow \frac{\partial \hat{i}_\alpha}{\partial \hat{E}_\alpha} = -k \ ; \tag{5.52.b}$$

$$\hat{E}_\alpha = \overline{\mu}_1 . f_1^{\,A} + \overline{\mu}_2 . f_2^{\,A} + \overline{\mu}_3 . f_3^{\,A} \Rightarrow \frac{\partial \hat{E}_\alpha}{\partial \overline{\mu}_1} = f_1^{\,A} ; \tag{5.52.c}$$

$$\overline{\mu}_1 = \frac{\mu_1}{\mu_1 + \mu_2 + \mu_3} \Rightarrow \frac{\partial \overline{\mu}_1}{\partial \mu_1} = \frac{(\overline{\mu}_2 + \overline{\mu}_3)}{\mu_1 + \mu_2 + \mu_3} ; \tag{5.52.d}$$

$$\mu_1 = \mu_{A_1} \cdot \mu_{B_1} \Rightarrow \frac{\partial \mu_1}{\partial \mu_{A_1}} = \mu_{B_1}; \tag{5.52.e}$$

$$\mu_{A_1} = \frac{X_1 - a_{A_1}}{b_{A_1} - a_{A_1}} \Rightarrow \frac{\partial \mu_{A_1}}{\partial a_{A_1}} = \frac{\mu_{A_1} - 1}{b_{A_1} - a_{A_1}}; \tag{5.52.b}$$

On computing all the terms of equation (5.52) and putting in equation (5.50), we can find the updated value of parameter a_{A1} as follows:

$$a_{A_1}(n+1) = a_{A_1}(n) - 2 \cdot \eta \cdot \xi_\alpha(n) \cdot k \cdot f_1^A(n) \cdot \mu_{B_1}(n) \cdot \frac{\bar{\mu}_2(n) + \bar{\mu}_3(n)}{\mu_1(n) + \mu_2(n) + \mu_3(n)} \cdot \frac{\mu_{A_1}(n) - 1}{b_{A_1}(n) - a_{A_1}(n)} \tag{5.53}$$

Similarly,

$$b_{A_1}(n+1) = b_{A_1}(n) + 2 \cdot \eta \cdot \xi_\alpha(n) \cdot k \cdot f_1^A(n) \cdot \mu_{B_1}(n) \cdot \frac{\bar{\mu}_2(n) + \bar{\mu}_3(n)}{\mu_1(n) + \mu_2(n) + \mu_3(n)} \cdot \frac{\mu_{A_1}(n)}{b_{A_1}(n) - a_{A_1}(n)} \tag{5.54}$$

In the same manner, the precondition parameters for the remaining fuzzy membership functions can be derived as follows:

$$b_{A_2}(n+1) = b_{A_2}(n) - 2 \cdot \eta \cdot \xi_\alpha(n) \cdot k \cdot f_2^A(n) \cdot \mu_{B_2}(n) \cdot \frac{\bar{\mu}_1(n) + \bar{\mu}_3(n)}{\mu_1(n) + \mu_2(n) + \mu_3(n)} \cdot \frac{1 - \mu_{A_2}(n)}{b_{A_2}(n)} \tag{5.55}$$

$$a_{A_3}(n+1) = a_{A_3}(n) - 2 \cdot \eta \cdot \xi_\alpha(n) \cdot k \cdot f_3^A(n) \cdot \mu_{B_3}(n) \cdot \frac{\bar{\mu}_1(n) + \bar{\mu}_2(n)}{\mu_1(n) + \mu_2(n) + \mu_3(n)} \cdot \frac{\mu_{A_3}(n) - 1}{b_{A_3}(n) - a_{A_3}(n)} \tag{5.56}$$

$$b_{A_3}(n+1) = b_{A_3}(n) + 2 \cdot \eta \cdot \xi_\alpha(n) \cdot k \cdot f_3^A(n) \cdot \mu_{B_3}(n) \cdot \frac{\bar{\mu}_1(n) + \bar{\mu}_1(n)}{\mu_1(n) + \mu_2(n) + \mu_3(n)} \cdot \frac{\mu_{A_3}(n)}{b_{A_3}(n) - a_{A_3}(n)} \tag{5.57}$$

Similarly, the precondition parameters for the fuzzy membership functions of second input can be found just by interchanging the subscripts α↔β and $A \leftrightarrow B$ in equations (5.53)-(5.57).

Consequent Parameter Tuning: To tune the consequent parameters as discussed in *Layer 4*, the following updated laws are developed:

$$a_{0_i}{}^{\alpha}(n+1) = a_{0_i}{}^{\alpha}(n) - \eta_c \cdot \frac{\partial \xi_\alpha{}^2}{\partial a_{0_i}{}^{\alpha}} \qquad i = 1,2,3. \tag{5.58}$$

$$a_{1_i}{}^{\alpha}(n+1) = a_{1_i}{}^{\alpha}(n) - \eta_c \cdot \frac{\partial \xi_\alpha{}^2}{\partial a_{1_i}{}^{\alpha}} \qquad i = 1,2,3. \tag{5.59}$$

where η_c is the learning rate for consequent parameters. The derivative terms in equations (5.58)-(5.59), can be found by the chain rule as already discussed in case of precondition parameters as follows:

$$\frac{\partial \xi_\alpha{}^2}{\partial a_{0_i}{}^{\alpha}} = \frac{\partial \xi_\alpha{}^2}{\partial \hat{i}_\alpha} \cdot \frac{\partial \hat{i}_\alpha}{\partial \hat{E}_\alpha} \cdot \frac{\partial \hat{E}_\alpha}{\partial a_{0_i}{}^{\alpha}} \qquad i = 1,2,3. \tag{5.60}$$

$$\frac{\partial \xi_\alpha{}^2}{\partial a_{1_i}{}^{\alpha}} = \frac{\partial \xi_\alpha{}^2}{\partial \hat{i}_\alpha} \cdot \frac{\partial \hat{i}_\alpha}{\partial \hat{E}_\alpha} \cdot \frac{\partial \hat{E}_\alpha}{\partial a_{1_i}{}^{\alpha}} \qquad i = 1,2,3. \tag{5.61}$$

In the above equations (5.60)-(5.61), the first two terms on R.H.S. are already known and the third terms can be derived as:

$$\frac{\partial \hat{E}_\alpha}{\partial a_{0_i}{}^{\alpha}} = \frac{\mu_i}{\mu_1 + \mu_2 + \mu_3} \qquad i = 1,2,3. \tag{5.62}$$

$$\frac{\partial \hat{E}_{\alpha}}{\partial a_{1_i}{}^{\alpha}} = \frac{\mu_i}{\mu_1 + \mu_2 + \mu_3} \cdot \hat{i}_{\alpha} \qquad i = 1, 2, 3. \tag{5.63}$$

On substituting the terms derived in equations (5.60)-(5.63) in to the equations (5.58)-(5.59), the updated value of consequent parameters can be derived as follows:

$$a_{0_i}{}^{\alpha}(n+1) = a_{0_i}{}^{\alpha}(n) - 2 \cdot \eta_c \cdot \xi_{\alpha} \cdot k \cdot \frac{\mu_i}{\mu_1 + \mu_2 + \mu_3} \qquad i = 1, 2, 3. \tag{5.64}$$

$$a_{1_i}{}^{\alpha}(n+1) = a_{1_i}{}^{\alpha}(n) - 2 \cdot \eta_c \cdot \xi_{\alpha} \cdot k \cdot \frac{\mu_i}{\mu_1 + \mu_2 + \mu_3} \cdot \hat{i}_{\alpha} \qquad i = 1, 2, 3. \tag{5.65}$$

Similarly, the consequent parameter for second input can be found just by replacing α by β in above equations.

5.4.3 Grid Side Inverter Control

The proposed system employs a 4-leg grid interfacing inverter as discussed in section 5.2. Here the inverter is a key element, since it delivers the power from renewable to grid and also solves the power quality problem arising due to unbalance non-linear load at PCC. The duty ratio of inverter switches are varied in a power cycle such that the combination of load and inverter injected power appears as balanced resistive load to the grid, resulting into the UPF grid operation. The schematic of grid interfacing inverter control with 3P4W non-linear unbalance load compensation is shown in Fig. 5.21.

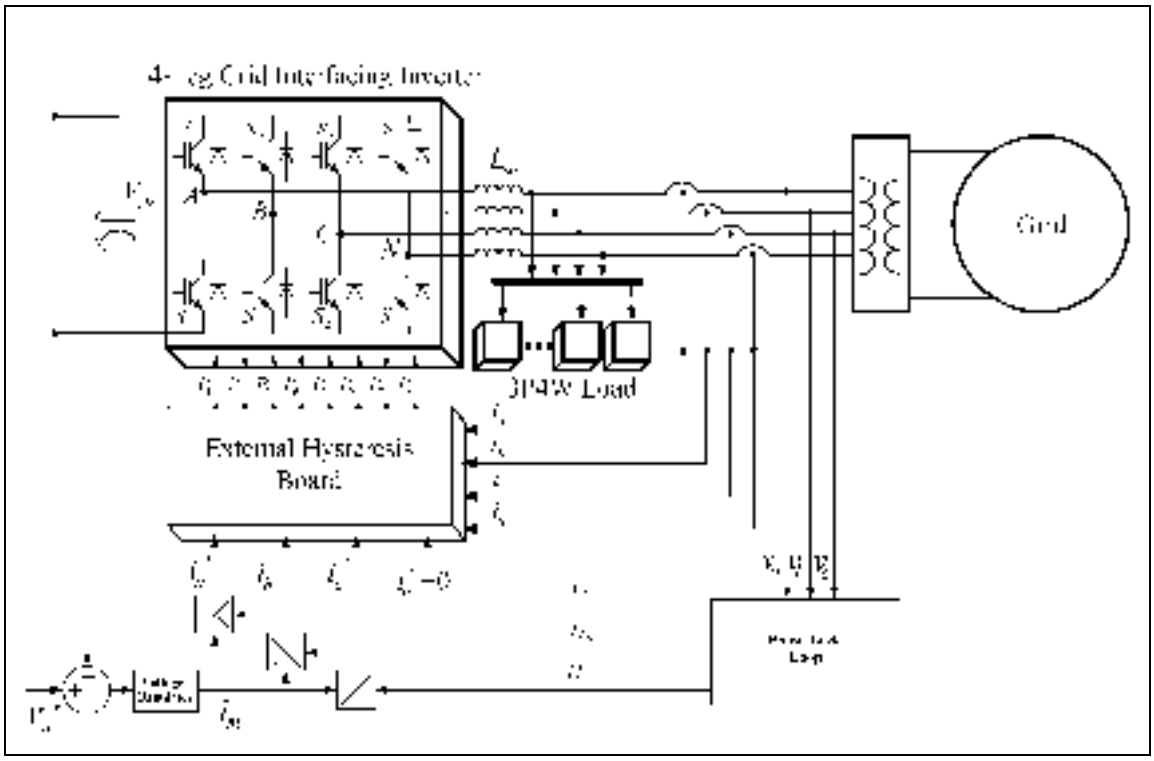

Figure 5.21 Control Diagram of Grid side Converter.

Usually, the load current and either of the grid or inverter currents are required to compensate the load unbalance, reactive power and harmonics. This makes it necessary to have at least 6 current sensors for a 3P4W distribution network. But, in the proposed control strategy, only grid current sensing is required to force the grid currents to be purely sinusoidal at UPF without having any knowledge of inverter and load current profile. The control of grid-side inverter comprises of two loops. The outer dc voltage control loop is used to set the current reference for active power control. The output of dc control loop (i_m) is multiplied with in-phase unity vector templates (U_a, U_b, and U_c) to generate the reference grid currents (i_a^*, i_b^*, and i_c^*). The reference grid neutral current (i_n^*) is set to zero, being the instantaneous sum of balanced grid currents. The in-phase unit vector templates U_a, U_b and U_c can be computed from three phase grid voltages v_a, v_b and v_c as in (Singh et Chandra, 2008).

5.4.4 Simulation Results and Discussion

The proposed system is simulated in MATLAB/Simulink environment using PMSG model and other necessary components from *SimPowerSystem* blockset. The simulation results under different operating conditions are provided to validate the proposed control strategy. The Fig. 5.22 demonstrates the generator side performance, where the traces for applied torque, generated voltage, actual & estimated speed, actual & estimated position, speed error and generated output power are shown. In Fig. 5.23, the traces of grid voltages, grid currents, load currents and inverter currents are shown. The traces of phase-a currents and neutral currents for grid, load and inverter are shown in Fig. 5.24, w.r.t. phase-a grid voltage, just to demonstrate the load harmonics, unbalance and neutral current compensation capabilities.

A variable torque available from wind turbine is applied on the PMSG as shown in Fig. 5.22(a). The corresponding change in amplitude and frequency of generator voltage can be easily noticed in Fig. 5.22(b). The Fig. 5.22(c) shows the actual and estimated speeds, whereas the actual and estimated positions are shown in Fig. 5.22(d). The ANFIS estimator estimates the PMSG position and speed accurately, as evident from the trace of speed error in Fig. 5.22(e), where estimated speed deviates little bit from actual speed only under dynamic conditions. The corresponding PMSG output power is shown in Fig. 5.22(f).

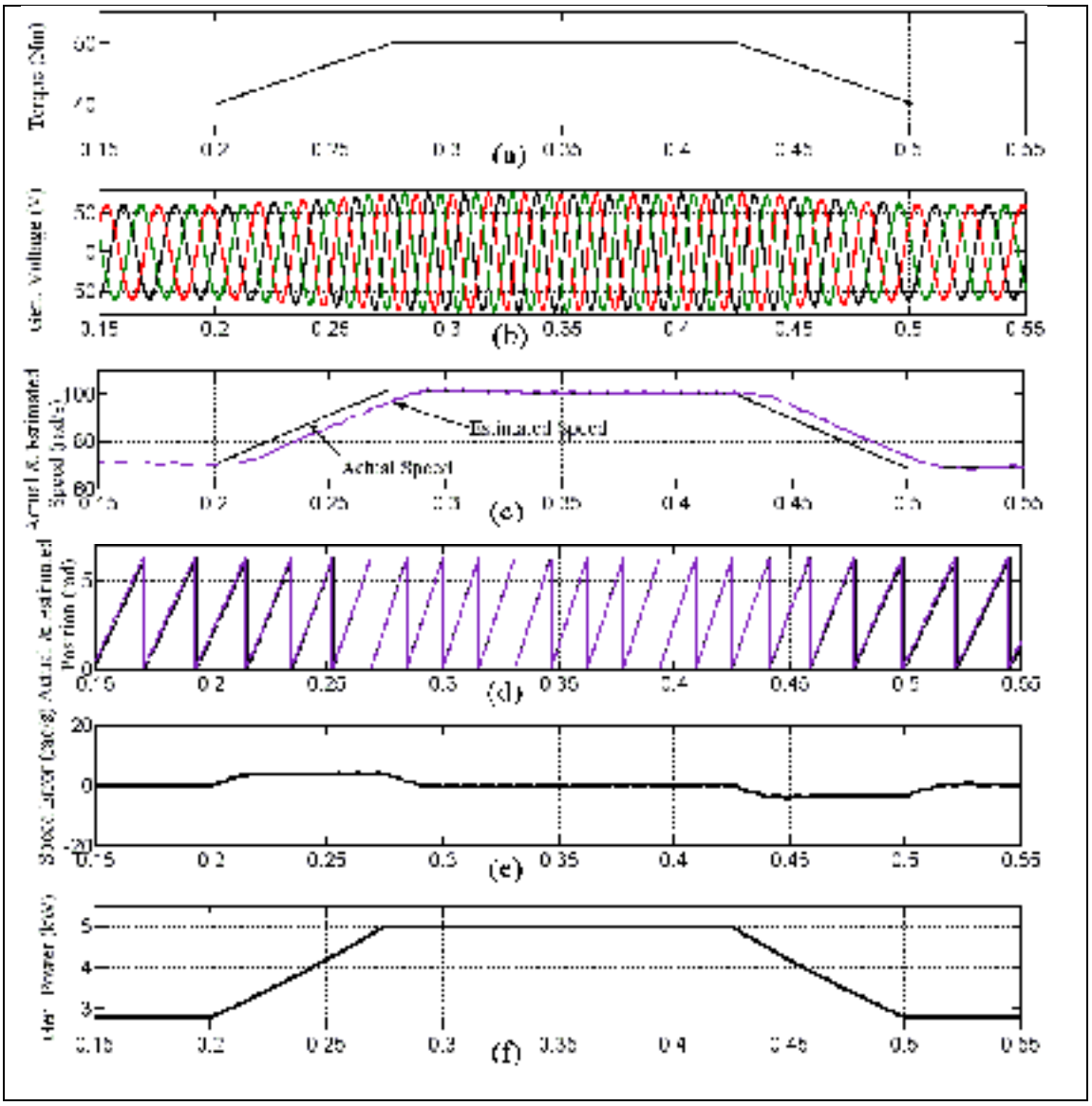

Figure 5.22 Simulation results for ANFIS Based Generator Control.

The performance of grid side inverter is shown in Fig. 5.23, where the grid side currents [Fig. 5.23(b)] are always kept as a balanced set of sinusoidal current at UPF, even in the presence of 3P4W unbalanced non-linear current [Fig. 5.23(c)]. The inverter supplies the load harmonics, load unbalance, load neutral current and generated power from PMSG as shown in Fig. 5.23(d). Initially, the inverter current is constant and it starts increasing at t=0.2s in response to increase in PMSG input torque. As the inverter

injected current is more than the load current demand, the difference of these is being injected into the grid with a sinusoidal and balanced profile. At t=0.425s, the input torque starts decreasing and this results in to the corresponding decrease in inverter and grid currents.

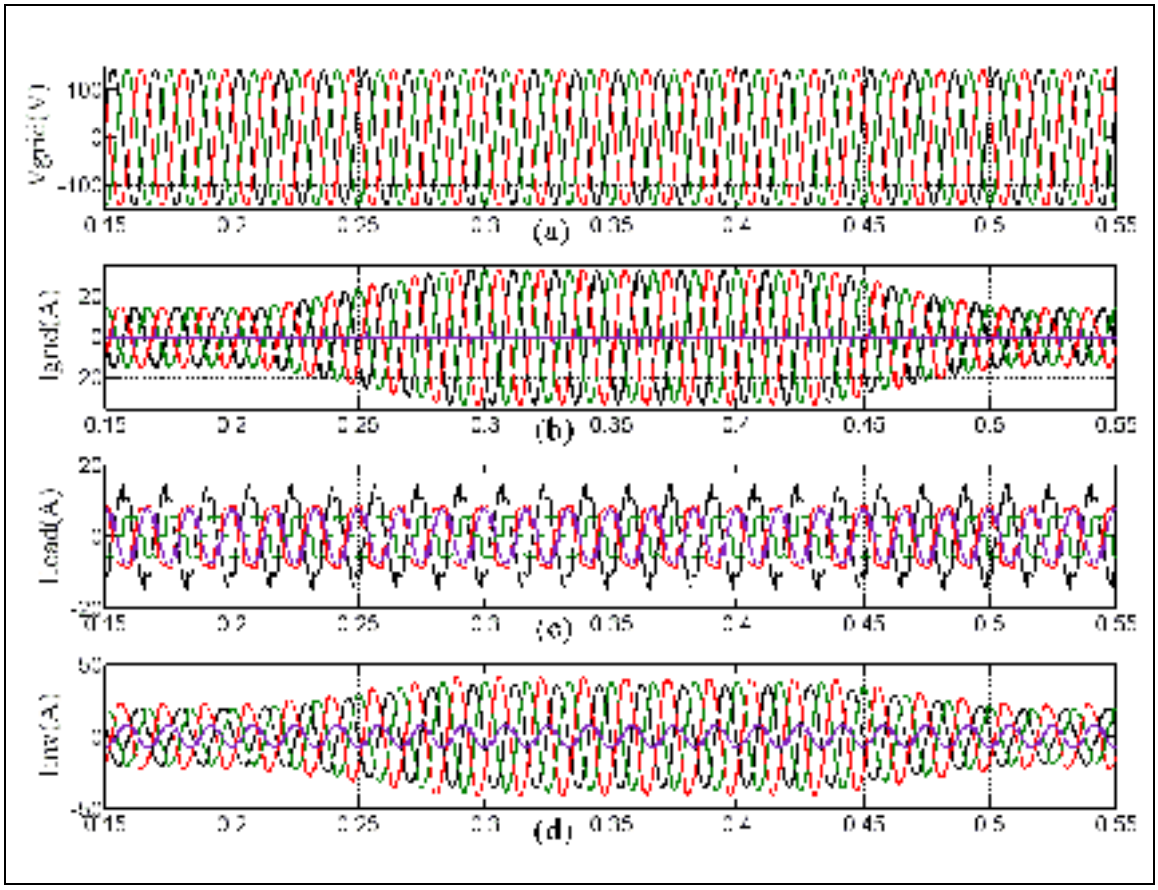

Figure 5.23 Simulation results for Grid Side Inverter.

In Fig. 5.24, it is shown that inverter current consists of load current harmonics component, load current reactive component and the active current component in proportion to generated wind power. Moreover, the inverter is fully able to supply the load neutral current locally, resulting into the zero grid neutral current and hence balanced grid operation. On visualizing the profile of all traces carefully in Fig.5.24, it

can be easily noticed that the grid phase-a current is in phase opposition to grid phase-a voltage. This indicates that the power is being injected in to the grid at UPF.

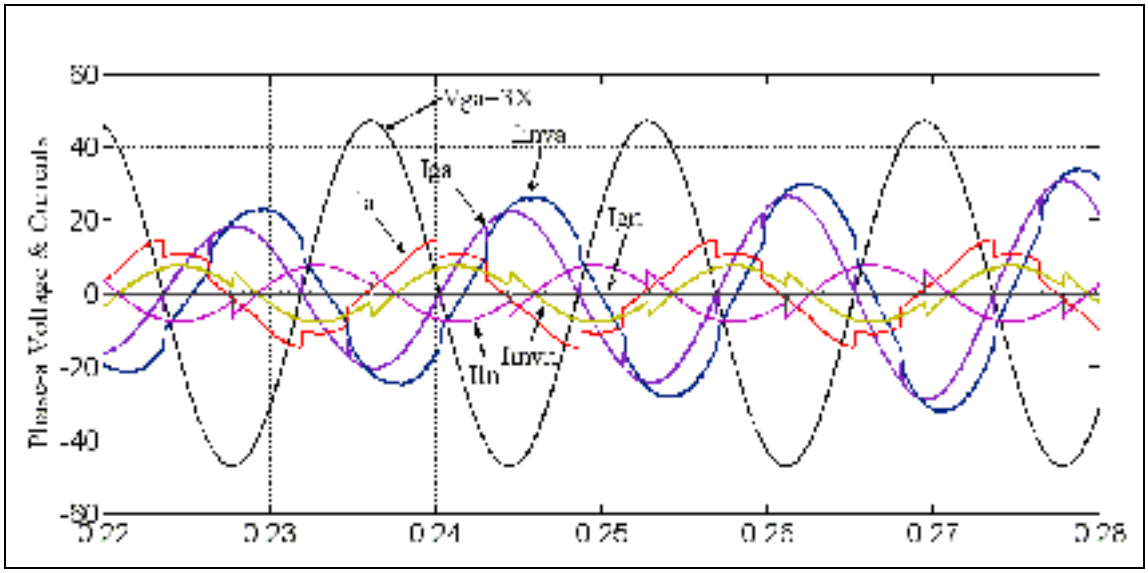

Figure 5.24 Simulation results: Grid, Load, Inverter currents of phase-a and neutral w.r.t. phase-a grid voltage.

5.4.5 Experimental Results and Discussion

A scaled hardware prototype is developed and implemented as shown in Fig. 5.25. The PMSG is mechanically driven by 3-phase induction motor coupled with *ACS800* drive from *ABB*. The variable torque command generated from MATLAB/Simulink file is applied to the drive, which in turns rotates the PMSG at variable speed. The output of PMSG is connected to grid by two back to back connected inverters with a common DC-link.

The proposed ANFIS speed & position estimation and control algorithm is implemented using *dSPACE 1104*. An extensive experimental study is carried out to validate the proposed strategy. The experimental results are shown in Fig. 5.26- Fig. 5.29.

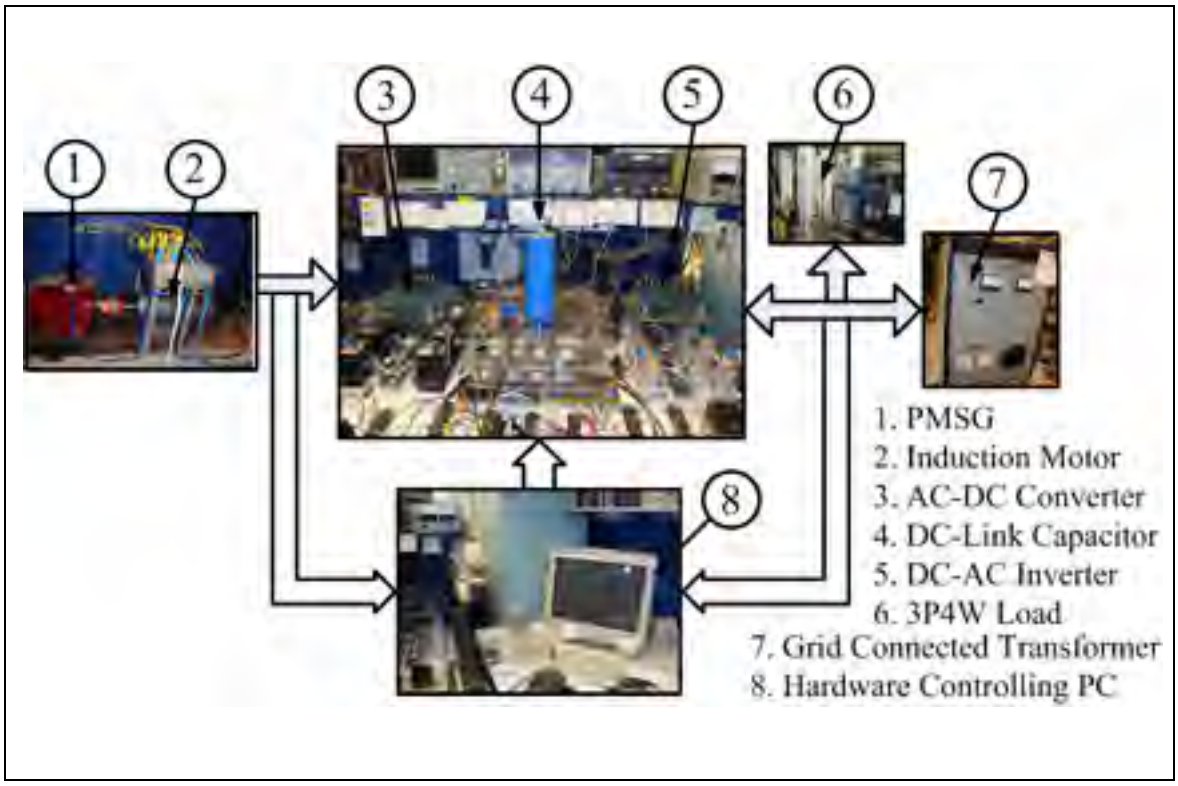

Figure 5.25 Experimental Set-up of Proposed System.

a) Generator Side Control Performance : The generator side experimental results are shown in Fig. 5.26., where the actual & estimated traces of generator speed & position under steady state condition are given. The generator speed is varied from 300rpm to 400 rpm, and the proposed ANFIS estimator estimates the speed & position accurately under dynamic conditions as evident from their respective traces. In Fig. 5.27., the traces of estimated and actual speed & position under dynamic operating condition are shown. The Fig. 5.28., shows the generated voltage and estimated position on the same plot to validate the fact that the estimated position is in same phase or in compliance of the generator output voltage waveshape. The generator voltage, current, actual speed and estimated speed are shown in Fig. 5.29.(a) under varying conditions. Moreover the traces are shown at 10X zoom factor to visualize the estimator performance under dynamic conditions, where the amplitude and frequency of the generator voltage and current varies with the variation in speed. In Fig. 5.29.(b), the traces of PMSG voltage,

current, speed and output power are shown, where the output power varies with the variation in generator speed.

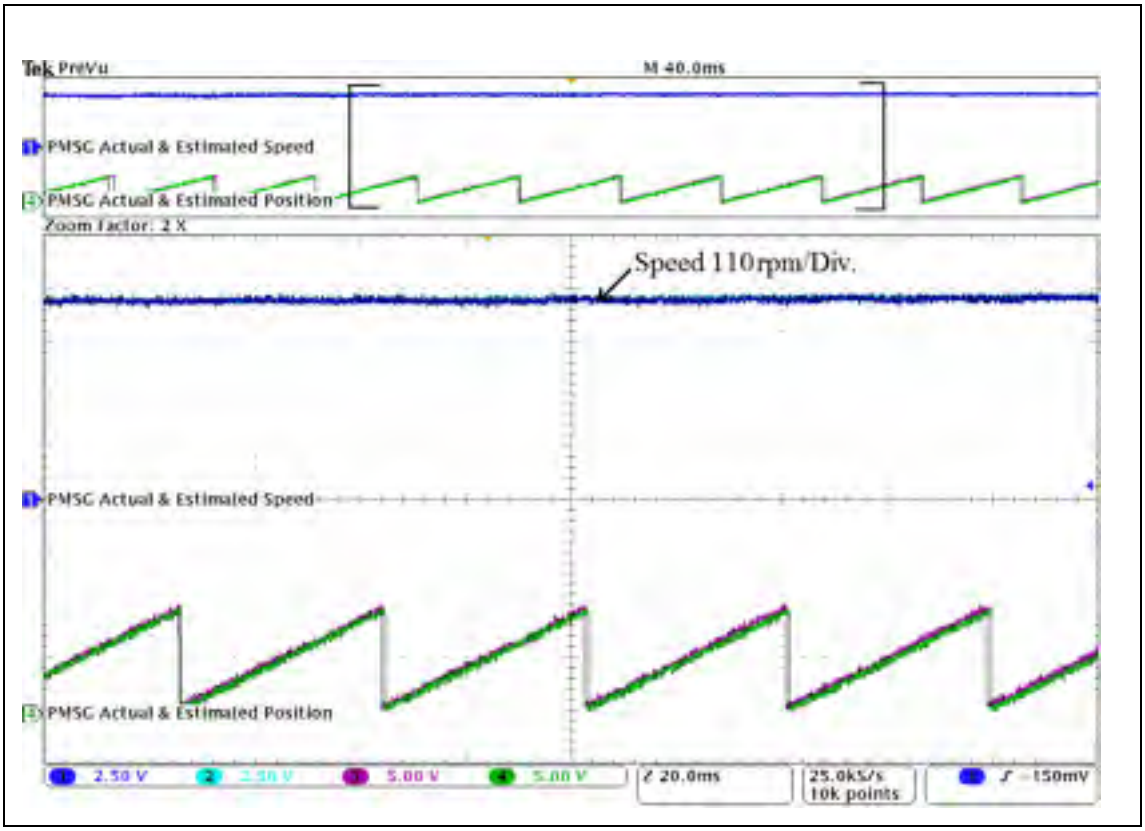

Figure 5.26 Experimental Results for ANFIS Based Generator Control: Actual and Estimated Speed and Position Under Steady State Condition.

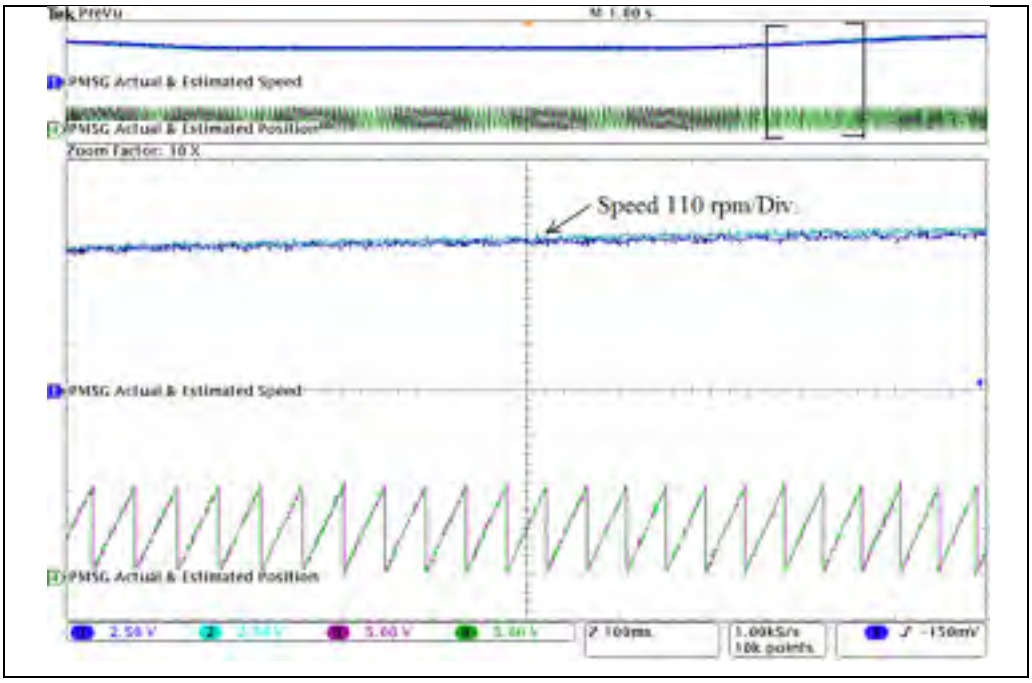

Figure 5.27 Experimental Results for ANFIS Based Generator Control: Actual and Estimated Speed and Position Under Dynamic Condition.

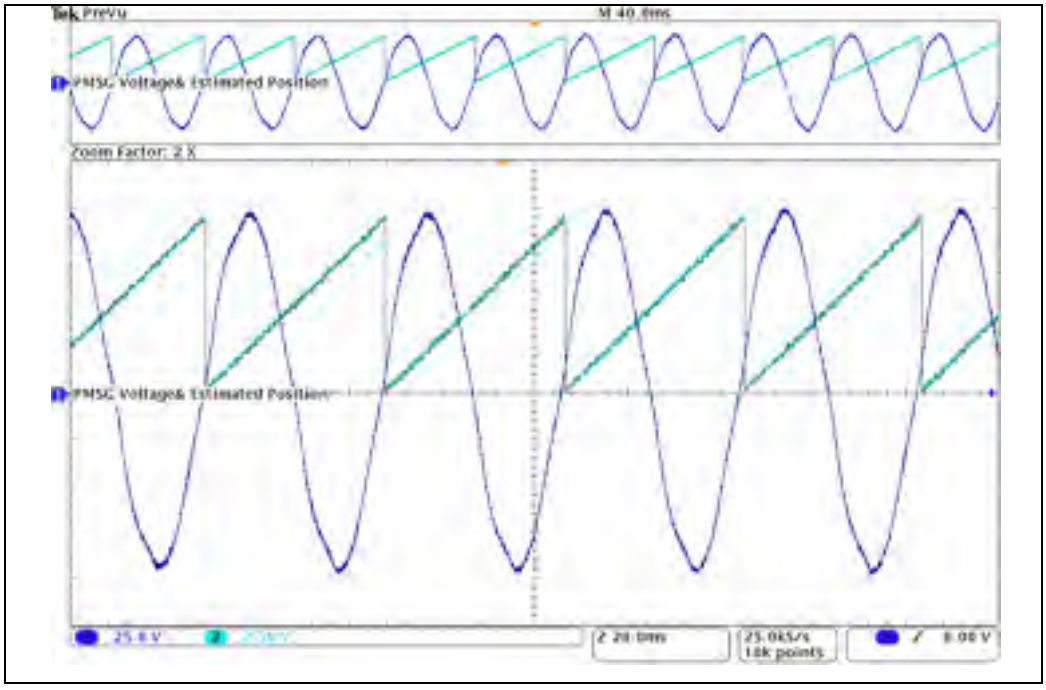

Figure 5.28 Experimental Results for ANFIS Based Generator Control: PMSG Voltage and Position.

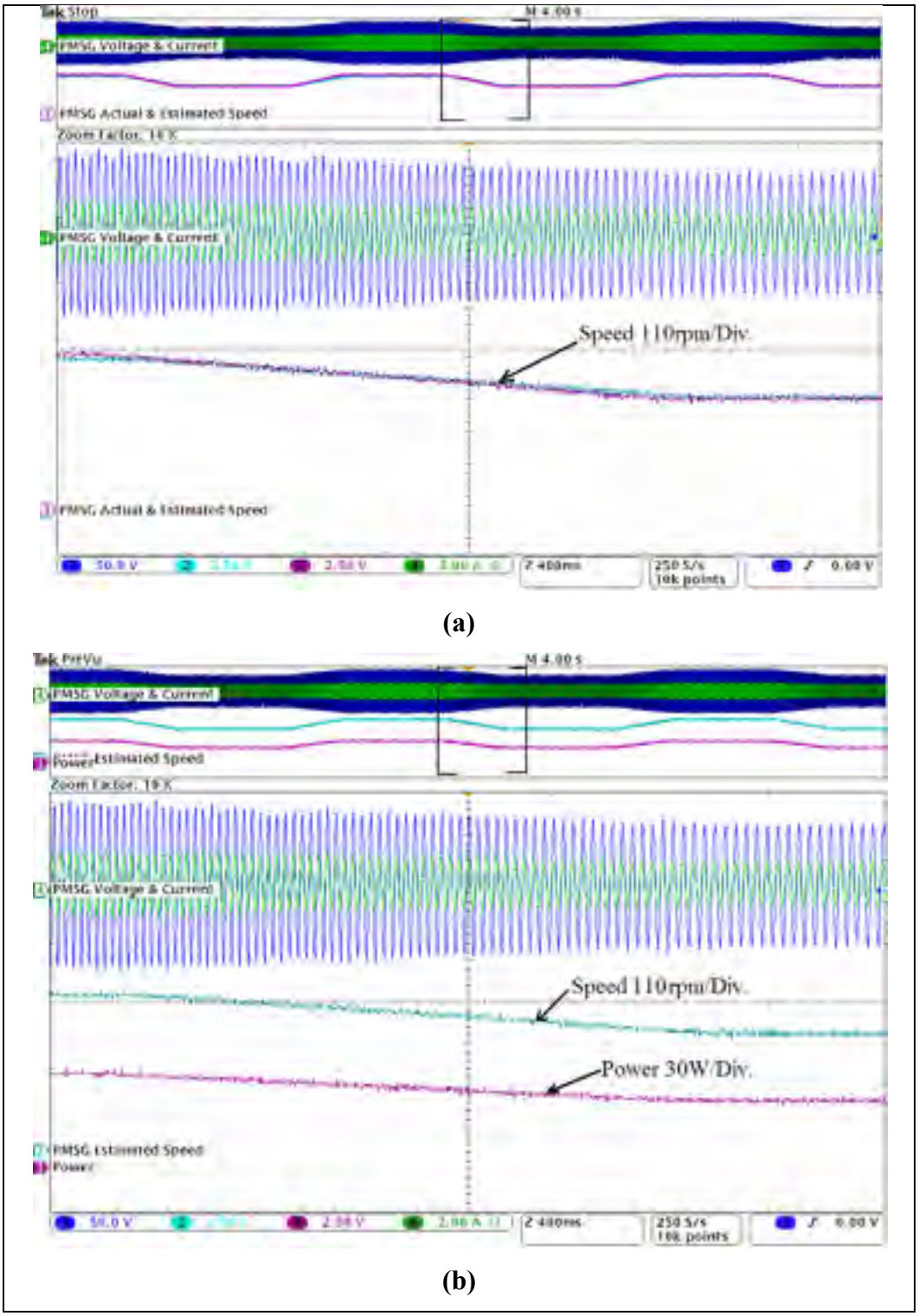

(a)

(b)

Figure 5.29 Experimental Results for ANFIS Based Generator Control: PMSG Voltage, Current, Speed, and Power.

b) Grid Side Control Performance: The performance of grid side inverter is shown in Fig. 5.30.- Fig. 5.34., where the inverter is utilized as multifunction device. In Fig. 5.30.- Fig. 5.33., the experimental results are shown only for active filtering application of grid interfacing inverter. The traces of grid voltage, grid currents, load current and inverter current just before and after compensation are shown for each phase-a, phase-b, phase-c, separately from Fig. 5.30. - Fig. 5.32., respectively. All the grid currents are shown together in Fig. 5.33.(a), just before and after compensation. Here it can be noticed that the grid is supplying a highly non-linear 3P4W unbalance current before compensation, which becomes perfectly balanced set of sinusoidal current once after the inverter is connected in circuit. The inverter injected currents are shown in Fig. 5.33.(b), where the inverter not only supplies the non-linear unbalance component of load current, but also compensates the load neutral current demand locally. This allows the grid to supply only the active balanced component of load current.

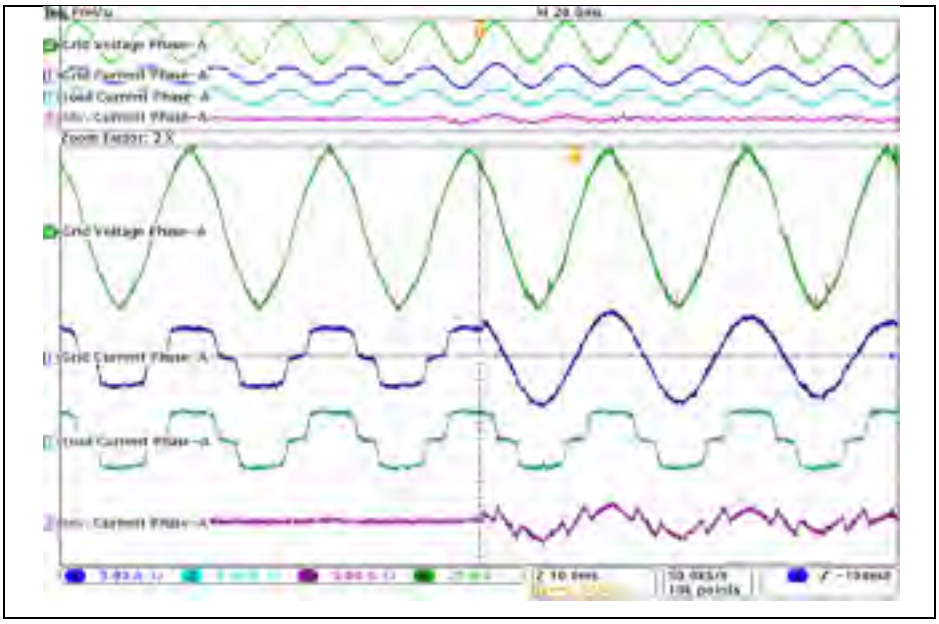

Figure 5.30 Experimental Results for Grid Side Inverter Control Under Active Filtering Mode: Traces of Phase-a Grid voltage, grid currents, load current and inverter current just before and after compensation.

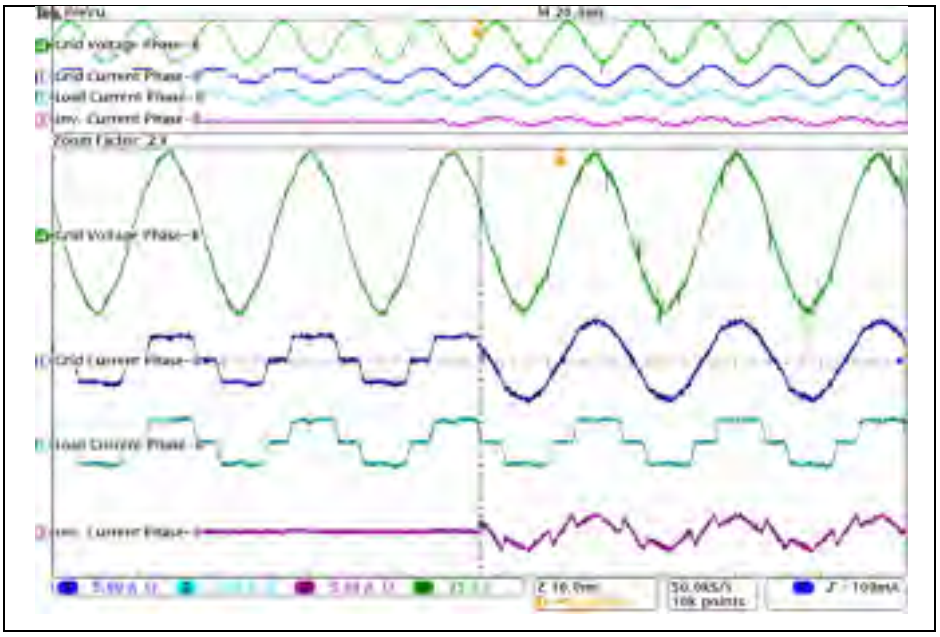

Figure 5.31 Experimental Results for Grid Side Inverter Control Under Active Filtering Mode: Traces of Phase-b Grid voltage, grid currents, load current and inverter current just before and after compensation.

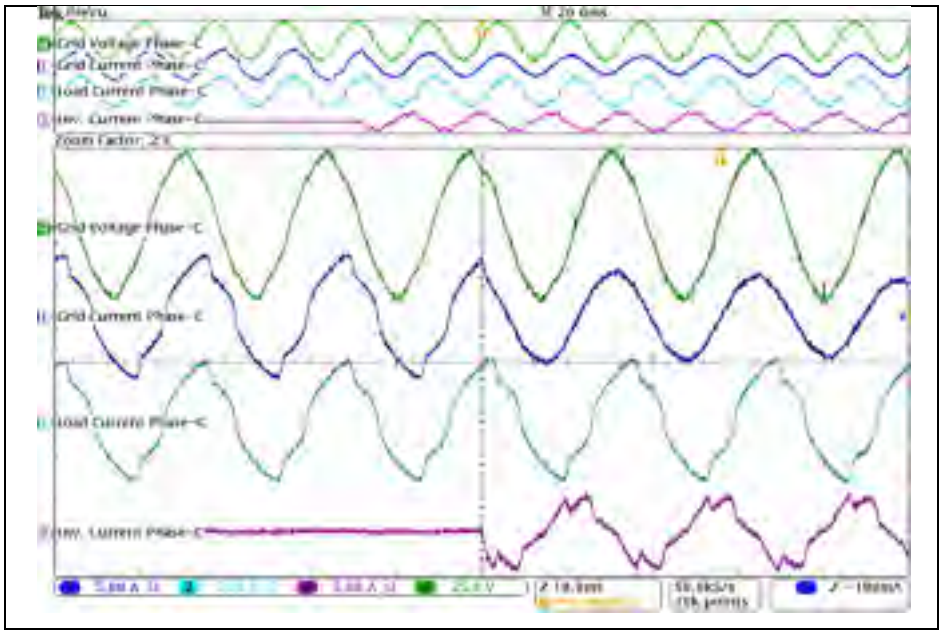

Figure 5.32 Experimental Results for Grid Side Inverter Control Under Active Filtering Mode: Traces of phase-c Grid voltage, grid currents, load current and inverter current just before and after compensation.

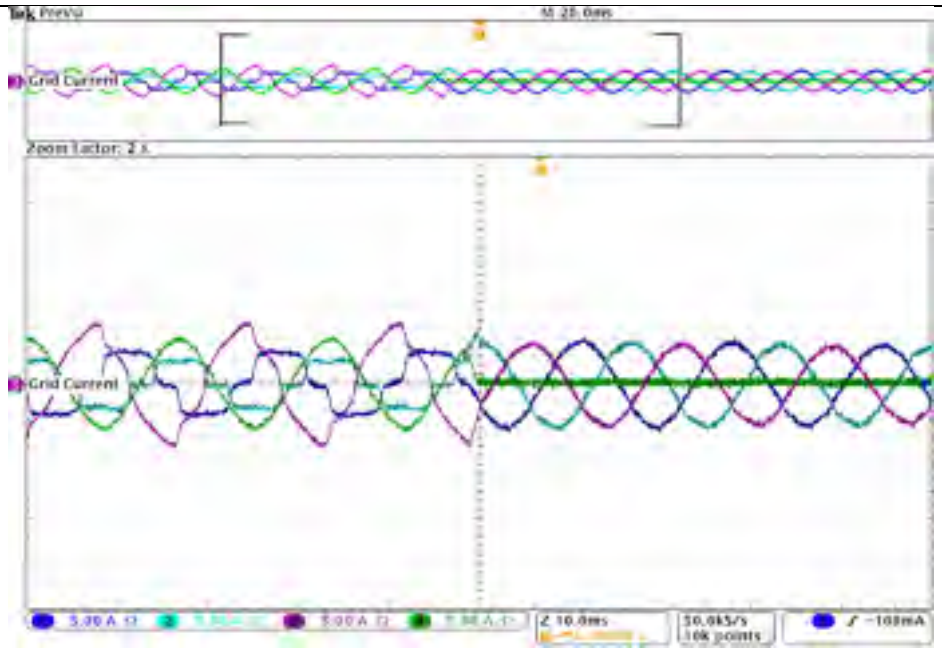

(a) Grid Currents.

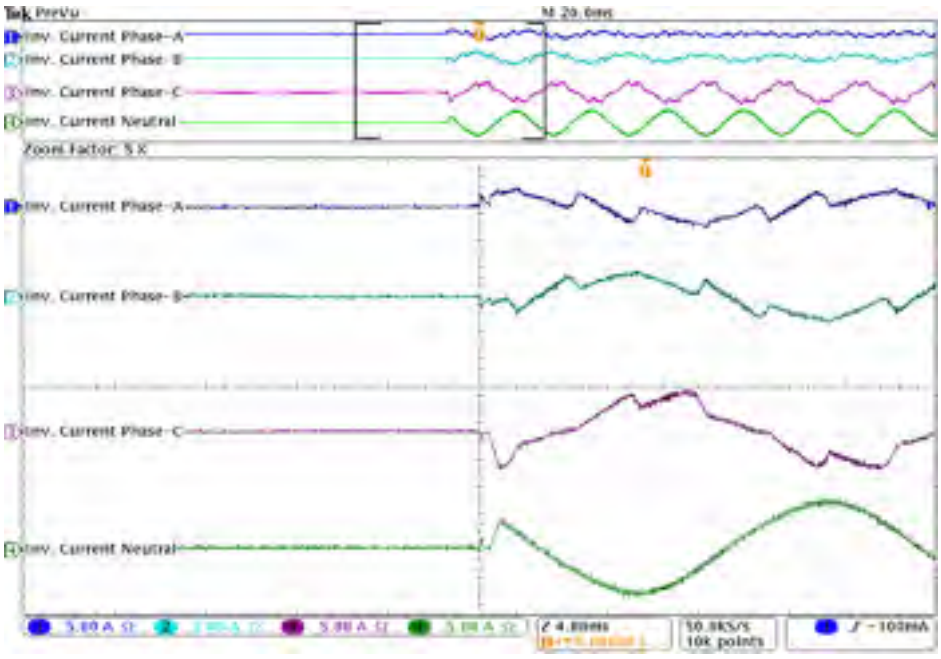

(b) Inverter Current, Just Before and After Compensation.

Figure 5.33 Experimental Results for Grid Side Inverter Control Under Active Filtering Mode.

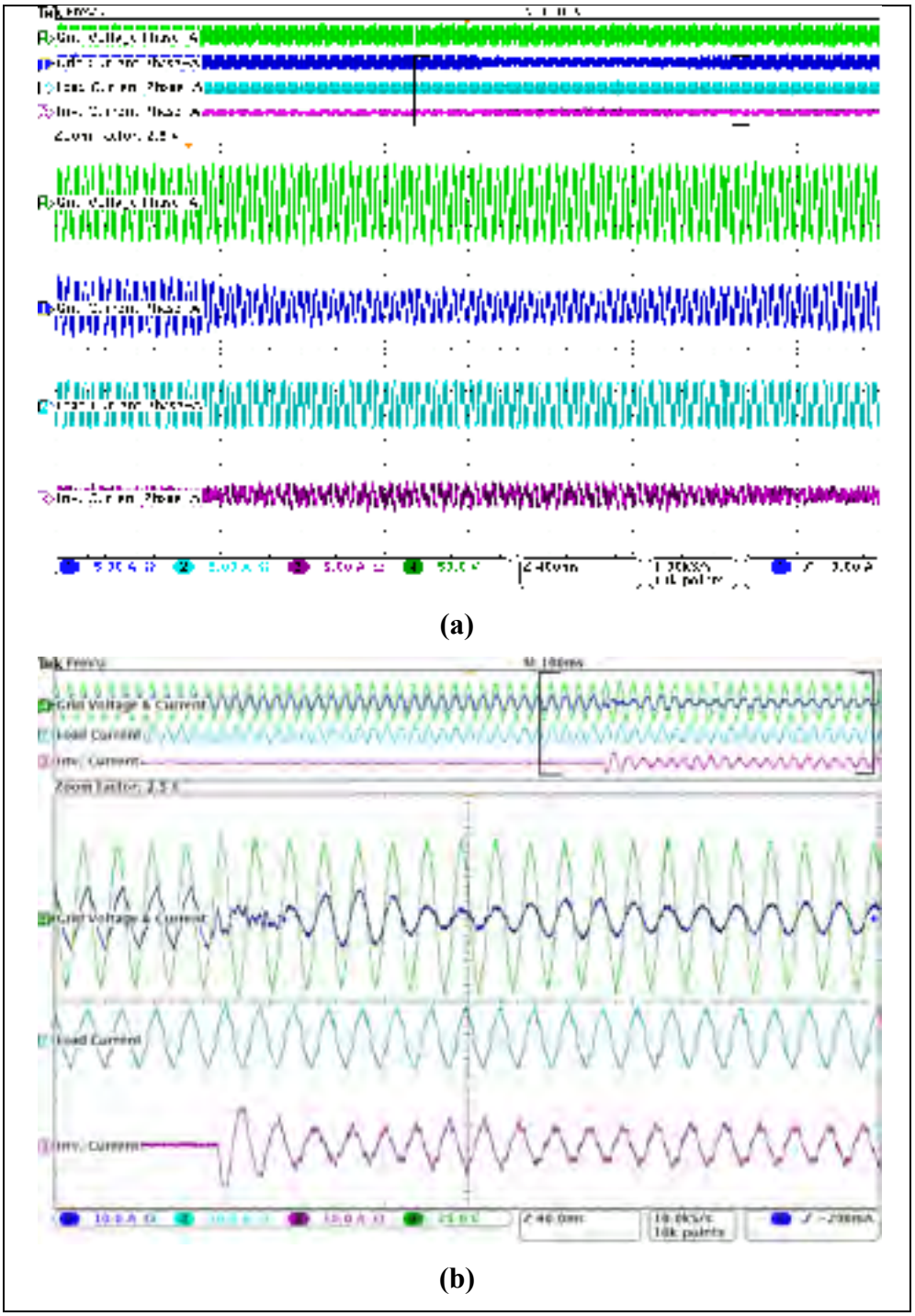

Figure 5.34 Experimental Results for Grid Side Inverter Control Under Active Filtering Mode and Active Power Injection Mode Simultaneously: Traces of grid voltage, grid current, load current and inverter current.

In Fig. 5.34, the performance of grid side inverter is shown, both in active filtering mode and renewable power injection mode simultaneously. The grid current is purely sinusoidal and starts decreasing with the increase in inverter injected current as shown in Fig. 5.34(a). This indicates that the grid is partially supporting the active power load demand, while the inverter is supplying the rest of active load demand, load harmonics and load reactive power demand simultaneously. This fact can be easily verified from Fig. 5.34(b), where the grid current starts decreasing and becomes purely sinusoidal and in phase with grid voltage, once after the inverter starts injecting the current in the network.

Table 5.2 Grid current details before and after compensation with Inverter in APF Mode

Grid Currents	**Before Compensation**			**After Compensation**		
	Current (r.m.s.)	**% THD**	**(%) Unbalance Factor**	**Current (r.m.s.)**	**% THD**	**(%) Unbalance Factor**
Phase-A	2.8	20.5	5.73	3.42	2.9	0.008
Phase-B	1.9	24.2	36.02	3.4	2.7	0.5
Phase-C	4.2	10.5	41.41	3.43	3.0	0.38
Neutral	3.75			0		

5.5 Comparative study of ANFIS and Sliding Mode Observers for Speed & Position Estimation

In this section a comparative study of ANFIS and sliding mode observers for speed and position estimation is presented. The ANFIS architecture is same as discussed in previous section. Here only the sliding mode based observer's deatailed description will be discussed. A detailed comparison of simulation results is also provided with sliding mode observer based results under variable speed PMSG operation. Moreover, the simulation study is also carried out for the different value of PMSG resistance and inductance to validate the robustness of proposed algorithm against parameter variation.

5.5.1 Modeling of Sliding Mode Observers for Speed & Position Estimation

On the basis of PMSG model discussed in section 5.4.2.1, the sliding mode observer can be easily designed to estimate the rotor position and speed. The sliding mode observer (SMO) is based on stator current estimation, where the sliding mode surface is defined as :

$$S = \begin{bmatrix} S_\alpha \\ S_\beta \end{bmatrix} = \begin{bmatrix} (\hat{i}_\alpha - i_\alpha) \\ (\hat{i}_\beta - i_\beta) \end{bmatrix} \tag{5.66}$$

On subtracting the equation (5.36) from equation (5.37), the dynamic sliding mode equation can be obtained as

$$\dot{S} = A.S + B.\hat{E}_{\alpha\beta} \tag{5.67}$$

Where, the equivalent control of sliding mode observer in equation (5.67) can be expressed as:

$$\hat{E}_{\alpha\beta} = \begin{bmatrix} \hat{E}_\alpha \\ \hat{E}_\beta \end{bmatrix} = \begin{bmatrix} -k_1 sign(S_\alpha) \\ -k_1 sign(S_\beta) \end{bmatrix} = \hat{\omega}_r \lambda_m \begin{bmatrix} -\sin(\hat{\theta}_r) \\ \cos(\hat{\theta}_r) \end{bmatrix} \tag{5.68}$$

In order to eliminate the high frequency components from the estimated e.m.f.s, the low pass filters (LPF) with sufficiently small time constant are used. On considering the effect of LPF, the equation (5.68) can be modified as:

$$\hat{E}_{\alpha\beta} = \begin{bmatrix} \hat{E}_\alpha \\ \hat{E}_\beta \end{bmatrix} = \begin{bmatrix} -k_1 sign(S_\alpha) \cdot \dfrac{\omega_c}{s+\omega_c} \\ -k_1 sign(S_\beta) \cdot \dfrac{\omega_c}{s+\omega_c} \end{bmatrix} \tag{5.69}$$

Where ω_c is the cut-off frequency of the LPF, which should be designed properly according to the frequency of estimated currents. If the estimated currents are able to track the actual currents accurately, then it is obvious that the error trajectories will reach the sliding surface ($S=0$). According to Lyapunov's stability criteria, the value of switching gain k_1 should be large enough to guarantee the stable operation of observer (Peixoto *et al.*, 1995), with the condition

$$\dot{S}^T . S \langle = 0 \tag{5.70}$$

Due to the discontinuous nature of sliding mode observer, it suffers from chattering problem at certain switching frequencies. To solve this problem, generally continuous functions, such as sigmoid function and saturation functions are used as shown in Fig. 5.35. But, it is very difficult to set the boundary limits and switching gain values under different operating conditions. The performance of sliding mode observer further deteriorates due to machine parameter variation with the passage of time.

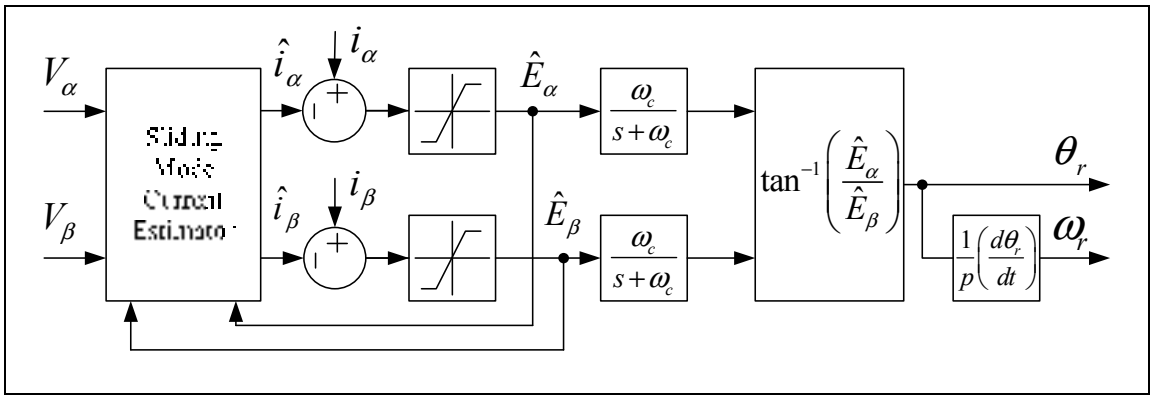

Figure 5.35 Sliding Mode Observer for Speed and Position Estimation.

5.5.2 Simulation Results and Discussion

The performance of proposed ANFIS based position and speed estimation for sensor less control of PMSG is demonstrated through the extensive simulation results as shown in Fig. 5.36- Fig. 5.38. Besides this, a detailed comparison is also provided w.r.t. the SMO based results under variable speed operation, with different value of PMSG parameters. The variable torque is applied to the PMSG and accordingly its speed and position are estimated. The traces of PMSG voltage, position, speed and speed errors are discussed in simulation results.

In Fig. 5.36, the simulation results with nominal value of PMSG parameters are shown. The Fig. 5.36(a) shows the traces of 3–phase PMSG voltage waveforms, where the variable frequency of these waveforms indicates the variable speed operation of PMSG. In Fig. 5.36(b), the traces of actual speed, ANFIS speed, and SMO speed are shown. The Fig. 5.36(c) shows the actual position, ANFIS position and SMO position. The errors between actual and estimated speed based on ANFIS and SMO estimators are shown in Fig. 5.36(d)., where the ANFIS estimator shows better performance than SMO estimator. The simulation results with 10% and 25% variation in PMSG resistance and inductance are shown in Fig. 5.37 and Fig. 5.38, respectively. The performance of SMO deteriorates with the variation in PMSG parameters, while the ANFIS estimator shows

promising immunity to any such kind of variation as evident from Fig. 5.37(d) and Fig. 5.38(d).

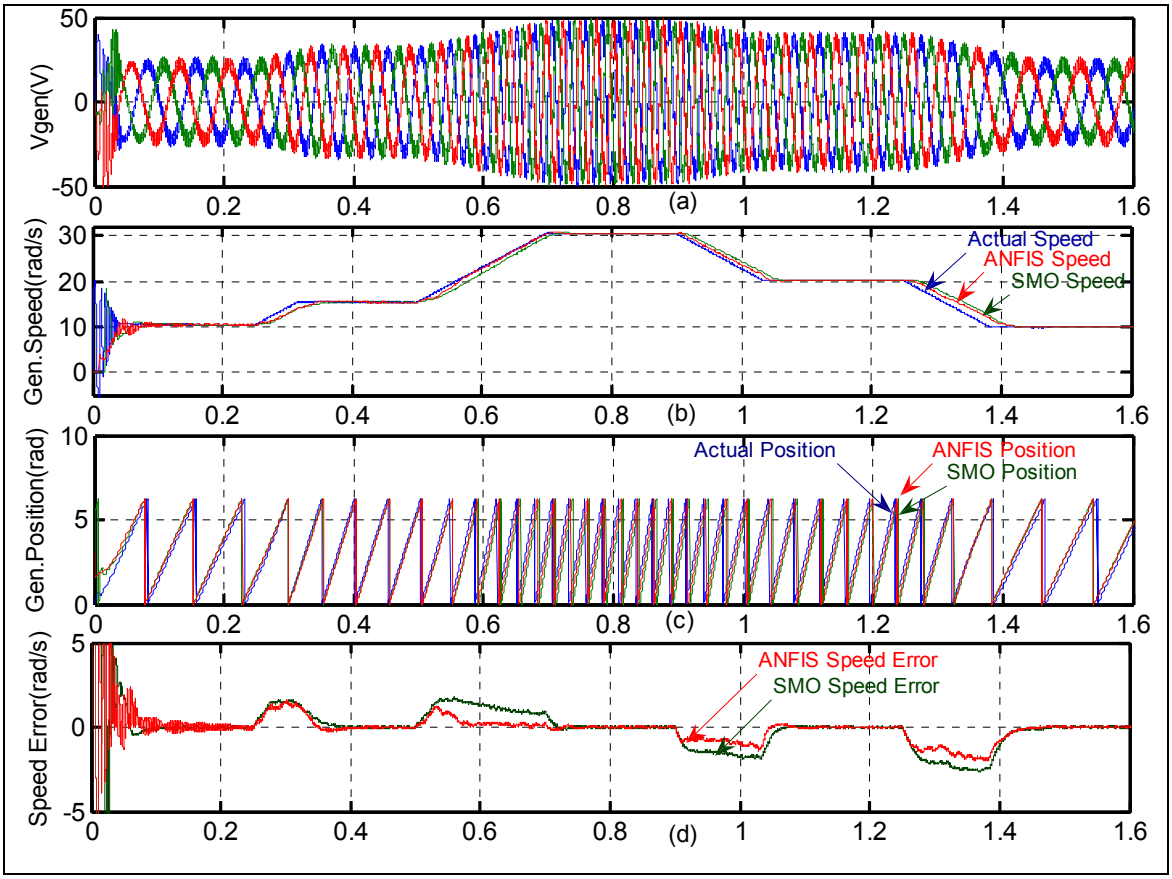

Figure 5.36 Simulation results for Comparative Study of ANFIS and Sliding Mode Observer for Speed & Position Estimation: With Nominal PMSG Parameters.

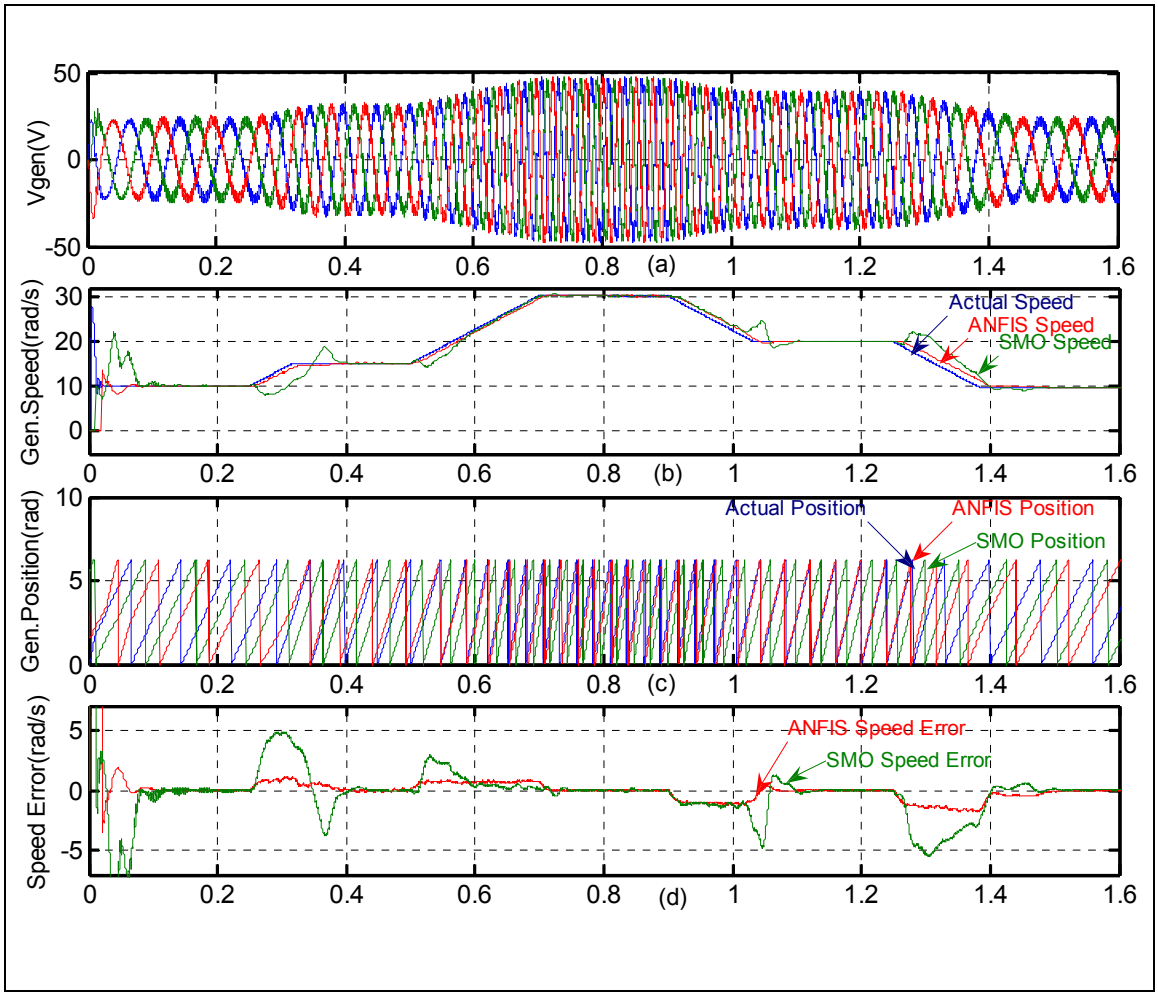

Figure 5.37 Simulation results for Comparative Study of ANFIS and Sliding Mode Observer for Speed & Position Estimation: With 10% variation in PMSG resistance and inductance.

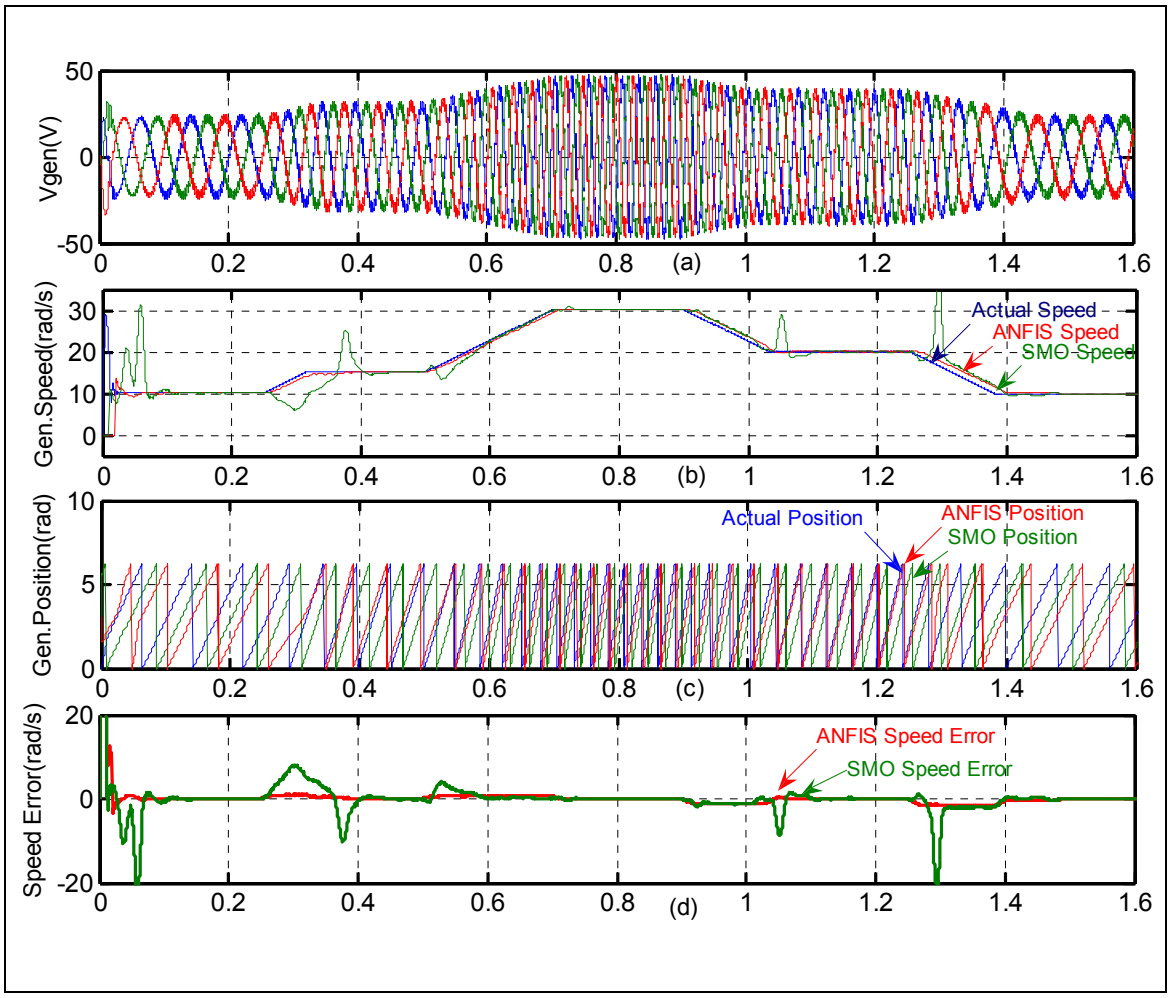

Figure 5.38 Simulation results for Comparative Study of ANFIS and Sliding mode Observer for Speed & Position Estimation: With 25% variation in PMSG resistance and inductance.

5.5.3 Experimental Results and Discussion

A scaled hardware prototype is developed and implemented using *dSPACE 1104*. The PMSG is mechanically driven by 3-phase induction motor coupled with ACS800 drive from ABB. The variable torque caused by variable wind speed command generated from MATLAB/Simulink file is applied to the drive, which in turns rotates the PMSG at variable speed. The variable amplitude and frequency of PMSG voltage, as shown in Fig. 5.39., indicates its variable speed operation (200-400rpm). The PMSG speed and

position is estimated in real-time. The experimental results based on ANFIS estimator and SMO estimator with varying parameters, are shown in Fig. 5.40., and Fig. 5.41.

The ANFIS estimator is able to estimate the PMSG position and speed accurately under nominal and varying parameter conditions as shown in Fig. 5.40.(a) and Fig. 5.41.(a) respectively. The SMO estimator works satisfactory under steady state condition with small error, but it shows some chattering problem during dynamic conditions. The performance of SMO estimator deteriorates further with the change in PMSG parameters, as evident from Fig. 5.40.(b) and Fig. 5.41.(b) respectively.

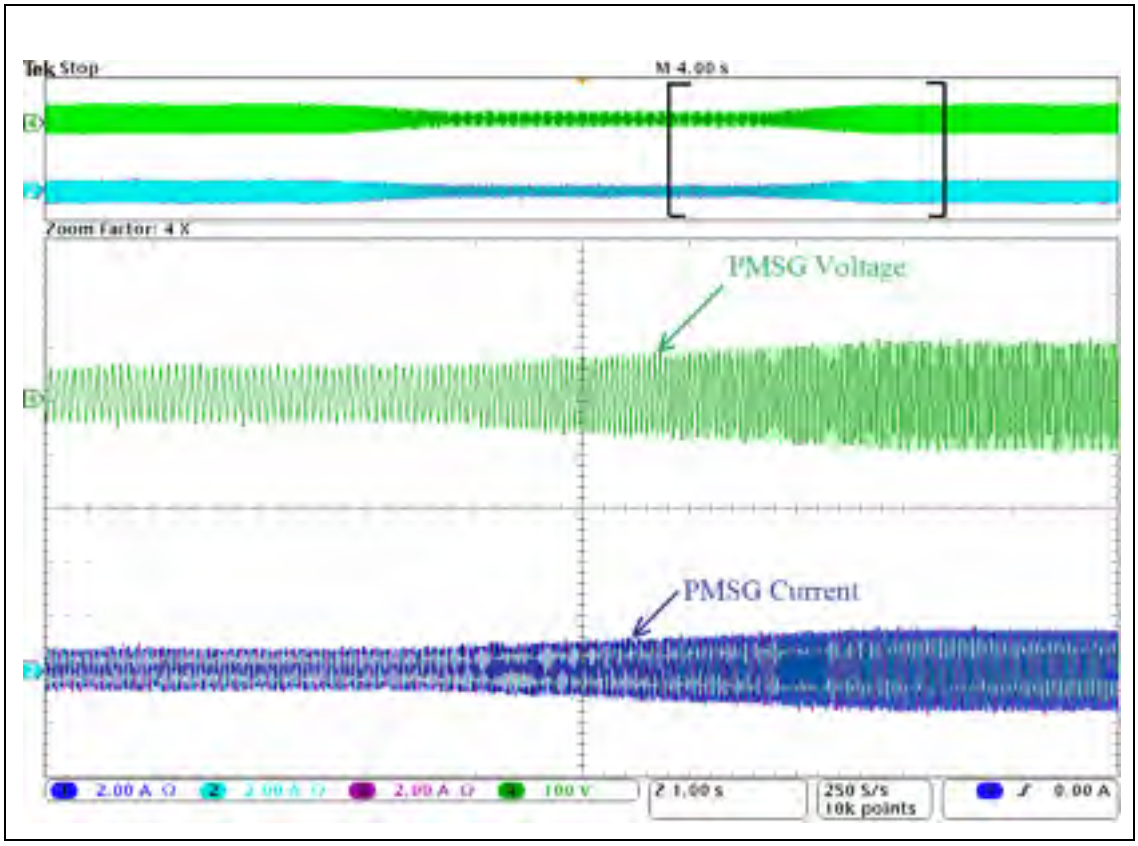

Figure 5.39 Experimental results for PMSG Voltage and Current.

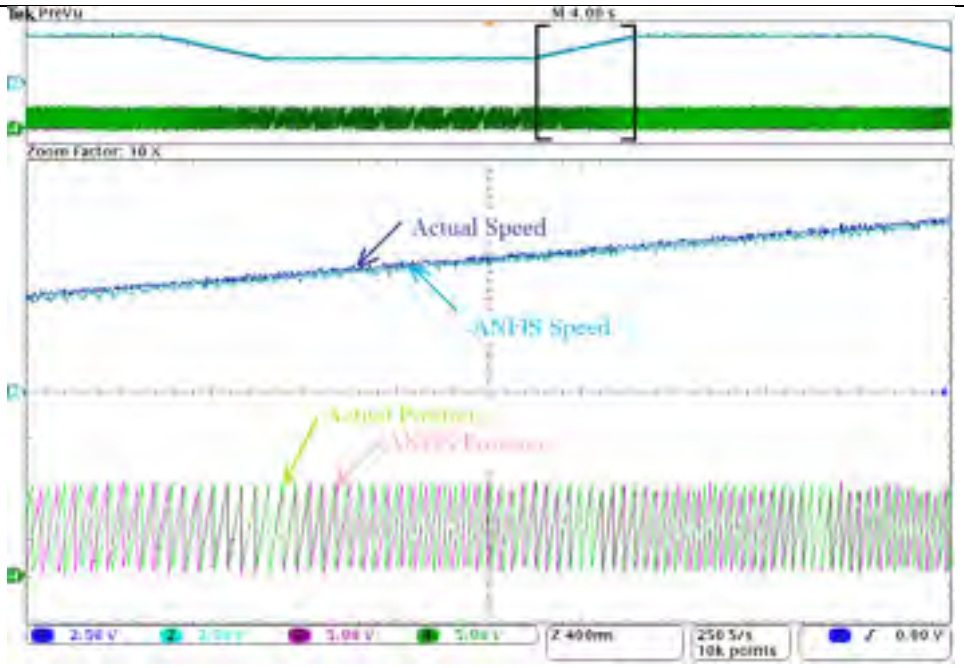

(a) ANFIS Estimator based results

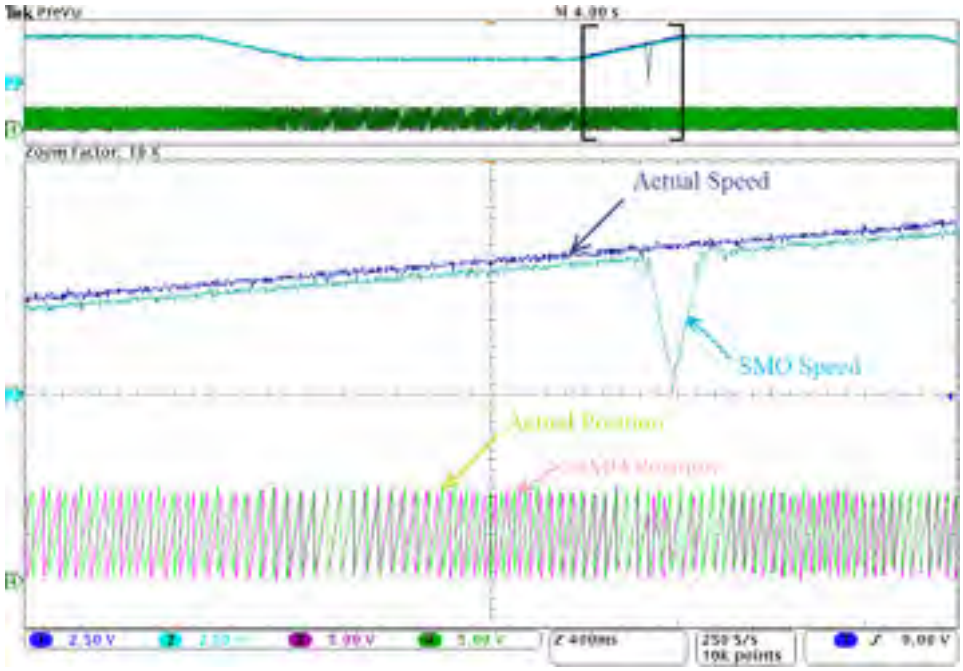

(b) SMO Estimator based results

Figure 5.40 Experimental results for Comparative Study of ANFIS and Sliding Mode Observer for Speed & Position Estimation with nominal PMSG Parameters.

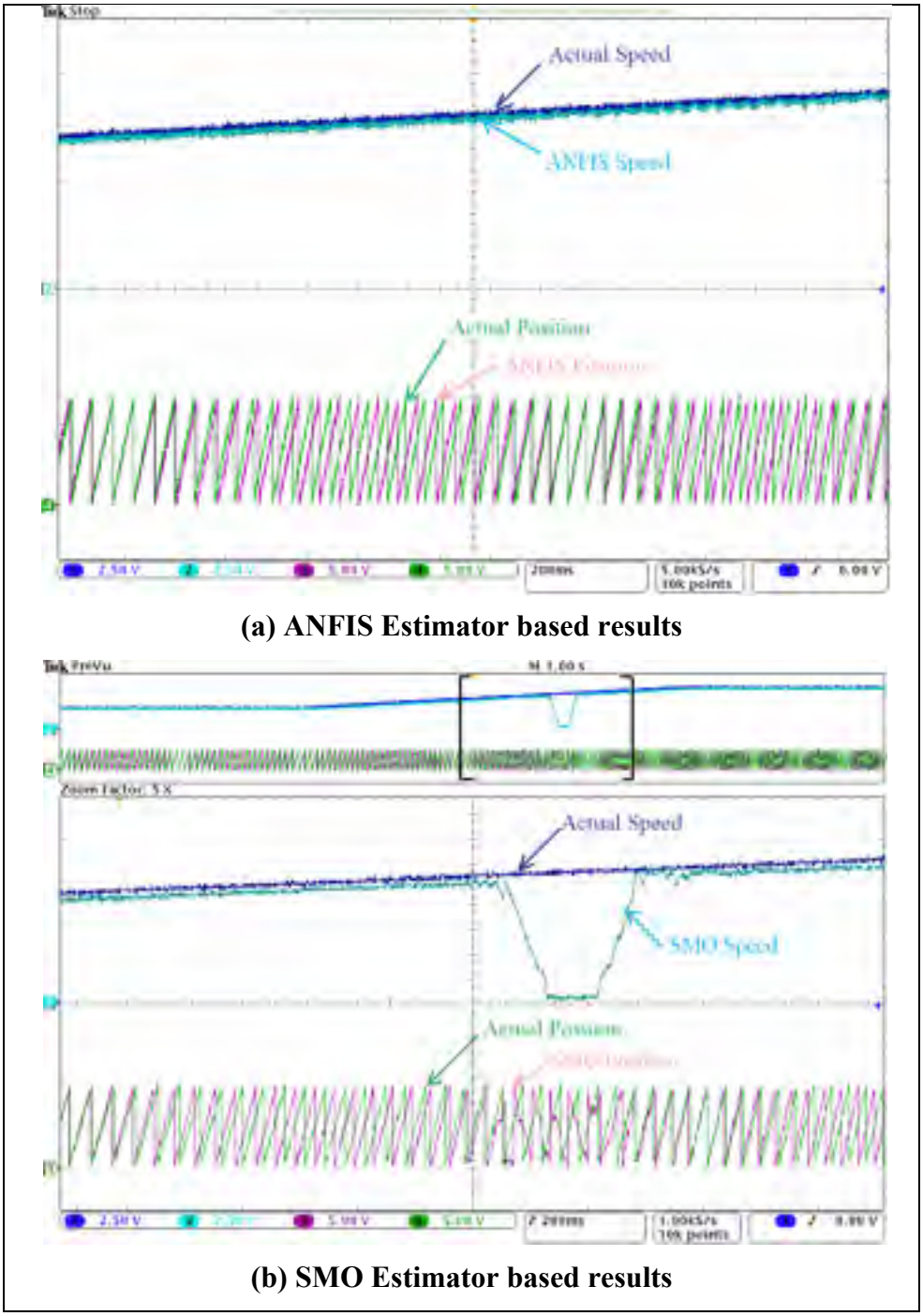

(a) ANFIS Estimator based results

(b) SMO Estimator based results

Figure 5.41 Experimental results for Comparative Study of ANFIS and Sliding Mode Observer for Speed & Position Estimation with 20% variation in PMSG resistance and inductance.

CONCLUSION

In this thesis, different kinds of control techniques for PMSG based WECS have been presented for both off-grid and grid connected application. The proposed control techniques are modelled, simulated and successfully implemented in laboratory. The extensive simulation results supported by experimental results are provided to validate the proposed control approach.

Some of the major achievements of the thesis are summarized as follows:

- For off-grid operation, a PMSG based wind/battery hybrid system is developed for different wind velocities under dynamic load conditions. The power balance between load, battery and WECS has been maintained while extracting maximum power. Under variable speed operation, the system is able to perform the maximum power point tracking, as generator speed is actively controlled according to the applied torque under varying wind conditions. The speed controller sets the reference torque command which is further utilized to obtain torque controlling current component. The system is also able to meet the variable load demand while maintaining load voltage constant.

- In grid-connected application of WECS, the capabilities of grid side inverter as multifunctional device are explored. The current regulated voltage source inverters have very wide range of applications such as grid synchronization of RES, static reactive power compensation (STATCOM), UPS, active power filters (APF) and adjustable speed drives (ASD). But in case of wind turbines, the installed inverter rating has very low utilization factor due to intermittent nature of wind, where the peak output rarely reaches to 60% of rated capacity, yet the annual capacity factor remains in between 20%-30% range. Therefore, the power quality improvement features have been incorporated in grid interfacing inverter to maximize its

utilization without any additional hardware cost of APF, usually required to compensate the non-linear load at PCC. Moreover, the proposed control strategy requires only the grid current sensing in comparision to other methods where both inverter current sensing and any one of the load or grid current sensing is required, which further reduces the cost and complexity. The grid-interfacing inverter injects the generated active power from wind turbine as well as also compensates the load reactive power, current harmonics and load imbalance in a 3-phase 4-wire system. This enables the grid to always supply/absorb a balanced set of sinusoidal currents at unity power factor (UPF) despite of non-linear unbalance load at PCC.

- Since the inverter works under highly fluctuating operating conditions, it is not possible to design a suitable PI regulator for inverter control. This may lead to false operation of inverter. To alleviate this problem an adaptive neuro-fuzzy controller is developed, which has well known advantages in modeling and control of a highly non-linear system. An adaptive error backpropagation method is used to update the weights of the system for the fast convergence of control. With the help of adaptive neuro-fuzzy controller, a smooth bidirectional power flow is achieved under the different load and variable PMSG speed operation.

- The maximum power in a wind turbine is almost the cubic function of generator speed for a given tip speed ratio. In order to achieve maximum power point tracking under variable speed operation, the continuous information of generator position and speed is essentially required. For this purpose, generally shaft mounted speed sensors are used, resulting into additional cost and complexity of the system. To alleviate the need of these sensors, a novel adaptive network-based fuzzy-inference system (ANFIS) algorithm is presented for PMSG rotor position and speed estimation over wide range of speed operation. Both the simulation and experimental studies are carried out to estimate the rotor speed and position under different operating conditions. A detailed comparison of ANFIS and sliding mode observer is also

provided under variable speed PMSG operation, where the ANFIS based observer outperforms the sliding mode observer. Both the simulation and experimental results are provided for the different values of PMSG resistance and inductance to validate the robustness of proposed algorithm against parameter variation.

- Besides this, the fault ride through capability PMSG based WECS is also presented under varying wind and voltage sag/swell conditions. Moreover, it is also demonstrated that the grid side inverter can also be used to maintain constant voltage at PCC for any dedicated load despite of voltage sag/swell and unbalance in grid side voltage.

In summary, this thesis work has presented several control strategies for variable speed PMSG based wind turbine to improve the performance of overall WECS. Moreover, it also proves that with the proper control and optimum utilization of available resources (grid side inverter), the maximum benefits from a WECS can be achieved. The work presented in this thesis with extensive simulation and experimental validation would certainly help in improving the way of wind power harvesting.

RECOMMANDATIONS

Although the research is conducted successfully, both with simulation and experimental validation, it is extremely difficult to generate the real wind operating conditions in laboratory. Therefore, the proposed algorithms can be implemented on real wind turbine to explore their maximum capabilities.

Some recommendations for future research work are as follows:

- The grid side inverter algorithms may also be utilised for other kinds of renewable energy sources. Moreover, a case study for the optimal sizing of inverter may be carried out to explore its multifunctional capabilities up to maximum extent at any given location.

- An analysis of the PMSG based wind farm may be carried out to study the voltage regulation and current sharing among the rectifier units of the wind farm.

- It has been noticed that the wind and solar enery are complimentary to each other, i.e. the wind farm generates more power during night, while the solar farm generates higher power during day time. Thus, the combination of wind and solar hybrid system may be explored in order to reduce the impact of power variation.

- Most of the power generated by Hydro-Quebec has to be transported through the long transmission lines, which requires series capacitance for transmission line compensation. It is quite possible that the use of DFIG based wind turbine may cause subsynchronous resonance (SSR) problem due to the DFIG inductance and series capacitor. Thus, a simulation study on Hydro-Quebec network with PMSG based wind turbines may be carried out to analyse the SSR problem.

ANNEXE 1

LABORATORY SETUP DETAILS

In order to implement the proposed control strategies, an experimental scaled hardware prototype is developed in laboratory. The wind turbine is emulated with the help of MATLAB/Simulink file, which rotates an induction motor at variable speed. The command signal of simulink file in real time is taken outside through D/A port of dSPACE – DS1104. Then the command signal obtained from dSPACE is applied to ACS800, an industrial drive from ABB, which further rotates the induction motor mechanically coupled to PMSG. The output of PMSG is connected to grid through two back-to-back connected inverters with a common dc-link. The schematic of laboratory experimental setup is shown in Fig. A1.1.

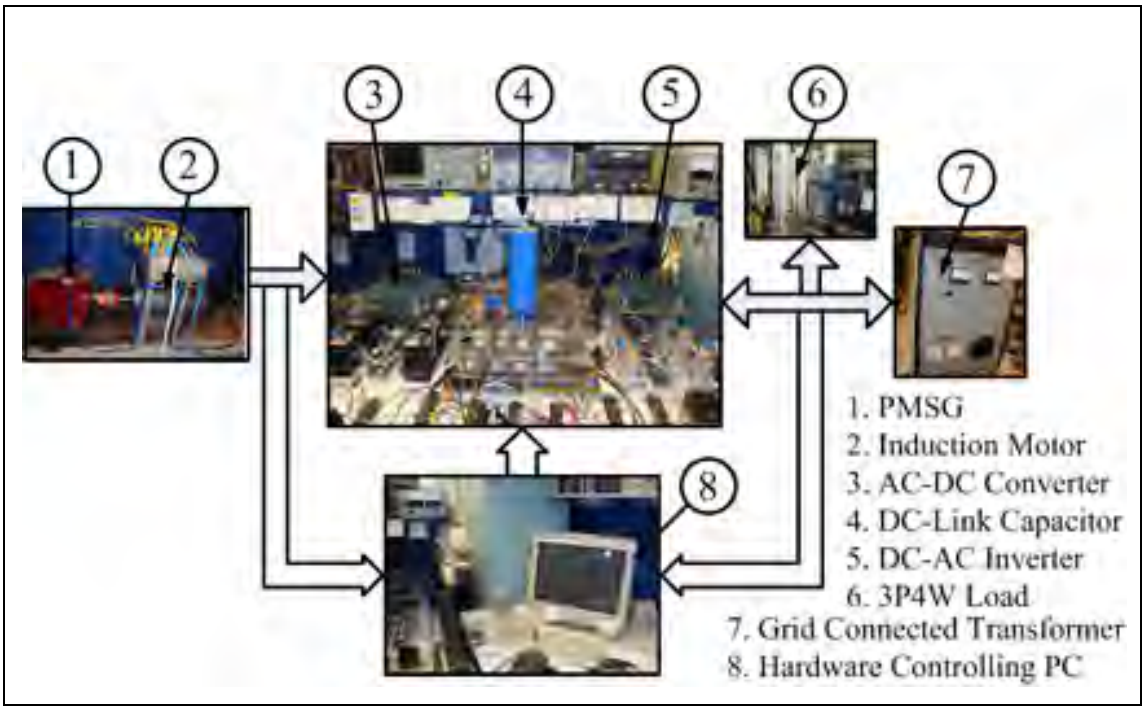

Figure A1.1 Experimental Setup.

The major components used in hardware prototype are as follows:

Voltage Source Inverters: Two voltage source inverters are realized using Insulated Gate Bipolar Transistor (IGBT) switches. The grid side inverter consists of 8-IGBT switches to perform in 3P4W system, while the generator side converter is built of 6-IGBT switches. Thus, the whole BBC configuration consists of 14-IGBT switches. The 4-leg grid side inverter can be configured into several different topologies, such as – (1) single-phase inverter (4-IGBT), (2) 3-leg inverter (6-IGBT) for 3P3W system, and (3) 4-leg inverter for 3P4W system (8-IGBT). 14 gate driver circuitries are used to drive all the 14-IGBTs simultaneously.

Sensors: To implement different algorithms and control techniques, the necessary voltages and currents are sensed using Hall-effect sensors LEM LA-55P. All the sensed signals are isolated using isolation amplifier, AD202.before sending to DSP.

Power Supplies: Most of the general purpose ICs requires +5V (or ±5V) DC supply for their operation, whereas, most of the special purpose ICs require ± 12V DC or ±15V DC supply voltages. Thus, the developed prototype requires +5V DC, ±12VDC, and ±15VDC supplies. Some of the power supplies are built in the laboratory, and some readily available DC power sources are used.

dSPACE: For real-time control of both the inverters a digital signal processor (DSP) is used. A rapid prototyping controller board from dSPACE – DS1104 is utilized for hardware implementation. With the help of DS1104 the MATLAB/ Simulink can be esily implemented in real time. The other option is the use of a core DSP process such as TMS320F2812 DSP from Texas Instruments. The TMS320F2812 requires coding the algorithm using *C* or *C*+ language, which is a time consuming task, especially when frequent changes are required in control algorithms or starting with a new algorithm. On the other hand, with the combination of MATLAB/ Simulink and dSPACE, the changes or even an entirely new control algorithm does not take much time to implement in real-

time. Moreover, it is also possible to generate *C*-codes for developed MATLAB/ Simulink Model and then can be used in a core DSP. However, the code generated in such a manner is not easy to understand and requires optimization for a better utilization of the DSP processor.

The DS1104 dSPACE board is built with – 1) a *master* microcontroller unit which has a *Motorola Power PPC 603e* processor (64 Bit Floating Point Processor with CPU Clock Frequency – 250 MHz), and 2) a slave DSP from Texas Instruments – TMS320F240 (16 Bit Fixed Point Processor). The DS1104 board consists of 8 channels for analog to digital conversion (ADC), 8 channels for digital to analog conversion (DAC), timers, interrupters, and 20 bit input – output (I/O) ports.

The actual integration between hardware and software is highlighted here:

- The *MATLAB/ Simulink* is first used as an offline simulation tool for the modeling, analysis, and design of the controller.
- The *Real-Time Interface* enhances the Simulink block library with additional blocks, which provide the link between Simulink and the real-time hardware.
- The Simulink model is transferred into real-time code using *real-time workspace* (RTW) which then generates automatic *C-codes* for developed Simulink model.
- The generated *C*-codes are then automatically loaded in then dSPACE master or slave unit, and are ready to use to achieve the desired tasks.

The sampling time in dSPACE based hardware system is determined by the MATLAB/ Simulink *real-time built procedure* depending on the complexity of the developed controller. More complex the system or higher the mathematical computations involved, longer will be the sampling time. Thus, there is always a certain minimum sampling time below which MATLAB/ Simulink build procedure gives an error – *"[#4] ds1104 – RTI: Task Overrun: Program cannot be executed in real-tim (12)"*. The user always

needs to find the minimum sample time for a particular controller using standard the *"trial and error"* procedure.

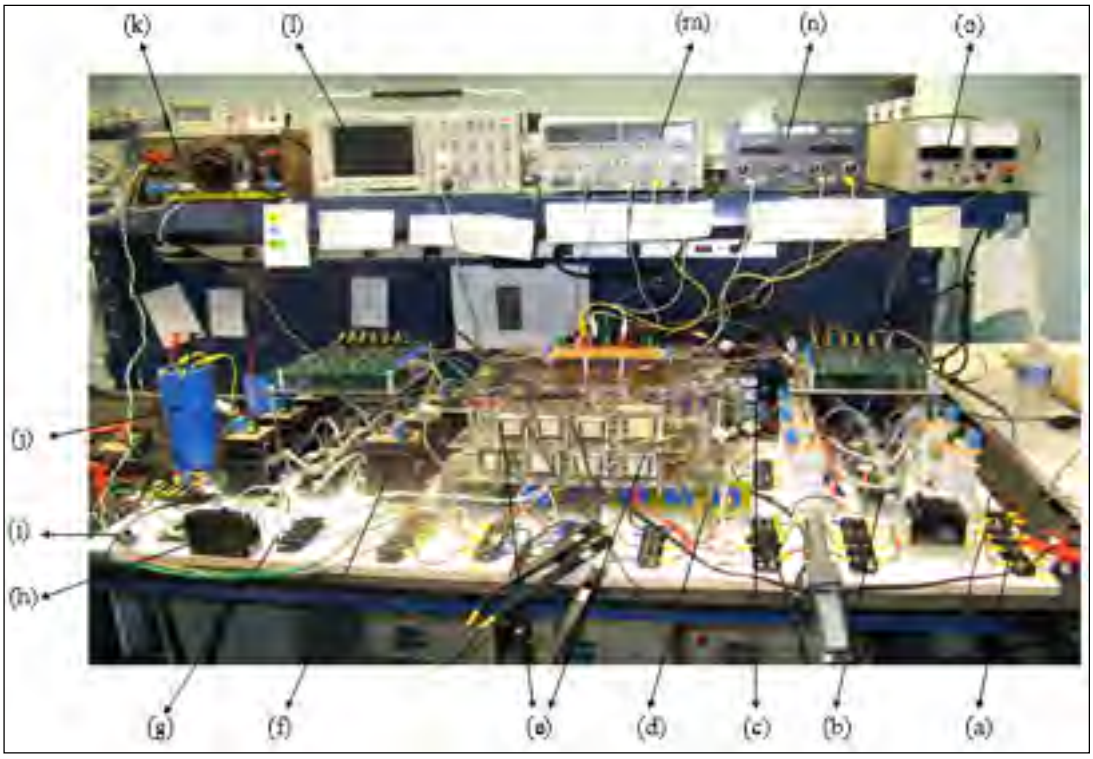

Figure A1.2 Experimental setup view: Overall BBC configuration.

(a) Source side
(b) Series inverter
(c) DS1104 dSPACE
(d) Current sensors
(e) Voltage sensors
(f) Shunt inverter
(g) Load side
(h) Manual switch to create single-phasing condition
(i) Switch to control magnetic actuator for load changing
(j) Self supporting DC bus capacitor
(k) Single phase 110V/60 Hz supply used for different interfacing circuits
(l) Oscilloscope to record experimental results (TDS3032B)
(m) ± 12V DC supply used for analog PWM board
(n) ± 10V DC supply used for dSPACE protection circuit
(o) +5V DC supply used for shunt and series inverter driver circuits

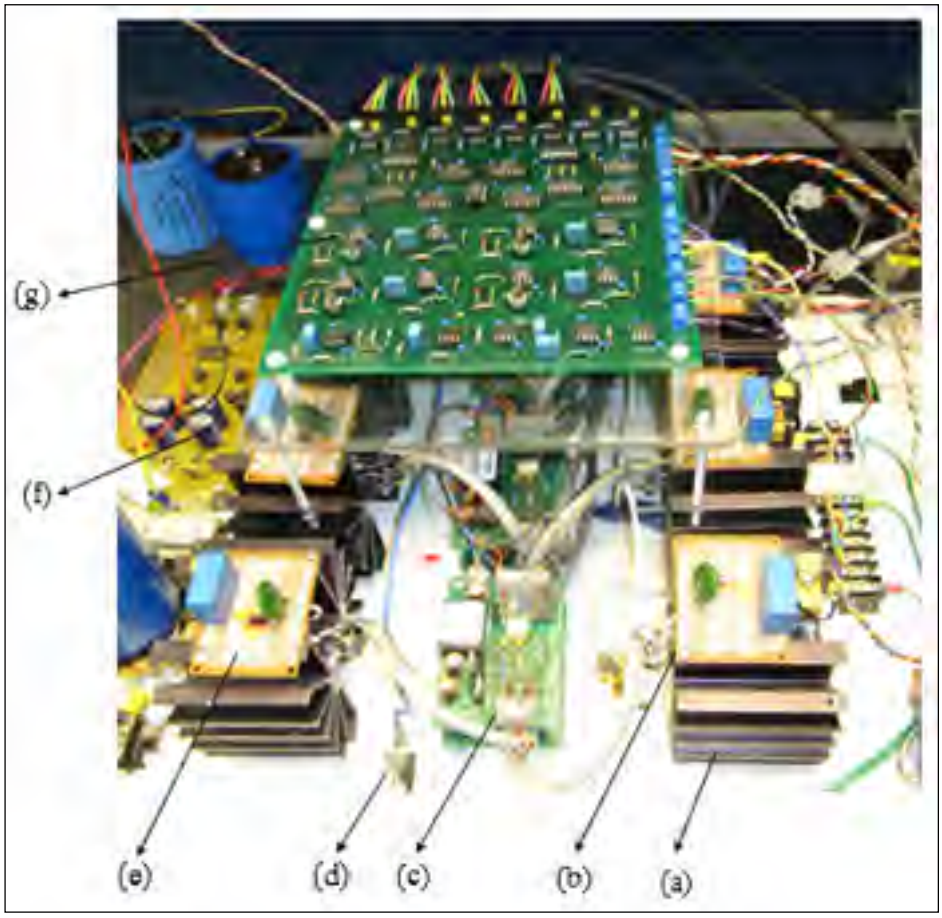

Figure A1.3 Experimental setup view: Grid Side Inverter with External PWM Circuitry.

(a) Heat sink
(b) IGBT (IXGH24N60CD1)
(c) IGBT gate driver
(d) Protection fuse
(e) Snubber circuit
(f) DC link voltage sensor
(g) Analog PWM/ Hysteresis Controller

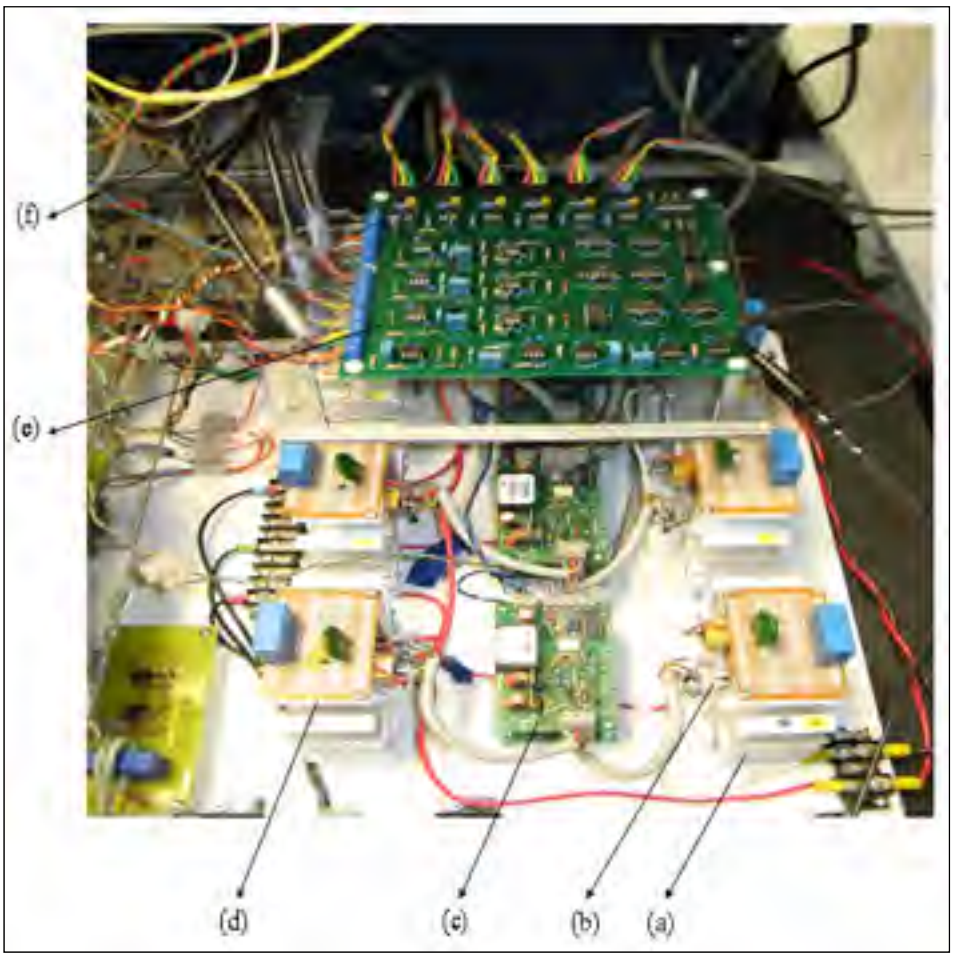

Figure A1.4 Experimental setup view: Generator Side Converter with external PWM circuitry.

(a) Heat sink
(b) IGBT (IXGH24N60CD1)
(c) IGBT gate driver
(d) Snubber circuit
(e) Analog PWM/ Hysteresis Controller
(f) DS1104 dSPACE

System Parameters

PMSG Parameters:		
Power Rating	:	2.5kW
Rated Speed	:	1800 rpm
No. of Poles	:	8@120*Hz*
Resistance	:	3.3 Ω
Inductance	:	30 *mH*
Grid Side Parameters:		
3-phase Supply (r.m.s.)	:	V_g=35 *V,* 60 *Hz*
3-phase Non-linear Load	:	R=26.66Ω
1-phase Linear Load (A-N)	:	R=60Ω, L=10 *mH*
1-phase Non-Linear Load (C-N)	:	R=26.66Ω, L=20 *mH*
DC-Link Capacitance & Voltage	:	C_{dc}=3000 μF, V_{dc}=90 *V*
Coupling Inductance	:	L_{sh}=2.0 *mH*

Inverter Switching Frequency = 5-7 kHz, L_f = 2 mH, C_f = 40 μF,
dSPACE sampling time = 80-150 μsec

ANNEXE 2

CONTROLLER GAINS

Chapter No.	Fig. No.		Inner Control Loop		Outer Control Loop	
			K_P	K_I	K_P	K_I
Chapter-3	Fig. 3.3		30	.5	8	20
	Fig. 3.4		4	20	.5	2
	Fig. 3.5		8	25	100	5
	Fig. 3.12	Gen. Side	Hysteresis Control		.5	10
		Grid Side	10	.5	1	0.1
	Fig. 3.15	V_{dc} Control	12	0.05	10	50
		V_{ac} Control	12	0.05	2	0.01
Chapter-4	Fig. 4.2		20	.1	8	7
	Fig. 4.13		Hysteresis Control		15	12
Chapter-5	Fig. 5.17		Hysteresis Control		5	100

REFERENCES

Abbes, Mohamed, Jamel Belhadj et Afef Ben Abdelghani Bennani. 2010. « Design and control of a direct drive wind turbine equipped with multilevel converters ». *Renewable Energy,* vol. 35, n° 5, p. 936-945.

Acarnley, P. P., et J. F. Watson. 2006. « Review of position-sensorless operation of brushless permanent-magnet machines ». *Industrial Electronics, IEEE Transactions on,* vol. 53, n° 2, p. 352-362.

Agarwal, V., R. K. Aggarwal, P. K. Patidar et C. K. Patki. 2010. « A Novel Scheme for Rapid Tracking of Maximum Power Point in Wind Energy Generation Systems ». *Energy Conversion, IEEE Transactions on,* vol. 25, n° 1, p. 228-236.

Alepuz, S., S. Busquets-Monge, J. Bordonau, J. Gago, D. Gonzalez et J. Balcells. 2006. « Interfacing Renewable Energy Sources to the Utility Grid Using a Three-Level Inverter ». *Industrial Electronics, IEEE Transactions on,* vol. 53, n° 5, p. 1504-1511.

Aredes, M., et E. H. Watanabe. 1995. « New control algorithms for series and shunt three-phase four-wire active power filters ». *Power Delivery, IEEE Transactions on,* vol. 10, n° 3, p. 1649-1656.

Asiminoaei, L., F. Blaabjerg et S. Hansen. 2007. « Detection is key - Harmonic detection methods for active power filter applications ». *Industry Applications Magazine, IEEE,* vol. 13, n° 4, p. 22-33.

Baroudi, Jamal A., Venkata Dinavahi et Andrew M. Knight. 2007. « A review of power converter topologies for wind generators ». *Renewable Energy,* vol. 32, n° 14, p. 2369-2385.

Batzel, T. D., et K. Y. Lee. 2003. « An approach to sensorless operation of the permanent-magnet synchronous motor using diagonally recurrent neural networks ». *Energy Conversion, IEEE Transactions on,* vol. 18, n° 1, p. 100-106.

Bayindir, R., I. Colak, E. Kabalci et E. Irmak. 2009. « The Fuzzy Logic Control of a Multilevel Converter in a Variable Speed Wind Turbine ». In *Machine Learning and Applications, 2009. ICMLA '09. International Conference on*. p. 787-790.

Behera, R. K., Gao Wenzhong et O. Ojo. 2009. « Simulation study of permanent magnet synchronous machine direct drive wind power generator using three level NPC converter system ». In *Power Electronics and Machines in Wind Applications, 2009. PEMWA 2009. IEEE*. p. 1-7.

Bernard, S., D. Beaulieu et G. Trudel. 2005. « Hydro-Quebec grid code for wind farm interconnection ». In *Power Engineering Society General Meeting, 2005. IEEE* (12-16 June 2005). p. 1248-1252 Vol. 2.

Bhowmik, S., et R. Spee. 1998. « Wind speed estimation based variable speed wind power generation ». In *Industrial Electronics Society, 1998. IECON '98. Proceedings of the 24th Annual Conference of the IEEE*. Vol. 2, p. 596-601 vol.2.

Bianchi, N., et A. Lorenzoni. 1996. « Permanent magnet generators for wind power industry: an overall comparison with traditional generators ». In *Opportunities and Advances in International Electric Power Generation, International Conference on (Conf. Publ. No. 419)*. p. 49-54.

Blaabjerg, F., R. Teodorescu, M. Liserre et A. V. Timbus. 2006. « Overview of Control and Grid Synchronization for Distributed Power Generation Systems ». *Industrial Electronics, IEEE Transactions on,* vol. 53, n° 5, p. 1398-1409.

Boccard, Nicolas. 2009. « Capacity factor of wind power realized values vs. estimates ». *Energy Policy,* vol. 37, n° 7, p. 2679-2688.

Boldea, I. 2008. « Control issues in adjustable speed drives ». *Industrial Electronics Magazine, IEEE,* vol. 2, n° 3, p. 32-50.

Bolognani, S., L. Tubiana et M. Zigliotto. 2003. « Extended Kalman filter tuning in sensorless PMSM drives ». *Industry Applications, IEEE Transactions on,* vol. 39, n° 6, p. 1741-1747.

Borup, U., F. Blaabjerg et P. N. Enjeti. 2001. « Sharing of nonlinear load in parallel-connected three-phase converters ». *Industry Applications, IEEE Transactions on,* vol. 37, n° 6, p. 1817-1823.

Brahmi, Jemaa, Lotfi Krichen et Abderrazak Ouali. 2009. « A comparative study between three sensorless control strategies for PMSG in wind energy conversion system ». *Applied Energy,* vol. 86, n° 9, p. 1565-1573.

Bueno, E. J., S. Cobreces, F. J. Rodriguez, A. Hernandez et F. Espinosa. 2008. « Design of a Back-to-Back NPC Converter Interface for Wind Turbines With Squirrel-Cage Induction Generator ». *Energy Conversion, IEEE Transactions on,* vol. 23, n° 3, p. 932-945.

Cardenas, R., R. Pena, G. Asher et J. Clare. 2004. « Power smoothing in wind generation systems using a sensorless vector controlled induction Machine

driving a flywheel ». *Energy Conversion, IEEE Transactions on,* vol. 19, n° 1, p. 206-216.

Cardenas, R., R. Pena, J. Clare et G. Asher. 2003. « Power smoothing in a variable speed wind-diesel system ». In *Power Electronics Specialist Conference, 2003. PESC '03. 2003 IEEE 34th Annual*. Vol. 2, p. 754-759 vol.2.

Cardenas, R., R. Pena, M. Perez, J. Clare, G. Asher et F. Vargas. 2006. « Vector Control of Front-End Converters for Variable-Speed Wind–Diesel Systems ». *Industrial Electronics, IEEE Transactions on,* vol. 53, n° 4, p. 1127-1136.

Carrasco, J. M., L. G. Franquelo, J. T. Bialasiewicz, E. Galvan, R. C. P. Guisado, Ma A. M. Prats, J. I. Leon et N. Moreno-Alfonso. 2006. « Power-Electronic Systems for the Grid Integration of Renewable Energy Sources: A Survey ». *Industrial Electronics, IEEE Transactions on,* vol. 53, n° 4, p. 1002-1016.

Chaudhari, M. A., et H. M. Suryawanshi. 2008. « Analysis and design of three-phase rectifier operating in discontinuous conduction mode using high-frequency current injection technique ». *Power Electronics, IET,* vol. 1, n° 4, p. 419-432.

Chen, Z., et Y. Hu. 2003. « A hybrid generation system using variable speed wind turbines and diesel units ». In *Industrial Electronics Society, 2003. IECON '03. The 29th Annual Conference of the IEEE*. Vol. 3, p. 2729-2734 Vol.3.

Chinchilla, M., S. Arnaltes et J. C. Burgos. 2006. « Control of permanent-magnet generators applied to variable-speed wind-energy systems connected to the grid ». *Energy Conversion, IEEE Transactions on,* vol. 21, n° 1, p. 130-135.

Ching-Yin, Lee, Chen Li-Chieh, Tsai Shao-Hong, Liu Wen-Tsan et Wu Yuan-Kang. 2009. « The Impact of SCIG Wind Farm Connecting into a Distribution System ». In *Power and Energy Engineering Conference, 2009. APPEEC 2009. Asia-Pacific*. p. 1-7.

Dehghan, S. M., M. Mohamadian et A. Y. Varjani. 2009. « A New Variable-Speed Wind Energy Conversion System Using Permanent-Magnet Synchronous Generator and Z Source Inverter ». *Energy Conversion, IEEE Transactions on,* vol. 24, n° 3, p. 714-724.

Denai, M. A., F. Palis et A. Zeghbib. 2004. « ANFIS based modelling and control of non-linear systems : a tutorial ». In *Systems, Man and Cybernetics, 2004 IEEE International Conference on*. Vol. 4, p. 3433-3438 vol.4.

Elbuluk, M. E., Tong Liu et I. Husain. 2002. « Neural-network-based model reference adaptive systems for high-performance motor drives and motion controls ». *Industry Applications, IEEE Transactions on,* vol. 38, n° 3, p. 879-886.

Elnashar, M., M. Kazerani, R. El Shatshat et M. M. A. Salama. 2008. « Comparative evaluation of reactive power compensation methods for a stand-alone wind energy conversion system ». In *Power Electronics Specialists Conference, 2008. PESC 2008. IEEE*. p. 4539-4544.

Enslin, J. H. R., et P. J. M. Heskes. 2004. « Harmonic interaction between a large number of distributed power inverters and the distribution network ». *Power Electronics, IEEE Transactions on,* vol. 19, n° 6, p. 1586-1593.

Fatu, M., C. Lascu, G. D. Andreescu, R. Teodorescu, F. Blaabjerg et I. Boldea. 2007. « Voltage Sags Ride-Through of Motion Sensorless Controlled PMSG for Wind Turbines ». In *Industry Applications Conference, 2007. 42nd IAS Annual Meeting. Conference Record of the 2007 IEEE*. p. 171-178.

Fu, Xunbo, Jindong Guo, Dongli Zhao et Honghua Xu. 2009. « Research on the characteristics of back to back full-size converter applied to direct drive wind power system ». In *Sustainable Power Generation and Supply, 2009. SUPERGEN '09. International Conference on*. p. 1-7.

Fujin, Deng, et Chen Zhe. 2009. « Low-voltage ride-through of variable speed wind turbines with permanent magnet synchronous generator ». In *Industrial Electronics, 2009. IECON '09. 35th Annual Conference of IEEE* (3-5 Nov. 2009). p. 621-626.

Garcia, A. M., D. G. Holmes et T. A. Lipo. 2006. « Reduction of Bearing Currents in Doubly Fed Induction Generators ». In *Industry Applications Conference, 2006. 41st IAS Annual Meeting. Conference Record of the 2006 IEEE*. Vol. 1, p. 84-89.

Goel, P., B. Singh, S. Murthy et N. Kishore. 2009. « Isolated Wind-Hydro Hybrid System Using Cage Generators and Battery Storage ». *Industrial Electronics, IEEE Transactions on,* vol. PP, n° 99, p. 1-1.

Gonzalez, L. G., E. Figueres, G. Garcera, O. Carranza et F. Gonzalez-Espin. 2009. « Synchronization techniques comparison for sensorless control applied to Wind Energy Conversion Systems (WECS) ». In *Power Electronics and Applications, 2009. EPE '09. 13th European Conference on*. p. 1-9.

Guerrero, J. M., L. G. de Vicuna, J. Matas, M. Castilla et J. Miret. 2004. « A wireless controller to enhance dynamic performance of parallel inverters in distributed

generation systems ». *Power Electronics, IEEE Transactions on,* vol. 19, n° 5, p. 1205-1213.

Ha, L. T., et T. K. Saha. 2004. « Investigation of power loss and voltage stability limits for large wind farm connections to a subtransmission network ». In *Power Engineering Society General Meeting, 2004. IEEE* (10-10 June 2004). p. 2251-2256 Vol.2.

Hamdi, M., G. Lachiver et M. Ghribi. 1995. « A sensorless control scheme based on fuzzy logic for AC servo drives using a permanent-magnet synchronous motor ». In *Electrical and Computer Engineering, 1995. Canadian Conference on*. Vol. 1, p. 306-309 vol.1.

Hansen, A. D., et G. Michalke. 2009. « Multi-pole permanent magnet synchronous generator wind turbines' grid support capability in uninterrupted operation during grid faults ». *Renewable Power Generation, IET,* vol. 3, n° 3, p. 333-348.

Haque, M. E., K. M. Muttaqi et M. Negnevitsky. 2008. « Control of a stand alone variable speed wind turbine with a permanent magnet synchronous generator ». In *Power and Energy Society General Meeting - Conversion and Delivery of Electrical Energy in the 21st Century, 2008 IEEE*. p. 1-9.

Haque, M. E., M. Negnevitsky et K. M. Muttaqi. 2010. « A Novel Control Strategy for a Variable-Speed Wind Turbine With a Permanent-Magnet Synchronous Generator ». *Industry Applications, IEEE Transactions on,* vol. 46, n° 1, p. 331-339.

Hui, Li, K. L. Shi et P. G. McLaren. 2005. « Neural-network-based sensorless maximum wind energy capture with compensated power coefficient ». *Industry Applications, IEEE Transactions on,* vol. 41, n° 6, p. 1548-1556.

Hurtado, S., G. Gostales, A. de Lara, N. Moreno, J. M. Carrasco, E. Galvan, J. A. Sanchez et L. G. Franquelo. 2002. « A new power stabilization control system based on making use of mechanical inertia of a variable-speed wind-turbine for stand-alone wind-diesel applications ». In *IECON 02 [Industrial Electronics Society, IEEE 2002 28th Annual Conference of the]*. Vol. 4, p. 3326-3331 vol.4.

IEEE Application Guide for IEEE Std 1547, IEEE « Standard for Interconnecting Distributed Resources with Electric Power Systems ». 2009. *IEEE Std 1547.2-2008*, p. 1-207.

Iglesias, I. J., L. Garcia-Tabares, A. Agudo, I. Cruz et L. Arribas. 2000. « Design and simulation of a stand-alone wind-diesel generator with a flywheel energy storage system to supply the required active and reactive power ». In *Power Electronics*

Specialists Conference, 2000. PESC 00. 2000 IEEE 31st Annual. Vol. 3, p. 1381-1386 vol.3.

Jang, J. S. R. 1993. « ANFIS: adaptive-network-based fuzzy inference system ». *Systems, Man and Cybernetics, IEEE Transactions on,* vol. 23, n° 3, p. 665-685.

Jingya, Dai, D. D. Xu et Wu Bin. 2009. « A Novel Control Scheme for Current-Source-Converter-Based PMSG Wind Energy Conversion Systems ». *Power Electronics, IEEE Transactions on,* vol. 24, n° 4, p. 963-972.

Jintakosonwit, P., H. Akagi, H. Fujita et S. Ogasawara. 2002. « Implementation and performance of automatic gain adjustment in a shunt-active filter for harmonic damping throughout a power distribution system ». *Power Electronics, IEEE Transactions on,* vol. 17, n° 3, p. 438-447.

Jintakosonwit, P., H. Fujita, H. Akagi et S. Ogasawara. 2003. « Implementation and performance of cooperative control of shunt active filters for harmonic damping throughout a power distribution system ». *Industry Applications, IEEE Transactions on,* vol. 39, n° 2, p. 556-564.

Keyuan, Huang, Huang Shoudao, She Feng, Luo Baimin et Cai Luoqiang. 2008. « A control strategy for direct-drive permanent-magnet wind-power generator using back-to-back PWM converter ». In *Electrical Machines and Systems, 2008. ICEMS 2008. International Conference on*. p. 2283-2288.

Kinjo, F., A. K. Wallace et A. von Jouanne. 2004. « Maximization of energy capture of passive, variable-speed wind turbine ». In *Power Electronics, Machines and Drives, 2004. (PEMD 2004). Second International Conference on (Conf. Publ. No. 498)*. Vol. 1, p. 379 Vol.1.

Li, Jian-lin, Shu-ju Hu, Mei Li, Ying Zhu, De-guo Kong et Hong-hua Xu. 2008. « Research on the application of parallel back-to-back PWM converter on direct-drive wind power system ». In *Electric Utility Deregulation and Restructuring and Power Technologies, 2008. DRPT 2008. Third International Conference on*. p. 2504-2508.

Lie, Xu, et Wang Yi. 2007. « Dynamic Modeling and Control of DFIG-Based Wind Turbines Under Unbalanced Network Conditions ». *Power Systems, IEEE Transactions on,* vol. 22, n° 1, p. 314-323.

Maiti, Suman, Chandan Chakraborty et Sabyasachi Sengupta. 2009. « Simulation studies on model reference adaptive controller based speed estimation technique for the vector controlled permanent magnet synchronous motor drive ». *Simulation Modelling Practice and Theory,* vol. 17, n° 4, p. 585-596.

Morren, J., et S. W. H. de Haan. 2005. « Ridethrough of wind turbines with doubly-fed induction generator during a voltage dip ». *Energy Conversion, IEEE Transactions on,* vol. 20, n° 2, p. 435-441.

Muljadi, E., C. P. Butterfield, B. Parsons et A. Ellis. 2007a. « Characteristics of Variable Speed Wind Turbines Under Normal and Fault Conditions ». In *Power Engineering Society General Meeting, 2007. IEEE* (24-28 June 2007). p. 1-7.

Muljadi, E., C. P. Butterfield, B. Parsons et A. Ellis. 2007b. « Effect of Variable Speed Wind Turbine Generator on Stability of a Weak Grid ». *Energy Conversion, IEEE Transactions on,* vol. 22, n° 1, p. 29-36.

Muyeen, S. M., R. Takahashi, T. Murata et J. Tamura. 2010. « A Variable Speed Wind Turbine Control Strategy to Meet Wind Farm Grid Code Requirements ». *Power Systems, IEEE Transactions on,* vol. 25, n° 1, p. 331-340.

Nayar, C. V., S. M. Islam, H. Dehbonei, K. Tan et H. Sharma. 2007. « Power electronics for renewable energy sources ». In *Power Electronics Handbook (Second Edition)*, sous la dir. de Muhammad, H. Rashid, Ph.D, I. E. E. Fellow et Ieee Fellow. doi: DOI: 10.1016/B978-012088479-7/50045-6. p. 673-716. Burlington: Academic Press.

Peixoto, Z. M. A., F. M. F. Sa, P. F. Seixas, B. R. Menezes et P. C. Cortizo. 1995. « Speed control of permanent magnet motors using sliding mode observers for induced EMF position and speed estimation ». In *Industrial Electronics, Control, and Instrumentation, 1995., Proceedings of the 1995 IEEE IECON 21st International Conference on*. Vol. 2, p. 1023-1028 vol.2.

Polinder, H., D. Bang, R. P. J. O. M. van Rooij, A. S. McDonald et M. A. Mueller. 2007. « 10 MW Wind Turbine Direct-Drive Generator Design with Pitch or Active Speed Stall Control ». In *Electric Machines & Drives Conference, 2007. IEMDC '07. IEEE International* (3-5 May 2007). Vol. 2, p. 1390-1395.

Polinder, H., F. F. A. van der Pijl, G. J. de Vilder et P. J. Tavner. 2006. « Comparison of direct-drive and geared generator concepts for wind turbines ». *Energy Conversion, IEEE Transactions on,* vol. 21, n° 3, p. 725-733.

Portillo, R. C., M. M. Prats, J. I. Leon, J. A. Sanchez, J. M. Carrasco, E. Galvan et L. G. Franquelo. 2006. « Modeling Strategy for Back-to-Back Three-Level Converters Applied to High-Power Wind Turbines ». *Industrial Electronics, IEEE Transactions on,* vol. 53, n° 5, p. 1483-1491.

Pregitzer, R., J. G. Pinto, L. F. C. Monteiro et J. L. Afonso. 2007. « Shunt Active Power Filter with Dynamic Output Current Limitation ». In *Industrial Electronics, 2007. ISIE 2007. IEEE International Symposium on*. p. 1021-1026.

Rahmani, S., A. Hamadi, N. Mendalek et K. Al-Haddad. 2009. « A New Control Technique for Three-Phase Shunt Hybrid Power Filter ». *Industrial Electronics, IEEE Transactions on,* vol. 56, n° 8, p. 2904-2915.

Renders, B., K. De Gusseme, W. R. Ryckaert, K. Stockman, L. Vandevelde et M. H. J. Bollen. 2008. « Distributed Generation for Mitigating Voltage Dips in Low-Voltage Distribution Grids ». *Power Delivery, IEEE Transactions on,* vol. 23, n° 3, p. 1581-1588.

Rossi, C., G. Grandi, P. Corbelli et D. Casadei. 2009. « Generation system for series hybrid powertrain based on the dual two-level inverter ». In *Power Electronics and Applications, 2009. EPE '09. 13th European Conference on*. p. 1-10.

Rubaai, A., A. R. Ofoli, L. Burge, III et M. Garuba. 2005. « Hardware implementation of an adaptive network-based fuzzy controller for DC-DC converters ». *Industry Applications, IEEE Transactions on,* vol. 41, n° 6, p. 1557-1565.

Saccomando, G., J. Svensson et A. Sannino. 2002a. « Improving voltage disturbance rejection for variable-speed wind turbines ». In *Power Engineering Society Summer Meeting, 2002 IEEE*. Vol. 1, p. 502 vol.1.

Saccomando, G., J. Svensson et A. Sannino. 2002b. « Improving voltage disturbance rejection for variable-speed wind turbines ». *Energy Conversion, IEEE Transactions on,* vol. 17, n° 3, p. 422-428.

Sanchez, J. A., N. Moreno, S. Vazquez, J. M. Carrasco, E. Galvan, C. Batista, S. Hurtado et G. Costales. 2003. « A 800 kW wind-diesel test bench based on the MADE AE-52 variable speed wind turbine ». In *Industrial Electronics Society, 2003. IECON '03. The 29th Annual Conference of the IEEE*. Vol. 2, p. 1314-1319 Vol.2.

Sánchez, J. A., C. Veganzones, S. Martínez, F. Blázquez, N. Herrero et J. R. Wilhelmi. 2008. « Dynamic model of wind energy conversion systems with variable speed synchronous generator and full-size power converter for large-scale power system stability studies ». *Renewable Energy,* vol. 33, n° 6, p. 1186-1198.

Senjyu, T., T. Kinjo, K. Uezato et H. Fujita. 2004a. « Analysis of terminal voltage and output power control of wind turbine generator by series and parallel compensation using SMES ». In *Power Electronics Specialists Conference, 2004. PESC 04. 2004 IEEE 35th Annual*. Vol. 6, p. 4278-4284 Vol.6.

Senjyu, T., S. Tamaki, N. Urasaki, K. Uezato, H. Higa, T. Funabashi, H. Fujita et H. Sekine. 2004b. « Wind velocity and rotor position sensorless maximum power point tracking control for wind generation system ». In *Industrial Electronics Society, 2004. IECON 2004. 30th Annual Conference of IEEE*. Vol. 2, p. 1957-1962 Vol. 2.

Shoudao, Huang, Chen Shun, Chen Zhe, Huang Keyuan et Luo Baimin. 2009. « Application of a novel soft phase-locked loop in directly-driven permanent magnet wind power generation system ». In *Electrical Machines and Systems, 2009. ICEMS 2009. International Conference on*. p. 1-6.

Shuhui, Li, et T. A. Haskew. 2007. « Analysis of Decoupled d-q Vector Control in DFIG Back-to-Back PWM Converter ». In *Power Engineering Society General Meeting, 2007. IEEE*. p. 1-7.

Singh, B., et G. K. Kasal. 2008. « Voltage and Frequency Controller for a Three-Phase Four-Wire Autonomous Wind Energy Conversion System ». *Energy Conversion, IEEE Transactions on,* vol. 23, n^{o} 2, p. 509-518.

Singh, M., et A. Chandra. 2008. « Power maximization and voltage sag/swell ride-through capability of PMSG based variable speed wind energy conversion system ». In *Industrial Electronics, 2008. IECON 2008. 34th Annual Conference of IEEE*. p. 2206-2211.

Singh, M., et A. Chandra. 2009. « Control of PMSG based variable speed wind-battery hybrid system in an isolated network ». In *Power & Energy Society General Meeting, 2009. PES '09. IEEE* (26-30 July 2009). p. 1-6.

Strachan, N. P. W., et D. Jovcic. 2008. « Improving wind power quality using an integrated Wind Energy Conversion and Storage System (WECSS) ». In *Power and Energy Society General Meeting - Conversion and Delivery of Electrical Energy in the 21st Century, 2008 IEEE*. p. 1-8.

Sun, T., Z. Chen et F. Blaabjerg. 2004. « Voltage recovery of grid-connected wind turbines with DFIG after a short-circuit fault ». In *Power Electronics Specialists Conference, 2004. PESC 04. 2004 IEEE 35th Annual*. Vol. 3, p. 1991-1997 Vol.3.

Tafticht, T., K. Agbossou et A. Cheriti. 2006. « DC bus control of variable speed wind turbine using a buck-boost converter ». In *Power Engineering Society General Meeting, 2006. IEEE*. p. 5 pp.

Tan, K., et S. Islam. 2004. « Optimum control strategies in energy conversion of PMSG wind turbine system without mechanical sensors ». *Energy Conversion, IEEE Transactions on,* vol. 19, n° 2, p. 392-399.

Taniguchi, S., S. Mochiduki, T. Yamakawa, S. Wakao, K. Kondo et T. Yoneyama. 2009. « Starting Procedure of Rotational Sensorless PMSM in the Rotating Condition ». *Industry Applications, IEEE Transactions on,* vol. 45, n° 1, p. 194-202.

Tonkoski, R., L. A. C. Lopes et F. Dos Reis. 2009. « A single-switch three-phase boost rectifier to reduce the generator losses in wind energy conversion systems ». In *Electrical Power & Energy Conference (EPEC), 2009 IEEE*. p. 1-8.

Tze-Fun, Chan, et L. L. Lai. 2007. « Permanent-Magnet Machines for Distributed Power Generation: A Review ». In *Power Engineering Society General Meeting, 2007. IEEE*. p. 1-6.

Valenciaga, F., et P. F. Puleston. 2008. « High-Order Sliding Control for a Wind Energy Conversion System Based on a Permanent Magnet Synchronous Generator ». *Energy Conversion, IEEE Transactions on,* vol. 23, n° 3, p. 860-867.

Varma, R. K., S. Auddy et Y. Semsedini. 2008. « Mitigation of Subsynchronous Resonance in a Series-Compensated Wind Farm Using FACTS Controllers ». *Power Delivery, IEEE Transactions on,* vol. 23, n° 3, p. 1645-1654.

Vilathgamuwa, D. M., S. D. G. Jayasinghe et U. K. Madawala. 2009. « Space vector modulated cascade multi-level inverter for PMSG wind generation systems ». In *Industrial Electronics, 2009. IECON '09. 35th Annual Conference of IEEE*. p. 4600-4605.

Wei, Qiao, R. G. Harley et G. K. Venayagamoorthy. 2009. « Coordinated Reactive Power Control of a Large Wind Farm and a STATCOM Using Heuristic Dynamic Programming ». *Energy Conversion, IEEE Transactions on,* vol. 24, n° 2, p. 493-503.

Wei, Qiao, Qu Liyan et R. G. Harley. 2009. « Control of IPM Synchronous Generator for Maximum Wind Power Generation Considering Magnetic Saturation ». *Industry Applications, IEEE Transactions on,* vol. 45, n° 3, p. 1095-1105.

Weihao, Hu, Wang Yue, Song Xianwen et Wang Zhaoan. 2009a. « A Novel Sensorless Unity Power Factor Control Method for Six-phase PMSG in Direct Drive Wind Energy Conversion Systems ». In *Applied Power Electronics Conference and Exposition, 2009. APEC 2009. Twenty-Fourth Annual IEEE*. p. 744-749.

Weihao, Hu, Chen Zhe, Wang Yue et Wang Zhaoan. 2009b. « Flicker Mitigation by Active Power Control of Variable-Speed Wind Turbines With Full-Scale Back-to-Back Power Converters ». *Energy Conversion, IEEE Transactions on,* vol. 24, n° 3, p. 640-649.

Xiaoyu, Wang, D. M. Vilathgamuwa, K. J. Tseng et C. J. Gajanayake. 2009. « Controller design for variable-speed permanent magnet wind turbine generators interfaced with Z-source inverter ». In *Power Electronics and Drive Systems, 2009. PEDS 2009. International Conference on*. p. 752-757.

Yacoubi, L., K. Al-Haddad, L. A. Dessaint et F. Fnaiech. 2006. « Linear and Nonlinear Control Techniques for a Three-Phase Three-Level NPC Boost Rectifier ». *Industrial Electronics, IEEE Transactions on,* vol. 53, n° 6, p. 1908-1918.

Yang, Liyong, Peie Yuan, Zhenguo Chang, Zhigang Chen et Zhengxi Li. 2009. « A novel control strategy of power converter used to direct driven permanent magnet wind power generation system ». In *Power Electronics and Intelligent Transportation System (PEITS), 2009 2nd International Conference on*. Vol. 1, p. 456-459.

Yazhou, Lei, A. Mullane, G. Lightbody et R. Yacamini. 2006. « Modeling of the wind turbine with a doubly fed induction generator for grid integration studies ». *Energy Conversion, IEEE Transactions on,* vol. 21, n° 1, p. 257-264.

Yuan-zhang, Sun, Lin Jin, Li Guo-jie et Li Xiong. 2009. « A review on the integration of wind farms with variable speed wind turbine systems into power systems ». In *Sustainable Power Generation and Supply, 2009. SUPERGEN '09. International Conference on* (6-7 April 2009). p. 1-6.

Zhang, S., K. Tseng, M. Vilathgamuwa et D. Nguyen. 2010. « Design of a Robust Grid Interface System for PMSG-based Wind Turbine Generators ». *Industrial Electronics, IEEE Transactions on,* vol. PP, n° 99, p. 1-1.

Zhe, Chen, J. M. Guerrero et F. Blaabjerg. 2009. « A Review of the State of the Art of Power Electronics for Wind Turbines ». *Power Electronics, IEEE Transactions on,* vol. 24, n° 8, p. 1859-1875.

Zhiqian, Chen, M. Tomita, S. Doki et S. Okuma. 2003. « An extended electromotive force model for sensorless control of interior permanent-magnet synchronous motors ». *Industrial Electronics, IEEE Transactions on,* vol. 50, n° 2, p. 288-295.

Zobaa, A. F., et M. Jovanovic. 2006. « A Comprehensive Overview on Reactive Power Compensation Technologies for Wind Power Applications ». In *Power Electronics and Motion Control Conference, 2006. EPE-PEMC 2006. 12th International* (Aug. 30 2006-Sept. 1 2006). p. 1848-1852.